ON PROPAGATION CHARACTERISTICS OF THREE-DIMENSIONAL ELASTIC WAVES GUIDED BY THICK-WALLED HOLLOW CYLINDER AND APPLICATION TO DETECTION OF DAMAGE IN TRAIN AXLE

ALEKSANDRA ZIAJA

Ph.D

The Hong Kong Polytechnic University

2016

The Hong Kong Polytechnic University

Department of Mechanical Engineering

On Propagation Characteristics of Three-dimensional Elastic Waves Guided by Thick-walled Hollow Cylinder and Application to Detection of Damage in Train Axle

Aleksandra Ziaja

A thesis
submitted in partial fulfilment of the requirements
for the degree of

Doctor of Philosophy

September 2015

CERTIFICATE OF ORIGINALITY

I hereby declare that this thesis is my own work and that, to the best of my knowledge and belief, it reproduces no material previously published or written, nor material that has been accepted for the award of any other degree or diploma, except where due acknowledgement has been made in the text.

____________________ (Signed)

Aleksandra Ziaja (Name of student)

To my parents and my better half.

Abstract

Development of reliable structural integrity assessment techniques requires a profound understanding of the physical phenomena existing in the structure under inspection. As an example, guided waves have been extensively studied to enhance their usability for Structural Health Monitoring in various fields of engineering. The knowledge on elastic wave propagation in various types of structures has enabled the development of effective damage detection methods with long range inspection capabilities. Despite the effort, there exists obvious lack of work on certain types of structures germane to industrial applications, an example of which is the high speed railway axle monitoring. Although guided wave-based approaches can potentially reduce the maintenance costs and allow for on-line monitoring, the lack of in-depth knowledge on thick-walled hollow cylindrical waveguides limits the current inspection techniques to non-destructive testing only.

The main aim of this thesis is to provide a quantitative understanding on the elastic wave propagation in hollow cylindrical waveguides with significant thickness-to-wavelength ratio. The work consists of two major parts: 1). Investigation of the cylindrical guided wave theory and understanding of various types of propagating waves and their characteristics; and 2). Utilization of the acquired knowledge to develop an effective damage detection methodology for railway axle inspection.

To this end, a semi-analytical analysis is first performed to investigate the characteristic features of cylindrical guided wave modes and to establish the relationship between a thick plate and a hollow cylindrical waveguide. The analysis reveals the pseudo-symmetry relations of displacement patterns, obtained using asymptotic approximations of Bessel functions. Hyperbolic behavior of the dispersion curves and mode-shape transitions due to the mode coupling phenomenon are also analysed. Theoretical solutions of the dispersion characteristics are compared with the numerical simulations with local interaction

simulation approach, and validated through experiments using laser vibrometry. It is shown that, due to the high thickness-to-wavelength ratio, ultrasonic waves propagating in thick-walled cylindrical structures such as train axles exhibit complex multimodal dispersive behaviour, thus causing significant difficulties to the conventional guided wave-based damage detection techniques. Through numerical analyses, a strong damage-related feature in the 'quasi-surface' longitudinal guided wave signals is revealed and confirmed by experiments. Namely, a near-field wave enhancement effect due to the outer diameter change in the structure is found to be highly effective for damage identification. Based on this phenomenon, a novel inspection method is proposed and explored. Finally, a complete monitoring strategy for hollow railway axles is established and validated.

Publications

Journal papers

[1]. **Ziaja A**, Cheng L., Su Z., Packo P, Pieczonka L., Uhl T., Staszewski W., (2015). Thick hollow cylindrical waveguides: A theoretical, numerical and experimental study, Journal of Sound and Vibration, 350, pp.73–90

[2]. **Ziaja A**, Cheng L., Radecki R., Packo P., Staszewski W. J. Near-field wave enhancement and 'quasi-surface' longitudinal waves in a segmented thick-walled hollow cylindrical waveguide, to be submitted

[3]. **Ziaja A**, Cheng L., Packo P., Staszewski W. J. Feasibility study of wave enhancement phenomenon for structural integrity assessment of hollow train axles, to be submitted

Conference papers

[1]. **Ziaja A.**, Cheng L., Su Z., Staszewski W. J., Uhl T., Packo P. (2014). Elastic waves characteristics in thick-walled hollow cylinders with internal/external surface excitation for train axle monitoring. In Far East Forum on Nondestructive Evaluation/Testing, Chengdu, China

[2]. **Ziaja A.**, Cheng L., Su Z., Staszewski W. J., Uhl T., Packo P. (2014). On the Coupling of Guided Cylindrical Waves in Thick-Walled Structures. In EWSHM-7th European Workshop on Structural Health Monitoring, Nantes, France

[3]. **Ziaja A.**, Cheng L., Su Z.(2014) Cylindrical guided wave-based approach for Structural Health Monitoring of thick-walled hollow axles. The 4th East Asia Mechanical and Aerospace Engineering Workshop, Hong Kong

[4]. **Ziaja A.**, Cheng L., Radecki R., Packo P., Staszewski W. J. (2015) Cylindrical guided wave approach for damage detection in hollow train axles. In IWSHM-10th International Workshop on Structural Health Monitoring, Stanford, USA

Acknowledgement

There are number of people whose support and assistance played an important role in completing this thesis.

First of all, I would like to express my gratitude to my advisor, Professor Li Cheng, for the continuous support through the length of the degree program and for numerous encouraging discussions.

I would like thank Doctor Zhongqing Su for his guidance at the beginning of my PhD studies.

I would also like to thank Professor Wiesław J. Staszewski and Professor Tadeusz Uhl for the cooperation and hosting me at the AGH University of Science and Technology in Krakow.

I would like to send my thanks to Doctor Łukasz Pieczonka, Doctor Andrzej Klepka and Doctor Łukasz Ambroziński for the technical help with the experiments using one- and three-dimensional laser vibrometry conducted at the AGH UST in Krakow. In particular for the time consuming calibration of the *RoboVib Test Station*.

I would also like to thank Doctor Paweł Paćko for the discussion and help on the numerical models used in this work.

Finally, I would like to thank Rafał Radecki for his help on the development of the cylindrical LISA model and his assistance in setting up some of the experiments.

Contents

Chapter 1

Introduction

1.1 Introduction

Hollow train axles are deemed to be one of the most crucial components of high-speed trains. Due to the high safety requirements, frequent inspections are necessary to prevent fatigue failures during their normal operation. Structural integrity evaluation of railway axles is based on common Nondestructive Testing (NDT) techniques such as visual inspection, magnetic particle inspection, eddy current or ultrasounds. Most of the aforementioned NDT techniques require dismounting of the bogie structure and inspection of the structure's surface in an off-line manner. On the other hand, in-service methods are mainly limited to visual inspection and ultrasonic scanning either from the outside surface or along the bore of the axle. An alternative approach is Structural Health Monitoring (SHM), which provides in-situ information about structural health status considering damages occurrence and structural ageing. However, to develop a fully efficient inspection methodology for railway axles, a complete understanding of the wave propagation phenomena is required.

This chapter serves as an introduction to the field of railway axle maintenance and inspection, starting with basic concepts of nondestructive testing. The discussion is followed by a review of the currently available inspection methods and suggestions on the future research directions. Some crucial limitations in the state of the art are pointed out to show the motivation of this work. For readability, this section does not include a comprehensive literature review on guided waves as it will be discussed separately in the following chapter. Section 1.3 presents the objective of the work and an overview of the thesis is given in section 1.4.

1.2 Motivation

Although train axles are designed assuming an infinite service life, their normal operation is typically limited to 40 years [52]. This huge discrepancy originates from many factors which cannot be easily considered in the design stage, e.g. stochastic loading conditions due to the irregularities of wheels or rails, corrosion, impact originating notches. Recently, a great amount of research has been conducted on the railway axle structural assessment and maintenance improvement [107, 52, 125]. This section serves as an overview of the existing methods and discussion on the future directions in hollow axle inspection.

1.2.1 Problem background

Cracks in train axles are widely considered as one of the most serious incidents. This is due to the fact that their appearance imminently lead to the fracture of the axle and the derailment of the train. Even though strict safety requirements are imposed on railway companies, including clear regulations on inspection methods and proper axle maintenance, between 2006 and 2012 only in Europe in total 484 railway axle failures were reported [115, 116]. Another important fact to consider while discussing the need of effective maintenance is that the costs of a train accident include also the infrastructure and environmental cost (e.g. due to spill of toxic chemical compound) and cost of delays.

Research on axle failures has identified three main sources of crack initiation as: corrosion pits, notches due to flying ballast impacts, and non-metallic inclusions [103]. The mechanism of crack formation due to corrosion can be explained as follows. Corrosion pits first develop into multiple surface microcracks whose coalescence forms a fatal mackrocrack [103, 10]. Furthermore, corrosion has detrimental effect on fatigue properties of the structure and influences the existing crack propagation (e.g., stress corrosion cracking) [10]. The second type of the aforementioned crack initiation sources, i.e. the notches due to the flying ballast impacts, is observed mostly for high-speed trains. The flying ballast phenomenon is associated with the mechanical and aerodynamic forces generated by the train passage acting on ballast particles [93]. Due to the local stress concentration at the edges of the notch, and often because of the damaged zones of protective surface coating, the notches generated by impacts are likely to develop into fatigue cracks. The third important factor in fatigue cracks initiation is the presence of the non-metallic inclusions. The high-speed train derailment in Cologne, Germany in July 2008 caused by a fatigue fracture of one of the driving axles resulted in intensified research interest into the effect of the non-metallic inclusions on axle fractures. Studies have shown that the presence of abnormal inclusions in a structure has significant influence on the axle lifetime due to the shortening of the crack initiation stage [53, 125]. Finally, it is worth mentioning that the strength of the axle may be also reduced by the temperature effects such as overheating due to a damaged bearing, which is a typical cause of fracture at the journal.

Another important aspect related to the train axle maintenance is the knowledge about the locations that are prone to fatigue crack initiations and about the geometry of a typical fatigue crack. The studies [128, 126] have shown that fatigue cracks often develop at the geometric transitions of the axle (e.g. between the shaft and the wheel seat) as well as at the press fit regions underneath the wheel/gear/break disk. This is related to the stress concentration and the loading conditions as discussed in [124]. Typically, at the initial stage the surface crack is of a semi-elliptical or semi-circular shape [127]; as the crack propagates through the wall of the axle, in the radial direction, its depth to circumferential length ratio decreases (see Fig. 1.1b). The initial size and geometry of the defect is an important factor for the residual lifetime analysis of a component, thus it has to be rigorously considered for establishment of an effective inspection intervals. As mentioned, due to the fatigue loading the surface crack extends both in circumferential and radial directions until the break-through of a crack through the wall of the axle occurs. Although, the crack break-through does not immediately lead to the axle failure, due to the rapid extension of relatively large cracks, the ‘break-through limit’ is considered as a *critical depth* of the crack for hollow axles [128].

Having discussed the typical origins of axle failures, the attention in the following

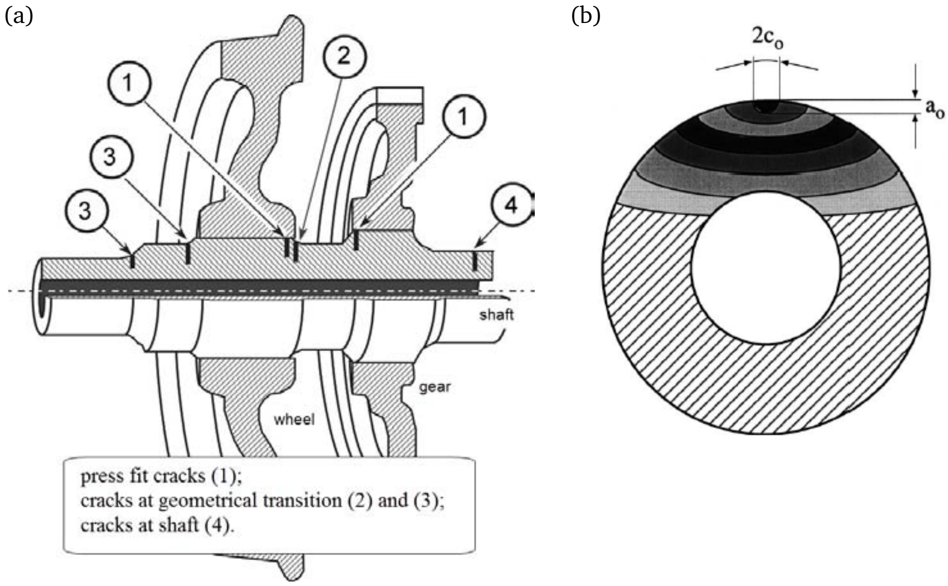

Figure 1.1: (a) Typical crack locations in a train axle. After [126]. (b) Common pattern of the fatigue crack propagation. a_0 - initial depth, c_0 - initial length of the crack. After [127]

subsection is turned to the introduction of the currently employed inspection methods of railway axles.

1.2.2 Overview of the existing axle inspection methods

To begin with, we may distinguish three levels of the assessment of structural integrity of a train axle following Zebrst *et al.* [125]. The primary safety level is carried out at the design stage. It corresponds to the fatigue strength analysis including fatigue crack propagation, investigation of typical crack initiation locations and service life expectancy analysis. The secondary level is based on periodic inspections with nondestructive testing methods. The inspections can be carried out either on bare axle during bogie and wheel overhaul or with the wheels, bearings and brake discs still mounted on the axle. These methods are examined in more detail later in this section. Finally the in-service damage detection procedures can be introduced as a third level of integrity assessment, allowing for axle monitoring during its normal operation or stopovers.

Since various inspection techniques have different sensitivity, the probability of detection (POD) of a crack is often used to characterize the method and than to develop an optimal maintenance schedule. It is well known that, for effective maintenance an inspection period needs to be shorter than the minimum time needed for a fatigue crack to grow beyond the axle failure limit (typically the wall breakthrough limit is applied). Assuming the initial crack size according to the POD value of the chosen inspection technique and using the crack propagation model, the inspection intervals are planned.

As mentioned earlier, numerous inspection approaches, which differ in various aspects such as detectability, costs or requirements on train downtime, are available. The maintenance scheme is usually a trade-off between costs and safety requirements. The following section provides an overview of the methods currently employed for train axle inspection.

Non-destructive testing of axles

Non-destructive testing (NDT) methods allow for inspection of material without damaging its structure. The NDT approaches are widely used for train axle inspection both at the manufacturing stage and in service in the depot or at the overhaul.

The most common type of NDT is *visual inspection*. Visual inspection is carried out under the appropriate lighting, with or without additional optical equipment. For train axles, this type of inspection typically covers the area of the axle-shaft surface between the wheels. The surface is examined by trained and qualified operators for any mechanical damage including fluting, pitting, notching or cracks and also for any sights of corrosion and coating damages [114].

Dye penetrant inspection (DPI) is a low-cost NDT method dedicated for surface-breaking defects. It requires careful pre-cleaning of the surface to assure fluid penetration –fluorescent or nonfluorescent dye– into the discontinuities. After adequate dwell time the penetrant is cautiously rinsed from the surface and a developer is applied. The developer draws the penetrant out to the surface resulting in visible crack indication.

Magnetic particle inspection (MPI) is a surface and subsurface inspection method based on the magnetic field leakage effect. The inspection is carried out by magnetizing the investigated structure and applying a suspension of the ferromagnetic particles on the surface. The discontinuity in the material causes the distortion of the magnetic field called leakage effect. This phenomenon results in the attraction of the ferromagnetic particles at the damage region, which can be then identified by visual inspection. Since the magnetic field has to be perpendicular (in ideal case) to the defect, thus for the detection of longitudinal cracks in an axle, a current flow through the axle is used, while for inspection of transversal cracks, coil magnetization moving along the part is required [71].

Eddy-current testing (EC) utilizes the electromagnetic induction for surface and sub-surface flaw detection. The principle of the method is as follows. An alternating current flowing through a wire coil generates a magnetic field, which if brought close to a conductive material, induces an eddy current flow. In the presence of a defect the magnetic field is interrupted. This results in changes of the impedance of the coil, which is used as a defect indication.

Ultrasonic NDT methods are based on the propagation of elastic waves in the structure; typically short pulse-waves with center frequencies of 0.1-15 MHz. When an ultrasonic transducer is passed over the surface of the inspected object, the reflection and/or wave mode conversion caused by the material discontinuity becomes a signature of a damage. Most of ultrasonic transducers require couplant e.g. oil or water for impedance matching, an exception is air-coupled transducer.

The ultrasonic methods for hollow axle inspection can be deployed in various ways. In general one should distinguish between *far end scan*, *near end scan*, *high angle scan* and *internal bore scan* [125]. During the far end scan the axle is inspected from its ends to the mid-span region or further. The near end scan is used for examination of the adjacent wheel/brake/gear seat, while for the high angle scan the inspection is carried out from the axle body across the seat. For hollow train axles the examination is conducted usually from the bore. Numerous approaches including phase array transducers [38] or semi-automatic systems [73] are available. The sensitivity of the ultrasonic scanning varies strongly depending on the exact technique used, axle geometry, crack location, probe type and by far on operator's skills. Typically the high angle scans and angled beam probes tend to give better results among all ultrasonic methods [101]. To enhance the sensitivity of the ultrasonic scanning, the synthetic aperture focusing technique (SAFT) can be additionally implemented [125].

Summing up, a great deal of research on train axle maintenance has been conducted in the past on NDT-based methods. As in the case of any damage detection technique, the choice of the suitable approach depends on various aspects such as: geometry of the structure, costs, reliability or possibility of automation. An interesting comparison of the common axle nondestructive testing methods, obtained via experimental tests, was done by Rudlin [101] as a part of WIDEM project. Some of the detectability findings are presented in the table 1.1. Note that most of the Rudlin's results agree with those presented earlier by Benyon and Watson [9].

Table 1.1: *Overview of NDT methods for train axle inspection. POD values after [101].*

inspection method	POD>90 %	main features
Magnetic particle	2 mm [13]	visual indication of crack
Eddy-current	0.2 mm	effective for small surface cracks
Ultrasound (far end)	13 mm	strongly depends on axle geometry
Ultrasound (near end)	3-8 mm	inspection of adjacent wheel seat (solid axles)
Ultrasound (high angle)	1-2.5 mm	inspection of inaccessible regions from axle body

Among widely used train axle inspection techniques, the magnetic particle and eddy current methods are recognised as the most effective, low cost approaches for inspection at overhauls. However, these methods require direct access to the surface, which significantly limits their application to periodic check-ups and introduces additional possibilities of scratching during dismounting. Ultrasonic inspection seems to have greater flexibility regarding in-service inspection. However, as pointed out in numerous studies [128, 101] the sensitivity of the manual ultrasonic methods depends on the axle geometry, crack location and operator's skills. An alternative to the manual techniques is semi-automatic systems, which may reduce the human involvement during the inspection.

State of the art in train axle inspection

Up to this point the NDT methods belonging to the second level of the structural integrity assessment, used for periodic inspections, were discussed. These techniques however, are time consuming and prone to human mistakes. Therefore, a considerable effort was made to employ some of the aforementioned methods as semi-automatic procedures. Three examples of the currently available automatized systems utilizing magnetic particle inspection, eddy currents and ultrasounds are shown in figure 1.2.

The systems based on MPI or EC techniques require free access to the inspected surface,

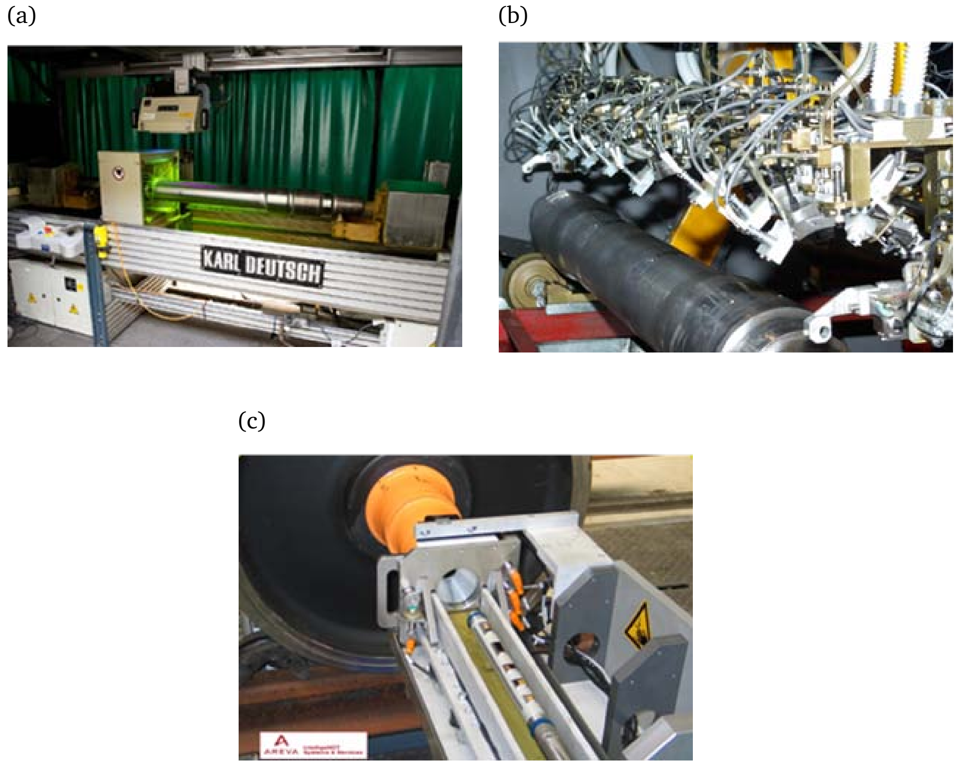

Figure 1.2: Commercially available axle inspection systems (a) MPI-based system DEUTROFLUX UWS systems of KARL DEUTSCH. Photography from [71], (b) Automated EC system SANK-3. Photography from [68], (c) Hollow Axle Inspection System (HPS2) Photography from [73].

thus limiting their applicability to inspections at the production stage and at overhauls with wheels removed. In both of the presented examples, the process of surface scanning was automatized. Nonetheless the operator is still needed to visually inspect the component in case of MPI, or to interpret the results for EC-solution. Another interesting solution is the hollow axle inspection system based on the rotating ultrasonic probes (figure 1.2(c)). In addition to stationary assembly for inspection of bare axles with dissembled wheel sets, this system allows also for in-service examination with a mobile unit. Although the solution is promising, some researchers claim that the rotating ultrasonic probe-method is only sensitive to the cracks of 10 mm deep or greater [101].

Several recent studies investigating the possibility of non-contact axle inspection have been carried out on laser-ultrasonic methods [78, 76, 16]. All the proposed techniques employ Rayleigh surface waves excited by a laser pulse and an air-coupled ultrasonic sensor. The scattering of the surface wave is the basis for the damage detection. The feasibility analysis of the laser-ultrasonic approach for a wayside crack detection system has been recently carried out by Transportation Technology Center of American Railroads [78]. Although some promising experimental results of surface wave-based detection were reported, many technical difficulties including optimal transducer placements, reliability and low signal-to-noise ratio were also encountered. To examine the propagation of a laser-excited elastic wave in a hollow train axle, Mineo *et al.* [76] used numerical simulations with finite element software - ABAQUS. The numerical results presented in that paper confirmed the changes in the Rayleigh wave amplitudes due to a crack occurrence. Unfortunately, the published analysis only examines surface waves disregarding other propagating wave modes. Cavuto *et al.* [16] proposed and experimentally validated a similar approach based on laser-ultrasonic surface scanning. The method however can only be implemented at overhauls as it requires dismounting the axle from the bogie and placing it on a rotating test bed.

Another novel inspection approach, using alternating currents and thermography, was developed under WOLAXIM project [103, 102]. The premise of this method is the heating of the component due to a high frequency electric current applied through the part. Since a crack presence causes distortion of the current flow, it also results in different heating pattern in the thermographic image. This phenomenon serves as a damage indication. Despite the obvious advantages of the method (i.e. non-contact measurements and visual crack indication), the experimental validation of this technique revealed miscellaneous technical challenges such as difficulties in obtaining the necessary currents flow through the axle or effective positioning of the thermal camera.

In view of all what has been mentioned so far, further studies on development of an efficient reliable automatic method is deemed necessary.

1.2.3 Introduction to Structural Health Monitoring

In contrast to the periodic inspections with NDT methods, there seems to be lack of solutions for axle monitoring during its normal operation or stopovers. An alternative to aforementioned non-destructive testing techniques can be Structural Health Monitoring (SHM). SHM methods provide a continuous monitoring on structural health status considering damages occurrence and structural ageing. The information obtained from permanently mounted sensors is further analysed for any abnormalities in the structure, preferably in a fully automatic mode. In order to develop effective monitoring system a complete understanding of the wave propagation phenomenon is necessary. One group of Structural Health Monitoring methods uses guided waves, which allows for fast inspection of large areas, even in case of limiting access to the structure body. A vast amount of the literature investigates ultrasound guided waves in basic geometry structures, such as plate-like structures, rods and thin-walled cylinders, showing their great potentials for aerospace and civil engineering applications [112]. For readability, an in-depth overview on guided waves studies will be given in the following chapter, here only the most important aspects for axles inspection are briefly discussed.

The foundation of the guided waves is attributed to Lord Rayleigh's work on free surface waves in semi-infinite media published in 1885. In a follow-up study, Sir Horace Lamb derived an analytical solution to wave propagation in a free isotropic elastic plate known as Rayleigh-Lamb frequency equations. An analytical framework for cylindrical guided waves was established by Gazis [40] in the late 1950s. That initial work discussed various groups of modes propagating in an isotropic hollow cylinder including axially propagating longitudinal, torsional and flexural modes. Further research in this field has been mostly concentrated on thin-walled structures with application to long distance pipeline inspection e.g. crack detection using torsional modes [30] or corrosion assessment [31] (refer to chapter 2 for more details).

Although the potential of the guided wave is well known, up to now far too little attention has been paid on feasibility of guided waves to damage detection in railway axles. Only the laser-ultrasonic approaches [76, 16] discussed earlier, consider the propagation of Rayleigh waves guided by the outer surface of the axle; however, the difficulties in achieving consistent results restrict their application. Moreover, the current studies lack in-depth analysis and understanding of the wave propagation and the wave-crack interaction phenomena considering multiple guided wave modes. This gap in the knowledge significantly hampers the development of effective guided wave-based inspection techniques for train axles. *Taking into consideration the aforementioned limitations of the currently available solutions, this thesis aims at broadening the knowledge* *about the wave guiding phenomena in thick-walled cylindrical structures required for a development of a new hollow axle monitoring approach.*

1.3 Thesis Objectives

The main goal of this thesis is to develop a broader understanding of elastic wave behaviour in thick-walled cylindrical waveguides. Apart from the scientific interest in guided waves, the practical application of the acquired knowledge became the motivation for this research. Thus, special consideration is made to the case of cylinder geometry parameters, such as wall thickness and radius-to-thickness ratio, typical for hollow train axles. The specific objectives of the work can be listed as follows:

- To gain an in-depth understanding of cylindrical guided waves modes existing in thick-walled structures;
- To establish relationship between the thick-walled cylindrical and plate-like waveguides;
- To explore numerically and experimentally the influence of geometric variations of a waveguide on the wave propagation characteristics;
- To apply the gained knowledge to developing a novel damage identification method;
- To test the feasibility of a well-developed guided wave method for a thick-walled cylinder inspection;
- To propose a hollow axle monitoring procedure;
- To validate the proposed approach via numerical simulations and experiments.

1.4 Overview of the thesis

The outline of this thesis is as follows. Chapter 1 presents the motivation of the work focusing on the real-life problem of railway axle inspection. In addition, an introduction to the basic ideas of structural health monitoring and the thesis objectives are given. Chapter 2 provides a theoretical framework for investigation of guided waves in simple geometric structures including a half-space, a plate and a cylinder. A literature overview on cylindrical guided waves and their applications for damage detection are also provided. Chapter 3 investigates guided wave characteristics of hollow cylindrical structures. The distinct phenomena for thick-walled cylinders and their correlation to the well-developed theories are addressed through analytical, numerical and experimental analyses. Chapter 4 discusses the numerical modelling methods used in the thesis. A two-dimensional axisymetric cylindrical simulation approach developed under the Local Interaction Simulation framework is also introduced and validated. In Chapter 5 the background of the near field enhancement effect is discussed first. On the premise of the enhancement phenomenon, a novel inspection method is proposed. Chapter 6 proposes a complete axle inspection strategy and investigates experimentally and numerically the components of this structural evaluation scheme. Chapter 7 concludes the thesis, discusses limitations and suggests future work.

Chapter 2

Theoretical background

2.1 Introduction

Wave propagation in elastic solids has held researchers' interest for many years. The work of Lord Rayleigh on surface waves [94] is considered as one of the most influential studies in this field. This pioneering paper also started an overall dispute on guided waves phenomenon. In 1917 Horace Lamb published another seminal paper[56] in this field, which proposed an analytical solution to the problem of wave propagation in an isotropic homogeneous plate in vacuum. This solution is now well-known as the Rayleigh-Lamb dispersion relation. Another group of waves are cylindrical guided waves, which are the main interest in this thesis.

This chapter aims to provide an extensive analysis of the guided wave theories established for simple geometric structures such as plates and cylinders. This is done to establish a general framework for the discussion with unified nomenclature, present the links between the theories and highlight some phenomena common for all investigated structures. Before the main discussion, an introduction of the basic concepts of the elastic wave theory and common notation is presented. Section 2.3 introduces the theory of Rayleigh waves, followed by the solution of guided waves in plates and a brief discussion on waves in solid cylinders. A comprehensive analysis of the analytical framework of hollow cylindrical waveguides is given in section 2.4. Finally the state of the art of cylindrical guided waves is discussed in section 2.5.

2.2 Waves in elastic solids - notation and basic concepts

This section presents the basic concepts related to guided wave propagation. It serves as an introduction of both physical understanding and the analytical notation used throughout this thesis.

2.2.1 Physical interpretation

Two types of waves propagating in an isotropic elastic body can be distinguished according to the direction of the particle motion: longitudinal wave when the particle motion is parallel to the direction of the wave propagation, and transverse wave when the particle motion is perpendicular to the wave propagation direction. An alternative terminology is based on a type of stress which they produce in the body (compressional and transverse waves) or the distortion of the body (dilatational and equivoluminal waves). Throughout this thesis these two principal bulk waves are called compressional (P) and shear (S) waves, and their velocities are denoted as v_c and v_s respectively. Considering the two-dimensional in-plane wave motion, it can be shown that neither of these two types of waves can exist by itself if any part of the boundary is traction-free [75]. Except for special cases which are discussed later, an incident P or S wave reflects at a traction-free boundary as both P and S-wave according to the Snell's law [7]. The wave vector component ξ along the propagation direction x must be the same for both P- and S-waves. Thus, defining the wavenumber associated with P-wave as $\gamma_p = \dfrac{\omega}{v_c}$ and the wavenumber associated with S-wave as $\gamma_s = \dfrac{\omega}{v_s}$, the following relations originating from the Snell's law are fulfilled

$$\xi = \gamma_p \sin\theta_p = \gamma_s \sin\theta_s, \tag{2.1}$$

where ω is a radial frequency and θ_p, θ_s are depicted in figure 2.1 .

It follows from Eq. (2.1) that for a certain value of θ_s called a *critical angle*, the reflected P-wave is tangential to the surface as $\sin\theta_p = 1$. For θ_s greater than the critical angle, the P-wave travels tangentially to the surface with amplitude decaying with depth y. Other special cases of wave reflections include waves at grazing incidence (Goodier-Bishop waves), shear waves reflecting at 45° and waves at normal incidence [42, 75].

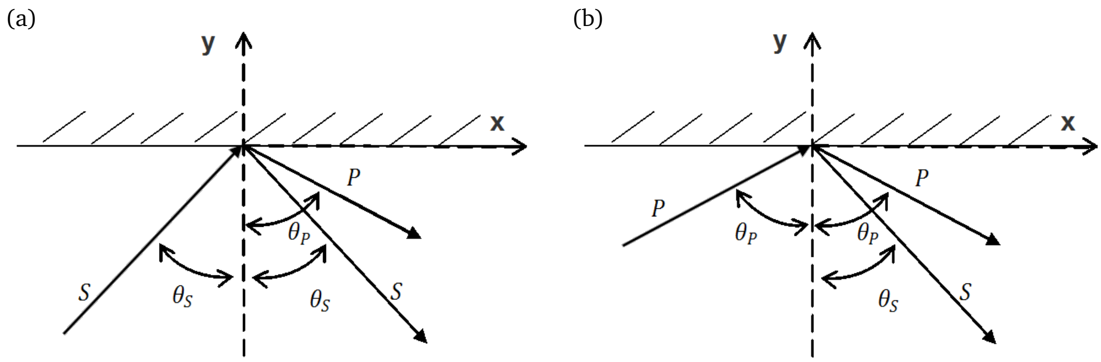

Figure 2.1: Reflection under traction-free boundary condition of (a) P wave and (b) S wave.

In general, any type of geometry in which waves are bounded by one or more surfaces can be regarded as a waveguide. The multiple reflections of the partial P- and S-waves from boundaries results in the total energy flow along the direction of the *waveguide*. The relationship between the wavenumber of the guided wave and the angular frequency ω is called the *dispersion relation*. The sources of the dispersion in elastic media can be listed as follows [104]

(i) the geometric dispersion due to the presence of boundaries,

(ii) material parameters being dependent on the frequency,

(iii) wave scattering due to densely distributed fine inhomogeneities in a material,

(iv) wave dissipation (e.g. energy losses into heat)

(v) the dependence of wave speed on the wave amplitude (nonlinear dispersion)

In this work only the geometric dispersion, which can be also understood as due to multiple wave propagation paths, is considered. Thus, the dispersion relation is obtained from the wave equation with boundary conditions resulting from the structural geometry. The solution to the dispersion equation characterised by a frequency and a mode shape defines a guided wave mode. At this point, another two basic concepts of guided waves should be introduced, namely *phase* and *group velocity*.

The phase velocity is defined by the ratio of the angular frequency and the wavenumber

$$v = \frac{\omega}{\xi}, \tag{2.2}$$

and represents the propagation with a constant phase. While the concept of the group velocity is associated with superposition of waves propagating in the same direction with the same amplitude, but with slightly different wavenumbers. This results in modulation of the signal. The group velocity is defined by

$$v_g = \frac{d\omega}{d\xi} \tag{2.3}$$

and can be interpreted as the velocity of the energy propagation. We may further differentiate among three cases of group-to-phase velocity relation. When $v > v_g$ the wave seems to originate at the rear of the group and travel to the front, when $v = v_g$ the wave package travels without change in shape and for $v < v_g$ the wave appears to originate at the front of the group and travel to the back [42]. Figure 2.2 illustrates the introduced phase and group velocity concepts in the wavenumber-frequency dispersion plot.

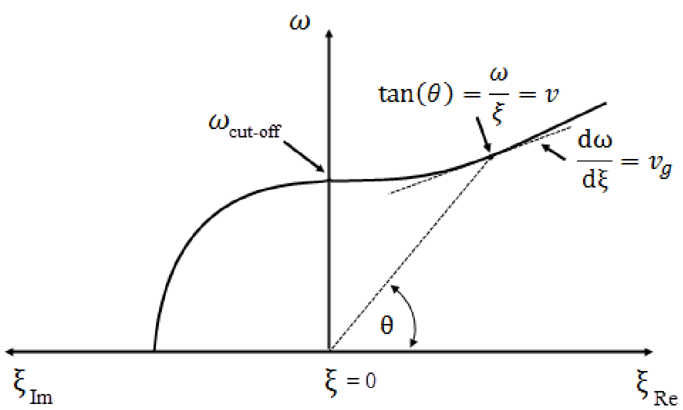

Figure 2.2: Two-dimensional representation of wavenumber-frequency dispersion curve.

As shown, below the cut-off frequency only modes with imaginary wavenumbers satisfy the dispersion relation. Under this condition a guided wave decays exponentially with distance and the character of the mode is changed to the nonpropagating one. The nonpropagating (evanescent) waves become important when analysing a near-field problems such as wave scattering from a defect, which will be discussed in chapter 5.

A useful graphical interpretation of phase and group velocity based on plane wavefronts' propagation is given in [90] and is also presented here in figure 2.3. From this representation one can see that the phase velocity can exceed the maximal velocity of the elastic bulk wave in a given medium i.e. the compressional wave velocity v_c. The

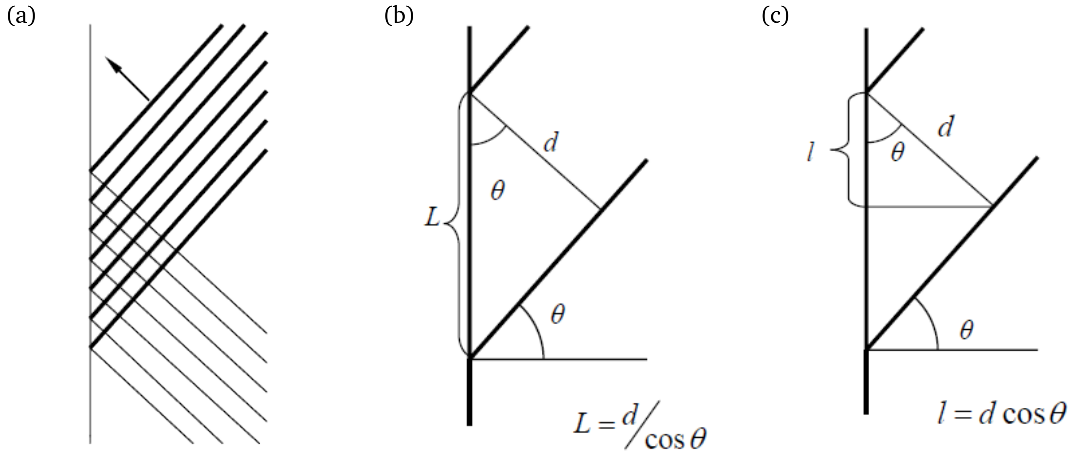

Figure 2.3: (a) Propagation of plane wavefronts, (b) phase velocity illustration with plane waves, (c) group velocity illustration with plane waves. After [90].

argument is as follows. It is noted that the lines of constant phase travel a distance L along the boundary during the same time the wavefront travels a distance d. When the angle θ approaches $\pi/2$, the distance L and correspondingly the phase velocity approaches infinity (while the wavenumber approaches zero). When θ is zero, the wavefronts travel perpendicularly to the boundary thus $L = l = d$. Therefore, the fastest group velocity for straight waveguide corresponds to the compressional plane waves.

Although the partial (or bulk) waves approach of analysing reflections of P- and S-waves is an intuitive method that provides physical understanding, a potentials based approach is often a more convenient way to develop guided wave solution and therefore, it is discussed in the following section.

2.2.2 Analytical description - general formulation

The equations of motion in an elastic, isotropic medium can be obtained from the following three relations [7]

1. Conservation of the linear momentum

$$\nabla \cdot \boldsymbol{\sigma} + \mathbf{F} = \rho \frac{\partial^2 \boldsymbol{u}}{\partial t^2}, \tag{2.4}$$

where $\boldsymbol{\sigma}$ is the stress field, $\boldsymbol{F}$ is the body force field, $\boldsymbol{u}$ corresponds to the displacement field, and ρ denotes density. The ∇ is the vector differential operator, which exact definition in Cartesian and cylindrical coordinates is given in Appendix A.

2. Constitutive equations (Hooke's law)

$$\boldsymbol{\sigma} = c : \boldsymbol{\varepsilon}, \tag{2.5}$$

where σ, ε denotes correspondingly the stress and strain tensor, c is a stiffness matrix and $(:)$ designates the inner product. For an isotropic medium the elastic stiffness matrix c has a form

$$c = \begin{bmatrix} \lambda+2\mu & \lambda & \lambda & 0 & 0 & 0 \\ \lambda & \lambda+2\mu & \lambda & 0 & 0 & 0 \\ \lambda & \lambda & \lambda+2\mu & 0 & 0 & 0 \\ 0 & 0 & 0 & \mu & 0 & 0 \\ 0 & 0 & 0 & 0 & \mu & 0 \\ 0 & 0 & 0 & 0 & 0 & \mu \end{bmatrix}, \tag{2.6}$$

where λ and μ are the two independent elastic constants called Lamè constants.

3. Strain-displacement relations

$$\boldsymbol{\varepsilon} = \frac{1}{2}(\nabla\mathbf{u} + \widetilde{\nabla\mathbf{u}}) = \nabla_s\mathbf{u}, \tag{2.7}$$

where symbol ($\widetilde{\ }$) denotes the transpose of the matrix and ∇_s is the symmetric gradient operator (see Appendix A.).

Substituting the relations (2.5) and (2.7) to the momentum conservation equation (2.4), neglecting the body force, leads to the well-known Navier's equation of motion for the displacement vector $\mathbf{u}$

$$\mu\nabla^2\mathbf{u} + (\lambda+\mu)\nabla\nabla\mathbf{u} = \rho\frac{\partial^2\mathbf{u}}{\partial t^2}. \tag{2.8}$$

To find a solution of the wave equation (2.8), it is convenient to use the Helmholtz decomposition of the displacement $\mathbf{u}$ into a ϕ -dilatational scalar potential and a

H -equivoluminal vector potential

$$\mathbf{u} = \nabla\phi + \nabla \times \mathbf{H}. \tag{2.9}$$

Consequently, the Navier's equation of motion is satisfied if the potentials satisfy the wave equations

$$\begin{aligned} v_c^2 \nabla^2 \boldsymbol{\phi} &= \partial^2 \boldsymbol{\phi} / \partial t^2, \\ v_s^2 \nabla^2 \boldsymbol{H} &= \partial^2 \boldsymbol{H} / \partial t^2, \end{aligned} \tag{2.10}$$

where velocities of compressional and shear waves are

$$v_c = \sqrt{\frac{c_{11}}{\rho}} = \sqrt{\frac{\lambda + 2\mu}{\rho}}, \qquad v_s = \sqrt{\frac{c_{44}}{\rho}} = \sqrt{\frac{\mu}{\rho}}. \tag{2.11}$$

Solving the wave propagation problem requires finding the appropriate particular solutions of Eq. (2.10), in terms of arbitrary functions or integrals over arbitrary functions, satisfying the boundary conditions and the initial conditions.

Note that up to this point, a general formulation was used without limitation to a specific coordinate system. The following sections will recall the solutions for wave propagation in half-space and plate using Cartesian coordinate system, and for solid and hollow cylinder using cylindrical coordinates.

2.3 Overview of fundamental guided waves solutions

This section provides an overview of the existing guided wave theories for the basic geometries. Since the thick hollow cylindrical waveguides are of main interest in this thesis, the solutions corresponding to the limiting values of the inner radius and thickness were chosen for the discussion. First, Rayleigh surface waves on a half-space are presented as a limiting case of a cylinder when its wall thickness approaches infinity (also when $\xi \longrightarrow \infty$). Then guided waves in a plate are analysed as the case of an infinite inner radius of the cylinder ($r_i \longrightarrow \infty$). Finally, wave propagation in a solid cylinder i.e. zero value of inner radius, is discussed.

2.3.1 Surface waves

The analytical description of surface waves was first introduced by Lord Rayleigh in 1885 [94] as a solution of a free vibration problem for an elastic half-space. Rayleigh postulated that in the presence of a boundary, a new type of wave can exist with motion confined to the surface with the velocity of propagation smaller than of a shear wave. This finding was fundamental for geophysics, as it allowed to explain the strong damage-causing tremor appearing during an earthquake. Rayleigh wave solution has also become highly valuable for ultrasonics. In this section of the thesis the discussion on surface waves closely follows another pioneer in this field, Viktorov [121].

Analytical formulation of Rayleigh waves on flat surfaces

Using the notation of scalar potential ϕ and vector potential $\mathbf{H}$ introduced in the previous section, while considering a half-space region ($y > 0$) and propagation direction x, the wave equations (2.10) can be rewritten as

$$\begin{aligned} &\frac{\partial^2 \phi}{\partial x^2} + \frac{\partial^2 \phi}{\partial y^2} + \gamma_c^2 \phi = 0, \\ &\frac{\partial^2 H_z}{\partial x^2} + \frac{\partial^2 H_z}{\partial y^2} + \gamma_s^2 H_z = 0, \end{aligned} \tag{2.12}$$

where γ_c and γ_s are the wavenumbers associated with P- and S-wave respectively.

The solutions to these wave equations are

$$\begin{aligned} \phi &= Ae^{-\gamma_c y}\, e^{i(\xi x - \omega t)}, \\ H_z &= Be^{-\gamma_s y}\, e^{i(\xi x - \omega t)}, \end{aligned} \tag{2.13}$$

that correspond to a plane harmonic wave propagating in the positive direction x with exponentially decaying motion with depth y.

By introducing the traction free boundary conditions (i.e. $\sigma_{yy} = 0, \sigma_{xy} = 0$, at $y = 0$), the characteristic equation of surface waves is obtained as

$$(2\xi^2 - \gamma_s)^2 - 4\xi^2 \alpha\beta = 0. \tag{2.14}$$

For convenience of the analytical solution the following definitions of α and β are also used

$$\alpha^2 = \omega^2/v_c^2 - \xi^2, \qquad \beta^2 = \omega^2/v_s^2 - \xi^2. \tag{2.15}$$

The dispersion relation can be expressed in the equivalent form of the phase velocity relation

$$\left(2 - \left(\frac{v}{v_s}\right)^2\right)^2 - 4\sqrt{1 - \left(\frac{v}{v_s}\right)^2}\sqrt{1 - \left(\frac{v}{v_c}\right)^2} = 0. \tag{2.16}$$

It can be shown that for any value of the Poisson's ratio ν of real media (i.e. ν between 0 and 0.5) the Eq. (2.14) has only one real root which can be approximated as $\xi_R = \gamma_s \dfrac{1+\nu}{0.87+1.12\nu}$ [121]. Figure 2.4 compares the displacements patterns for various values of Poisson's ratio.

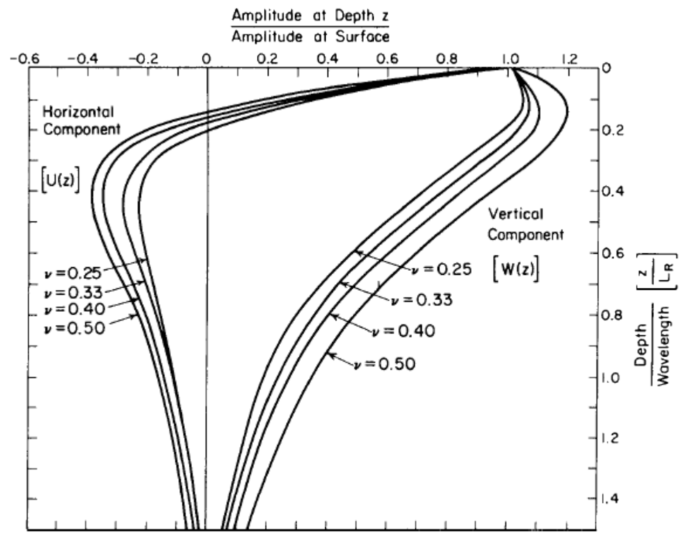

Figure 2.4: Rayleigh wave particles displacement components for various values of Poisson's ratio ν. After [98]

It can be seen, that the surface wave amplitude decays exponentially with the depth. Moreover, the dependence of the magnitude of both vertical and horizontal displacement components on the Poisson's ratio is revealed.

Waves on cylindrical surfaces

Up to this point only the waves propagating along a flat surface were considered; however, surface waves similar to Rayleigh waves can propagate also on convex or concave cylindrical surfaces [121].

In contrast to Rayleigh waves, cylindrical surface waves have dispersive nature. If the dependence on the angular coordinate θ is assumed according to the law $e^{ip\theta}$, where p is the angular wavenumber, the frequency equation of waves on convex cylindrical surface with the curvature of radius R is [121]

$$\frac{J_{p+2}(\gamma_p R) + J_{p-2}(\gamma_p R) - 2\left(\dfrac{\gamma_s^2}{\gamma_p^2} - 1\right) J_p(\gamma_p R)}{J_{p+2}(\gamma_p R) - J_{p-2}(\gamma_p R)} = \frac{J_{p+2}(\gamma_s R) + J_{p-2}(y\gamma_s R)}{J_{p+2}(\gamma_s R) + J_{p-2}(\gamma_s R)}, \tag{2.17}$$

and for concave surface is given as [121]

$$\frac{H^{(1)}_{p+2}(\gamma_p R) + H^{(1)}_{p-2}(\gamma_p R) - 2\left(\dfrac{\gamma_s^2}{\gamma_p^2} - 1\right) H^{(1)}_p(\gamma_p R)}{H^{(1)}_{p+2}(x) - H^{(1)}_{p-2}(\gamma_p R)} = \frac{H^{(1)}_{p+2}(\gamma_s R) + H^{(1)}_{p-2}(y\gamma_s R)}{H^{(1)}_{p+2}(\gamma_s R) + H^{(1)}_{p-2}(\gamma_s R)}. \tag{2.18}$$

Here $J_p(x)$ and $H^{(1)}_p(x)$ are the Bessel and Hankel function the first kind and order p respectively.

It should be noted that for real values of $\gamma_p R$ and $\gamma_s R$, Eq. (2.18) is satisfied only for complex angular wavenumber p. This implies that *a surface wave propagating on concave cylindrical surface propagates with attenuation, radiating energy into the body medium*. This observation is important when analysing the circumferential waves in a hollow cylinder, as will be discussed later in this chapter.

2.3.2 Plate

The analytical solution for a straight crested elastic wave propagation in an isotropic plate with free boundary conditions was developed by Rayleigh [95] in 1889 and Lamb [56] in 1917. Here however, the general frequency equation for a plate involving also shear horizontal waves is recalled after [42]. Only the key equations are reproduced, as they are the foundation for later discussion. Then, a detailed analysis of the dispersion curves of the Rayleigh-Lamb solution for two-dimensional case is discussed following [75]. This comprehensive introduction is believed to be crucial for later comparative analysis of thick plate and hollow cylinder guided wave solutions given in chapter 3.

Analytical formulation

A homogeneous isotropic plate with thickness of $2b$ is considered in Cartesian coordinate system, with the y axis assumed to be normal to the plate with origin at its medial plane. Assuming a straight-crested wave propagating in x-direction, the wave equations (2.10) are satisfied by the potential functions

$$\begin{aligned}
\phi &= (A\cos\alpha y + B\sin\alpha y)\, e^{i(\xi x-\omega t)},\\
H_x &= (C\cos\beta y + D\sin\beta y)\, e^{i(\xi x-\omega t)},\\
H_y &= (E\cos\beta y + F\sin\beta y)\, e^{i(\xi x-\omega t)},\\
H_z &= (G\cos\beta y + H\sin\beta y)\, e^{i(\xi x-\omega t)}.
\end{aligned} \tag{2.19}$$

By Helmholtz decomposition (2.9), the corresponding displacement components are

$$\begin{aligned}
u_x &= i\xi(A\cos\alpha y + B\sin\alpha y) + \beta(-G\sin\beta y + H\cos\beta y)\, e^{i(\xi x-\omega t)}\\
u_y &= \alpha(-A\sin\alpha y + B\cos\alpha y) - i\xi(G\cos\beta y + H\sin\beta y)\, e^{i(\xi x-\omega t)}\\
u_z &= -\beta(-C\sin\beta y + D\cos\beta y) + i\xi(E\cos\beta y + F\sin\beta y)\, e^{i(\xi x-\omega t)}.
\end{aligned} \tag{2.20}$$

Applying the traction free boundary condition at the upper and lower surfaces $y = \pm b$

$$\begin{aligned}
\sigma_{yy} &= (\lambda + 2\mu)\frac{\partial u_y}{\partial y} = 0,\\
\sigma_{yx} &= \mu(\frac{\partial u_y}{\partial x} + \frac{\partial u_x}{\partial y}) = 0,\\
\sigma_{yz} &= \mu\frac{\partial u_z}{\partial y} = 0,
\end{aligned} \tag{2.21}$$

gives six equations with eight unknowns.The remaining two equations result from divergence condition on vector potential **H** (i.e. $\dfrac{\partial H_z}{\partial x} + \dfrac{\partial H_y}{\partial y} = 0$). From the necessary and sufficient condition for the existence of a solution for this set of equations i.e.

vanishing of the determinant, the dispersion relations of a plate are obtained as

$$\cos \beta b = 0, \tag{2.22a}$$

$$\sin \beta b = 0, \tag{2.22b}$$

$$\frac{\tan \beta b}{\tan \alpha b} = -\frac{4\alpha\beta\xi^2}{(\xi^2 - \beta^2)^2} \tag{2.22c}$$

$$\frac{\tan \beta b}{\tan \alpha b} = -\frac{(\xi^2 - \beta^2)^2}{4\alpha\beta\xi^2}, \tag{2.22d}$$

where $\alpha^2 = \omega^2/v_c^2 - \xi^2$ and $\beta^2 = \omega^2/v_s^2 - \xi^2$ (Eq. 2.15). The first two equations describe antisymmetric (Eq. 2.22a) and symmetric (Eq. 2.22b) shear horizontal (SH) group of modes. The particle motion of SH waves is perpendicular to the x-y plane. The latter two equations yield the well-known symmetric (Eq. 2.22c) and antisymmetric (Eq. 2.22d) Rayleigh-Lamb modes. The terms *symmetric* and *antisymmetric* corresponds respectively to a wave mode which in-plane displacement component is symmetrical and antisymmetric about the mid-plane of the plate.

Discussion on dispersion characteristics of Rayleigh-Lamb modes

In more common notation the Rayleigh-Lamb frequency equations are presented as

$$\frac{\tan \beta b}{\tan \alpha b} = -\left(\frac{4\alpha\beta\xi^2}{(\xi^2 - \beta^2)^2}\right)^{\pm 1}. \tag{2.23}$$

The sign " $+$ " at the right-hand side of Eq. (2.23) corresponds to symmetric (extensional) modes and " $-$ " to antisymmetric (flexural) ones.

An exemplary solution of the real branches of the Rayleigh-Lamb equation is presented in figure 2.5. To understand the physical background of the dispersion characteristics, one has to realize that the Rayleigh-Lamb modes are composed of pairs of P- and S- waves reflecting between two boundaries. As mentioned in subsection 2.2.1, at a traction free surface the P- and S-waves exhibit both reflection and mode conversion; however, when a mixed-boundary condition is considered (i.e. $u_y = 0, \sigma_{xy} = 0$ at $y = \pm b$) these two types of waves are uncoupled and reflect only as themselves. The solutions to the characteristic equation of a plate with mixed-boundary condition can be obtained from the following relations [42]

$$\beta b = n\pi/2, \quad \text{for } n = 1, 2, \ldots, \tag{2.24}$$

$$\alpha b = m\pi/2, \quad \text{for } m = 0, 1, 2, \ldots. \tag{2.25}$$

The former equation refers to the S-waves and the latter to the P-waves. The solutions to these mixed boundary condition equations are drawn in figure 2.5 as dashed lines. Note that Eq. (2.24) describes also shear horizontal waves (compare to Eqs. (2.22a-2.22b)).

To systematize the discussion we may first distinguish between three regions of the dispersion curves depending on the phase velocity v values [7]: (a) $v > v_c$, (b) $v_s < v < v_c$ and (c) $v < v_s$. These regions correspond to different behaviour of the partial P- and S-waves which can be conveniently studied with the slowness diagrams shown in figure 2.6.

When the phase velocity is greater than the velocity of the compressional wave, the wavevectors of the partial waves are real. Thus, the compressional and shear parts of the mode field vary trigonometrically with the thickness. At this region in the phase velocity-frequency characteristics, the higher order symmetric and antisymmetric branches form so called *terrace-like* structures [75] (see figure 2.5b).

As noticed by Mindlin [75], the dispersion curves of Lamb modes are bounded between the mixed boundary solutions crossing them only at m even with n even and m odd with n odd. These crossing points coincide with an interesting modeshape pattern; the antisymmetric modes for intersections of even m and n are predominantly equivoluminal, and for intersection of odd m and n are predominantly dilatational [75]. The converse behaviour holds for the symmetric modes. Recently, the experimental validation of the expected minima and maxima of in-plane and out-of-plane displacements at the crossing points has been presented by Veres *et al.* [120].

Second distinct phenomenon occurs when the phase velocity of a mode crosses the compressional wave velocity. At these points the symmetric and asymmetric modes become Goodier-Bishop waves (S-wave reflects from the boundary while P-wave propagates parallel to the surface). With the increase in frequency, the intersection points

(a)

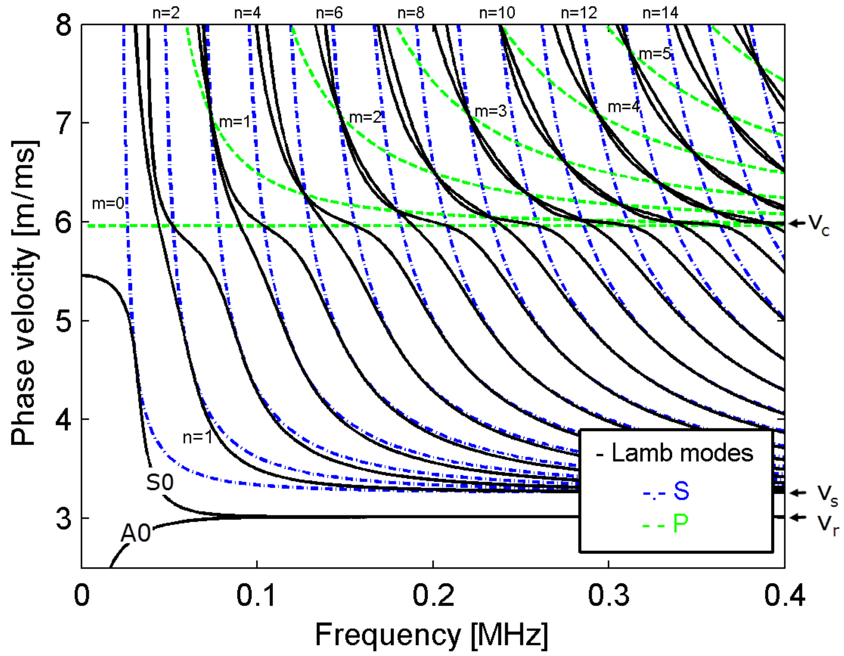

(b)

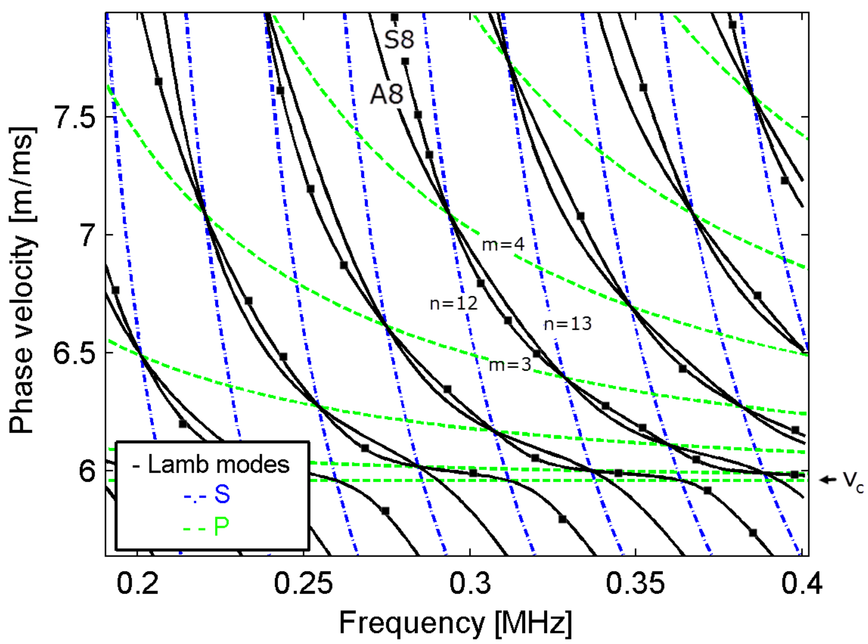

Figure 2.5: Dispersion characteristics of a 75 mm thick plate (steel: $\nu = 0.29$, $E = 216.9$ GPa, $\rho = 7.9 \frac{g}{cm^3}$) with mixed boundary and free boundary conditions, (b) detailed view: terrace-like structures of interlacing symmetric (-□) and antisymmetric (solid–) Lamb wave modes.

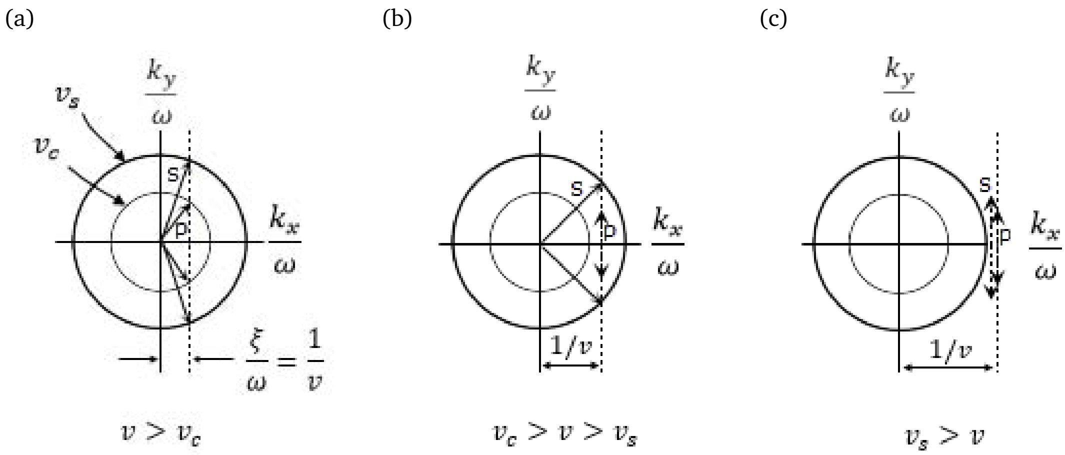

Figure 2.6: Wave slowness diagrams for Lamb waves. v_c, v_s refer to compressional and shear bulk wave velocities. Following [1]

of the symmetric modes with $m = 0$ and $m = 1$ curves become close to each other resulting in nearly constant group velocity with value close to the compressional bulk wave velocity. A similar behaviour can be observed for a solid and a hollow cylinder dispersion curves.

For $v_s < v < v_c$, the compressional part of the field is confined to the boundaries as the wavenumber of the P-wave becomes imaginary (see figure 2.6b). Further in frequency, all modes except of the lowest antisymmetric one intersect with the bounds $n = 1, 2, 3...$ At the intersection point a mode becomes purely equivoluminal, the so-called Lamé mode, composed of pure S-waves reflecting at 45 degrees. It can be seen that except for the two lowest branches labelled as A0 and S0, all modes become dominated by the S-waves as the phase velocity tends to the bulk shear wave velocity. At the intersection of the S0 with shear wave velocity, the second type of the Goodier-Bishop waves occurs, with the incident S-wave parallel to the boundary.

Finally the wavenumbers of both P- and S- partial waves become imaginary and the phase velocities of the two lowest modes tend to the Rayleigh surface waves velocity. To be more precise it can be shown that as $\xi \to \infty$ a linear combination ($\pm$) of the displacements of the lowest symmetric and antisymmetric modes S0 and A0 yields the Rayleigh surface wave solution at the surface of a plate [7].

2.3.3 Solid cylinder

The wave propagation equation in a solid cylinder was independently presented by Pochhammer [87] in 1876 and Chree [22] in 1889. The detailed derivation of the characteristic equation will not be discussed here, since it follows the same approach as for the hollow cylinder solution, which will be given in the following section. Here, only the key equations and a brief discussion on some of the most important features will be presented.

For a wave propagating in the axial direction of a solid cylinder, the solution to the wave equations (2.10) is found as

$$\begin{aligned}
\phi &= AJ_n(\alpha r)\cos n\theta \; e^{i(\xi z-\omega t)} \\
H_z &= B_3 J_n(\beta r)\sin n\theta \; e^{i(\xi z-\omega t)} \\
H_r &= B_2 J_{n+1}(\beta r)\sin n\theta \; e^{i(\xi z-\omega t)} \\
H_\theta &= -B_2 J_{n+1}(\beta r)\cos n\theta \; e^{i(\xi z-\omega t)},
\end{aligned} \tag{2.26}$$

where r corresponds to the radial coordinate of the cylindrical coordinate system (r, θ, z) with z axis assigned to the axis of symmetry of the cylinder. A, B_3, B_2 are the integration constants which can be obtained from the boundary conditions and $n = 0, 1, 2\ldots$ is the circumferential order. In contrast to the Rayleigh-Lamb wave solution discussed in the previous section, the modes propagating in a solid cylinder are not described with trigonometric functions, but with first order Bessel functions J_n.

Applying the traction free boundary condition at $r = r_o$ and solving for the nonzero determinant yields the characteristic equation of the solid cylinder; the exact formulae can be found in various sources see for instance [1, 42]. The Pochhammer-Chree solution describes the uncoupled axially symmetric modes with zero circumferential order –longitudinal and torsional modes–, and double infinite number of flexural modes. The longitudinal modes undergo axial and radial displacements only, while the torsional modes bear only displacements in the circumferential direction.

An interesting phenomenon of dispersion curve plateau regions was observed by Redwood and Lamb [97] for the phase velocity of the longitudinal modes near the compressional bulk wave velocity. At this frequency-wavenumber regions the group velocity of a mode is maximal and the particle displacements are mainly longitudinal [90]. As discussed, similar behaviour can be found for higher order symmetric Lamb modes, but also for the 'pseudo-symmetric' longitudinal hollow cylinder modes which will be introduced later in chapter 3.

Another aspect which is worth mentioning is the occurrence of the so called *trailing pulses* [96] for broad and narrow band frequency excitation. Puckett and Peterson [91] showed that the Pochhammer-Chree theory correctly describes the trailing pulses phenomenon as a superposition of the multiple longitudinal waves propagating with similar group velocities. That observation contradicted the previous understanding of this phenomenon proposed by Redwood [97]. The significance of those findings lies in the ability to directly link the complex multi-modal Pochhammer-Chree solutions with the experimental and numerical results through careful interpretation of the decomposed signal. Moreover, it can be shown that each of the propagating modes contributes to each of the trailing pulses forming the repetitive pattern of pulses.

2.4 Hollow cylinders - theoretical background

This section serves as a comprehensive introduction of the guided waves solutions for a hollow cylinder. The theoretical derivation presented here combines and compares various literature sources to provide a general overview with a consistent notation. The guided wave discussion presented in this section is primarily divided on axially propagating waves and circumferential waves. Among each of these groups, other subgroups of solutions are later distinguished. Note that the analysis of the dispersion characteristics for specific mode types is not presented here, as it will be discussed in the following chapter in detail.

2.4.1 General background

For the clarity of further discussion, a brief introduction to basic notations and expressions is given first. It originates mainly from [42].

An isotropic infinitely long hollow cylinder is considered with the inner radius r_i, the outer radius r_o in the cylindrical coordinate system assigned as shown in figure 2.7.

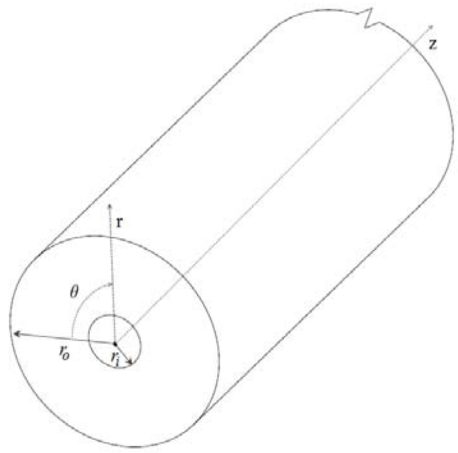

Figure 2.7: Cylindrical coordinate system assigned to an infinite cylinder with the inner radius r_i and outer radius r_o

The wave equation can be derived from the Navier's equation

$$\mu\nabla^2\mathbf{u} + (\lambda+\mu)\nabla\nabla\mathbf{u} = \rho\frac{\partial^2\mathbf{u}}{\partial t^2}, \tag{2.8}$$

using the Helmholtz decomposition (Eq. 2.9) of the displacement vector $\mathbf{u}$ into a diletational scalar potential ϕ and a equivoluminal vector potential $\mathbf{H}$, and the divergence condition on the vector potential $\mathbf{H}$

$$\nabla\cdot\mathbf{H} = F(\mathbf{r},t), \tag{2.27}$$

where $F(\mathbf{r},t)$ is an arbitrary function [40]. The wave equations in form of potential functions is given as

$$\nabla^2\phi = \frac{1}{v_c^2}\frac{\partial^2\phi}{\partial t^2}, \tag{2.28}$$

$$\nabla^2 H_z = \frac{1}{v_s^2}\frac{\partial^2 H_z}{\partial t^2} \tag{2.29}$$

$$\nabla^2 H_r - \frac{H_r}{r^2} - \frac{2}{r^2}\frac{\partial H_\theta}{\partial\theta} = \frac{1}{v_s^2}\frac{\partial^2 H_r}{\partial t^2} \tag{2.30}$$

$$\nabla^2 H_\theta - \frac{H_\theta}{r^2} - +\frac{2}{r^2}\frac{\partial H_r}{\partial\theta} = \frac{1}{v_s^2}\frac{\partial^2 H_\theta}{\partial t^2}, \tag{2.31}$$

According to Eq. (2.9) the components of the displacement vector can be calculated from the solutions to Eqs. (2.28-2.31) as

$$\begin{aligned}
u_r &= \frac{\partial \phi}{\partial r} + \frac{1}{r}\frac{\partial H_z}{\partial \theta} - \frac{\partial H_\theta}{\partial z} \\
u_\theta &= \frac{1}{r}\frac{\partial \phi}{\partial \theta} + \frac{\partial H_r}{\partial z} - \frac{\partial H_z}{\partial r} \\
u_z &= \frac{\partial \phi}{\partial z} + \frac{1}{r}\frac{\partial (r H_\theta)}{\partial r} - \frac{1}{r}\frac{\partial H_r}{\partial \theta},
\end{aligned} \tag{2.32}$$

and the strain-displacement relations can be obtained from the following relations

$$\begin{aligned}
e_{rr} &= \frac{\partial u_r}{\partial r} \\
e_{\theta\theta} &= \frac{u_r}{r} + \frac{1}{r}\frac{\partial u_\theta}{\partial \theta} \\
e_{zz} &= \frac{\partial u_z}{\partial z} \\
e_{\theta z} &= \frac{1}{2}(\frac{\partial u_\theta}{\partial z} + \frac{1}{r}\frac{\partial u_z}{\partial \theta}) \\
e_{rz} &= \frac{1}{2}(\frac{\partial u_r}{\partial z} + \frac{\partial u_z}{\partial r}) \\
e_{r\theta} &= \frac{1}{2}(\frac{1}{r}\frac{\partial u_r}{\partial \theta} + \frac{\partial u_\theta}{\partial r} - \frac{u_\theta}{r}).
\end{aligned} \tag{2.33}$$

Consequently, the stresses in cylindrical coordinates can be evaluated by Hooke's law as

$$\sigma_{ij} = \lambda \Delta \delta_{ij} + \mu e_{ij}, \quad i, j = r, \theta, z, \tag{2.34}$$

where Δ is the dilatation defined as $\Delta = e_{rr} + e_{\theta\theta} + e_{zz}$ and δ denotes the Kronecker delta. (For details of the formulae see Appendix A and B.)

With all the key equations defined, the solutions to an elastic wave propagating in axial (z) and circumferential (θ) directions can be discussed now.

2.4.2 Axial waves

The propagation of harmonic waves in a hollow cylinder under the restriction of the axial symmetry was investigated in the past by McFadden [74] and Herman and Mirsky [50]. A complete theoretical solution including the propagation of the non-axisymmetric waves was established in 1959 by Gazis [40]. The Gazis's solution has become a basis for numerous studies in the field of ultrasonics see for instance [85, 5]. However, since various notations exist and inaccuracies or mistakes can be encountered in many publications including Gazis's paper, it is necessary to present a complete derivation of the analytical solution.

Assuming a harmonic wave propagating in the positive axial direction of the cylinder by denoting the propagation term as $e^{i(\xi z - \omega t)}$ - where ξ and ω are the wavenumber and angular frequency - solutions to the wave equations (Eq. 2.28-2.31) are sought in the form of radius r and angle θ dependent functions

$$\begin{aligned} \phi &= f(r)\Theta_\phi(\theta)\ e^{i(\xi z - \omega t)} \\ H_r &= h_r(r)\Theta_r(\theta)\ e^{i(\xi z - \omega t)} \\ H_\theta &= h_\theta(r)\Theta_\theta(\theta)\ e^{i(\xi z - \omega t)} \\ H_z &= h_z(r)\Theta_z(\theta)\ e^{i(\xi z - \omega t)}. \end{aligned} \tag{2.35}$$

From the wave equation for the dilatational potential ϕ (Eq. 2.28) by separation of variables the following two differential equations are obtained

$$\frac{\partial^2 f}{\partial r^2} + \frac{1}{r}\frac{\partial f}{\partial r} + \left(\frac{\omega^2}{v_c^2} - \xi^2\right) f - \frac{n^2}{r^2} f = 0, \tag{2.36}$$

$$\frac{\partial^2 \Theta}{\partial \theta^2} + n^2 \Theta = 0. \tag{2.37}$$

The solutions of Eq. (2.37) for $\Theta_\phi(\theta)$ are sines and cosines of argument $n\theta$, while n can be either zero or integers (the function has to be periodic in the circumferential direction). Different forms of the Θ function can be found in the literature. Here Gazis's notation is followed, i.e.

$$\begin{aligned} \phi &= f(r)\cos n\theta\ e^{i(\xi z - \omega t)} \\ H_r &= h_r(r)\sin n\theta\ e^{i(\xi z - \omega t)} \\ H_\theta &= h_\theta(r)\cos n\theta\ e^{i(\xi z - \omega t)} \\ H_z &= h_z(r)\sin n\theta\ e^{i(\xi z - \omega t)}, \end{aligned} \tag{2.38}$$

since it clearly demonstrates the character of longitudinal and torsional modes. However, as pointed out by Achenbach [1] the expressions for the potentials can also have a different form

$$\begin{aligned}
\phi &= f(r)\sin n\theta\ e^{i(\xi z-\omega t)} \\
H_r &= h_r(r)\cos n\theta\ e^{i(\xi z-\omega t)} \\
H_\theta &= h_\theta(r)\sin n\theta\ e^{i(\xi z-\omega t)} \\
H_z &= h_z(r)\cos n\theta\ e^{i(\xi z-\omega t)},
\end{aligned} \tag{2.39}$$

Some researchers claim that the solutions proposed by Gazis are only accurate for longitudinal modes [99]. The complete form solutions given in [54] and [99] are respectively

$$\begin{aligned}
\phi &= f(r)\cos(n\theta+\theta_0)\ e^{i(\xi z-\omega t)} && \text{or} && \phi = f(r)\ e^{in\theta}\ e^{i(\xi z-\omega t)} \\
H_r &= h_r(r)\sin(n\theta+\theta_0)\ e^{i(\xi z-\omega t)} && \text{or} && H_r = h_r(r)\ e^{in\theta}\ e^{i(\xi z-\omega t)} \\
H_\theta &= h_\theta(r)\cos(n\theta+\theta_0)\ e^{i(\xi z-\omega t)} && \text{or} && H_\theta = h_\theta(r)\ e^{in\theta}\ e^{i(\xi z-\omega t)} \\
H_z &= h_z(r)\sin(n\theta+\theta_0)\ e^{i(\xi z-\omega t)} && \text{or} && H_z = h_z(r)\ e^{in\theta}\ e^{i(\xi z-\omega t)},
\end{aligned} \tag{2.40}$$

where θ_0 is an arbitrary constant.

In general, n refers to the circumferential mode order, which for axisymmetric modes is zero and for flexural modes takes integer values from 1 to infinity. This range of possible n values implies double infinite number of modes that can exist in a hollow cylinder.

Substituting the general form of the solutions into the three remaining wave equations yields

$$\frac{\partial^2 h_z}{\partial r^2}+\frac{1}{r}\frac{\partial h_z}{\partial r}-\frac{n^2}{r^2}h_z+\beta^2 h_z=0 \tag{2.41}$$

$$\frac{\partial^2 h_r}{\partial r^2}+\frac{1}{r}\frac{\partial h_r}{\partial r}+\frac{1}{r^2}(-n^2 h_r+2nh_\theta-h_r)-\xi h_r+\frac{\omega^2}{v_s^2}h_r=0 \tag{2.42}$$

$$\frac{\partial^2 h_\theta}{\partial r^2}+\frac{1}{r}\frac{\partial h_\theta}{\partial r}+\frac{1}{r^2}(-n^2 h_\theta+2nh_r-h_r)-\xi h_\theta+\frac{\omega^2}{v_s^2}h_\theta=0 \tag{2.43}$$

Equations (2.36) and (2.41) can be easily recognised as Bessel equations. To obtain the similar form of equations for potential functions h_r and h_θ, one should add and subtract Eq. (2.42) and (2.43). It can be shown that the above wave equations are satisfied by the

the following potential functions

$$
\begin{aligned}
f(r) &= AZ_n(\alpha_1 r) + BW_n(\alpha_1 r)\\
h_z(r) &= CZ_n(\beta_1 r) + DW_n(\beta_1 r)\\
h_r(r) - h_\theta(r) &= 2A_1 Z_{n+1}(\beta_1 r) + 2B_1 W_{n+1}(\beta_1 r)\\
h_r(r) + h_\theta(r) &= 2A_2 Z_{n-1}(\beta_1 r) + 2B_2 W_{n-1}(\beta_1 r),
\end{aligned}
$$

where the Z_n and W_n represent the Bessel functions J and Y or modified Bessel functions I and K of order n. The arguments are given as $\alpha_1 r = |\alpha r|$ and $\beta_1 r = |\beta r|$, where $\alpha^2 = \omega^2/v_c^2 - \xi^2$ and $\beta^2 = \omega^2/v_s^2 - \xi^2$, for the compressional v_c and shear v_s bulk wave velocities. The proper selection of Bessel functions should be made depending on the argument of the function - following Table 2.1. The integration constants A, B, C, D, A_1, B_1 are determined from the relevant boundary conditions.

As the next step the *gauge invariance property* ($\nabla \cdot \mathbf{H} = 0$), known also as equal volume condition, is used to eliminate two integration constants resulting in an additional condition of

$$
h_r = -h_\theta := h_1. \tag{2.44}
$$

Table 2.1: *Bessel functions of Eq. (2.44)*

interval	functions
$\alpha^2,\ \beta^2 > 0$	$J_n(\alpha r)$ and $Y_n(\alpha r)$, $J_n(\beta r)$ and $Y_n(\beta r)$,
$\alpha^2 < 0,\ \beta^2 > 0$	$I_n(\alpha_1 r)$ and $K_n(\alpha_1 r)$, $J_n(\beta r)$ and $Y_n(\beta r)$
$\alpha^2,\ \beta^2 < 0$	$I_n(\alpha r)$ and $Y_n(\alpha r)$, $I_n(\beta_1 r)$ and $K_n(\beta_1 r)$

The displacement field associated with potential functions from Eq. (2.44) is

$$
\begin{aligned}
u_r &= (f' + \frac{n}{r}h_z + i\xi h_1)\cos(n\theta)\, e^{i(\xi z - \omega t)}\\
u_\theta &= (-\frac{n}{r}f + i\xi h_1 - h_z')\sin(n\theta)\, e^{i(\xi z - \omega t)}\\
u_z &= (i\xi f - \frac{n+1}{r}h_1 - h_1')\cos(n\theta)\, e^{i(\xi z - \omega t)}.
\end{aligned} \tag{2.45}
$$

Here the prime denotes the derivative with respect to r. Finally, the stress components can be evaluated from the strain field using Hooke's law

$$
\begin{aligned}
\sigma_{rr} &= \mu\left[-\frac{\lambda}{\mu}(\alpha^2+\xi^2)f + 2f'' + \frac{2n}{r}h_z' - \frac{2n}{r^2}h_z + 2i\xi h_1'\right]\cos n\theta\, e^{i(\xi z-\omega t)} \\
\sigma_{r\theta} &= \mu\left[-\frac{2n}{r}f' + \frac{2n}{r^2}f - \frac{n+1}{r}i\xi h_1 + i\xi h_1' - 2h_z'' - \beta^2 h_z\right]\sin n\theta\, e^{i(\xi z-\omega t)} \\
\sigma_{rz} &= \mu\left[2i\xi f' + \frac{n}{r}i\xi h_z' - \frac{n}{r}h_1' - \frac{n(n+1)}{r^2}h_1 + (\beta^2-\xi^2)h_1\right]\cos n\theta\, e^{i(\xi z-\omega t}.
\end{aligned}
\tag{2.46}
$$

To obtain the similar form of the expressions for stresses as the one presented in [40], the relations resulting from Bessel equations Eq. (2.36) and Eqs. (2.41 - 2.43) were used. Note the discrepancies between Eq. (2.46) and the formulas given by Gazis [40]. Some of the mistakes have been correctly pointed out in [86]. Here, the expressions for σ_{rr}, $\sigma_{r\theta}$ match with those presented in [54]; however, in σ_{rz} the term $(\beta^2-\xi^2)h_1$ has an opposite sign. All of the aforementioned mistakes are not propagated to other results.

The traction free boundary conditions $\sigma_{rr}=\sigma_{r\theta}=\sigma_{rz}=0$ at the outer r_o and the inner r_i surface lead to the set of six homogeneous equations defining an eigenvalue problem of axially propagating modes. For the existence of a non-trivial solution, the vanishing determinant condition has to be satisfied, resulting in the characteristic equation of a hollow cylinder

$$
\mid c_{ij} \mid = 0 \quad \text{for} \quad i,j = 1,2,...,6 \tag{2.47}
$$

where the elements of the first three rows of c_{ij} are given by

$$
\begin{aligned}
c_{11} &= [2n(n-1) - (\beta^2 - \xi^2)r_i^2]Z_n(\alpha_1 r_i) + 2\lambda_1\alpha_1 r_i Z_{n+1}(\alpha_1 r_i),\\
c_{12} &= 2i\xi\beta_1 r_i^2 Z_n(\beta_1 r_i) - 2i\xi r_i(n+1)Z_{n+1}(\beta_1 r_i)\\
c_{13} &= 2n(n-1)Z_n(\beta_1 r_i) - 2\lambda_2 n\beta_1 r_i Z_{n+1}(\beta_1 r_i)\\
c_{14} &= [2n(n-1) - (\beta^2 - \xi^2)r_i^2]W_n(\alpha_1 r_i) + 2\alpha_1 a W_{n+1}(\alpha_1 r_i)\\
c_{15} &= 2i\lambda_2\xi\beta_1 r_i^2 W_n(\beta_1 r_i) - 2i\xi(n+1)r_i W_{n+1}(\beta_1 r_i)\\
c_{16} &= 2n(n-1)W_n(\beta_1 r_i) - 2n\beta_1 r_i W_{n+1}(\beta_1 r_i).\\
c_{21} &= -2n(n-1)Z_n(\alpha_1 r_i) + 2\lambda_1 n\alpha_1 r_i Z_{n+1}(\alpha_1 r_i)\\
c_{22} &= \xi\beta_1 r_i^2 Z_n(\beta_1 r_i) - 2\xi r_i(n+1)Z_{n+1}(\beta_1 r_i)\\
c_{23} &= -[2n(n-1) - \beta^2 r_i^2]Z_n(\beta_1 r_i) - 2\lambda_2\beta_1 r_i Z_{n+1}(\beta r_i)\\
c_{24} &= -2n(n-1)W_n(\alpha_1 r_i) + 2n\alpha_1 r_i W_{n+1}(\alpha_1 r_i)\\
c_{25} &= \lambda_2\xi\beta_1 r_i^2 W_n(\beta_1 r_i) - 2\xi r_i(n+1)W_{n+1}(\beta_1 r_i)\\
c_{26} &= -[2n(n-1) - \beta^2 r_i^2]W_n(\beta_1 r_i) - 2\lambda_2\beta_1 r_i W_{n+1}(\beta r_i)\\
c_{31} &= 2in\xi r_i Z_n(\alpha_1 r_i) - 2i\lambda_1\xi\alpha_1 r_i^2 Z_{n+1}(\alpha_1 r_i)\\
c_{32} &= -n\beta_1 r_i Z_n(\beta_1 r_i) + (\beta^2 - \xi^2)r_i^2 Z_{n+1}(\beta_1 r_i)\\
c_{33} &= in\xi r_i Z_n(\beta_1 r_i)\\
c_{34} &= 2in\xi r_i W_n(\alpha_1 r_i) - 2i\xi\alpha_1 r_i^2 W_{n+1}(\alpha_1 r_i)\\
c_{35} &= -\lambda_2 n\beta_1 r_i W_n(\beta_1 r_i) + (\beta^2 - \xi^2)r_i^2 W_{n+1}(\beta_1 r_i)\\
c_{36} &= in\xi r_i W_n(\beta_1 r_i).
\end{aligned}
$$

The parameters λ_1 and λ_2 are equal to $+1$ when the Bessel functions J and Y are used and to -1 in the case of the modified Bessel functions I and K. The introduction of the λ_1 and λ_2 parameters originates from the differences in recurrence relations for J and Y, and I and K.

Substitution of r_o for r_i in the first three rows of c_{ij} leads to the formulas for the three remaining rows. Note that to simplify the expressions, the formulas for stresses were multiplied by $\dfrac{r^2}{\mu}$. Except this scaling difference they closely match the formulas derived in [54]. Similarly when compared to [40] and [86] the expressions presented here differ only by the scaling factor i or (-1) for some terms.

The dispersion curves can be obtained by evaluation of Eq. (2.47) for a given inner radius r_i, outer radius r_o and circumferential order n. One can shown that for the axisymmetric modes i.e. modes with the circumferential order n zero, the characteristic equation decouples for the longitudinal $L(0, m)$ and torsional modes $T(0, m)$, where $m = 1, 2, \ldots$ For the non-zero circumferential order the group of flexural modes $F(n, m)$ is obtained. In the following we will analyse each group of the solutions more closely.

Axisymmetric modes

The determinants of the characteristic equation for longitudinal modes (D_L) and torsional modes (D_T) are formed from the determinant $|c_{ij}|$ as

$$D_L = \begin{vmatrix} c_{11} & c_{12} & c_{14} & c_{15} \\ c_{31} & c_{32} & c_{34} & c_{35} \\ c_{41} & c_{42} & c_{44} & c_{45} \\ c_{61} & c_{62} & c_{64} & c_{65} \end{vmatrix}, \xrightarrow[\xi=0]{} \begin{array}{c} \textit{extensional} \\ \begin{vmatrix} \boxed{\begin{matrix} c_{11} & c_{14} \\ c_{41} & c_{44} \end{matrix}} & \begin{matrix} 0 & 0 \\ 0 & 0 \end{matrix} \\ \begin{matrix} 0 & 0 \\ 0 & 0 \end{matrix} & \boxed{\begin{matrix} c_{32} & c_{35} \\ c_{62} & c_{65} \end{matrix}} \end{vmatrix} \\ \textit{longitudinal shear}_{(n=0)} \end{array} \qquad D_T = \begin{vmatrix} c_{23} & c_{26} \\ c_{53} & c_{56} \end{vmatrix},$$

where the terms c_{ij} are defined by Eq. (2.47) with $n = 0$. The decoupled subgroups of the matrix D_L for $\xi = 0$ will not be described here, as it is discussed separately in the later paragraph on non-propagating modes.

The requirement of vanishing of the determinant D_T of torsional modes gives the following two equations

$$\beta = 0, \quad \text{or} \quad J_2(\beta r_o)Y_2(\beta r_i) - J_2(\beta r_i)Y_2(\beta r_o) = 0. \tag{2.48}$$

The solution of $\beta = 0$ corresponds to the lowest nondispersive torsional mode.

According to Eq. (2.45) the longitudinal modes involve only radial u_r and axial u_z displacements. On the other hand, for the torsional modes the particles exhibit only angular u_θ displacements; however, as pointed out in [1, 99] the alternative formulas for displacements have to be used for this case (Eq. 2.40).

The dispersion characteristics of the axisymmetric modes will be studied in detail in the following chapter; now the attention will be turned to the non-propagating modes.

Non-propagating modes

When the wavenumber ξ is set to zero (non-propagating modes), the determinant $|c_{ij}|$ from Eq. (2.47) decouples for the following two subdeterminants

$$D_1 = \begin{vmatrix} c_{11} & c_{13} & c_{14} & c_{16} \\ c_{21} & c_{23} & c_{24} & c_{26} \\ c_{41} & c_{43} & c_{44} & c_{46} \\ c_{51} & c_{53} & c_{54} & c_{56} \end{vmatrix} \xrightarrow[\text{n=0}]{} \begin{array}{c} \textit{extensional} \\ \begin{vmatrix} c_{11} & c_{14} & 0 & 0 \\ c_{41} & c_{44} & 0 & 0 \\ 0 & 0 & c_{23} & c_{26} \\ 0 & 0 & c_{53} & c_{56} \end{vmatrix} \\ \textit{shear} \end{array}, \qquad D_2 = \begin{vmatrix} c_{32} & c_{35} \\ c_{62} & c_{65} \end{vmatrix}$$

where c_{ij} are given by Eq. (2.47) with $\xi = 0$.

From the condition of vanishing determinant $D_1 = 0$ the plane-strain vibrations are obtained (i.e. $u_r, u_\theta \neq 0, u_z = 0$). Limiting the solution to the axially symmetric vibrations yields decoupled extensional and shear vibrations. It is noteworthy that since the characteristic equation of shear vibrations is described by exactly the same equation as of the torsional waves i.e. Eq. (2.48), the frequencies of plane-strain shear vibrations are the cut-off of the torsional modes.

Consequently, the dispersion characteristics resulting from vanishing determinant D_2 is

$$J_n'(\beta r_i) Y_n'(\beta r_o) - J_n'(\beta r_o) Y_n'(\beta r_i) = 0, \tag{2.49}$$

corresponds to *longitudinal shear vibrations* i.e. only the displacements in the axial direction z are involved. The lowest mode in this group may be viewed as a shearing of the cylinder across its diameter with zero displacement along $2n$ radial planes defined by zeros of function $\cos(n\theta)$.

Flexural modes

When the non-zero circumferential order is considered i.e. $n = 1, 2, \ldots$, the eigenvalues of Eq. (2.47) yield the dispersion curves for the group of flexural modes $F(n, m)$. Some researchers [113, 99] distinguish between the *torsional-flexural* and *longitudinal-flexural* modes according to the mode particles displacement character (see figure 2.8). This however, is not followed throughout this thesis to avoid ambiguities in the description. Nevertheless, if following [99] the terms *wave structures* and *angular profiles* are used for the energy distributions in the radial (r) and the circumferential (θ) direction correspondingly, it can be shown that the modes in the group associated with the same value of mode number m, have similar wave structures, while the angular profile is associated only with the circumferential order n.

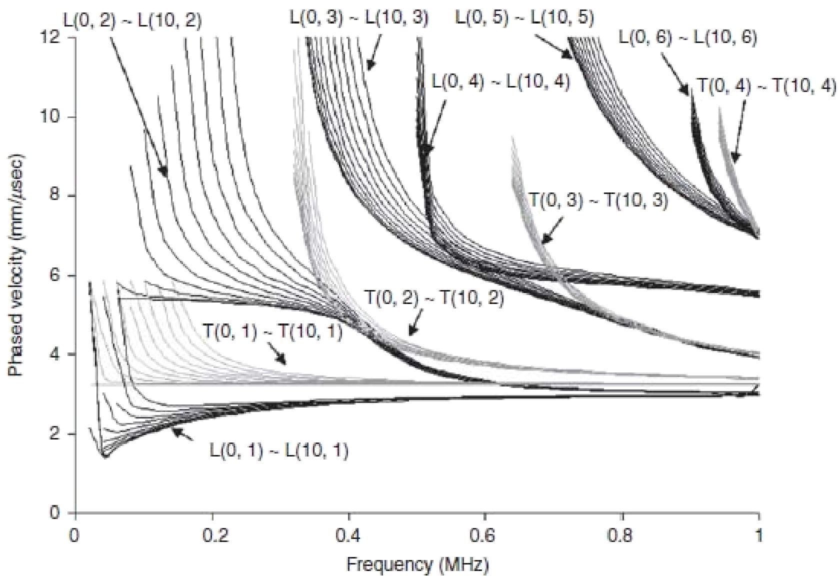

Figure 2.8: Dispersion curves of three-inch schedule 40 steel pipe including the axisymmetric longitudinal L(0,m) and torsional T(0,m) modes (m=1,2,3, ...), and non-axisymmetric longitudinal-flexural L(n,m) and torsional-flexural T(n,m) (n=1,2,3,... 10; m=1,2,3,...). After [99]

An interesting interpretation of flexural waves from plate ray perspective was proposed in [64]. The authors of that paper noticed that, when a hollow cylinder is considered as a wrapped plate, a flexural mode can be analysed as a plate ray propagating at tilt angle ϕ with respect to the cylinder axis. Consequently, the wavefield at a given point is than calculated as a superposition of all plate rays at this point. The wavenumber k_i associated with any plate ray mode can be decomposed into axial and circumferential component as

$$k_i = k_i \sin\phi, \mathbf{e}_\theta + k_i \cos\phi, \mathbf{e}_z. \tag{2.50}$$

Than using the normal mode analysis (refer to [99] for details), the relation between the circumferential order n and the tilt angle ϕ is obtained as

$$k_i \sin\phi, R_m = n, \tag{2.51}$$

where R_m corresponds to the radius of undeformed middle surface (i.e. $R_m = (r_o + r_i)/2$). However, using this 'wrapped plate' interpretation one should have in mind the differences in the behaviour of a wave when the curvature of the path is included (e.g. the dispersion of the surface waves), thus only relatively thin-walled cylinders with sufficiently large inner radius should be considered. Nonetheless, this interpretation can also be treated as a link between the axially and circumferentially propagating waves which are discussed in what follows.

2.4.3 Circumferential waves

Up to this point, wave propagation in the axial direction of a cylinder by assuming resonant modes around the circumference was discussed. The second case which can be considered is a harmonic wave propagating in the circumferential θ direction. It is important to notice that in contrast to the axially propagating waves, this type of waves are guided along a curved path. The curved path condition was briefly analysed in subsection 2.3.1 for Rayleigh surface waves on convex and concave surfaces. For a hollow cylinder, the discussion on circumferential waves can be reduced to an analysis of a two-dimensional annulus. Here, the shear horizontal and plain-strain circumferential waves will be addressed separately.

Circumferential plain-strain waves

The plain-strain waves (i.e. $u_z = 0$) propagation in the circumferential direction of a hollow cylinder is analogue to the Rayleigh-Lamb waves in a plate. Often in the literature this group of waves is referred to as circumferential Lamb waves. Their dispersion characteristics were developed by Liu and Qu [61] and can be obtained using the following approach.

When the time harmonic wave propagating in the circumferential direction θ is analysed, only the displacement potentials ϕ and H_z in the form

$$\begin{aligned} \phi &= f(r)\ e^{i(k_\theta \theta - \omega t)} \\ H_z &= h_z(r)\ e^{i(k_\theta \theta - \omega t)}, \end{aligned} \tag{2.52}$$

are considered, where k_θ is *circumferential wavenumber*. The substitution of solutions (2.52) to the general formula of wave equations (Eqs. 2.28 and2.29) yields the wave equations in the Bessel form

$$f'' + \frac{1}{r} f' + \left[\left(\frac{\omega}{v_c} \right)^2 - \left(\frac{k_\theta}{r} \right)^2 \right] f = 0 \tag{2.53}$$

$$h_z'' + \frac{1}{r} h_z' + \left[\left(\frac{\omega}{v_s} \right)^2 - \left(\frac{k_\theta}{r} \right)^2 \right] h_z = 0 \tag{2.54}$$

with the solutions

$$\begin{aligned} \phi &= \left[A_1 J_{k_\theta} \left(\frac{\omega}{v_c} r \right) + A_2 Y_{k_\theta} \left(\frac{\omega}{v_c} r \right) \right]\ e^{i(k_\theta \theta - \omega t)} \\ H_z &= \left[B_1 J_{k_\theta} \left(\frac{\omega}{v_s} r \right) + B_2 Y_{k_\theta} \left(\frac{\omega}{v_s} r \right) \right]\ e^{i(k_\theta \theta - \omega t)}, \end{aligned} \tag{2.55}$$

The introduction of traction free boundary conditions $\sigma_{rr} = \sigma_{r\theta} = 0$ at inner ($r = r_i$) and outer($r = ro$) surfaces results in a set of four linear homogeneous equations with four unknown constants A_1, A_2, B_1, B_2. The characteristic equation is obtained from the vanishing determinant of this system of equations (see for instance [61] for exact formulae).

Liu and Qu [61] noticed that each radial line of the cylinder can be understood as a wavefront of the propagating circumferential wave with the angular velocity α_θ defined as

$$\alpha_\theta = \frac{\omega}{k_\theta}. \tag{2.56}$$

Therefore, the linear phase velocity at any point on the radius line $r_i \leqq r \leqq r_o$ can be evaluated as

$$v = \alpha_\theta r. \tag{2.57}$$

Two aspects of the discussion presented in [61] should be briefly confronted. Firstly, the authors mentioned the crossing points between modes' dispersion curves of thick-walled cylinder; however, it seems due to the coupling between the modes in the cylinder, the exact crossing points of the dispersion curves does not occur (the details will be given in the chapter 3 while analysing the longitudinal modes). The second aspect is the observation of the group velocity of some modes which is greater that compressional bulk velocity. This in fact may seem extraordinary. The explanation given by the authors is that $v_g > v_c$ "means that the waves will appear to originate at the front of the group, travel to the rear, and disappear" [61], however this statement is somehow vague. The problem can be better understood when the group velocity is illustrated accordingly to what has been discussed for a straight waveguide case in subsection 2.2.1. Figure 2.9 presents a comparison between curved and straight waveguide.

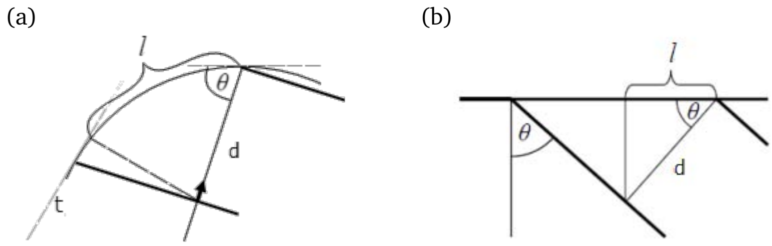

Figure 2.9: Plane wave interpretation of group velocity greater than compressional bulk velocity (- - t tangent line). (a) Curved waveguide and (b) plate (see also figure 2.3).

The d corresponds to the distance travelled by a wavefront at given time, thus for straight boundary $l \leqslant d$. However, as shown in (b) due to the curvature of the waveguide, the distance l can be greater than d and consequently v_g can be greater than the compressional bulk wave velocity.

Circumferential shear horizontal

The second group of modes which can propagate as circumferential waves in a hollow cylinder are shear horizontal (SH) waves. The analytical foundation for their description was developed by Grindin et. al. [43] and by Zhao and Rose [129]. For SH waves, only the displacement in the axial (z) direction should be considered.

Thus, the solution to the Navier's wave equation (2.8) should be of the form

$$\rho \frac{\partial^2 u_z}{\partial t^2} = \mu\bigg(\frac{\partial^2 u_z}{\partial r^2} + \frac{1}{r}\frac{\partial u_z}{\partial r} + \frac{1}{r^2}\frac{\partial^2 u_z}{\partial \theta^2}\bigg), \tag{2.58}$$

where u_z is a function of r, θ and t. Assuming wave propagation in the circumferential direction we look for a general solution

$$u_z = \psi(r)\, e^{i(k_\theta \theta - \omega t)}, \tag{2.59}$$

where k_θ is circumferential wavenumber. Equation (2.58) can be transformed to Bessel type of equation

$$\psi'' + \frac{1}{r}\psi' + \left[\left(\frac{\omega}{v_s}\right)^2 - \left(\frac{k_\theta}{r}\right)^2\right]\psi = 0, \tag{2.60}$$

with solutions

$$\psi = AJ_{k_\theta}\left(\frac{\omega}{v_s}r\right) + BY_{k_\theta}\left(\frac{\omega}{v_s}r\right), \tag{2.61}$$

Using the traction free conditions at the inner and outer surfaces, a homogeneous system of two equations for the unknown constants A and B is obtained. Therefore, the dispersion relation is given by [43]

$$J'_{k_\theta}(\frac{\omega}{v_s}r_i)Y'_{k_\theta}(\frac{\omega}{v_s}r_o) - J'_{k_\theta}(\frac{\omega}{v_s}r_o)Y'_{k_\theta}(\frac{\omega}{v_s}r_i) = 0, \tag{2.62}$$

Note that $\frac{\omega}{v_s}$ is the wavenumber γ_s associated with the partial shear wave. Also it can be seen that Eq. (2.62) and Eq. (2.49) are of the same form. In fact the longitudinal shear vibrations described by Eq. (2.49) are the special case when k_θ are integers i.e. resonant modes in circumferential direction [129].

2.5 Overview of studies on cylindrical guided waves

Previous sections have introduced the analytical solutions of guided waves in a hollow cylinder along with the historical background of their development. The great progress in computational capabilities and instrumentation (piezoelectric transducers, high frequency and high voltage signal amplifiers etc.), allowed for detailed analysis of the established solutions and a development of alternative approaches. This section summarises the major findings in this field and their application to the structural health evaluation.

Early research on feasibility of axially propagating cylindrical waves for damage detection includes a gas pipe inspection technique proposed by Thomson [117] in 1972 and flaws detection in pipes with pulse-echo approach [77] published in 1976. First experimental investigations on the propagation of the two basic longitudinal modes in thin-walled bended tube were carried out by Silk and Bainton [106]. Twelve years later, the theoretical dispersion characteristics including higher order modes, were validated experimentally [81]. In the '90s the cylindrical guided waves have become a promising tool for chemical plant pipework evaluation with Alleyne and Cawley [2, 4, 3] being pioneers in this field.

The capabilities of axisymmetric torsional modes for nondestructive evaluation have been also widely studied in the last few years. This is due to their much simpler dispersive characteristics when compared to longitudinal and flexural modes. In particular, scattering of the fundamental torsional mode T(0,1) from various types of surface discontinuities has been analysed in numerous studies including cracks and notches [30], multiple holes [69], pit clusters [70] and complex geometry defects [14].

A great deal of previous research has focused also on circumferential guided waves and their applications for damage detection. Among many publications on this topic one can find crack characterisation using time-frequency digital signal processing technique [119] or application of wavelet transform [65]. The recent work of by Liu *et al.* [67] using the time reversal focusing method for inspection of a thick-walled cylinder in the circumferential direction is also worth mentioning.

Apart from the damage detection applications some new analytical and numerical approaches have also been developed. Significant contribution to the description and understanding of generation and propagation of cylindrical waves has been done by Ditri and Rose by establishing the Normal Mode Expansion (NME) technique [32]. The NME method allows to evaluate the amplitude response to applied surface loading, using the decomposition of the final response on the orthogonal normal modes bases. An extension of that work to the experimental study on non-axisymmetric modes, can be found in [58]. Further research based on the normal mode expansion concentrates mostly on the mode focusing technique for nonaxisymmertic flexural waves [47, 60]. In recent years, similarly to other guided waves methods, the attention has been turned to the development of the non-linear cylindrical guided waves theory [63, 66, 64]. In fact, the non-linear formulation shows a great potential for further studies.

Although there exist vast literature on wave propagation in pipe-like structures, there is a lack of comprehensive studies on thick-walled cylindrical waveguides. With the increase of thickness, the number of modes satisfying the dispersion relation at a given frequency increases and thus the complexity of the propagating waves. As a result, the interpretation of the ultrasonic signals become strenuous, particularly if waveguide geometry changes causing multiple reflections and mode conversions. For axially propagating waves, the work of Mineo *et al.* [76] on Rayleigh waves for defect detection in train axles, discussed in the previous chapter, can be regarded as one of the few developments in this field. Aiming at the same application (i.e. train axles), a guided wave approach was lately investigated by Fucai *et al.* [57] using numerical simulations. Although, the idea of analysing mode types conversions presented in that paper is interesting, the paper lacks of rigor in many aspects including nomenclature, selection of simulation parameters and the theoretical foundation.

2.6 Summary and conclusions

From a damage detection view point, a clear physical understanding of various wave modes in monitored structures is of paramount importance as the first step in the development of a new structural assessment technique. This chapter has reviewed the existing guided waves solutions for basic geometries, namely a free elastic half-space, a plate, a solid and a hollow cylinder. This was done to establish a general framework for broader discussion in the rest of the thesis. In addition, to allow for comparison of the different solutions, a common notation and derivation approach was followed. Due to the fact that various analytical solutions to elastic wave propagation in a hollow cylinder are available in the literature, the discrepancies and differences were also discussed. Finally an overview of the literature on cylindrical guided waves was presented.

While analysing the characteristics of different waveguide types, the analogous phenomena were pointed out such as interlacing of dispersion curves, group velocity approaching the compressional bulk wave velocity limit for high order modes, or the development of the wavefield confined to the boundaries for the two lowest wave modes. Many of the aforementioned shared features will be studied in details in chapter 3.

The literature overview on cylindrical guided waves has shown that in contrast to thin-walled hollow cylinders, for which research studies have been vibrantly evolving, little research work has been conducted for thick-walled cylindrical structures. Due to this lack of understanding of the complex wave propagation behaviour, there is also little development in damage detection methods for thick-walled cylinders. The next chapter aims to address this knowledge gap, by presenting the theoretical, numerical and experimental studies on cylindrical guided waves characteristics.

Chapter 3

Cylindrical guided waves characteristics

3.1 Introduction

This chapter aims to give a broader understanding of guided waves phenomena in thick-walled cylindrical structures for waves propagating in the axial direction. In particular various wave features specific to thick-walled cylindrical structures are discussed in relation to the well-established theories of plate and solid cylinder waveguides.

The chapter is structured as follows. Section 3.2 introduces an analytical analysis of pseudo-symmetry of axisymmetric longitudinal modes in relation to Lamb waves using approximations of the Bessel functions. Then, the numerically evaluated dispersion characteristics are investigated to understand the sensitivity on geometrical parameters such as inner radius and wall thickness, this study is followed by the discussion on mode interlacing and modeshape transition phenomena. Section 3.4 presents the results of experimental evaluation of dispersion characteristics using a laser vibrometry technique. Finally, the findings are concluded in section 3.5.

3.2 Plate-to-hollow cylinder relation - analytical analysis

3.2.1 Introduction

The analytical framework for the following investigations was presented in details in chapter 2. The nomenclature and notation introduced in that chapter is also followed here.

Typically, the case of low thickness-to-radius ratio of hollow cylinders is considered in the literature as equivalent to the case of thin-walled pipes. Therefore plate theory approximations are frequently employed when wave propagation is investigated. However, since the focus of this work is in the thick-walled cylindrical waveguides, a more general analysis is presented in this section. A paradigm relating wave propagation in hollow cylinders and plates is established analytically using an asymptotic approximation of Bessel functions. This part of the work may be treated as a supplementary analysis that aims to establish the correspondence between Lamb wave modes in a plate and axisymmetric longitudinal modes in a hollow cylinder.

3.2.2 Analytical analysis of pseudo-symmetry of modes

Often the plate theory approximations are employed for thin wall pipes by requiring the radius of the pipe being much larger than the thickness of the wall [60]. This simplification is however invalid for relatively thick-walled tubes. Thus, in order to establish a relation between the plate and cylindrical guided waves, physical phenomena observed in both types of waveguides are here discussed and compared. To facilitate the analysis of displacement and stress components, an asymptotic approximation of Bessel functions is used.

Assuming only propagation of axisymmetric modes in the axial direction of the cylinder, the general solutions to dilatational f, and equivoluminal h_r potentials (Eq. 2.44) in the interval of $v_c\xi < \omega$ are reduced to the form

$$\begin{aligned} f &= AJ_0(\alpha r) + BY_0(\alpha r) \\ h_r &= A_1 J_1(\beta r) + B_1 Y_1(\beta r), \end{aligned} \tag{3.1}$$

where $J_n(x), Y_n(x)$ denote the Bessel functions of first and second kind of order n, and argument x.

When an asymptotic approximation of the Bessel functions [89]

$$\begin{aligned} J_n(x) &\sim \sqrt{\frac{2}{\pi x}}\cos(x - \frac{n\pi}{2} - \frac{\pi}{4}) \\ Y_n(x) &\sim \sqrt{\frac{2}{\pi x}}\sin(x - \frac{n\pi}{2} - \frac{\pi}{4}) \end{aligned} \tag{3.2}$$

is used, the following relations can be obtained

$$\begin{aligned} f &= (A+B)\frac{1}{\sqrt{\pi\alpha r}}\sin(\alpha r) + (A-B)\frac{1}{\sqrt{\pi\alpha r}}\cos(\alpha r) \\ h_1 &= (A_1+B_1)\frac{-1}{\sqrt{\pi\beta r}}\cos(\beta r) + (A_1-B_1)\frac{1}{\sqrt{\pi\beta r}}\sin(\beta r), \end{aligned} \tag{3.3}$$

where, by correspondence to the Lamb waves solution, the components with amplitudes $(A-B)$ and (A_1-B_1) can be identified as corresponding to the pseudo-symmetric parts of the wave, while the $(A+B)$ and (A_1+B_1) to pseudo-antisymmetric parts of the wave. The prefix 'pseudo' refers here to decaying displacements with the radius, as will be discussed later.

The radial and axial displacements are (by substituting Eq. (2.44) to (2.45))

$$\begin{aligned} u_r = \Big[& A\big[\frac{n}{r}J_n(\alpha r) - \alpha J_{n+1}(\alpha r)\big] + B\big[\frac{n}{r}Y_n(\alpha r) - \alpha Y_{n+1}(\alpha r)\big] \\ & + i\xi A_1 J_{n+1}(\beta r) + i\xi B_1 Y_{n+1}(\beta r)\Big] \cos(n\theta)\, e^{i(\xi z - \omega t)}, \end{aligned} \tag{3.4}$$

$$u_z = \Big[Ai\xi J_n(\alpha r) + Bi\xi Y_n(\alpha r) - A_1\beta J_n(\beta r) - B_1\beta Y_n(\beta r)\Big] \cos(n\theta)\, e^{i(\xi z - \omega t)} \tag{3.5}$$

with circumferential order $n = 0$. Then employing the approximation formulae for Bessel functions (Eq. 3.2) and grouping all elements into pseudo-symmetric and pseudo-antisymmetric parts, yield the approximated radial and axial displacements of the form

$$\begin{aligned} u_r = & [\frac{\alpha}{\sqrt{\pi\alpha r}}\cos(\alpha r)(A+B) - \frac{i\xi}{\sqrt{\pi\beta r}}\cos(\beta r)(A_1+B_1)] \\ & + [\frac{-\alpha}{\sqrt{\pi\alpha r}}\sin(\alpha r)(A-B) + \frac{i\xi}{\sqrt{\pi\beta r}}\sin(\beta r)(A_1-B_1)] \end{aligned} \tag{3.6}$$

$$
\begin{aligned}
u_z = &[\frac{\beta}{\sqrt{\pi\beta r}}\sin(\beta r)(A_1+B_1)+\frac{i\xi}{\sqrt{\pi\alpha r}}\sin(\alpha r)(A+B)] \\
&+[\frac{-\beta}{\sqrt{\pi\beta r}}\cos(\beta r)(A_1-B_1)+\frac{i\xi}{\sqrt{\pi\alpha r}}\cos(\alpha r)(A-B)].
\end{aligned}
\tag{3.7}
$$

Note that the propagation term $e^{i(\xi z-\omega t)}$ was skipped here for brevity.

In order to calculate the displacements at the surfaces of the cylinder, the relation between the outer r_o and inner radius r_i in form $r_o = r_i + 2d$ is used, where d is the half-thickness. Finally, by the transverse resonance principle [7] (i.e. partial waves must experience a phase shift of some integral multiple of 2π during the round trip from the outer surface back to the same point) one can observe that

$$
\begin{aligned}
\cos\alpha r_i &= \cos\big(\alpha(r_i+2d)\big) \\
\sin\alpha r_i &= -\sin\big(\alpha(r_i+2d)\big).
\end{aligned}
\tag{3.8}
$$

Thus, the relations for radial and axial displacements at the outer $u(z, r_o)$ and inner $u(z, r_i)$ surfaces of the cylinder can be expressed for the pseudo-antisymmetric case as

$$
\begin{aligned}
u_r(z,r_o) &= \sqrt{\frac{r_i}{r_i+2d}}\,u_r(z,r_i) \\
u_z(z,r_o) &= -\sqrt{\frac{r_i}{r_i+2d}}\,u_z(z,r_i)
\end{aligned}
\tag{3.9}
$$

and for the pseudo-symmetric case as

$$
\begin{aligned}
u_r(z,r_o) &= -\sqrt{\frac{r_i}{r_i+2d}}\,u_r(z,r_i) \\
u_z(z,r_o) &= \sqrt{\frac{r_i}{r_i+2d}}\,u_z(z,r_i).
\end{aligned}
\tag{3.10}
$$

The reasons of using prefix 'pseudo' to describe the wave mode character are twofold. First, to clearly distinguish between a hollow cylinder and a plate structure solution, and second, to highlight the dependence of the curvature on the displacement patterns revealed through $\sqrt{\frac{r_i}{r_i+2d}}$ factor. It can be observed that for the inner radius approaching infinity or the thickness being sufficiently small comparing to r_i, well-known *symmetry* and *antisymmetry* relations of the Lamb wave modes are obtained. Exemplary results illustrating displacements patterns will be given in section 3.3.2.

In contrast to the Lamb waves in plate, the stress components in a hollow cylinder do not follow any form of symmetry or pseudo-symmetry. This can be shown with the same asymptotic approximation approach as was done in the case of the displacements relations. Consequently, applying the asymptotic approximations for radial and axial stresses gives

$$\sigma_{rr_{p-sym}}(r) = \frac{\mu}{\sqrt{r}}\{\frac{1}{\sqrt{\pi\alpha}}[-(\beta^2-\xi^2)\cos\alpha r + \frac{2}{r}\alpha\sin\alpha r](A-B) \\ + \frac{i}{\sqrt{\pi\beta}}[2\xi\beta\cos\beta r - \frac{2}{r}\xi\sin\beta r](A_1-B_1)\} \tag{3.11}$$

$$\sigma_{rz_{p-sym}}(r) = \frac{\mu}{\sqrt{r}}\{i[-2\xi\alpha\frac{1}{\sqrt{\pi\alpha}}\sin\alpha r](A-B) \\ + (\beta^2-\xi^2)\frac{1}{\sqrt{\pi\beta}}\sin\beta r](A_1-B_1)\}. \tag{3.12}$$

Here, only the components of $(A - B)$ and $(A_1 - B_1)$ terms, i.e. pseudo-symmetric displacements, are studied; the relevant stresses for pseudo-antisymmetric components follow the same procedure. Comparison of stresses at the inner and outer surfaces of the cylinder shows the pseudo-symmetry for axial stresses i.e.

$$\sigma_{rz_{p-sym}}(r_o) = -\sqrt{\frac{r_i}{r_i+2d}}\,\sigma_{rz_{p-\ sym}}(r_i). \tag{3.13}$$

However, one can notice that the corresponding relation is not valid for the radial component of stress, due to the $\frac{2}{r}\alpha\sin\alpha r$ and $\frac{2}{r}\xi\sin\beta r$ terms in Eq. (3.11). These coupling terms are inversely proportional to the cylinder radius. At the limiting case of $r\to\infty$, the problem converges to the well-known Lamb waves relations.

3.2.3 Limitations and conclusions

It is important to note that although the accuracy of the evaluated formulae of displacement and stress is increasing with mode order, some limitations apply here. These limitations concern the Bessel function approximations, such as for the case of the inner radius equal to zero (i.e. for a solid cylinder case). Also, since only the first and the second kind Bessel functions were considered here, the discussion corresponds only to phase velocities above the compressional bulk velocity. However, the intention was to investigate the characteristic features of hollow cylinder modes in correspondence to the well-developed Lamb waves theory, thus the approach that relates the Bessel functions of cylindrical structures with cosine/sine functions of a plate was chosen.

Figure 3.1 compares the dispersion characteristics calculated using the exact analytical formulation, and the asymptotic approximation of Bessel functions. As shown, despite the discrepancies in low frequency range, the approximation can be successfully used to evaluate the higher order longitudinal modes.

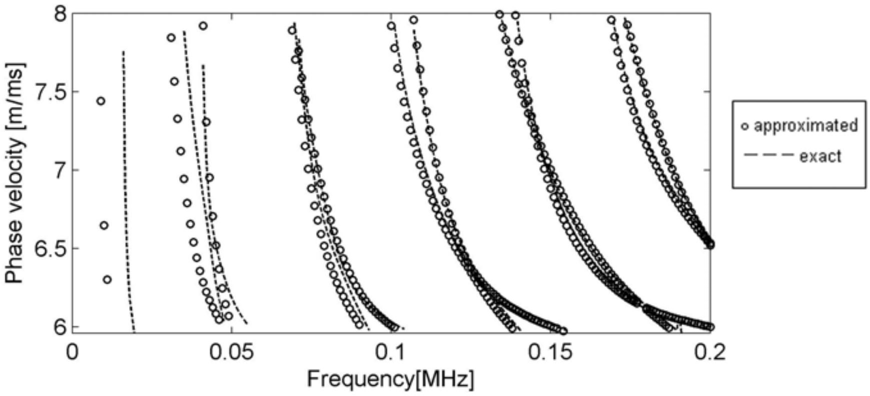

Figure 3.1: Comparison of - - exact theoretical and -o approximated dispersion curves of the hollow cylinder (inner radius 25 mm, thickness 75 mm, steel) longitudinal modes, above compressional velocity limit v_c =5.96 m/ms

The analytical analysis of displacement patterns points out the pseudo-symmetry of the longitudinal modes across the wall thickness. It is important to note that although the findings of the research presented in this section are similar to the conclusions reached in [18] for thin-walled pipes with a high radius approximation, a more general case of hollow cylinder - with an arbitrary radius and wall thickness - was considered here. In practice, the pseudo-symmetry implies that in general, larger displacements for a given mode are expected at the inner rather than at the outer surface of the cylinder.

3.3 Dispersion characteristics of a hollow cylinder

As discussed in chapter 2, the dispersion characteristics for axially propagating modes can be obtained from the vanishing determinant c_{ij} condition Eq. (2.47). The procedure of numerically extracting the roots of the characteristic equation can be found for instance in [99]. In this work the numerical solutions were evaluated with MATLAB software using Newton–Raphson method as a root-finding approach, and assuming fixed step for wavenumber and frequency; typically values of $\Delta\xi = 0.3$ and $\Delta f = 1$ kHz were used.

In this section the properties of the axisymmetric longitudinal modes are first discussed considering the influence of geometrical parameters on the dispersion characteristic and relation to Lamb waves theory. Then the analysis of the dispersion curves of flexural modes is given.

3.3.1 Influence of geometrical parameters

For the sake of clarity of the following discussion, firstly the relation between a thin-walled and thick-walled structures needs to be established. In the work on non-axisymetric guided waves in large-diameter pipes, reported in [60], the argument is given that waves in a hollow cylinder can be treated as Lamb waves propagating in an unwrapped plate –with periodicity condition imposed in the 'unwraped radial' direction–, under the assumption that the diameter of the cylinder is much greater than its thickness. The authors point out that the similarity between behaviour of plate waves and cylindrical guided waves is also frequency dependent. Thus, the division of dispersion plots into the lower frequency region (where the wall thickness is much lower than the wavelength) and the higher frequency region (where the wavelength is comparable to or less than the wall thickness) was proposed. However, this frequency-related separation was based only on visual comparison of phase velocity of corresponding plate and cylinder modes, and neither an explicit condition nor an error estimate have been proposed.

In common engineering practice (e.g. for pressurized cylinders), the thin wall assumption requires that the radial stress component in the wall is negligibly small when compared with the tangential and axial components; this is typical for structures of thickness not larger than 1/10 of the diameter [25]. In the ultrasonic wave propagation analysis the strict division upon thin and thick wall structures has not been clearly stated in the literature; however, the influence of the Mean Radius-to-Thickness (MRT) and the

Thickness-to-Wavelength Ratio (TWR) on dispersion characteristics can be summarised with the two following observations [5]: (i) the TWR is a determining factor for the nature of dispersion curves; (ii) as the MRT ratio tends to infinity the solution uncouples for Rayleigh-Lamb and shear horizontal waves of infinite plate waves. Figure 3.2 illustrates the MRT variation on a longitudinal mode dispersion spectrum. In this example the wall thickness of the cylinder is kept constant (75 mm) and the MRT ratios of 0.6, 1, and 5 were selected for the analysis. In addition, the dispersion curves for a plate of the same thickness solid cylinder with radius 75 mm are presented in the same figure. One should be reminded that the Lamb waves solution can be considered as the limiting case for a hollow cylinder with the infinite mean radius, while solid cylinder case is represented by MRT equal to 0.5 .

The results show that the curves of different MRT parameters become indistinguishable and follow a similar pattern. On the other hand, the sensitivity of the curves to the MRT parameter is relatively large in the low frequency range, where wavelengths are of the same order as the wall thickness of the cylinder. Since the thickness was held constant throughout the entire analysis the key factor influencing the phase velocity is the curvature. The analysis of the results in figure 3.2 also points out that the parameter determining the nature of dispersion characteristics is the MRT-to-frequency ratio, which represents the relationship between the wall thickness, cylinder radius and excitation frequency. This observation implies that when damage detection applications were considered in thick-walled cylindrical structures (for which wavelengths suitable for crack detection are much less than the wall thickness) the curvature influence on dispersion of axisymmetic modes would be relatively small. For such cases the classical plate theory seems to provide a very useful approximation of dispersion characteristics. Despite only small differences in phase velocities between a hollow cylinder and a plate, the relevant particle displacement distributions along the radial direction are significantly different (to be illustrated in the following section). Therefore, the approximations suitable for the analysis of thin-walled large diameter pipes, cannot be simply used for high frequency waves in an arbitrary cylinder. This implication is important when damage detection in such cylinders is considered.

(a)

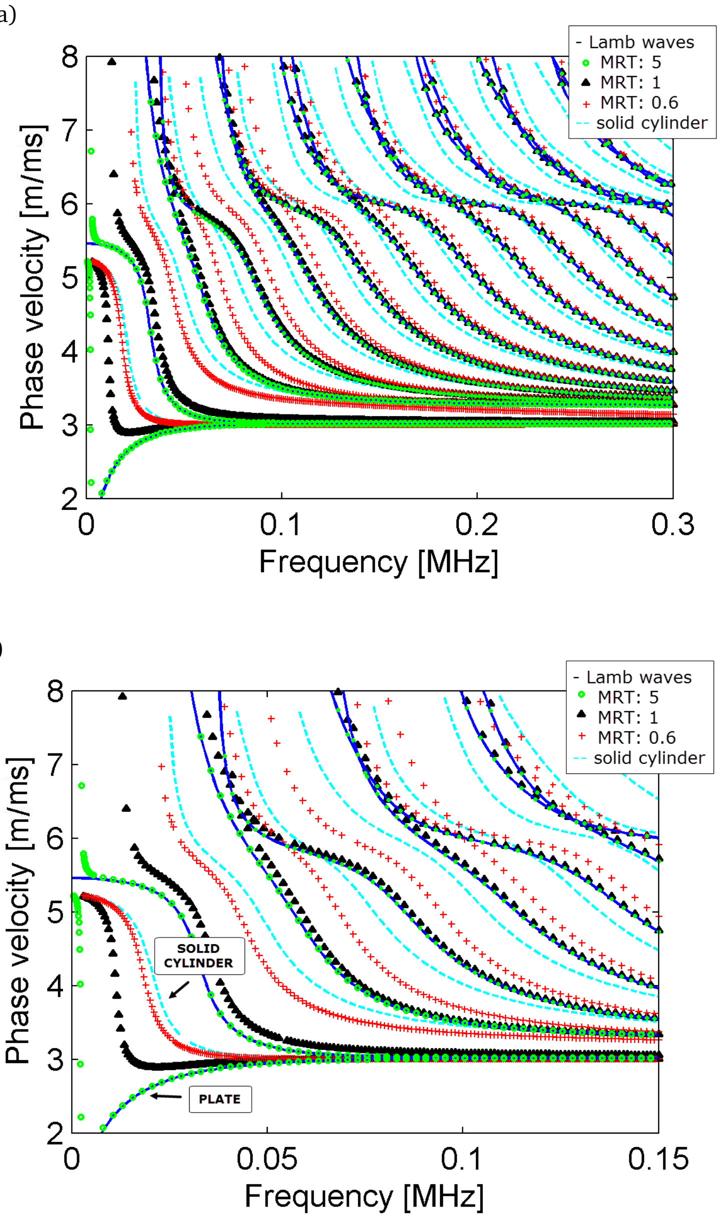

(b)

Figure 3.2: Mean Radius-to-Thickness (MRT) parameter influence on phase velocity dispersion curves for a steel hollow cylinder of wall thickness equal 75 mm in: (a) broad spectrum range, (b) zoomed view displaying lower order modes. Only the longitudinal modes are shown.

3.3.2 Modes interlacing phenomenon

The study related to the influence of the MRT parameter on phase velocity dispersion curves has revealed a regular pattern in the behaviour of higher order axisymmetric modes for a hollow cylinder. This section investigates the characteristic features related to this behaviour. The discussion of dispersion plots analysed follows the order from high to low phase velocity values (i.e. the increasing wavenumber order) .

An example of numerically evaluated dispersion characteristics of axisymmetric modes is illustrated in figure 3.3.

(a)

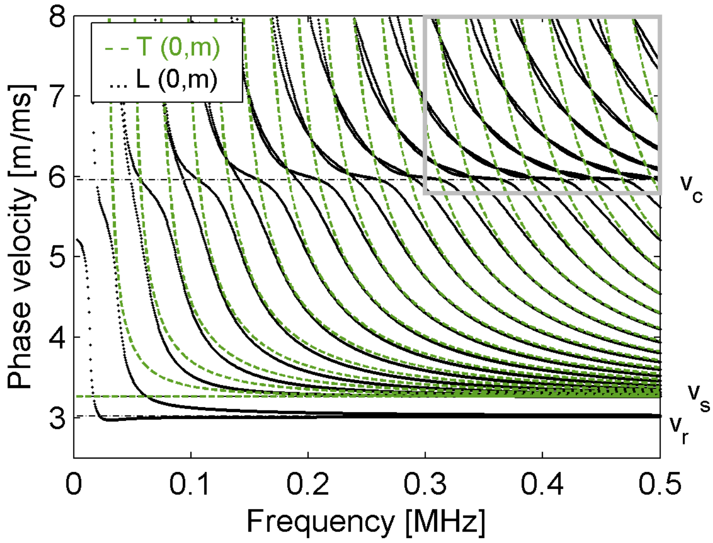

(b)

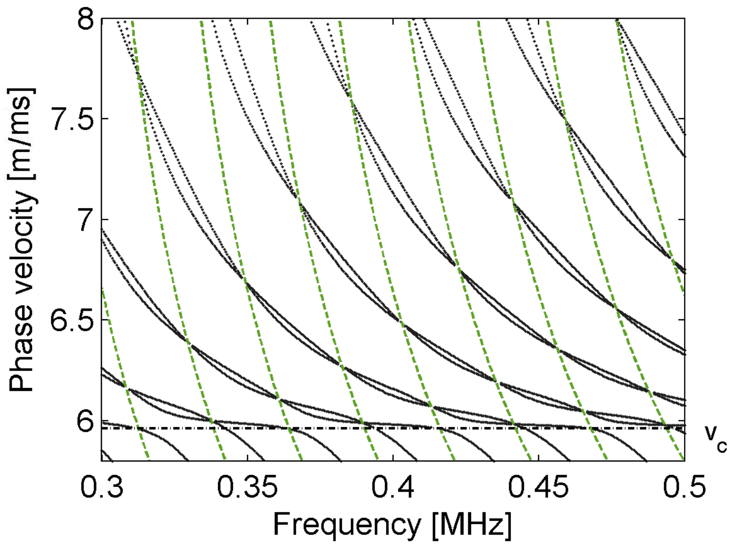

Figure 3.3: Numerically evaluated dispersion characteristics for axisymmetric modes in a steel hollowed cylinder (inner radius - 25 mm; thickness - 75 mm): (a) repetitive pattern of longitudinal $L(0,m)$ and torsional $T(0,m)$ wave modes; (b) terrace-like structures of 'interlacing' $L(0,m)$ modes. The dot-dashed ($-\cdot$) lines indicate the Rayleigh (v_r), shear (v_s) and compressional (v_c) bulk wave velocity limits.

The results show that except the first few wave propagation modes, pairs of longitudinal modes seems to interlace in the phase velocity range above the compressional bulk wave velocity (this velocity for steel is equal to $v_c = 5960$ m/s) and separate below this phase velocity limit. This behaviour is identical for all higher order modes regardless the geometrical parameters of the cylinder, as discussed in the previous section. The exemplary higher order pseudo-symmetric and antisymmetric longitudinal mode shapes - evaluated from the exact solution of the characteristic equation - are presented in figure 3.4. For the case investigated - i.e. for the inner radius equal to 25 mm and the wall thickness equal to 75 mm - the amplitudes of radial and axial displacements at the inner surface of the cylinder are about twice the value of the displacements at the outer surface, as expected from Eq. (3.9-3.10).

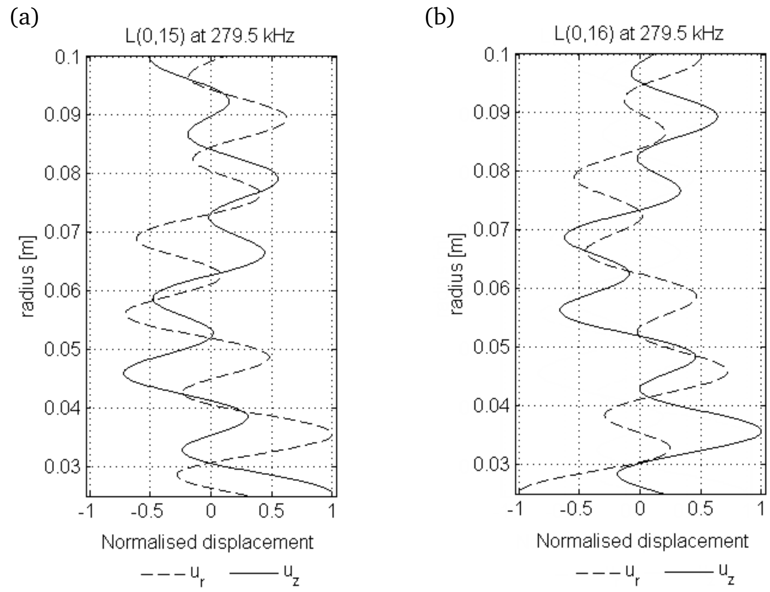

Figure 3.4: Comparison of normalised displacement plots in the axial u_z and radial u_z direction for a steel hollow cylinder (inner radius equal to 25 mm; thickness equal to 75 mm):(a) pseudo-antisymmetric $L(0,15)$ mode; (b) pseudo-symmetric $L(0,16)$mode.

When the relations for thick plates and thick wall cylinders - discussed in sections 3.3.1 and 3.2 - are recalled, the dispersion curve interlacing phenomenon can be examined here more closely, following the elaboration on higher order plate modes and the so-called terrace-like structures [75] presented in chapter 2.

Firstly, the mixed boundary conditions i.e $u_r = 0$ and $\sigma_{rz} = 0$ at $r = r_i$ and $r = r_o$, for axisymmetric modes of a hollow cylinder needs to be found. Similarly to the case of a solid cylinder, torsional modes of a hollow cylinder already satisfy these boundary conditions. The other solutions were evaluated numerically using Eq. (3.4) and (2.46). The results are shown in figure 3.5a. The results show that in the higher frequency region, the torsional modes and decoupled axially polarised shear type cylindrical-modes (SA) overlap. To

(a)

(b)

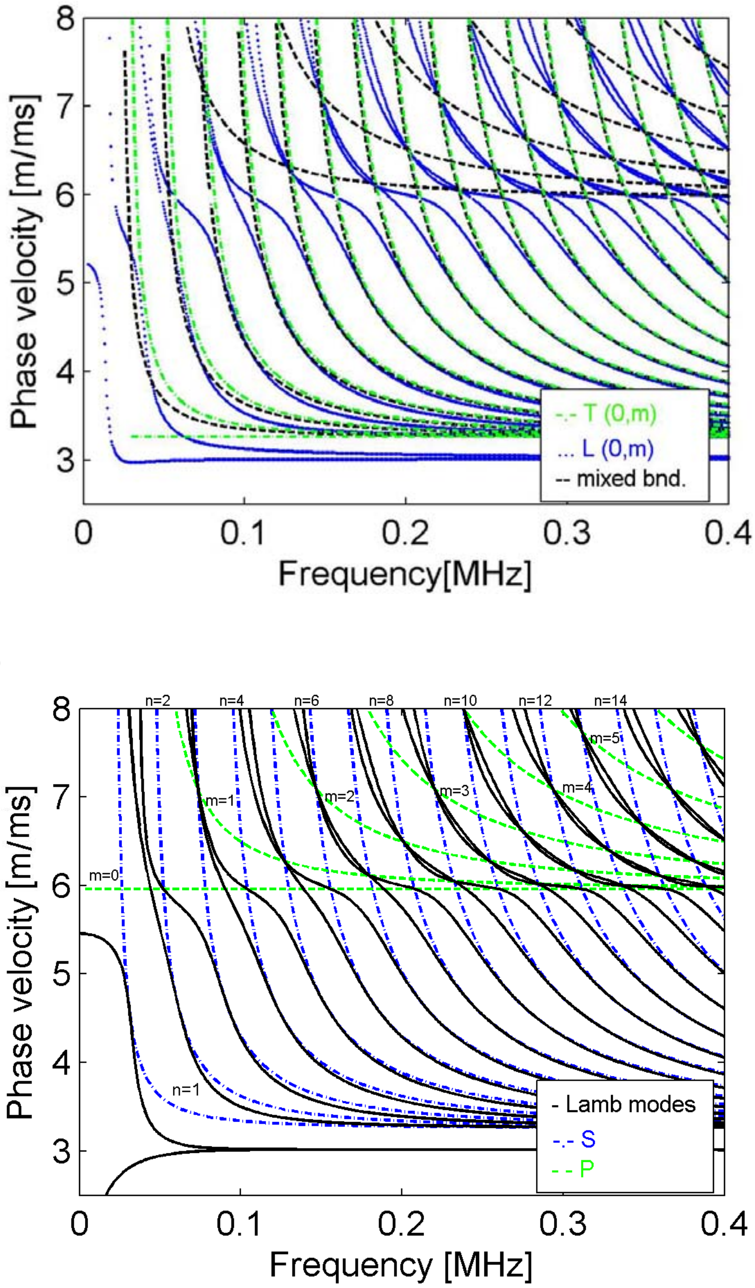

Figure 3.5: Comparison of dispersion curves for 75 mm thick steel: (a) hollow cylinder (axisymmetric modes); (b) plate (Lamb wave modes), for mixed and traction free boundary conditions.

demonstrate the analogy between a hollow cylinder and a plate, the solutions to the plate's characteristic equation - with both mixed and traction free boundary conditions - are presented in figure 3.5b. The mixed-boundary curves for a plate were obtained from relations (2.24) and (2.25).

Similarities in the dispersion characteristics calculated for a thick plate and a thick-walled cylinder can be clearly observed. One should note that the cylinder case $\beta = 0$, equivalent to the plate solution $m = 0$, is not included the dispersion curves for the cylinder due to an asymptotic behaviour of the second kind Bessel function for the argument equal to zero. The terrace-like structures bounded by mixed boundary-modes can be easily distinguished in the analysed results. In contrast to the hollow cylinder solution, the crossing points of the symmetric and antisymmeric plate modes (figure 3.5b) satisfy the characteristic equation with both mixed and traction free boundary conditions. These crossing points coincide with an interesting modeshape pattern, i.e. the antisymmetric modes for intersections of even m and n are predominantly equivoluminal, and for intersection of odd m and n are predominantly dilatational [75]. The converse relevant behaviour holds for the symmetric modes. Although the pseudo-symmetric and pseudo-asymmetric longitudinal modes can be also differentiated according to the displacement patterns, the pairs of modes are coupled via radial stress components, as discussed in the previous section. This coupling manifests itself in the dispersion characteristics by a hyperbolic (non-crossing) behaviour of the curves in the coupling region, as shown in figure 3.6a.

These observations are consistent with the classical understanding of coupled system spectrum behaviour [17]. In the coupling regions, the displacement patterns assigned to a single dispersion curve exhibit transitions between pseudo-symmetric and pseudo-antisymmetric character as depicted in figure 3.7.

The interlacing of longitudinal modes can be also studied from the point of view of the group velocity. This velocity corresponds to the rate of energy transfer in an analysed structure. Figure 3.6b illustrates the interchanging of group velocities for two longitudinal modes in the analysed coupling region. For an uncoupled set of modes (e.g. Lamb waves), the crossings of dispersion curves in a phase velocity spectrum, corresponds to the local minima and maxima of the modes group velocities i.e. resonances and anti-resonances of the modes [118]. It appears that for hollow cylinder longitudinal modes, there is no energy transfer between the two coupled modes and the energy associated with each of the modes travels with the same rate. Thus, one can expect that the waveforms associated with these modes will be almost indistinguishable at any location away from the excitation source.

For frequencies below the modes interlacing region in the phase velocity dispersion curves,

(a)

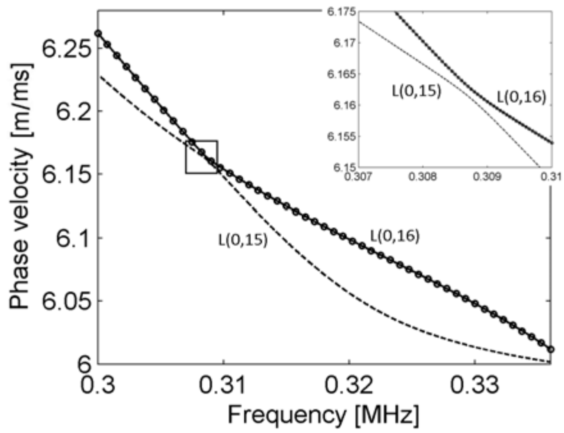

(b)

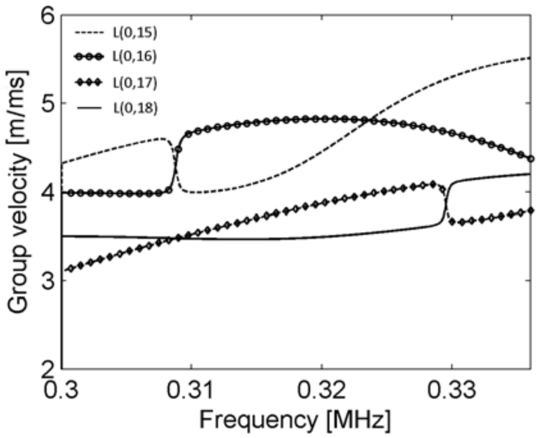

Figure 3.6: (a) Hyperbolic behaviour of a pair of longitudinal modes in a mode coupling region (one should refer to figure 3.3 for the wider phase velocity spectrum); (b) group velocity interchanging behaviour.

another interesting feature can be observed. For higher order pseudo-symmetric modes, the plateau regions around compressional wave velocity v_c can be noticed (figure 3.3). This local phase velocity flat character implies that the group velocity at this region is nearly constant, with an actual value slightly below the compressional bulk wave velocity. Any excitation of modes at this narrow frequency range will result in propagation of almost a non-dispersive wave with a dominant compressional wave component. The described behaviour can be understood as equivalent to the plateau regions observed in the past for solid cylinders [97] and high order Lamb modes [75, 118].

With an increase of frequency, all (except of the lowest pseudo-antisymmetric one) cylinder dispersion curves for longitudinal modes intersect with the ones of mixed boundary cylindrical wave of S-type. At these points the equivoluminal Lamé type modes -

(a)

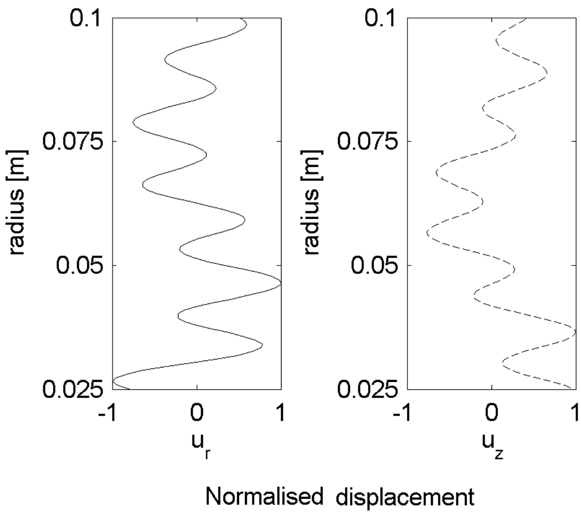

(b)

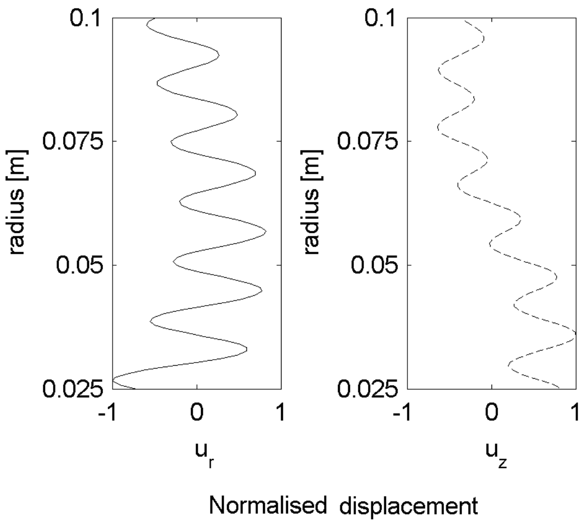

Figure 3.7: Change of the mode character alongside the L(0,16) dispersion curve. Displacement patterns for the frequency: (a) 290 kHz, (b) 320 kHz. The results were calculated using the DISPERSE® software.

composed of shear waves reflecting at 45 degrees - are obtained [40]. When even higher frequencies are analysed, all longitudinal modes except the two first axisymmetric modes: L(0,1) and L(0,2), tend to the shear bulk wave velocity, whereas the phase velocity of the two lowest longitudinal modes approaches the Rayleigh wave velocity and form displacement behaviour comparable to surface waves i.e. energy of the modes is concentrated at the vicinity of the inner/outer surface of the cylinder. This type of waves for both longitudinal and flexural modes is called throughout this thesis *'quasi-surface'* waves.

To complete the discussion it is worth mentioning that, the asymptotic approximations of the dispersion equation for the L(0,1) and L(0,2) in the large wavenumber limit were obtained by Grinchenko [44] as

$$\left(2-\left(\frac{v}{v_s}\right)^2\right)^2-4\sqrt{1-\left(\frac{v}{v_s}\right)^2}\sqrt{1-\left(\frac{v}{v_c}\right)^2}+\frac{2}{\xi}\left(\frac{v}{v_s}\right)^2\sqrt{1-\left(\frac{v}{v_c}\right)^2}=0, \quad (3.14a)$$

$$\left(2-\left(\frac{v}{v_s}\right)^2\right)^2-4\sqrt{1-\left(\frac{v}{v_s}\right)^2}\sqrt{1-\left(\frac{v}{v_c}\right)^2}-\frac{2}{r_1\xi}\left(\frac{v}{v_s}\right)^2\sqrt{1-\left(\frac{v}{v_c}\right)^2}=0, \quad (3.14b)$$

where v corresponds to the phase velocity, $r_1 = r_i/r_o$; and v_c and v_s is the compressional and shear bulk wave velocities respectively. These equations differ from the Rayleigh equation (Eq. 2.16 in chapter 2) by the presence of the third term, which is inversely proportional to the wavenumber. Since this supplementary term is positive in Eq. (3.14a), the phase velocity of the *'exterior quasi-surface mode'* – L(0,1), is somewhat less than the Rayleigh wave velocity. For the wave described by Eq. (3.14b) i.e. *'interior quasi-surface mode'* L(0,2), the phase velocity is slightly greater than of Rayleigh wave. Because this difference in the velocity also depends on the relative thickness of the cylinder through $\frac{1}{r_1}$ factor, it is more pronounced for a thick-walled cylinder. The formation and application of 'quasi-surface' modes will be studied further in chapter 5.

3.3.3 Flexural modes

So far, only the axisymmetric modes i.e. longitudinal $L(0, m)$ and torsional $T(0, m)$, were considered. However, as shown in [58], any partial loading results in the excitation of both, i.e. longitudinal and flexural, $F(n, m)$ modes. Thus, a brief study on non-axisymmetric modes in thick wall cylinders is presented in this section. Figure 3.8 illustrates a change in the nature of the dispersion curves with an increase of the circumferential order. Due to the complexity of the results, the dispersion curves presented were calculated numerically with the fine resolution of 0.1 rad/m in the wavenumber domain and the frequency step of 500 Hz.

The flexural modes dispersion characteristics for thick-walled cylinders are significantly different from thin-walled cylinders (compare figure 3.8 with figure 3.9). The phase velocity-frequency curves for thin-walled cylinders seem to follow the pattern of the axisymetric modes, deflecting to higher phase velocity values with the increase of the circumferential order in the lower frequency range and converging to a single pattern for higher frequencies. On the other hand, for a thick-walled cylinder, the higher circumferential order results in unraveling of the lower flexural modes as marked by a dashed circle in figure 3.8.

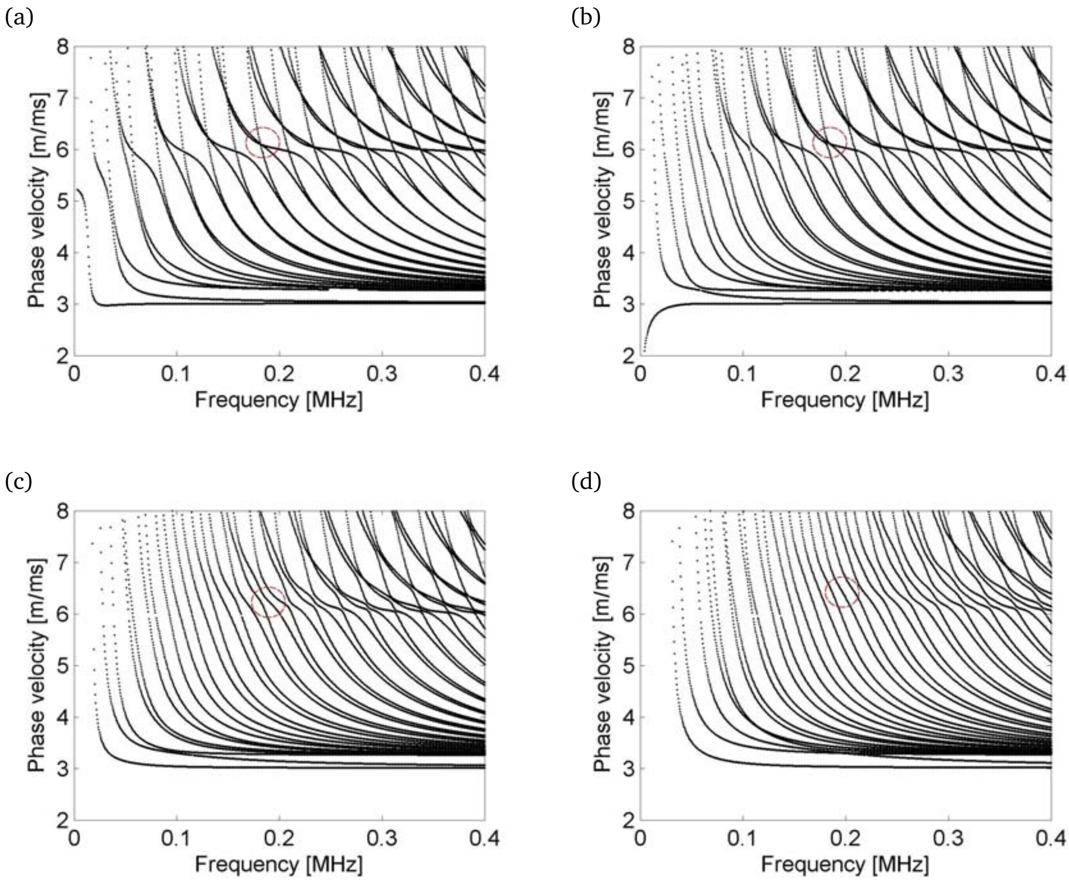

Figure 3.8: Comparison of dispersion curves for axisymmetric $n = 0$ and non-axisymmetric $n = 1, 3, 5$ modes for a steel hollow thick-walled cylinder (inner radius equal to 25 mm; thickness equal to 75): (a) longitudinal and torsional modes; (b) $F(1, m)$ mode; (c) $F(2, m)$ mode; (d) $F(3, m)$ mode.

It is also important to note that in contrast to torsional and longitudinal modes, the flexural modes do not intersect with each other but instead follow a hyperbolic behaviour as illustrated in figures 3.9-3.10. The results also indicate the coupling between the three consecutive flexural modes analysed. The coupling depends on the geometrical parameters and decreases with an increase of the MRT parameter. In addition, a transition

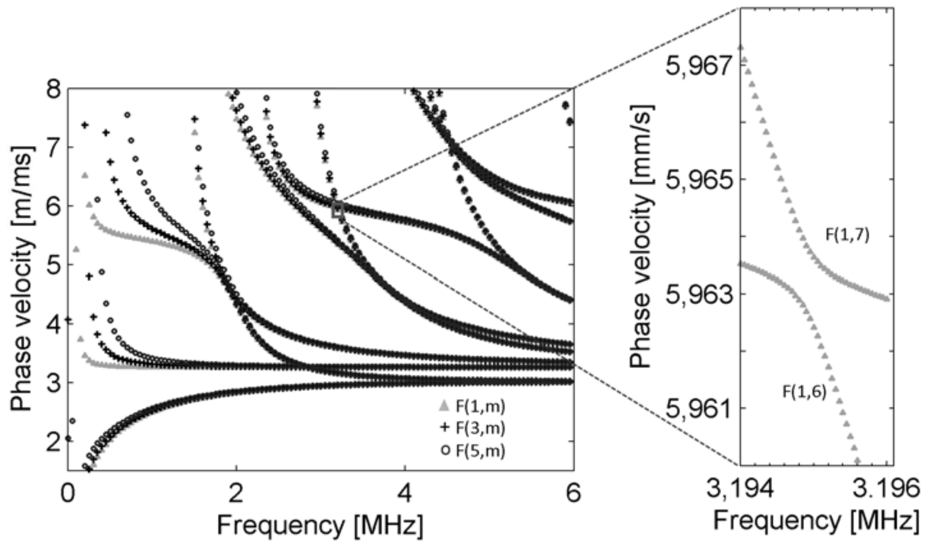

Figure 3.9: Comparison of higher circumferential order $F(1,m)$, $F(3,m)$ and $F(5,m)$ modes in a steel hollow thin-walled cylinder (inner radius equal to 8.2 mm, thickness equal to 1.22 mm).

of the dominant mode character along the curve - analogues to the one discussed previously for the coupled longitudinal modes - can be observed.

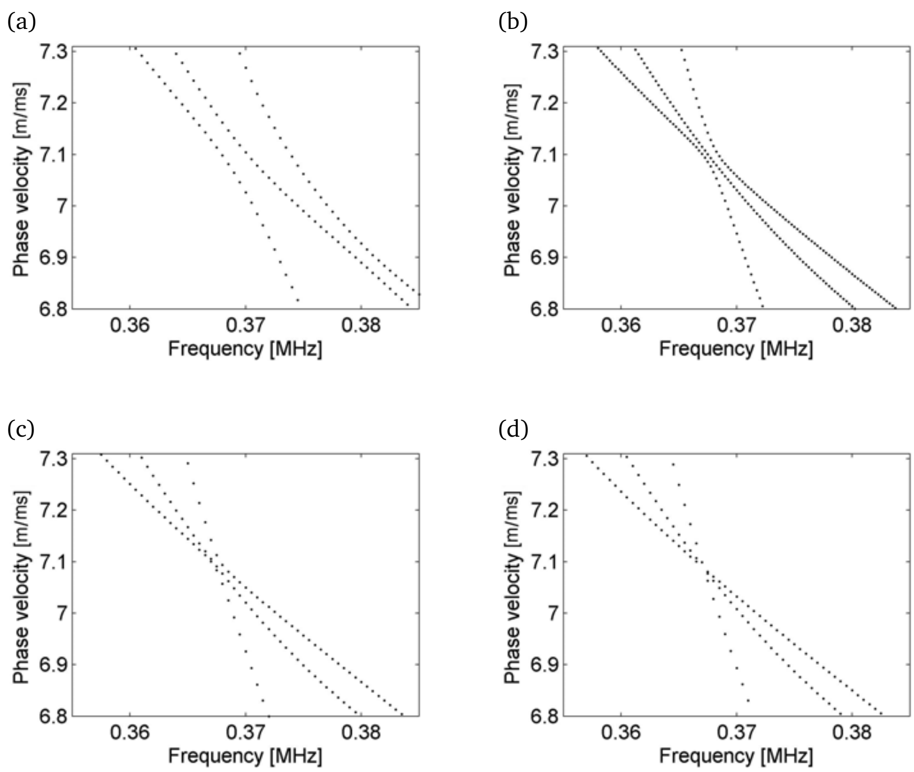

Figure 3.10: Hyperbolic behaviour of flexural modes n=1 in a mode coupling region (cylinder wall thickness equal to 75 mm): (a) MRT=0.6, (b) MRT=0.8, (c) MRT=1, (d) MRT=5.

3.3.4 Summary

Theoretical investigation of an elastic wave propagation in a hollow cylinder, using the analysis of dispersion characteristics and particle displacement patterns, has been discussed in this section. The influence of structural geometrical variations on both, i.e. axisymmetric and non-axisymmetric, types of modes was also addressed. The most important observations and their implications for damage detection applications can be summarised as follows.

In theory, a double infinite number of dispersive modes can propagate in an axial direction of any hollow cylinder structure. The analysis of the dispersion characteristics shows that the complexity of wave modes increases significantly for thick-walled cylinders. This complexity becomes a real challenge when damage detection methods - based on elastic wave propagation - need to be developed and implemented in such structures. Although numerous multiple wave modes can propagate in thick-walled structures, a common pattern - analogues to the terrace-like structures in plates - has been observed in the dispersion characteristics for higher order axisymetric longitudinal modes above the frequency range corresponding to the compressional bulk velocity limit. For this high frequency region, relevant wavelengths are significantly smaller than the cylinder wall thickness. Therefore the cylinder's curvature will manifest its effects only by the coupling between the modes. In the low frequency region, the mean radius-to-thickness ratio has been identified as an important geometrical parameter, which influences the shape of the dispersion curves. In addition, dispersion characteristics and particle displacements were investigated to reveal mode coupling phenomena through hyperbolic behaviour of the dispersion curves and transition between modeshapes.

3.4 Experimental studies

This section presents results from a series of experiments conducted with laser vibrometry at AGH-University in Krakow, to investigate the dispersion characteristics of thick-walled cylinder. The experiments aimed to reveal opportunities and limitations related to wave propagation scenarios that could be used for structural damage detection. Before the experimental investigation, a number of numerical simulations were carried out to determine optimal parameters for the experiments and to obtain reference results; for the sake of readability the simulation-based studies are presented in the following chapter along with broader discussion on used numerical simulation methods.

The structure of this section is as follows. After a brief introduction to laser vibrometry the experimental setup is described. This is followed by the dispersion characteristics results from one- and three-dimensional measurements. Section 3.4.3 presents wave propagation experiment. The findings are summarised in section 3.4.4.

3.4.1 Experimental arrangements

The investigations presented here were carried out with laser vibrometry. This technique has been widely employed for vibration measurements [108, 109] and recently has also gained much attention in the field of ultrasonic guided waves propagation [110, 111]. Laser vibrometry allows for non-contact measurements of the surface vibration velocity by utilizing the Doppler shift phenomenon. The dense mesh of measurement points can obtained in a convenient automatic mode. Also, since no physical sensor needs to be bonded to the structure, the effect of adding an additional mass is avoided.

During the conducted experiments wave propagation responses were captured using two non-contact measuring systems, i.e. one-dimensional (1-D) *Polytec PSV-400* and three-dimensional (3-D) *Polytec PSV-400-3D* scanning laser vibrometers. Both laser vibrometers were controlled using a PC.

To automate positioning of the heads of the 3-D scanning laser vibrometer, the *RoboVib Structural Test Station* - that uses an industrial *KUKA* robot - was employed. Figure 3.11 shows the experimental setup used for the 3-D laser vibrometer measurements.

Using *RoboVib Station* required the following preparation of the measurement procedure. First, the system was calibrated to link the global coordinate system of the robot with the local system assigned for the structure. Than, the scan points were defined (e.g. line, rectangular grid or circular grid) and the 3-D coordinates were determined by the geometry scanner. In the next step the robot positions, used to capture the consecutive views, were

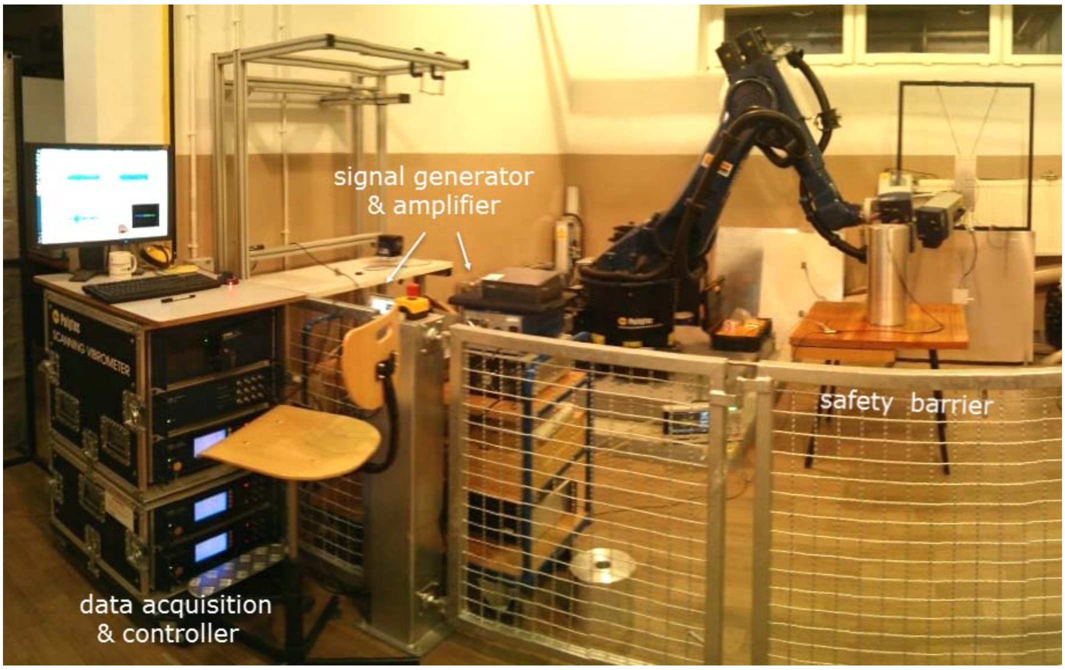

Figure 3.11: Experimental setup used for the experiments with 3-D scanning laser vibrometer and the *RoboVib Structural Test Station*.

programmed using the *Teaching mode* with the control pad. Finally, the software calculated and assigned each measurement point to the optimal robot position.

For both the 1-D and the 3-D measurements, the excitation signal was generated with Agilent 33522A waveform generator and amplified using EC Electronics PAQ-G signal amplifier. As an investigated structure a hollowed aluminium cylinder of total length of 500 mm, inner radius of 25 mm and wall thickness of 75 mm was used (figure 3.12). Two piezo-stack NOLIAC transducers of $2 \times 2 \times 2$ mm were used for wave excitation. The transducers were bonded to the inner and outer surfaces of the cylinder using a two-component adhesive glue. The location of the transducers is shown in figure 3.12. A retro-reflective coating of the surface was applied to enhance the signal to noise ratio.

3.4.2 Experimental results of dispersion characteristics

The first experiment aimed at evaluating the dispersion characteristics of the structure. Two excitation scenarios, i.e. the excitations with the transducer located on the outer and inner surfaces of the cylinder were involved. In both cases, a chirp signal was used for excitation in order to maximise the energy of the input signal. The sweeping frequency of

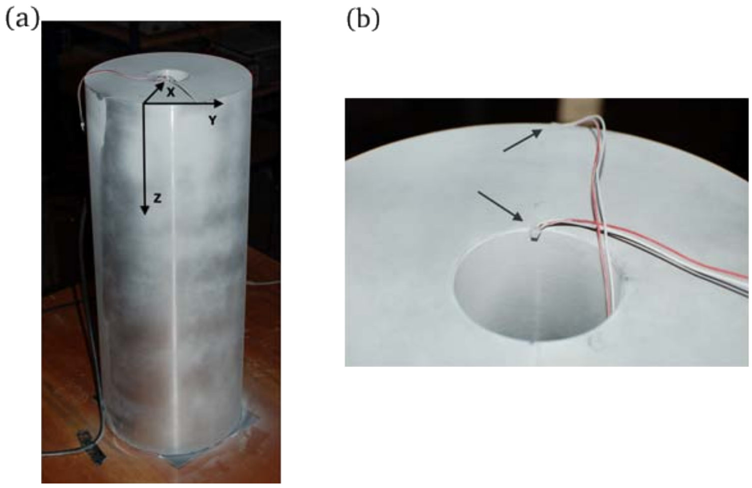

Figure 3.12: Thick hollowed aluminium cylinder used in experimental investigations. (a) General view with a 3-D coordinate system used in measurements; (b) and locations of transducers used for wave excitation.

the chirp run from 50 to 800 kHz. The total duration of the chirp excitation signal was 250μs.

3.4.2.1 One-dimensional measurements

The out-of-plane wave propagation response signals were measured using the 1-D scanning laser vibrometer. The response measurements were taken at 400 points located on the outer-surface of the cylinder, alongside the line parallel to its axis of symmetry. These velocity measurements were taken with the spatial resolution of 1 mm and acquired using the sampling frequency of 5.12 MHz. All signal responses were averaged using 100 data records in order to improve the signal-to-noise ratio.

The dispersion characteristics were obtained by applying the two-dimensional Fourier Transform to the response data. The Hanning window was used to reduce the leakage effect in the involved Fourier spectra. Figure 3.13 presents the results for the outer surface excitation scenario. The black dashed lines in this figure correspond to the theoretical velocity limits for guided (Rayleigh) and bulk (shear and compressional) wave propagation in aluminium. The experimental dispersion characteristics shown in figure 3.13 can be compared with the relevant analytical characteristics given figure in figure 4.3c.

The results for the outer surface excitation exhibit strong (high amplitude) Rayleigh velocity modes. The displacements of these modes are confined to the cylinder surfaces. The lower

(a)

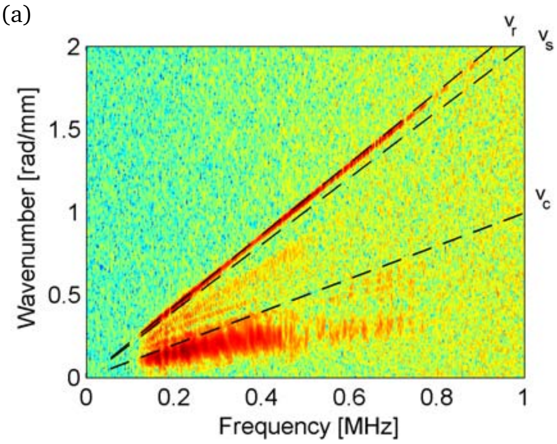

(b)

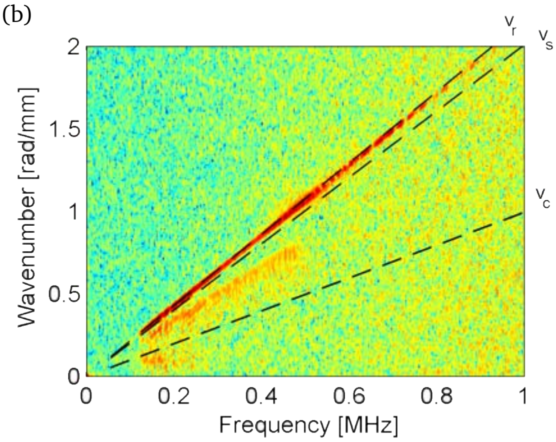

Figure 3.13: Experimental wavenumber-frequency dispersion characteristics evaluated from the 1-D response data resulting from the outer surface excitation. The results were obtained using: (a) 1 ms long signals (interferences from circumferential surface waves can be observed); (b) windowed 0.3 ms long signals. The dashed (−−) lines indicate the velocity limits for the guided Rayleigh wave (v_r), shear bulk wave (v_s) and compressional bulk wave (v_c) bulk wave.

part of the wavenumber spectrum in figure 3.13a is dominated by circumferential surface waves travelling around the cylinder outer-surface. These results are similar to what has been observed in the numerical simulations (see chapter 4). In order to minimize the influence of circumferential 'surface' waves on other wave modes, the windowed time signals of 0.3 ms were also used to evaluate the dispersion characteristics. The results are presented in figure 3.13b. Additional modes with higher amplitudes can be observed in the region between the shear wave and the compressional wave limits. However, it is very difficult to distinguish (or separate) between these consecutive modes. Interestingly, when the inner surface excitation was used the dispersion characteristics are significantly different, as demonstrated in figure 3.14. On top of the strong 'quasi-surface' wave modes, a number of higher order modes - closely spaced in the wavenumber domain - can be observed in the 200-700 kHz frequency range. There are two explanations behind the differences in the dispersion characteristics obtained using the outer and inner excitations. The experimental tests have demonstrated that for the outer excitation the strong 'outer-surface' waves mask the higher order cylinder modes, and the inner excitation better excites the flexural modes. It is also important to note that due to relatively weak piezo-based excitation - that was used intentionally - the results above 500 kHz are noisy and the mode behaviour is blurred.

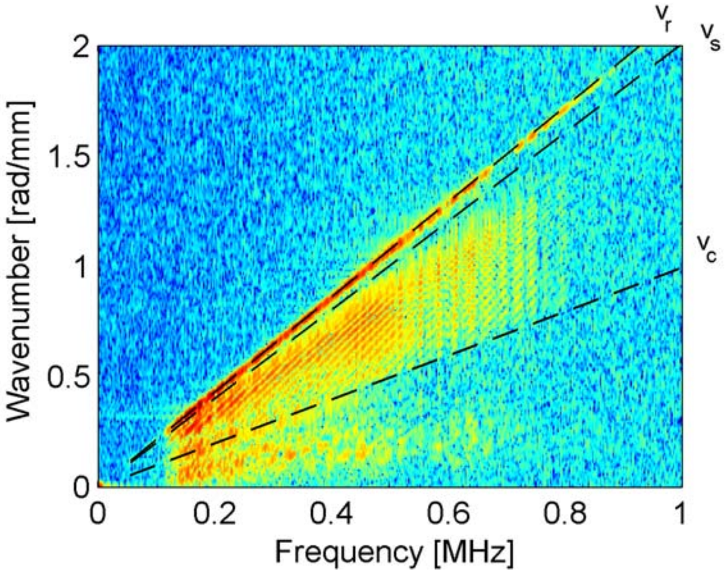

Figure 3.14: Experimental wavenumber-frequency dispersion characteristics evaluated from the 1-D response data resulting from the inner surface excitation. The dashed $(--)$ lines indicate the velocity limits for the guided Rayleigh wave (v_r), shear bulk wave (v_s) and compressional bulk wave (v_c) bulk wave.

3.4.2.2 Three-dimensional dispersion measurements

Additional experimental tests were performed to verify dispersion characteristics and to identify the dominant wave components. The 3-D scanning laser vibrometer was used in these tests in order to obtain the velocity responses in the X (normal), Z (axial) and Y (tangential) directions. The velocity responses were acquired with the 2.56 MHz sampling frequency.

The 3-D results - presented in figures 3.15 and 3.16 for the outer and inner surface excitations, respectively - are in good agreement with the 1-D measurements. The out-of-plane measurements exhibit the strongest amplitudes in the dispersion characteristics for both excitations used. Again, the 'quasi-surface' wave components are dominant in these out-of-plane characteristics.

In addition, weak amplitudes of the axial wave components can be also observed in the dispersion characteristics, particularly for the inner surface excitation (figure 3.16b). In addition, wave components in the tangential direction can be only distinguished in figure 3.15c. This confirms the previous finding that the inner surface excitation leads to stronger flexural modes. It is important to note that the torsional modes were not excited by the piezo-transducers used in the experimental tests.

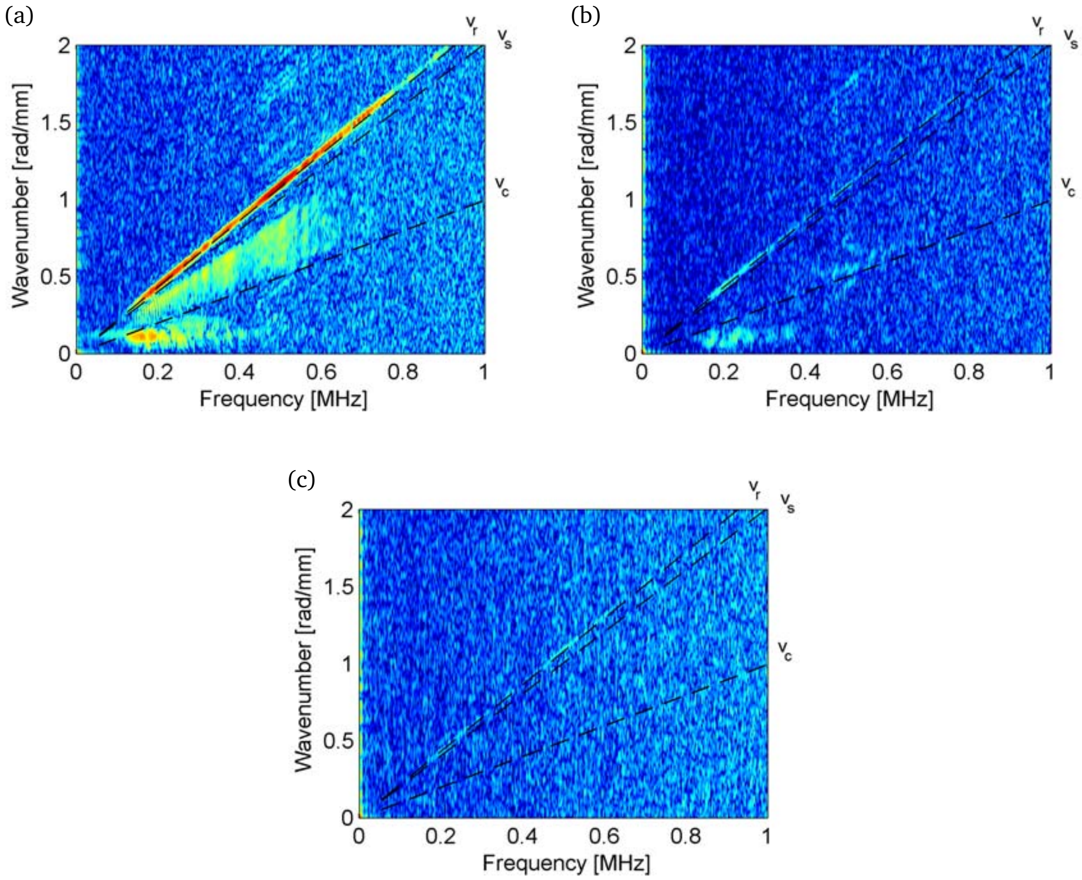

Figure 3.15: Experimental wavenumber-frequency dispersion characteristics evaluated from the 3-D response data resulting from the outer surface excitation: (a) X - normal direction; (b) Z - axial direction; (c) Y - tangential direction. The dashed (−−) lines indicate the velocity limits for the guided Rayleigh wave (v_r), shear bulk wave (v_s) and compressional bulk wave (v_c) bulk wave.

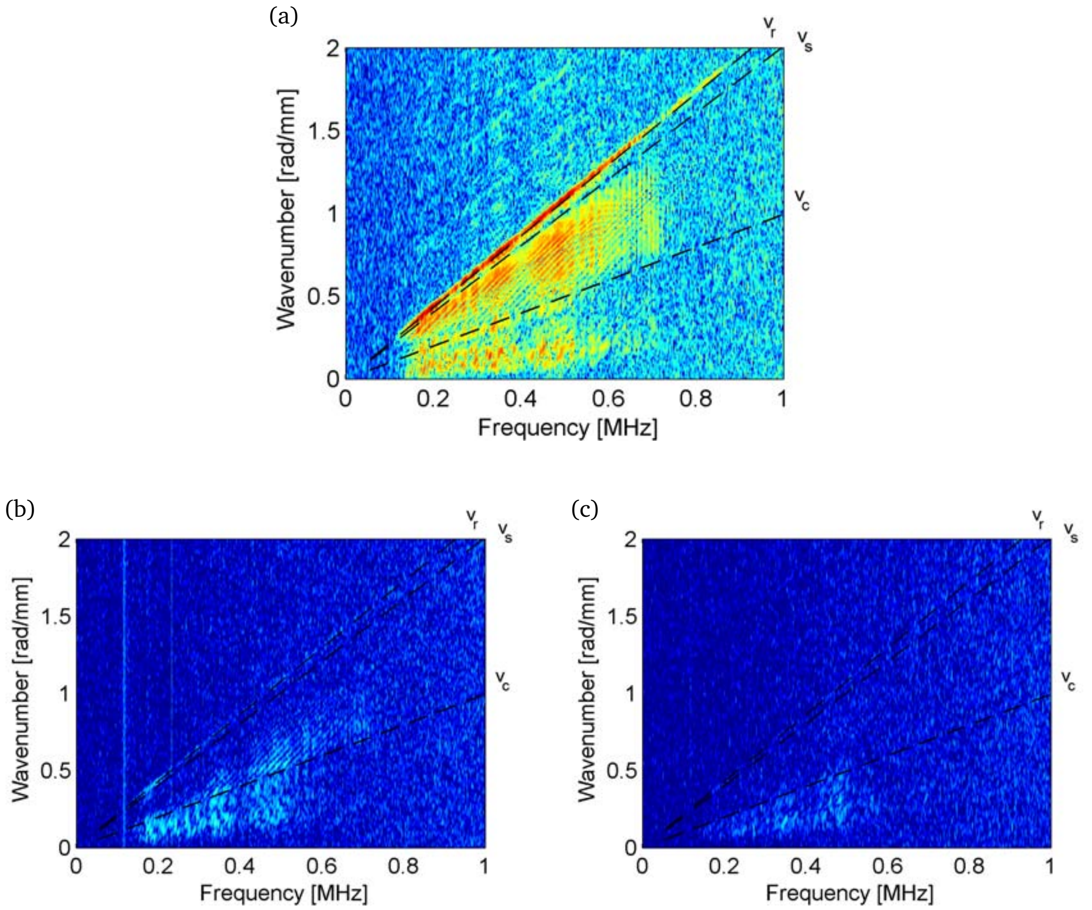

Figure 3.16: Experimental wavenumber-frequency dispersion characteristics evaluated from the 3-D response data resulting from the inner surface excitation: (a) X - normal direction; (b) Z - axial direction; (c) Y - tangential direction. The dashed (−−) lines indicate the velocity limits for the guided Rayleigh wave (v_r), shear bulk wave (v_s) and compressional bulk wave (v_c) bulk wave.

3.4.3 Experimental results -wave propagation measurements

The wave propagation measurements require relatively dense scanning of the structure surface. For the presented results the regular grid consisting of 3141 measurement points was used for the 'top' face surface(figure 3.17), while for the side view the rectangular area of 69×160 points was covered. Both the outer and the inner-surface excitation scenarios were investigated with the 200 kHz ten-cycle sine wave enveloped by the Hanning window. The results are shown in figure 3.18 and 3.19.

One can observe that when the inner-surface excitation was used, the strong (i.e. high-amplitude) wavefront - travelling across the wall of the cylinder can be observed in figure 3.18a. Also, the existence of waves propagating in the circumferential direction with high amplitudes confined to the outer surface of the cylinder - observed in the

Figure 3.17: Position of the scanner heads for the ‘top view’ propagation measurements.

numerical simulations (see chapter 4) - was confirmed by the experimental tests, as illustrated in figure 3.18b.

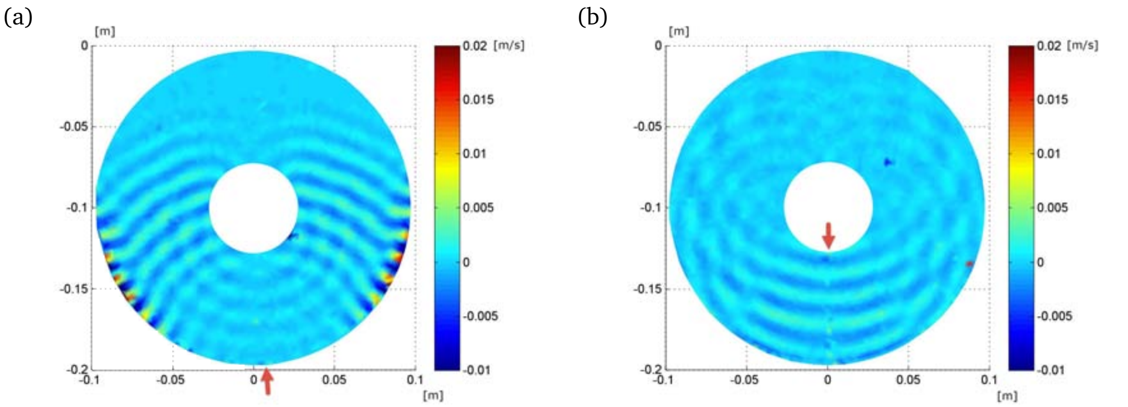

Figure 3.18: Experimental wave propagation out-of-plane velocity patterns acquired after 0.1 ms for: (a) outer-surface excitation; (b) inner-surface excitation. The excitation points are marked with the arrows.

Although the circumferential waves were not of the main interest in the experiments, due to the type of the excitation that was chosen i.e. by a single cubic piezo-stack transducer, the circumferentially propagating waves clearly influenced the results. In particular strong wavefronts could be seen for the excitation at the external surface e.g. figure 3.19b at

(a)

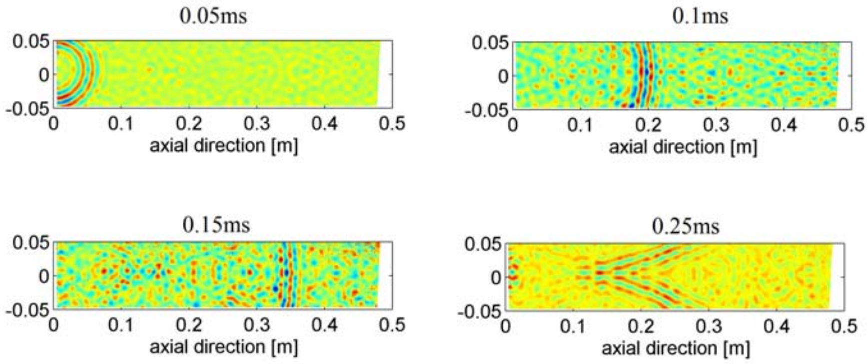

(b)

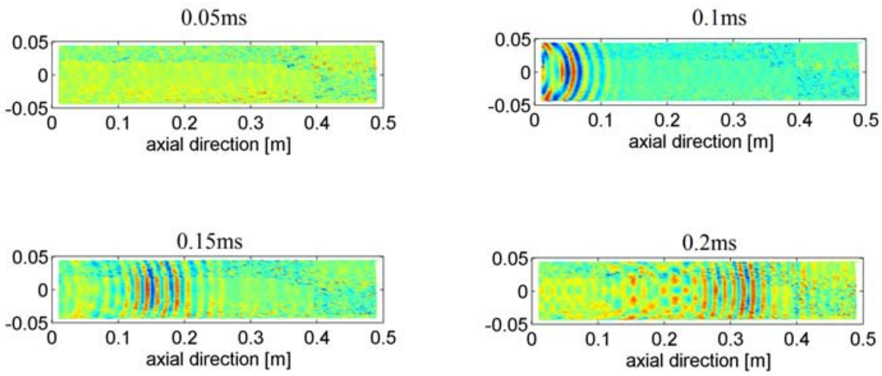

Figure 3.19: Visualisation of wave propagation by out-of-plane velocity patterns acquired experimentally for: (a) outer-surface excitation; (b) inner-surface excitation. Darker color corresponds to higher amplitudes.

0.2 ms. Interestingly, the secondary wave packets - induced by the circumferential waves but propagating in the axial direction - were also observed as shown in figure 3.20. This phenomena may be related also to the interaction of waves at the 90 degrees face-to-side corner.

Another feature observed is the difference in arrival time of the high amplitude waves for the two excitation locations. Comparing the wavefields in figures 3.19 for the consecutive time instances reveals that for the excitation placed at the inner surface the strong wavefront travels with a delay of about 0.05 ms as compared to the outer surface excitation case. This can be associated with Rayleigh velocity waves guided along the face of the cylinder, which will be studied in more details in chapter 5.

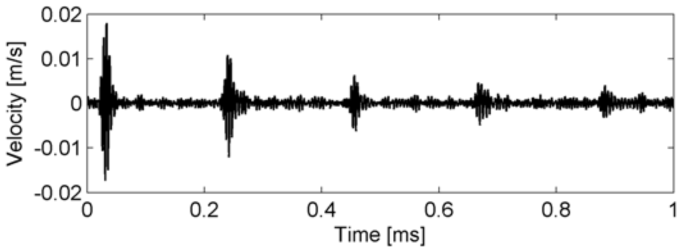

Figure 3.20: Experimental out-of-plane response velocity signal displaying the secondary wave packets induced by the circumferential waves. The outer-surface signal was acquired 1mm below the outer-surface excitation point.

3.4.4 Summary

The experimental results presented in this section confirm the propagation of guided waves in both axial and circumferential direction of the cylinder. It is clear that the Rayleigh velocity wave modes - with high amplitudes confined to the surfaces - are the dominant wave propagation modes in the thick hollow cylinder. Also, there are significant differences in the evaluated dispersion characteristics when the two excitations scenarios (i.e. outer-surface and inner-surface excitations) are used.

The results reveal a complex pattern of high-order modes for the single-point, inner-surface excitation. Although these multiple and interlacing modes are difficult to separate, some information can be obtained with respect to the range of velocities involved in the propagation of these modes.

During the experiments, an attempt was made to investigate also the wave propagating in the circumferential direction of the cylinder. Unfortunately, the measurement results appear to be strongly corrupted by noise and yield little useful information; thus, they were not shown here. The difficulties in performing the measurements around the cylinder circumference are related to the need of precise control of the robot position (in the discussed case, eighteen consecutive positions were defined) as well as to the optical challenges in focusing of the laser beam.

3.5 Conclusions

In this chapter elastic waves in thick-walled hollow cylindrical structures have been investigated theoretically, numerically and experimentally. These investigations were carried out to facilitate understanding of various wave propagation phenomena typical for thick-walled cylinders. Firstly, the semi-analytical analysis was performed to analyse the characteristic features of guided modes and to establish the correlation between a thick plate and a thick cylinder waveguide. Then experimental tests were conducted to investigate outer- and inner-surface excitation scenarios. The major conclusions from this part of the work can be summarized as follows.

The theoretical analysis of displacement patterns has demonstrated the pseudo-symmetry of the axisymmetric longitudinal modes across the wall thickness. In practice, the pseudo-symmetry implies that in general, larger displacements for a given mode are expected at the inner rather than the outer surface of the cylinder. The investigations of dispersion characteristics have revealed a common pattern of higher order axisymetric modes - analogous to terrace-like structures in plates - above the compressional wave velocity limit (at phase velocity-frequency plots). Since the wavelengths are significantly smaller in this high-frequency region, the cylinder's curvature manifests its effects only by the coupling between the modes. In the low-frequency region, the mean radius-to-thickness ratio has been identified as an important geometrical parameter, influencing the shape of the dispersion curves. The theoretical study has revealed that the weak coupling between pairs of consecutive longitudinal modes - caused by the radial stress component - results in a hyperbolic behaviour of the dispersion curves in the mode interlacing region.

Experimental tests have confirmed a complex pattern of multiple wave modes in the thick-walled hollow cylinder. Also, significant differences in the evaluated dispersion characteristics have been observed, when the two investigated excitation scenarios - i.e. the outer-surface and inner-surface excitations - were used. The experiments have also shown that the Rayleigh velocity waves are dominant in the high-frequency region. However, the study has indicated that for inner surface excitations, amplitudes of the 'quasi-surface' waves are much weaker on the outer surface of the cylinder than for the outer-surface wave excitation. Since additionally it seems that the excitation inside the cylinder produced better results in terms of excitation of the higher order modes than the excitation at the outer surface, the inner-surface excitation appears to be superior for damage detection applications.

The results of these preliminary theoretical and experimental investigations have demonstrated that damage detection based on ultrasonic wave propagation is possible in thick-walled hollow cylinders. However, any practical application will require thorough understanding of complex wave propagation phenomena involved and appropriate monitoring strategies (i.e. excitation sources, positions and frequencies). The former will require high-resolution dispersion characteristics that can be obtained using both numerical simulations and experimental tests. Since both antisymmetric and flexural modes are present in the dispersion characteristics, a very fine resolution in the wavenumber domain will be needed in practical applications to differentiate between various wave propagation modes. A very large number of measurements will be required on the surface of the cylinder to achieve this accuracy. Therefore, in order to obtain more accurate dispersion curves the analysis of longer cylinders will be needed in practice; additionally the types of the propagating modes can be restricted by excitation of the structure using an array of transducers. The following chapter will explore the latter possibility -the excitation of only longitudinal modes- in more detail.

Chapter 4

Numerical simulation methods

4.1 Introduction

The complexity of elastic wave characteristics including multimodal behaviour, dispersion and reflections from the boundaries, often results in inability of obtaining an exact analytical solution to the wave propagation problem. In particular for structures with non-uniform geometry (e.g. with thickness variation) or when the wave scattering from a crack is involved, the numerical simulations become extremely valuable tools.

A considerable amount of research has been conducted into computer simulation techniques for elastic waves propagation [112, 123]. Various methods have been established including semi-analytical approaches such as boundary element methods (BEMs) [8, 20], semi-analytical finite element method (SAFE) [48, 49], numerical algorithms based on finite differences (FDM) [27] or finite elements (FEM) [131, 51], or spectral element method (SEM) [80, 41] – FEM formulated in the frequency domain. The choice of appropriate computational method depends on the exact research area e.g. dispersion analysis, complex geometry models, actuator-sensing models with bonding condition or propagation of higher order modes.

In this work numerical simulations were used for numerous aspects which can be summarised as follows

- as a preliminary investigation to develop the experimental setup discussed in chapter 3; i.e. reference results and selection of optimal excitation;

- to provide an insight into the mechanisms of wave interaction with structural features such as boundaries and defects;
- in the development of the damage detection approach, to adjust the excitation settings and choose optimal sensors' position;
- to examine the structure's monitoring approach for various damage configurations;

To achieve the aforementioned goals, the finite difference and finite element schemes were used; therefore a short introduction to FEM is given in the section 4.2.1, followed by an overview of the finite difference formalism and presentation of local interaction simulation approach (LISA). A complete derivation of LISA for a two-dimensional case is provided in this chapter, since it was a basis for a development of a two-dimensional axisymmetric LISA in cylindrical coordinates, which is given in section 4.3. Section 4.4 presents the results of the numerical simulations carried out as preliminary investigations before conducting the experiments with laser vibrometry discussed in chapter 3. Finally, this part of the work is summarised and concluded in section 4.5.

4.2 Overview of simulation methods

This section gives the theoretical background on the finite element and finite difference methods. The main concepts and procedures are introduced to allow for the comparison of the methods and to introduce the framework for discussion. Particularly the local interaction simulation approach is discussed, since it has been chosen as a primary numerical simulation technique in this thesis. It is also believed that the introduction of the solid theoretical foundation of LISA is necessary for presenting the proposed axisymmetric model in the following section.

4.2.1 Finite element methods

The finite element method (FEM) is an approach that allows for solving differential equations by dividing the whole problem domain into smaller subdomains called *elements* in which the solution type is assumed to be known. Although there are different formulations of FEM, the two main group of approaches can be distinguished: based on variational method and on weighted residuals methods [112].

Mathematically, the variational formulation is used to solve the partial differential equations, by finding the conditions that make the *functional* stationary to arbitrary changes δu of the unknown function u. In elasticity problems, the functional is the total potential energy (TPE) and the stationary condition of the minimum total potential energy leads to the equilibrium equations. The displacement field of the element is approximated by the *shape function matrix* $N(x, y, z)$ and a time-dependent vector of unknown nodal displacements u_e via *trial function* expansion

$$u \approx u_e(x, y, z) = \sum_{i=1}^{n_d} N_i(x, y, z)u_i = N(x, y, z)u_e, \tag{4.1}$$

where superscript e denotes approximation, n_d is the number of nodes forming the element, $u_i = [u_1 u_2 ... u_{n_f}]$ is the nodal displacement at node i, and n_f refers to the number of Degrees of Freedom (DOF) at a node. For three-dimensional solids n_f=3. The total DOF for the element is therefore $n_d \times n_f$. Note that the shape function which is predefined to assume the shapes of the displacement variations, interpolate the internal displacement within the element u_e directly from the displacement value at the node. For more information regarding formulation of the shape functions the reader may refer to [131, 62, 39].

Methods of *weighted residuals* derive the solutions directly from the differential formulations of a problem by substituting the trial solution and checking the resulting residual (error). Consequently, finding the smallest possible residual provides the best solution. Various approaches of minimizing the residual corresponds to different methods such as collocation method or mean square error based approach. When instead of making the the residual equal to zero it is multiplied by *weight function* and integrated, the approach is called weighted residual method. Since only the average (integrated) satisfaction of the equilibrium condition is required it is *weak form* formulation. One of the well-known approaches from this group is the *Galerkin' method*, for which the weight function is the same as the trial function. Another example of the finite element formulation using a weak form of the equilibrium equations is based on the virtual work principle. This approach is introduced in the ABAQUS/Explicit commercial software, which was used a supplementary simulation tool in this thesis.

4.2.2 Local interaction simulation approach

The local interaction simulation approach (LISA) was developed by Delsanto [29, 27, 28] as an extension of the finite difference method. The approach introduces sharp interface model for treatment of the cells boundaries, allowing for modelling inhomogeneous media and “a more physical and unambiguous treatment of interface discontinuities" [27]. LISA formulation is well suited for parallel processing, which makes the algorithm extremely efficient. The following paragraphs describe the background of the FD and LISA in details.

Taylor expansion

The finite difference method is based on the direct substitution of the Taylor expansions into the governing equations. The Taylor expansion relates the unknown value of the function at the point x_{i+1} to the derivatives at x_i as

$$f(x_{i+1}) = f(x_i) + \Delta x f'(x) + \frac{\Delta x^2}{2!} f"(x_i) + ... + \frac{\Delta x^n}{n!} f^{(n)}(x_i), \tag{4.2}$$

where the $\Delta x = x_{i+1} - x_i$ is the distance between the points and f' denotes the differentiation with respect to x.

Considering only the two first terms of Eq. (4.2) leads to the *forward difference estimate* [112]

$$f'(x_i) = \frac{f(x_{i+1}) - f(x_i)}{\Delta x}. \tag{4.3}$$

Similarly the formulas for second order derivatives, given in Appendix C, can be obtained. Note that the formulas obtained by Taylor expansion may be used for time or space discretization.

Finite difference (FD) formalism

After [84] the two-dimensional finite differences method (FDM) scheme can be described as follows.

The Navier's wave equation (2.8) for a two-dimensional problem can be conveniently written in the matrix form

$$AW_{,11} + BW_{,22} + CW_{,12} = \rho \ddot{W}, \tag{4.4}$$

where

$$A = \begin{bmatrix} \lambda + 2\mu & 0 \\ 0 & \mu \end{bmatrix}, \quad B = \begin{bmatrix} \mu & 0 \\ 0 & \lambda + 2\mu \end{bmatrix}, \quad C = \begin{bmatrix} \lambda + \mu & 0 \\ 0 & \lambda + \mu \end{bmatrix}, \quad W = \begin{bmatrix} u \\ v \end{bmatrix}.$$

Here, u, v are the unknown displacement components, and λ and μ are Lam constants. $W_{,11}$, $W_{,22}$ correspond here respectively to the second derivative with respect to x and y.

Discretizing the structure into a grid of square cells of size ϵ with the constant material parameters for each cell, and using the FD formalism yields the displacement in the grid point (i, j) at the time step $t + 1$

$$\begin{aligned} W_{t+1} = 2W - W_{t-1} + \frac{(\Delta t)^2}{\rho \epsilon^2}[&A(W_{i+1} + W_{i-1} - 2W) + B(W_{j+1} + W_{j-1} - 2W) \\ &+ C(W_{i+1,j+1} + W_{i-1,j-1} - W_{i-1,j+1} - W_{i+1,j-1})], \end{aligned} \tag{4.5}$$

where Δt denotes the time step, γ is the density of a cell, and the single subscripts t, i, j were omitted for convenience.

The framework for the finite difference method was stated in the 1930s [26] and with the development in the computational techniques, it has become one of the most popular methods for wave propagation simulation. In what follows the local interaction simulation approach, which is based on FDM is explained.

Extension to local interaction simulation approach

An extension of the FDM that allows for the treatment of the inhomogeneous media –with the sharp interface framework– is the local interaction simulation approach (LISA). In LISA model the material parameters are constant for each cell, but may differ from cell to cell (see figure 4.1).

To obtain the iteration formula of the crosspoints between the cells, the second time derivatives of displacement vectors across the four adjacent cells are required to converge towards a common value Ω at the cells' junction point P. This ensures that if the displacements are continuous at this nodal point for the two initial time instants (say, t = 0 and t = 1), they remain continuous for all later times.

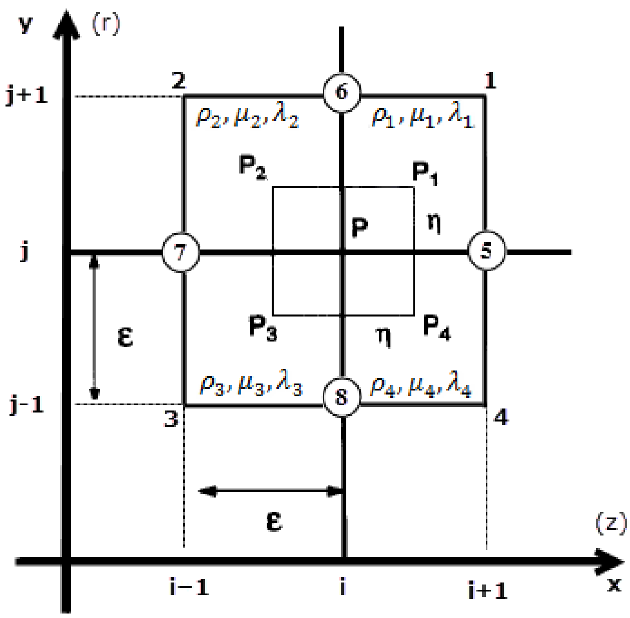

Figure 4.1: Representation of the two-dimensional LISA domain discretization. Following [27].

Therefore, using finite difference formalism for space derivatives of the Eq. (4.4) for four points P_k when distance $\eta \rightarrow 0$ results in following four equations with eight unknowns [84]

$$
\begin{aligned}
-2A_1W_{1,1} - 2B_1W_{1,2} + 2A_1(W_5 - W) + 2B_1(W_6 - W) + C_1(W_1 + W - W_5 - W_6) &\approx \rho_1\Omega \\
2A_2W_{2,1} - 2B_2W_{2,2} + 2A_2(W_7 - W) + 2B_2(W_6 - W) + C_2(W_6 + W_7 - W_2 - W) &\approx \rho_2\Omega \\
2A_3W_{3,1} + 2B_3W_{3,2} + 2A_3(W_7 - W) + 2B_3(W_8 - W) + C_3(W + W_3 - W_7 - W_8) &\approx \rho_3\Omega \\
-2A_4W_{4,1} + 2B_4W_{4,2} + 2A_4(W_5 - W) + 2B_4(W_8 - W) + C_4(W_5 + W_8 - W - W_4) &\approx \rho_4\Omega,
\end{aligned} \tag{4.6}
$$

where $W_{k,1}$ and $W_{k,2}$ denotes the x- and y- differentiation of W in point P_k. Note that without loss of generality the time and the space discretization can be assumed $\Delta t = \epsilon = 1$ [27].

Imposing stress continuity across neighbouring cells defined as

$$
\sigma_1 = AW_{,1} + DW_{,2}; \quad \sigma_2 = EW_{,1} + BW_{,2}, \tag{4.7}
$$

where

$$
D = \begin{bmatrix} 0 & \lambda \\ \mu & 0 \end{bmatrix} \quad E = \begin{bmatrix} 0 & \mu \\ \lambda & 0 \end{bmatrix}
$$

and approximating the space derivatives gives the additional four equations

$$
\begin{aligned}
A_2W_{2,1} - A_1W_{1,1} &= (D_1 - D_2)(W_6 - W) \\
A_3W_{3,1} - A_4W_{4,1} &= (D_4 - D_3)(W - W_8) \\
B_4W_{4,2} - B_1W_{1,2} &= (E_1 - E_4)(W_5 - W) \\
B_3W_{3,2} - B_2W_{2,2} &= (E_2 - E_3)(W - W_7).
\end{aligned} \tag{4.8}
$$

Finally, using Eqs. (4.6) and (4.8) the final iteration formulae for the displacement components u and v in the crosspoint P are

$$
\begin{aligned}
u_{t+1} = 2u - u_{t-1} + \frac{1}{\rho}[&s_5u_5 + s_7u_7 + \mu_6u_6 + \mu_8u_8 - 2(s+\mu)u_t \\
&- \frac{1}{4}\sum_{k=1}^{4}(-1)^k v_k v_t - \frac{1}{4}\sum_{k=1}^{4}(-1)^k v_k v_k \\
&+ \frac{1}{2}((g_4 - g_1)v_5 + (g_1 - g_2)v_6 + (g_2 - g_3)v_7 + (g_3 - g_4)v_8],
\end{aligned} \tag{4.9}
$$

$$
\begin{aligned}
v_{t+1} = 2v - v_{t-1} + \frac{1}{\rho}[&\mu_5 v_5 + s_6 v_6 + \mu_7 v_7 + s_8 v_8 - 2(s+\mu)v_t \\
&- \frac{1}{4}\sum_{k=1}^{4}(-1)^k v_k u_t - \frac{1}{4}\sum_{k=1}^{4}(-1)^k v_k u_k \\
&- \frac{1}{2}((g_4 - g_1)u_5 + (g_1 - g_2)u_6 + (g_2 - g_3)u_7 + (g_3 - g_4)u_8],
\end{aligned}
\tag{4.10}
$$

where

$$
\begin{aligned}
&s_i = \lambda + 2\mu, \quad g_i = \lambda - \mu, \text{for cell } i \\
&\mu = \frac{1}{4}\sum_{k=1}^{4}\mu_k, \quad \rho = \frac{1}{4}\sum_{k=1}^{4}\rho_k, \quad s = \frac{1}{4}\sum_{k=1}^{4}s_k, \\
&s_5 = (s_1 + s_4)/2, \quad s_6 = (s_1 + s_2)/2, s_7 = (s_2 + s_3)/2, \quad s_8 = (s_3 + s_4)/2.
\end{aligned}
\tag{4.11}
$$

4.2.3 Summary

Up to this point the finite element and the local interaction simulation approaches have been presented as two alternative simulation methods. However, there are some aspects which are common for both techniques including differentiation with respect to time and the stability criteria; thus, they are addressed briefly in the following.

Time derivatives can be treated in both FEM and FD methods with the same approach, namely the direct explicit integration using the explicit central finite difference formulation. However, the central-difference operator is conditionally stable, therefore the stability condition has to be fulfilled. For wave propagation problems this stability criterion (Courant criterion) is often approximated as the time step cannot exceed the smallest transit time of a compressional wave across any of the elements (L_{min}) in the mesh

$$
\Delta t \leqslant \frac{L_{min}}{v_c}, \tag{4.12}
$$

In addition the spatial criterion on the element size has to be considered,

$$
\Delta L_{min} \leqslant \frac{\lambda_{min}}{M}, \tag{4.13}
$$

where in the literature the number of elements M is suggested from eight to twenty elements per wavelength (λ_{min}). In this work the condition of was $M = 10$ commonly imposed.

The differences in the formulation of finite element and finite difference methods have been introduced in details in previous sections. At this point some general comments on the application aspects should be made.

Firstly, when comparing these two approaches one should note that FEM is well suited for modelling an arbitrary shape due to the various type and size of elements that can be used. In contrast, the uniform cubical(3D)/rectangular(2D) discretization required by FD-based approaches leads to the well-known *'staircase' problem of curvature representation* [112], which can be only reduced through refining the mesh of the model.

The main drawbacks of FEM are related to the computational efficiency, especially when high spatial and temporal resolution are required, or in the case of large -in sense of the degrees of freedom- models. On the other hand, the LISA can be efficiently employed with parallel computing approach, as developed by Packo *et al.* [84] through graphical card technology (CUDA).

In the following section a two-dimensional LISA derived in cylindrical coordinate system is proposed.

4.3 Axisymetric two-dimensional LISA

It has been noticed, that the total number of elements necessary to mesh a three-dimensional model of a train axle, for wavelengths suitable for detection of a crack of several millimetres, requires a great amount of computational power for both three-dimensional finite element and finite difference methods. However, by implying the axisymmetry condition of the structure, the simplification of the model to a two-dimensional case can be done.

In the following section a two-dimensional axisymmetric wave propagation model, developed in cylindrical coordinates within the LISA framework and solely supporting the axisymmetric longitudinal modes is established.

4.3.1 Method derivation

The equations of motion in cylindrical coordinates for the axisymmetric longitudinal modes (i.e. $n = 0, u_\theta = 0, \dfrac{\partial}{\partial\theta} = 0$) are given by

$$\mu\left(\frac{\partial^2 u_r}{\partial r^2} + \frac{1}{r}\frac{\partial u_r}{\partial r} + \frac{\partial^2 u_r}{\partial z^2} - \frac{u_r}{r^2}\right) + (\lambda+\mu)\left(\frac{\partial^2 u_r}{\partial r^2} + \frac{1}{r}\frac{\partial u_r}{\partial r} - \frac{1}{r^2}u_r + \frac{\partial^2 u_z}{\partial z \partial r}\right) = \rho\ddot{u}_r \tag{4.14}$$

$$\mu\left(\frac{\partial^2 u_z}{\partial r^2} + \frac{1}{r}\frac{\partial u_z}{\partial r} + \frac{\partial^2 u_z}{\partial z^2}\right) + (\lambda+\mu)\left(\frac{1}{r}\frac{\partial u_r}{\partial z} + \frac{\partial^2 u_r}{\partial r \partial z} + \frac{\partial^2 u_z}{\partial z^2}\right) = \rho\ddot{u}_z \tag{4.15}$$

where r, z, θ correspond to the cylindrical coordinates assigned to the cylinder central axis, and u is displacement vector in cylindrical coordinates.

In matrix notation

$$AW_{,11} + BW_{,22} + CW_{,12} + \frac{1}{r}AW_{,1} + \frac{1}{r}DW_{,2} - \frac{1}{r^2}EW = \rho\ddot{W}, \tag{4.16}$$

where

$$A = \begin{bmatrix} \lambda+2\mu & 0 \\ 0 & \mu \end{bmatrix}, \quad B = \begin{bmatrix} \mu & 0 \\ 0 & \lambda+2\mu \end{bmatrix}, \quad C = \begin{bmatrix} \lambda+\mu & 0 \\ 0 & \lambda+\mu \end{bmatrix}, \quad F = \begin{bmatrix} 0 & 0 \\ \lambda+\mu & 0 \end{bmatrix},$$
$$G = \begin{bmatrix} \lambda+2\mu & 0 \\ 0 & 0 \end{bmatrix}, \quad W = \begin{bmatrix} u_r \\ u_z \end{bmatrix},$$

where u_r, u_z are the unknown displacement components and the index after comma denotes the derivative with respect to a given quantity e.g. $W_{,12} = \dfrac{\partial^2}{\partial r \partial z}W$.

By finite difference formalism for four points P_k (see figure 4.1) when distance $\eta \to 0$ we obtain the following set of equations

$$
\begin{aligned}
-2A_1W_{1,1} - 2B_1W_{1,2} + R_1 &\approx \rho_1\Omega \\
-2A_2W_{2,1} + 2B_2W_{2,2} + R_2 &\approx \rho_2\Omega \\
2A_3W_{3,1} + 2B_3W_{3,2} + R_3 &\approx \rho_3\Omega \\
2A_4W_{4,1} - 2B_4W_{4,2} + R_4 &\approx \rho_4\Omega,
\end{aligned}
\tag{4.17}
$$

where

$$
\begin{aligned}
R_1 =& 2A_1(W_6 - W) + 2B_1(W_5 - W) + C_1(W_1 + W - W_5 - W_6) \\
&+ \frac{1}{r}A_1(W_6 - W) + \frac{1}{r}F_1(W_5 - W) - \frac{1}{r^2}G_1W \\
R_2 =& 2A_2(W_6 - W) + 2B_2(W_7 - W) + C_2(W_6 + W_7 - W_2 - W) \\
&+ \frac{1}{r}A_2(W_6 - W) + \frac{1}{r}F_2(W - W_7) - \frac{1}{r^2}G_2W \\
R_3 =& 2A_3(W_8 - W) + 2B_3(W_7 - W) + C_3(W + W_3 - W_7 - W_8) \\
&+ \frac{1}{r}A_3(W - W_8) + \frac{1}{r}F_3(W - W_7) - \frac{1}{r^2}G_3W \\
R_4 =& 2A_4(W_8 - W) + 2B_4(W_5 - W) + C_4(W_5 + W_8 - W - W_4) \\
&+ \frac{1}{r}A_4(W - W_8) + \frac{1}{r}F_4(W_5 - W) - \frac{1}{r^2}G_4W.
\end{aligned}
\tag{4.18}
$$

Here, $W_{k,1}$ and $W_{k,2}$ denotes the z- and r- differentiation of W in point P_k.

The time and the space discretization were assumed here as $\Delta t = \epsilon = 1$, for the simplicity of the notation. However, for the sake of completeness of the solution they are included as parameters in the final form of the iteration equation.

Imposing stress continuity across each two neighbouring cells

$$
\sigma_1 = AW_{,1} + DW_{,2} + \frac{1}{r}MW; \quad \sigma_2 = EW_{,1} + BW_{,2} + \frac{1}{r}NW, \tag{4.19}
$$

where

$$
\sigma_1 = [\sigma_{rr}, \sigma_{rz}], \quad \sigma_2 = [\sigma_{rz}, \sigma_{zz}], \tag{4.20}
$$

and

$$
D = \begin{bmatrix} 0 & \lambda \\ \mu & 0 \end{bmatrix}, \quad E = \begin{bmatrix} 0 & \mu \\ \lambda & 0 \end{bmatrix}, M = \begin{bmatrix} \lambda & 0 \\ 0 & 0 \end{bmatrix}, \quad N = \begin{bmatrix} 0 & 0 \\ \lambda & 0 \end{bmatrix}.
$$

Approximating the space derivatives gives the additional four equations

$$
\begin{aligned}
B_2W_{2,2} - B_1W_{1,2} &= (E_1 - E_2)(W_6 - W) + \frac{1}{r}(N_1 - N_2)W, \\
B_4W_{4,2} - B_3W_{3,2} &= (E_3 - E_4)(W - W_8) + \frac{1}{r}(N_3 - N_4)W, \\
A_3W_{3,1} - A_2W_{2,1} &= (D_2 - D_3)(W - W_7) + \frac{1}{r}(M_2 - M_3)W, \\
A_4W_{4,1} - A_1W_{1,1} &= (D_1 - D_4)(W_5 - W) + \frac{1}{r}(M_1 - M_4)W,
\end{aligned}
\tag{4.21}
$$

where the first index corresponds to the point number (see figure 4.1 for reference).

From Eqs. (4.17) and (4.21) using the finite difference approximations the final iteration formulae for displacement components u_r and u_z at the crosspoint P can be evaluated as

$$
\begin{aligned}
u_{t+1} = 2u - u_{t-1} + \frac{(\Delta t)^2}{\rho}\Bigg(&\frac{1}{r}\Big[\lambda_1(v+v_5) - \lambda_2(v+v_7) + \lambda_4(v+v_5) - \lambda_3(v+v_7) \\
&- \mu_1(u - u_6 + v - v_5) - \mu_2(u - u_6 - v + v_7) + \mu_4(u - u_8 - v + v_5) \\
&+ \mu_3(u - u_8 + v - v_7)\Big]/\epsilon + \Big[\mu_1(4u_5 - 6u + 2u_6 - v + v_1 + v_5 - v_6) \\
&+ \mu_2(2u_6 - 6u + 4u_7 + v - v_2 + v_6 - v_7) + \mu_4(4u_5 - 6u + 2u_8 + v - v_4 - v_5 + v_8) \\
&+ \mu_3(4u_7 - 6u + 2u_8 - v + v_3 + v_7 - v_8) - \lambda_1(2u - 2u_5 + v - v_1 + v_5 - v_6) \\
&- \lambda_2(2u - 2u_7 - v + v_2 + v_6 - v_7) - \lambda_4(2u - 2u_5 - v + v_4 - v_5 + v_8) \\
&- \lambda_3(2u - 2u_7 + v - v_3 + v_7 - v_8)\Big]/\epsilon^2\Bigg);
\end{aligned}
\tag{4.22}
$$

$$
\begin{aligned}
v_{t+1} = 2v - vt - 1 + \frac{(\Delta t)^2}{\rho}\Bigg(&\frac{1}{r}\Big[\lambda_1(v+v_6) + \lambda_2(v+v_6) - \lambda_3(v+v_8) - \lambda_4(v+v_8) \\
&- \mu_1(2v - 2v_6) - \mu_2(2v - 2v_6) + \mu_3(2v - 2v_8) + \mu_4(2v - 2v_8)\Big]/\epsilon \\
&+ \Big[\mu_1(u_1 - u - u_5 + u_6 - 6v + 2v_5 + 4v_6) + \mu_2 * (u - u_2 - u_6 + u_7 - 6v + 4v_6 + 2v_7) \\
&+ \mu_4 * (u - u_4 + u_5 - u_8 - 6v + 2v_5 + 4v_8) + \mu_3 * (u3 - u - u_7 + u_8 - 6v + 2v_7 + 4v_8) \\
&- \lambda_1(u - u_1 - u_5 + u_6 + 2v - 2v_6) + \lambda_2(u - u_2 + u_6 - u_7 - 2v + 2v_6) \\
&- \lambda_3(u - u_3 - u_7 + u_8 + 2v - 2v_8) + \lambda_4(u - u_4 - u_5 + u_8 - 2v + 2v_8)\Big]/\epsilon^2 \\
&+ (-\lambda_1 v - \lambda_2 v - \lambda_3 v - \lambda_4 v - 2\mu_1 v - 2\mu_2 v - 2\mu_3 v - 2\mu_4 v)/r^2\Bigg),
\end{aligned}
\tag{4.23}
$$

where $\rho = \sum_{k=1}^{4} \rho_k$. Note that for the radial coordinate, the following relation needs to be introduced $r = r_i + (k-1)\epsilon$, where k is the node number in the radial direction. Also, the assumption of non-zero inner radius was made.

4.3.2 Method verification and comments

To validate the method, a comparison of the proposed axisymmetric LISA numerical model with the commercial ABAQUS/Explicit solution was performed. An axisymmetric two-dimensional hollow cylinder of length 500 mm, with inner radius of 50 mm and wall thickness of 50 mm was modelled with both methods assuming the same simulation parameters. Material properties equivalent to aluminium (Young's modulus E = 70GPa, Poisson ratio ν = 0.3 and density $\rho = 2700\frac{kg}{m^3}$) were assumed. The cylinder was meshed with 0.5 mm square elements and to ensure the stability of the explicit time integration algorithm the time step was set to $0.05\mu s$. The excitation with eight cycles of Hanning windowed sine signal of central frequency of 265 kHz was introduced as in-plane displacement of a single node at the edge of the cylinder inner surface. Figure 4.2 compares the in-plane displacement signals obtained from the inner and outer surfaces of the cylinder, 200 mm from the excitation point. A good agreement between the two models was observed.

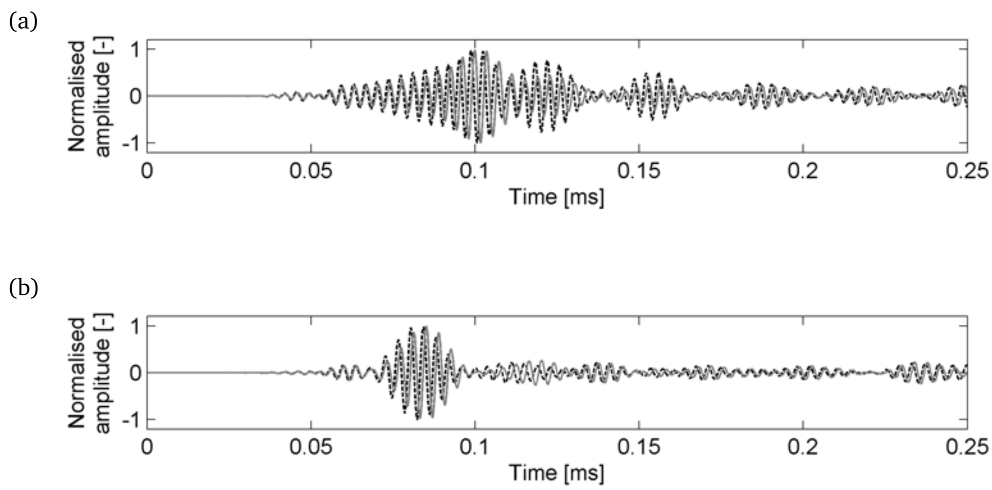

Figure 4.2: Comparison of the in-plane displacement signals obtained with the axisymmetric two-dimensional model with - - LISA and – ABAQUS/Explicit. Signals were acquired at 200 mm from (a) outer and (b) inner surface of the model.

4.3.2.1 Limitations and comments

The proposed two-dimensional cylindrical LISA allows to avoid the 'staircase' problem of meshing a curved surface with finite number of square/cubic elements, which is intrinsic for three-dimensional Cartesian LISA models. It also provides a tool for efficient and fast handling of large/long cylindrical models with little computing power requirements.

The major limitation of the proposed simulation approach is the modelling of local discontinuities, since in principle those changes have to be uniform over the entire circumference of the model. Also no treatment of the case with an inner radius equal to zero i.e. solid cylinder model, was considered, as this case is beyond the interests of this thesis.

Finally, in contrast to the available axisymmetric model in ABAQUS, the proposed 2D LISA method does not consider the displacement along the circumferential direction of the cylinder i.e. it disregards the torsional modes. This simplification is convenient when an analysis of purely longitudinal modes is desirable; an example will be shown in the following section.

4.4 Simulation of the experimental setup with LISA

This section presents a set of numerical simulations performed with the local interaction simulation approach, as a preliminary investigation for the experimental studies in chapter 3.

4.4.1 Introduction

The numerical results presented first, were obtained with the three-dimensional LISA implemented using parallel computing and the graphical card technology (CUDA) [83]. The parallel computing architecture allowed to significantly reduce the computational effort and the total calculation time. Through the model-based LISA the excitation-sensing procedures as expected in the experimental investigations were simulated.

A hollow cylinder with an inner radius of 25 mm and wall thickness of 75 mm was modelled. Due to the limitations of the computational capacity, the model length was reduced to 250 mm as compared to 500 mm for the cylinder used in the experiments. The model was meshed using 0.5 mm cubic elements. This resulted in a total of 65M elements and 195M degrees of freedom. Material properties equivalent to aluminium were assumed, i.e. Young's modulus E = 70GPa, Poisson ratio ν = 0.3 and density $\rho = 2700\frac{kg}{m^3}$. Time step was equal to $0.05\mu s$ to ensure the stability of the explicit time integration algorithm.

The excitation was introduced as out-of-plane displacement for a single node. Displacement responses were acquired at selected nodal points during the simulation. Several calculations were performed in order to determine the most convenient measurement conditions, and to investigate various guided waves propagation properties.

4.4.2 Results for broad-band excitation

Firstly, wideband excitation was used to estimate dispersion characteristics of the cylinder. A chirp signal of the frequency range from 50 to 1500 kHz was used. Two excitation points - located at the inner and outer edges of the cylinder - were selected. In both cases, the responses were acquired at the outer surface along a line parallel to the cylinder's axis. Altogether 471 responses were gathered. The response time was set to 0.5 ms, allowing for double wave reflections from the flat end surfaces. Simulated signals were processed using a two-dimensional Fourier transform resulting in the wavenumber-frequency representation. The results for the two considered excitation scenarios are presented in figures 4.3a and 4.3b. The brighter colours indicate the higher amplitudes.

The results demonstrate that for the two excitation scenarios used (i.e. inside and outside surface excitation) a complex pattern can be observed in the dispersion characteristics. Both analyses show a strong wave propagating with Rayleigh velocity at the outer surface, as indicated by a straight diagonal line. These results can be compared with the analytical solution given in figure 4.3c, however note that only the axisymmetric modes are presented in this figure. A significant difference in the distribution of wave amplitudes can be also observed when the results for the two simulated excitation scenarios are compared. Once a

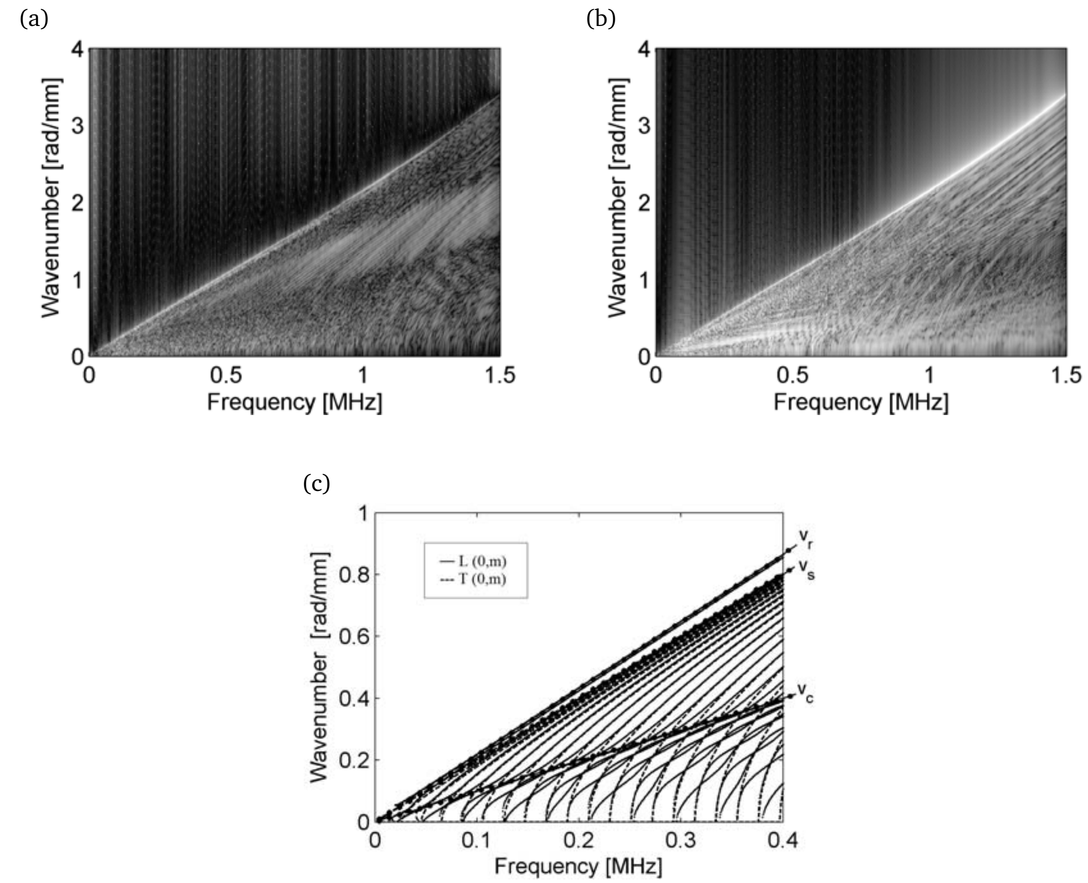

Figure 4.3: Dispersion characteristics of a aluminium hollowed cylinder (inner radius - 25 mm; thickness - 75 mm): simulation-based (3D LISA model) with (a) inner surface, (b) outer surface excitation and (c) theoretical axisymmetric modes (Eq. (2.47)). The dot-dashed (—·) lines indicate the Rayleigh (v_r), shear (v_s) and compressional (v_c) bulk wave velocity limits. The brighter colours indicate the higher amplitudes.

large portion of the energy - introduced by the excitation at the outer surface - is carried by the 'quasi-surface' wave, its amplitude dominates the wavefield. Figure 4.3b for the outside excitation demonstrates that, except for the 'quasi-surface' modes and higher amplitudes in the low frequency range, no clear mode can be distinguished. On the other hand, when the inside excitation is used, the wavefield recorded at the outer cylinder surface shows a number of higher order modes of similar amplitudes to the amplitude of the Rayleigh velocity modes. This behaviour is manifested in figure 4.3a as a pattern of parallel curves above the compressional velocity line.

The propagation of both axisymmetric and flexural modes hampers the possibility of differentiation between various wave modes. To improve the separation of the dispersion curves, the single point excitation of the three-dimensional LISA model was substituted with a continuous ‘ring’ type excitation placed at the inner circumference of the cylinder. This allowed to limit the excited number of modes to the axisymetric modes only. Figure 4.5 presents an example of the dispersion characteristics evaluated from the ‘ring’ excitation configuration. Clear similarities with the theoretical dispersion curves are observed.

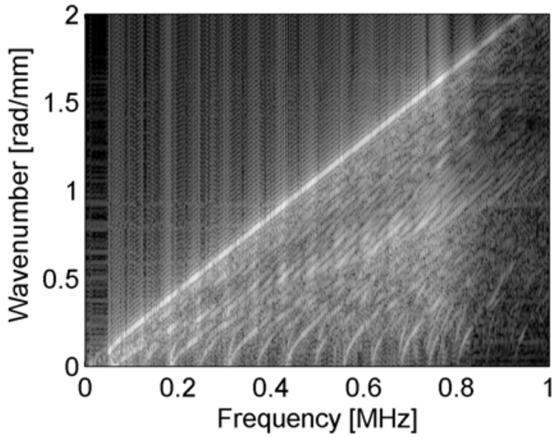

Figure 4.4: Simulation-based dispersion characteristics of an aluminium hollowed cylinder (inner radius - 50 mm; thickness - 50 mm): simulation-based with inner surface ring excitation. The brighter colour indicates the higher amplitudes. Excitation signal: half-cycle of sine function of a frequency of 500 kHz.

In the next stage, the results from three-dimensional model were compared with the two-dimensional axisymmetric LISA model developed in section 4.3. Since 2D modelling requires significantly less computational power, for this case the total length of the model was chosen as 2 m. As presented in figure 4.5, for the axisymmetric model, a distinctive pattern of seemingly interlacing modes can be easily recognized.

4.4.3 Results for narrow-band excitation

Subsequently, a narrowband excitation was used in numerical simulations for wave propagation analysis. The excitation signal was generated as 10 cycles of sine function windowed using the Hanning window, with the central frequency equal to 200 kHz. Again, the two excitation points – inside and outside the cylinder – were selected for these simulations. The results are shown in figure 4.6. An edge-guided wave mode can be observed for both investigated excitation cases. The mode clearly separates as an edge wave at the outer diameter as depicted in figure 4.6b for the excitation applied at the

(a)

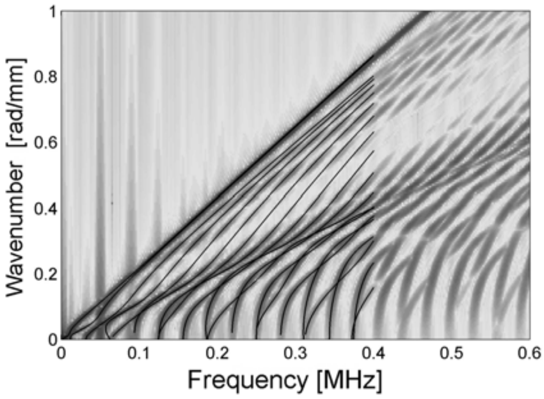

(b)

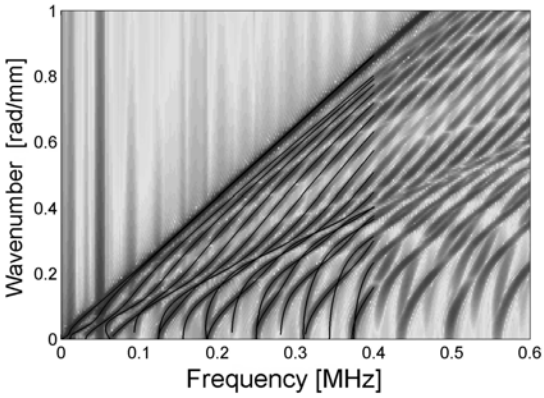

Figure 4.5: Wavenumber - frequency dispersion characteristics of axisymmetric longitudinal modes calculated for an aluminium hollow cylinder with inner diameter 100 mm from (a) axial and (b) radial displacements. Theoretical dispersion curves are shown in solid black lines. The darker colours indicates the higher amplitudes.

inner surface. In all numerical simulations performed, the wave propagates across the thickness as well as in the circumferential and axial directions of the cylinder. Strong amplitudes of wave part travelling around the cylinder is visible on the outer surface for outside excitation.

The results also show that the excitation of the circumferential guided waves (i.e. modes that propagate in the circumferential direction of the cylinder) has a significant implication on the responses. Although these waves are not of main interest in this thesis, two interesting observations can be made. Firstly, after the wave circulates around the cylinder, a new wave packet is generated at the origin. This wave packet propagates in the axial direction of the cylinder. An experiment-based example of this phenomenon was provided at the end of the section 3.4.3. Secondly, the circumferential waves interfere with the axially propagating modes, introducing additional components in the dispersion

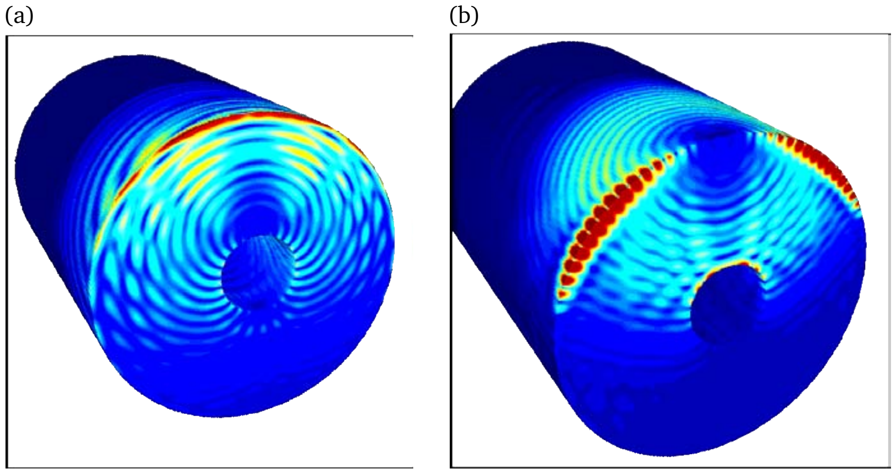

Figure 4.6: Numerical simulations of wave propagation after 0.08 ms for: (a) inner surface excitation; (b) outer surface excitation.

characteristics. The results show that the circumferential ‘surface’ waves can be expected in the dispersion measurements particularly for the outside excitation.

4.4.4 Summary

Numerical simulations have revealed a number of wave propagation modes in the dispersion characteristics of a thick-walled hollow cylinder. However, these characteristics are dominated by the Rayleigh velocity modes. The results show that the excitation inside the cylinder produces better results than the excitation outside the cylinder for both types excitations used (i.e. broadband and narrowband excitations) as it facilitates propagation of the higher order modes, allowing for inspection of the cylinder’s wall throughout its thickness.

Since both antisymmetric and flexural modes are propagating for this type of excitation a very fine resolution in the wavenumber domain is required to differentiate between various wave modes. In order to obtain more accurate dispersion curves, the analysis of the two-dimensional cylinder model supporting solely longitudinal modes was carried out.

4.5 Conclusions

The multimodal, dispersive nature of elastic wave propagation in thick-walled cylindrical structures hampers the derivation of an exact analytical solution to the guided-wave propagation problem. In particular for structures with complex geometry the wave scattering from boundaries introduces additional difficulties in the investigation of the wave behaviour using analytical or experimental approaches. On the other hand, the numerical simulations are effective and efficient tools especially valuable at the stage of the primary analysis and during the optimisation process. This chapter aimed at giving necessary background for the discussion on numerical simulation analyses that are presented throughout this thesis.

Two simulation approaches are employed in this work, namely finite element method implemented in commercial software ABAQUS and finite difference LISA method. Due to the differences in the formulation of these two methods, their effectiveness depends on the problem definition. In general, FEM is considered as more suitable for simulation of complex geometries since it supports various size of the mesh at different regions of the same structure (i.e. it gives a possibility of refining the mesh at the boundaries of the body). Finite element methods provide also a wide selection of base elements for meshing the geometry. On the other hand, the three-dimensional LISA implemented in the parallel processing architecture is capable of efficiently computing models with high spatial and temporal resolution. An excellent review of the performance of 3D LISA solver implemented with CUDA technology and its comparison to finite element models is given in [83]. This ability of fast and convenient handling of large models was one of the major reasons why LISA was chosen as the primary simulation tool in this research.

The results from the numerical simulations of broadband and narrowband excitation presented at the end of this chapter were used at the stage of designing the experimental setup and as a reference results during for the experiments. The simulations reveal the difficulties in the interpretation of the dispersion curves due to the presence of the flexural modes. Nevertheless, some characteristic features were observed such as strong Rayleigh velocity modes and the presence of strong edge guided wave in the circumferential propagation direction. These observations were confirmed later experimentally.

The two-dimensional axisymmetric formulation of local interaction simulation method that employs the governing equations in cylindrical coordinates (r, z) was also established in this chapter. The main motivation for deriving this wave propagation model with the assumption of the axisymmetry, was the high computational power needed to simulate a three-dimensional model of a thick-walled railway axle. Another reason for this development was the preliminary studies that have shown the complex behaviour of the propagating modes for a single point excitation. Thus, the focus has been turned to limiting the number of analysed modes. This was conveniently achieved with the proposed axisymmetric cylindrical LISA method. Other application examples of the 2D LISA scheme will be given in the following chapter, while discussing the local wave enhancement effect.

Chapter 5

Local wave enhancement effect

5.1 Introduction

This chapter investigates the influence of geometrical transitions on propagation of elastic waves in thick-walled cylindrical structures and proposes a structural evaluation technique based on the observed near field wave enhancement phenomena. The organisation of this chapter is as follows. First, a brief theoretical background on 'quasi-surface' wave formation is given, followed by an analysis of the near-field wave enhancement effect due to crack-wave interaction. Influence of the waveguide geometry on wave enhancement is then discussed in section 5.3. Based on the acquired understanding, in section 5.4, an inspection method dedicated to thick-walled structures with geometrical transitions is proposed. Finally, the method is verified experimentally using two beam-type elements and a hollow cylinder with thickness variations.

5.2 Physical insight into the near-field wave enhancement

Although, the near-field enhancement effect due to a surface-breaking crack has been observed in the past for Rayleigh waves [35, 33, 34] and Lamb waves [23, 24], there is no research on enhancement effect of the cylindrical guided waves, neither on the feasibility of this effect for thick-walled structure inspection. This section investigates theoretically and numerically the mechanism of crack-induced local enhancement, in a thick-walled hollow cylinder, for excitation and sensing located on the opposite surface to the crack occurrence.

5.2.1 Development of 'quasi-surface' waves

Prior to discussing the wave enhancement effect, it is important to address the mechanism of the formation of guided modes in a thick-walled structure. As discussed in chapter 2, the guided wave field depends on various excitation features such as exact frequency range, excitation area (shape of the transducers, number and location of excitation points etc.). In contrast to a thin-walled waveguide, when the development of the guided modes in a thick-walled cylinder is discussed, a special consideration is required for through thickness wave propagation.

To analyse the guided wave generation, a numerical model of an aluminium hollow cylinder of 500 mm long, with an inner radius of 50 mm and wall thickness of 50 mm was simulated with axisymmetric 2D LISA developed in chapter 4. The simulation parameters –time and space discretisation– were chosen as $dx = 0.5\ mm$ and $dt = 0.5\ \mu s$. The cylinder was excited with eight cycles of sine signal with a central frequency of 265 kHz windowed with Hanning function. The dispersion characteristics of the analysed structure are shown in figure 5.1. Note that due to the axisymmetry condition of the model, propagation of only longitudinal modes is considered, which significantly simplifies the discussion.

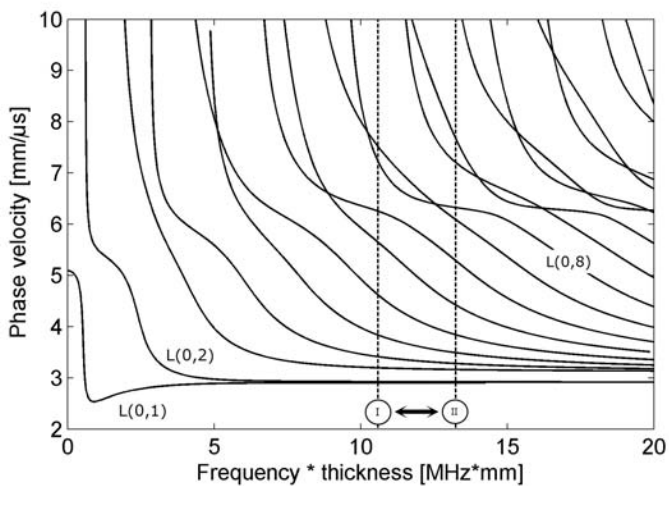

Figure 5.1: Phase velocity dispersion characteristics of axisymmetric longitudinal modes for an aluminium hollow cylinder with inner diameter 100 mm. (Material properties: $\nu = 0.33$, $E = 70\ GPa$, $\rho = 2700\ kg/m^3$)

The two vertical lines (I,II) refer to the product of the excitation frequency (265 kHz) and thickness of 40 mm and 50 mm, respectively. As discussed in chapter 3, in the high frequency range – short wavelength region – the two basic modes named L(0,1) and L(0,2), exhibit almost non-dispersive behaviour with propagation velocities asymptotically approaching Rayleigh wave velocity (here, v_r = 2.9 m/ms). In this limit, the displacement patterns of these two modes become localised at the inner and outer surfaces of the structure as depicted in figure 5.2. Due to the displacement patterns it is convenient to call these two modes 'quasi-surface' waves. (The existence of two surface modes in a hollow cylinder – 'exterior quasi-surface mode' and 'interior quasi-surface mode' was first discussed in [100].)

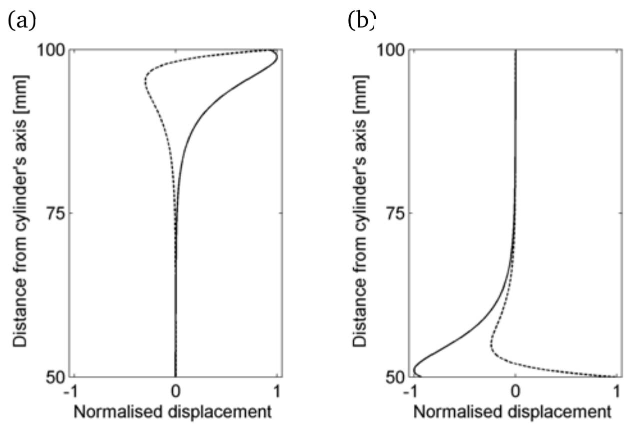

Figure 5.2: Concentration of – radial and - - axial displacements at the cylinder surfaces for: (a) L(0,1) and (b) L(0,2) modes at frequency 265 kHz.

Figure 5.3 illustrates the guided wave development due to a single nodal excitation at the edge of the inner surface of the cylinder in the axial direction (for three-dimensional model this corresponds to an inner ring-type excitation). As expected, the simulation results reveal two distinct 'quasi-surface' waves formed in the waveguide: at the inner and outer surfaces, respectively.

The specific outcomes of the selected excitation scenario are the following. Firstly, a strong 'quasi-surface' wave is formed at the inner surface of the cylinder – the L(0,2) mode. The mode propagates in the axial direction of the structure practically without dispersion. Secondly, part of the wave energy is dissipated as partial/bulk waves and by reflections from the boundaries forming higher order longitudinal modes. Finally, a surface wave travels in the radial direction along the cylinder face, and then is reflected from the outer

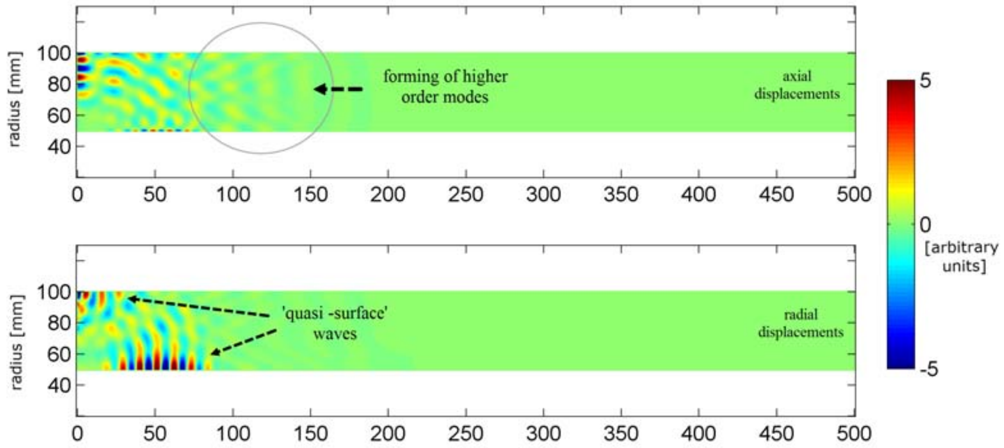

Figure 5.3: Guided wave formation. (Cross-sectional view)

surface 90° edge. Due to this reflection, part of the surface wave propagates backward to the cylinder inner surface, part is converted to the partial waves, and the remainder of the energy travels around the corner and leaves along the cylinder outer surface as second 'quasi-surface' wave – the L(0,1) mode.

The influence of the excitation location on the formation of the guided modes is further studied in figure 5.4. In this example the comparison of the 'quasi-surface' wave formation in two different hollow cylinder models –with and without an outer diameter change– both excited at a single node in the middle section of the cylinder is shown.

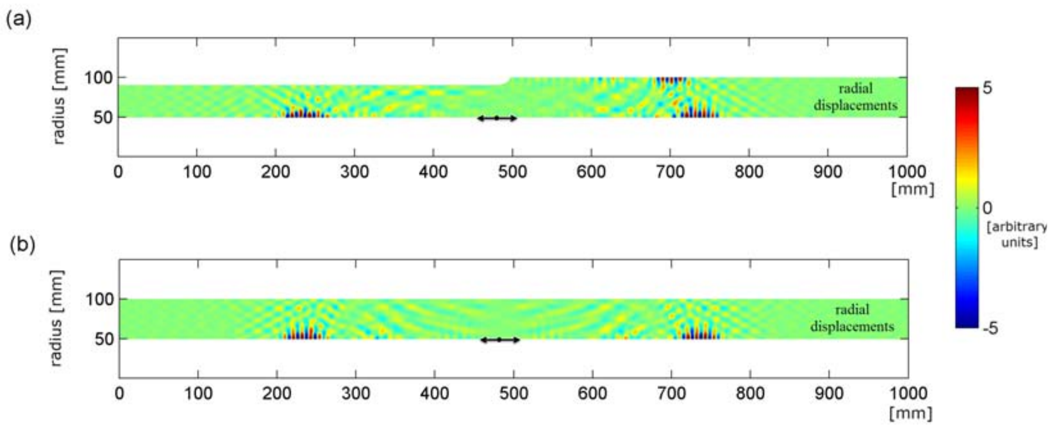

Figure 5.4: Radial displacement field at 0.1 ms for two different cylindrical geometries excited at the middle section of the structure (at 485 mm). Hollow cylinder with (a) a change of outer diameter from 200 to 180 mm, (b) constant thickness. (Cross-sectional view)

As expected, the 'exterior quasi-surface' wave is only formed in the model with outer diameter change in the near-field of the excitation. This can be attributed to the scattering of the incident partial wave – propagating through the thickness– from the outer surface discontinuity and energy concentration and formation of the ‘exterior quasi-surface’ wave. The observed phenomena may be considered as analogue to the body to Rayleigh wave mode-conversion at steps [105]; however, further studies are needed to establish a general framework for this effect.

After the introductory analysis of the guided waves excitation, we will now proceed to the discussion on the crack-wave interaction.

5.2.2 Wave enhancement due to crack-wave interaction

In this section the near-field wave enhancement effect developed due to the wave interaction with a surface breaking-crack is investigated. Firstly, the physical mechanism is briefly discussed, then the influence of the defect severity is addressed.

Background

The basis of the enhancement effect can be explained as follows. When an ultrasonic wave propagating in a structure encounters a defect, the wave scattering (i.e. reflection, conversion and transmission of the wave) occurs. The superposition of the incident, reflected and mode converted waves leads to the wave enhancement when the signals interfere constructively [36]. Note that in contrast to the bulk wave scattering, for guided waves, mode conversion can occur between all possible guided wave modes supported by the structure at a given thickness$\times$frequency value.

In Rayleigh wave-based applications typically a non-contact measurement system with electromagnetic acoustic transducers or laser interferometer is used for scanning the inspected surface. When a scanning or an excitation point of an ultrasonic wave (e.g. a laser beam) passes over a defect, local wave enhancement can be observed and used to pinpoint a defect occurrence. This phenomenon is especially appealing due to the fact that the signature of the crack can be seen even for a defect much smaller than the wavelength of the used Rayleigh wave as shown in [35]. In what follows the enhancement effect is investigated using numerical simulations.

Numerical simulations

Figure 5.5 is a pictorial representation of the enhancement phenomenon due to the crack-wave interaction in a 2D hollow cylinder model. To avoid the interference of reflections from the end boundary, the model length was 1000 mm. Due to the selected excitation type –single node excitation at the inner edge– two high amplitude 'quasi-surface' waves, formed at the inner and outer surfaces, can be distinguished in the radial displacement field. Since the energy of these modes is confined to the surfaces of the structure, their propagation is strongly affected by any on-surface discontinuities. To investigate this behaviour, a crack was introduced to the model at 280 mm as a 5 mm deep rectangular slot with 1 mm of width. It can be seen that, the interaction of the 'exterior quasi-surface' wave with the crack results in through thickness propagation of a part of the reflected wave (strong S-wave). This effect contributes to the local enhancement observed at the inner surface of the structure.

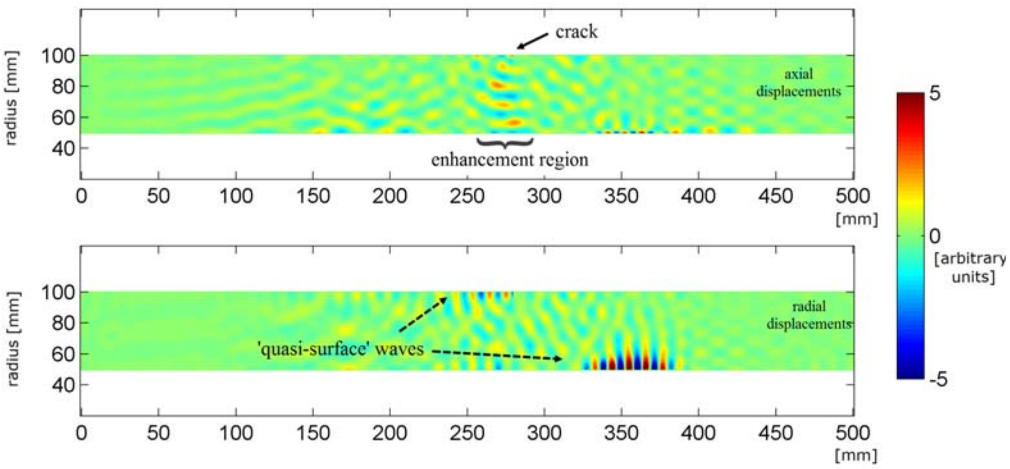

Figure 5.5: 'Exterior quasi-surface' wave-crack interaction. Cross-sectional view of displacement fields at 0.136 ms.

On the premise of guided wave theory, the enhancement effect can be explained as follows. When an elastic wave propagating in a structure encounters a local discontinuity, the wave mode conversion occurs between all possible guided wave modes supported by the structure at a given thickness×frequency. The interference of the incident, reflected and converted modes leads to the enhancement effect.

Exemplary axial displacement signals from the undamaged cylinder and model with a 5 mm deep crack are shown in figure 5.6. Four on-surface points were selected for the analysis: two points at 260 mm – before the damage, and two at 290 mm – after the damage.

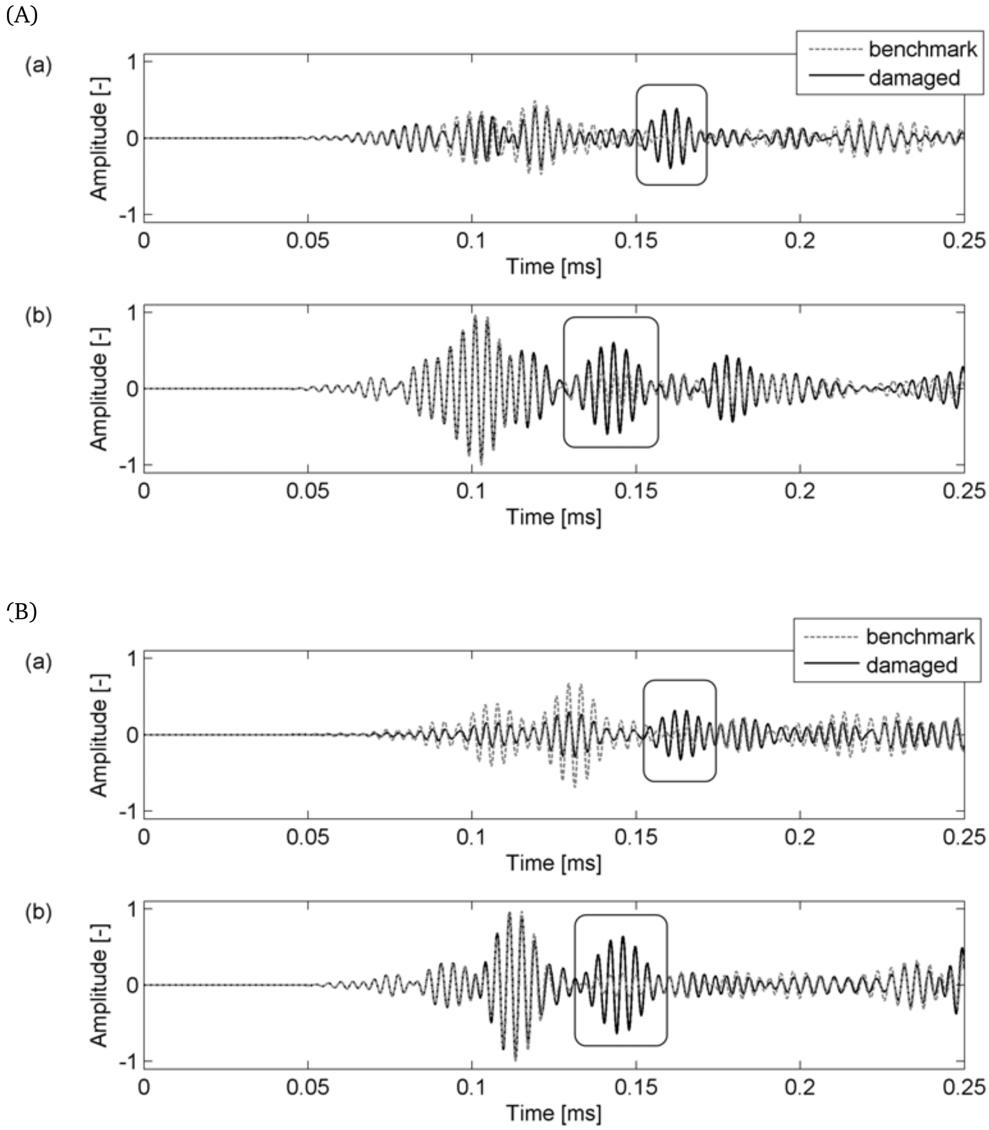

Figure 5.6: Waveforms of in-plane displacements at: (A) 260 mm and (B) 290 mm from the excitation point; at (a) outer, (b) inner surface of the hollow 2D cylinder .

For all four sensing locations, the wave enhancement effect (marked in the figure with boxes) can be easily distinguished. Although other signatures of the crack presence can be noticed e.g. a decrease of the amplitudes of the outer surface signal in figure 5.6B(a), for both locations at the inner-surface, the near-field enhancement effect is by far the dominant damage-related feature.

Influence of the crack geometry on the wave enhancement

Having discussed the mechanism of the wave enhancement effect, this section moves to investigate the sensitivity of this phenomenon to various surface-breaking crack types.

First, three different on-surface cracks models with depth of a 5 mm, located at 280 mm from the excitation point, are analysed, namely a clapping crack, a narrow 1 mm wide slot and a 5 mm wide slot. The relationship between the damage geometry and the local enhancement observed at the inner surface is illustrated in figure 5.7. For the convenience in modelling of crack clapping mechanism (i.e. surface contact between the crack faces was assumed), all results presented in this figure were obtained with finite element modelling approach using commercial ABAQUS software.

The high energy (brighter) line at each of the sub-figures corresponds to the propagation of the 'interior quasi-surface' wave. The distinctive region at around 0.14 ms for models with the crack is the enhancement effect due to the 'exterior quasi-surface' wave interaction with the damage. Similar enhancement patterns can be observed for different geometries of the defect; for instance, the effect from the narrow (1 mm wide) slot is almost indistinguishable from the clapping crack model (compare figure 5.7b and 5.7d). This confirms the expectation that the major contribution to the enhancement effect is the scattering of the incident wave from the crack interface. For conciseness, additional results from damage of geometry other than rectangular base slot are not presented here; however, it is expected that the enhancement effect should follow the same pattern as in the case of Rayleigh waves and readers may refer to [36, 33] for more details.

Damage severity assessment

Finally, the influence of the defect severity on the near-field enhancement effect is analysed. Cylinder models with various crack depths but at the same location (i.e. 280 mm) were simulated. The spectrogram time-frequency representation is used in figure 5.8 for convenient visual comparison of the signals' energy, considering the strong dispersion of higher order modes and almost non-dispersive character of the 'quasi-surface' waves. The spectrograms were evaluated from the axial displacement

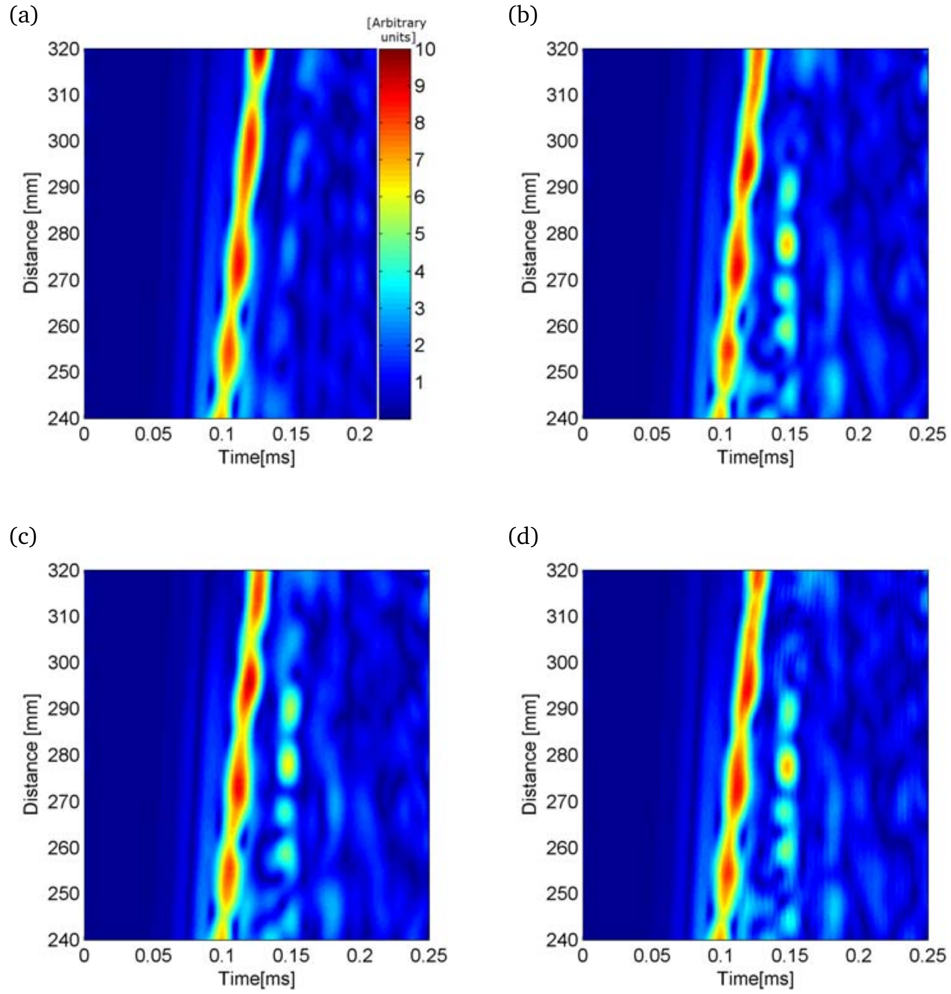

Figure 5.7: Energy distribution at the inner surface (calculated as envelopes of the axial displacements) for (a) undamaged case and cylinder with 5 mm deep crack at 280 mm modelled as: (b) slot of 1 mm width, (c) slot of 5 mm width, (d) clapping crack. The colour scale has arbitrary units, but is the same for all results.

signals, collected at the inner surface 260 mm from the excitation point. The wave enhancement effect can be observed at around 0.14 ms.

It is noted that the magnitude of the wave enhancement is clearly correlated with the damage severity. Further detailed qualitative analysis is presented in figure 5.9. Here, an *enhancement factor* was defined as the ratio of the maximal amplitude of the enhanced wave package to the benchmark signal (packages marked with rectangle in figure 5.6(b)).

The enhancement factor of the signals measured: before (260 mm), exactly below (280 mm) and after (290 mm) the defect, were compared. The results indicate that for all three locations a significant wave enhancement effect can be observed for a defect of a depth grater than 3 mm. Also, an increasing value of the enhancement factor can be noted

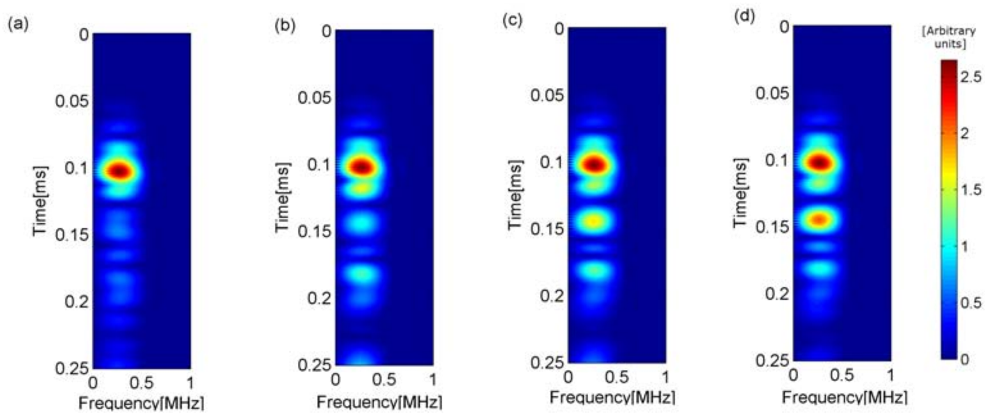

Figure 5.8: Correlation of the magnitude of the near-field enhancement effect with the damage depth, visible at around 0.14 ms. Signals acquired at the inner surface at 260 mm. Spectrograms of (a) benchmark signal and signals from model with the crack of a depth: (b) 2.5 mm (c) 5 mm, (d) 10 mm.

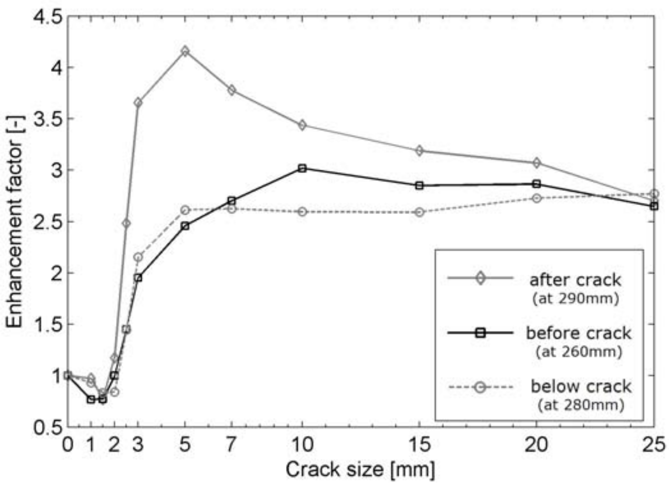

Figure 5.9: Changes in the enhancement factor with the crack depth; calculated from displacement signals at: 260 mm, 280 mm, and 290 mm. The enhancement factor was evaluated as a ratio of the maximal amplitude of the enhanced (with damage) to benchmark wave package.

for cracks between 2 and 5 mm. The results can be justified considering the mode shape of the L(0,1) mode at the selected frequency (figure 5.2). The positive correlation of the magnitude of the enhancement effect with the crack size is consistent with the findings for Lamb modes [23].

5.2.3 Summary

In this section, the near-field wave enhancement effect in a hollow cylinder has been investigated. To fully understand the origin of the phenomenon, the formation of the so-called ‘quasi-surface’ waves and their relation to cylindrical guided waves were also discussed.

The results from the numerical simulation reveal that a ring-type excitation at the edge of the inner surface results in the development of relatively weak higher order longitudinal modes and two strong ‘quasi-surface’ waves – at the inner and at the outer cylinder surface, propagating in the axial direction of the cylinder. The observations on ‘quasi-surface’ wave reflections from the boundaries are consistent with the findings on Rayleigh wave scattering at $90°$ corners presented in [79, 1, 11] and the work by Portz *et al.* [88] on surface wave reflection at plate edges. Yet, significantly different wave fields can be obtained for different excitation types. For instance, if the entire face of the cylinder is excited with the same frequency signal, it results in an instantaneous formation of the guided longitudinal modes near the excitation location. In that case, the pseudo-symmetric L(0,8) mode becomes a dominant mode and only the pseudo-symmetric ‘internal surface mode’ – L(0,2) is formed, while the L(0,1) mode is not visible (refer to figure 5.1 for dispersion characteristics). On the other hand, when the thick-walled structure is excited at high frequencies at the location far from the structure’s edges or other thickness discontinuities, the near-field is expected to be similar to wave propagation in a half-space excited by a harmonic point source (i.e. the disturbance spreads away in the form of an annular wave field of longitudinal, shear and Rayleigh waves [55]).

The numerical simulation results allow to identify the ‘quasi-surface’ wave as the major contributor to the enhancement effect in thick-walled cylinder. It was shown that the local enhancement can be caused by geometrical discontinuity such as clapping crack or a slot. The influence of the crack size on the magnitude of the effect was also shown. The presented findings are to some extend similar to those discussed by Clough and Edwards [23, 24] for a wave-crack interaction in Lamb wave supporting structures; however, due to the significant thickness-to-wavelength ratio in the presented cases, different behaviour of the wave were observed and the Rayleigh wave enhancement analysis [35, 36] was also incorporated into the discussion.

The presented results suggest that the investigation of the near-field enhancement effect has potential for the monitoring of hollow axles. Particularly since the information about a outer-surface defect is transferred to the inner surface, both the excitation and the sensing could be carried out from the bore of the axle. Moreover, it is expected that wave scattering due to a geometrical transition in a waveguide –which is also a type of a local surface discontinuity– may result in a similar near-field enhancement effect as the crack-wave interaction. In the next section this phenomenon is examined.

5.3 Geometrical transition as a source of wave enhancement

Although, inspection methods based on the near-field enhancement effect provide direct indication of a crack, they require the scanning of the entire structure's surface either by excitation or by sensing. The scanning for defect presence, restrains the method from being fully effective in particular for hardly accessible surfaces. This section analyses wave enhancement mechanism due to a change in the waveguide geometry and discusses the possibility of using this phenomenon for structural evaluation.

5.3.1 Background on wave scattering at geometrical transitions

Numerous studies have shown that thickness variation within a waveguide results in wave scattering (i.e. partial reflection and conversion of the propagating modes) [19, 37, 45, 92]. The phenomenon depends on the geometry of the transition region including its slope or symmetry. Moreover, in contrast to bulk waves, guided waves scattering involves not only the incident mode, but all possible modes supported by the structure at a given frequency. This implies that for a particular condition the thickness change can result in different number of propagating modes in the transmitted and reflected waveguide regions (refer to figure 5.1).

To analyse the complex behaviour of cylindrical guided waves, it is necessary to refer first to a simple geometry case. Two case studies from the literature are discussed here: a single Lamb wave mode in a plate [19], and a Rayleigh wave [11, 12] propagation.

Following [19] the influence of various step discontinuities on the propagation of the basic symmetric (S0) are summarised below in bullet points.

- A change of a waveguide thickness (either a decrease or an increase of the thickness) results in wave mode scattering. The phenomenon depends both on the slope of the transition and the frequency of the wave.

- For nonsymmetric thickness reduction, mode conversion from the incident symmetric S0 mode increases proportionally to the slope of the transition.

- For thickness increase, some mode conversion of the incident S0 mode occurs; however, with a decrease of a slope between the two sections of the waveguide, the transmitted field is dominated with the S0 mode.

- A remarkable mode conversion occurs at the frequencies at which a new cut-off mode appears.

For sufficiently small wavelengths compared to the plate thickness, the wave propagation analysis converges to the discussion on surface waves behaviour. Blake and Bond [11, 12] presented a numerical investigation on Rayleigh wave scattering from various surface features including wedges, downward steps, upward steps and troughs. Some of their findings are given in tables 5.1 and 5.2. Note that the transmission and reflection coefficients are given as mean values, due to the fact that they were found to oscillate depending on the step depth-to-wavelength ratio.

Table 5.1: Rayleigh wave scattering coefficients. Downward step [11].

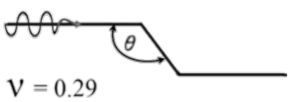

Angle $[deg]$	Reflection $[\%]$(mean)	Transmission $[\%]$(mean)
90	35	18.4
135	12.5	37.2

Table 5.2: Rayleigh wave scattering coefficients. Upward step [12]

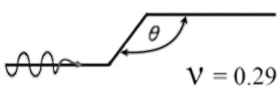

Angle $[deg]$	Reflection $[\%]$(mean)
90	7.2
135	4.7

The results indicate that the Rayleigh wave reflection coefficients decease with the decease of the slope of the transition. The authors were not able to evaluate the transmission coefficients for the up-step geometry, because of the presence of strong converted shear wave. Unfortunately, there has been no analysis of the energy associated with the converted compressional and shear waves; it seems that especially the investigation of the shear wave could contribute to the discussion on near-field enhancement effect.

To complete the discussion, it is important to mention that guided waves propagating in a plate with a slowly varying thickness are called adiabatic modes [6, 37, 45]. The phase velocity of an adiabatic mode changes continuously depending on the local thickness of a waveguide. Furthermore, an interesting phenomenon of mode reflection and backward propagation, at mode's thickness$\times$frequency cut-off was observed in [37, 45].

To sum up, when a structure with varying geometry is considered, a change in thickness or in surface features causes wave scattering. This phenomenon involves local reflections and conversions of the propagating modes. In both guided waves scattering examples presented here i.e. Lamb wave mode and Rayleigh wave, the slope of the transition and wavelength-to-step depth ratio were found critical for the wave behaviour. In the literature, the complex physics underlying the elastic wave scattering is frequently emphasized. In particular, for thick-walled structures where propagation of numerous guided wave modes is possible, the reflection and conversion phenomenon of a single mode is difficult to trace. Therefore, this wave propagation aspect and its link to the near-field wave enhancement effect are analysed in the following section via numerous simulations.

5.3.2 Cylindrical waveguide with thickness transition - broadband excitation

Having in mind the general relationship between reflection/conversion of modes and the waveguide transition geometry, we may now continue the discussion on thick-walled cylindrical structures. This is performed using numerical simulations and qualitative analysis of the dispersion characteristics.

The influence of the outer diameter variation of the hollow cylinder on guided wave propagation characteristics is first investigated through the evaluation of the dispersion characteristics of various cylindrical geometries. To this end, a two meters long hollow cylinder with an inner diameter of 100 mm was modelled with 2D LISA. Various transition geometries of the outer diameter were investigated. For convenience and conciseness of the description, the variations of the outer diameter are referred in the text as thickness changes; however readers are reminded that the inner diameter was kept constant for all simulated cases. The following models with thickness changes defined as: downward step from 50 mm to 40 mm, downward step from 50 mm to 25 mm, upward step from 40 mm to 50 mm and downward step from 50 mm to 40 mm with a curvature of radius of 15 mm, were analysed. For all analysed cases, a broadband excitation of half period of sine signal with a central frequency of 265 kHz was used. The dispersion characteristics were evaluated from the axial displacement signals (inner surface), using two-dimensional Fourier Transform [2]. The results are shown in figure 5.10. The negative wavenumbers in the plots correspond to the backward propagation i.e. reflected waves. The colour levels –from blue to red– indicate the values of the modulus of two-dimensional Fast Fourier Transform in a logarithmic scale. The signals were normalised with respect to the maximal magnitude obtained for each of the geometries separately. (In the corner of each figure, a sketch of the type of the transition geometry is given.)

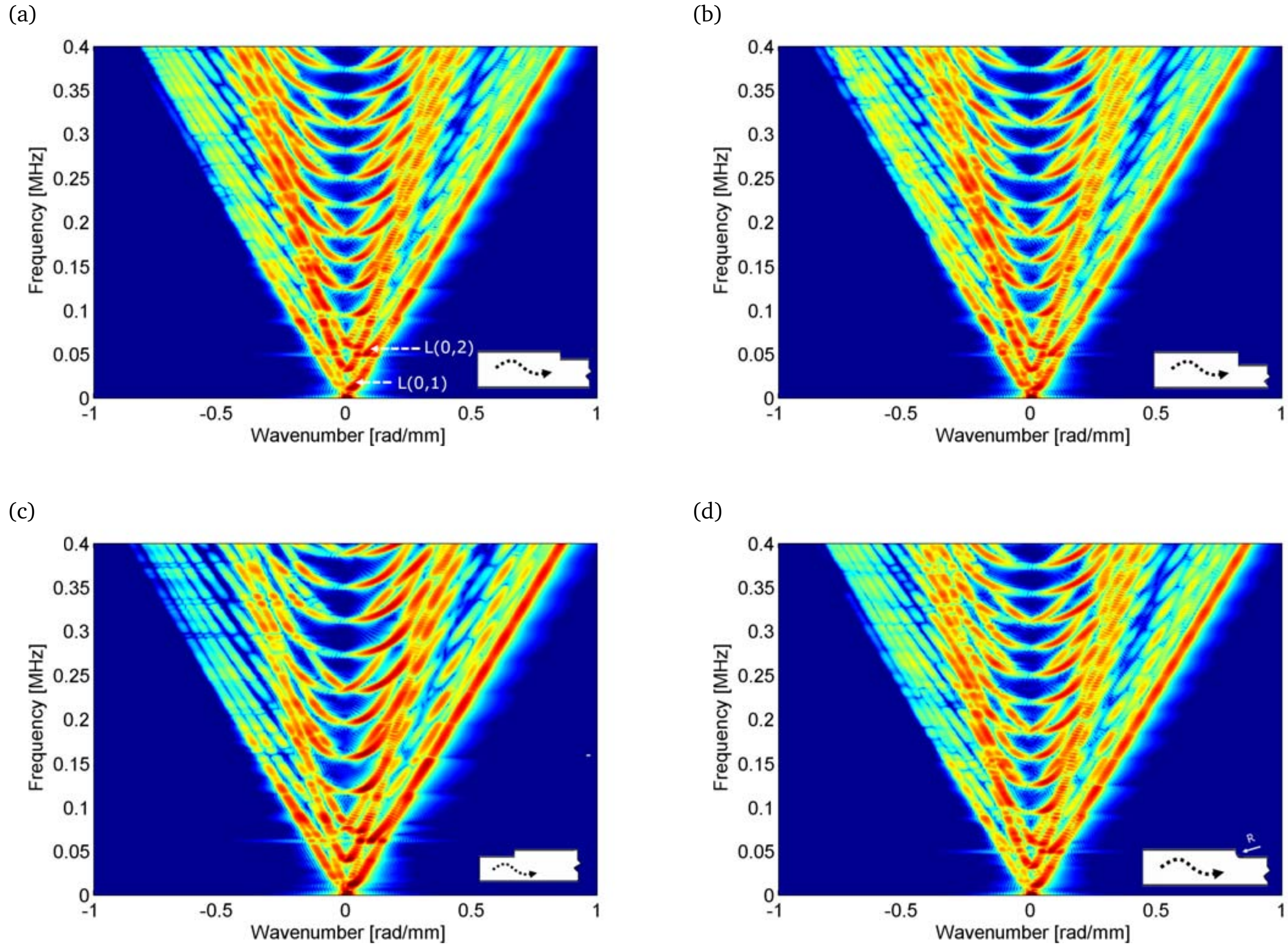

Figure 5.10: Simulation-based dispersion characteristics for thickness change modelled as: (a) downward step from 50 mm to 40 mm, (b) downward step from 50 mm to 25 mm , (c) upward step from 40 mm to 50 mm, (d) downward step from 50 mm to 40 mm with curvature of radius 15 mm.

The comparison of the energy distribution of the reflected and the incident modes gives an insight into the wave propagation characters. As expected, weaker reflection of the L(0,1) and L(0,2) modes is seen for the cylinder model with downward step with curvature of 15 mm (figure 5.10d) than for other waveguides. Another observed feature is that when the thickness of the waveguide increases (figure 5.10c) most of the wave energy is transmitted to the subsequent section of the structure; an exception is a significant reflection energy of the two first modes in the long wavelengths region (low frequency). These findings are to some extent consistent with the previously discussed ones in section 5.3.1 on Rayleigh and Lamb waves.

Figure 5.11 illustrates guided wave behaviour in a hollow cylindrical waveguide with a 10 mm thickness reduction at 500 mm. Time-distance representation of the envelopes of displacement signals obtained at the inner surface of the cylinder is shown. The high magnitude (in red) line across the figure corresponds to the strong ‘quasi-surface’ L(0,2) mode- propagating at the inner surface of the cylinder. A weaker energy line of the similar character, starting at 0.035 ms is also noticed. This line can be associated with the secondary ‘interior quasi-surface’ wave, which begins to propagate in the axial direction after a round through-thickness propagation as the face-guided wave.

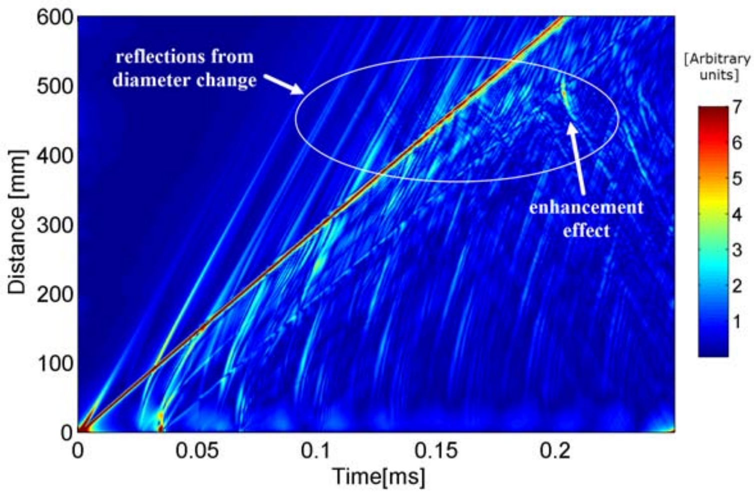

Figure 5.11: Energy distribution (envelope of the axial displacement signals) at the inner surface of the hollow cylinder for cylinder with geometrical transition at 500 mm. Step change of thickness from 50 mm to 40 mm.

As marked in the figure, the wave is partially reflected at the transition region – 500 mm. The analysis of the wave fields (not shown here for conciseness) has shown that similarly to the crack-wave interaction, in particular the scattering of the ‘exterior quasi-surface’ wave appeared as strong reflections at the inner surface of the cylinder (the brighter area marked with an arrow). This phenomenon contributes to the strong near-field enhancement effect which is examined closely in the following paragraphs.

Hence, the dispersion characteristics confirmed that the guided wave scattering depends on the exact transmission region geometry, the near-field enhancement effect is expected to exhibit a similar behaviour. Figure 5.12 depicts the wave enhancement phenomenon for various waveguide geometry changes. As in the case of the crack-wave interaction, the magnitude of the enhancement effect for a step discontinuity depends on the degree of the thickness change (compare figure 5.12a and 5.12b). Also the influence of the curvature/slope of the transition is noticed in figure 5.12d, namely the energy is 'shifted forward' in comparison to the sharp downward step transitions. Another important fact to be noticed is that the enhancement effect is not visible for the increase of the thickness (figure 5.12c). This can be explained as a consequence of significantly weaker reflections of the 'quasi-surface' modes; mostly conversion to the higher order modes was observed.

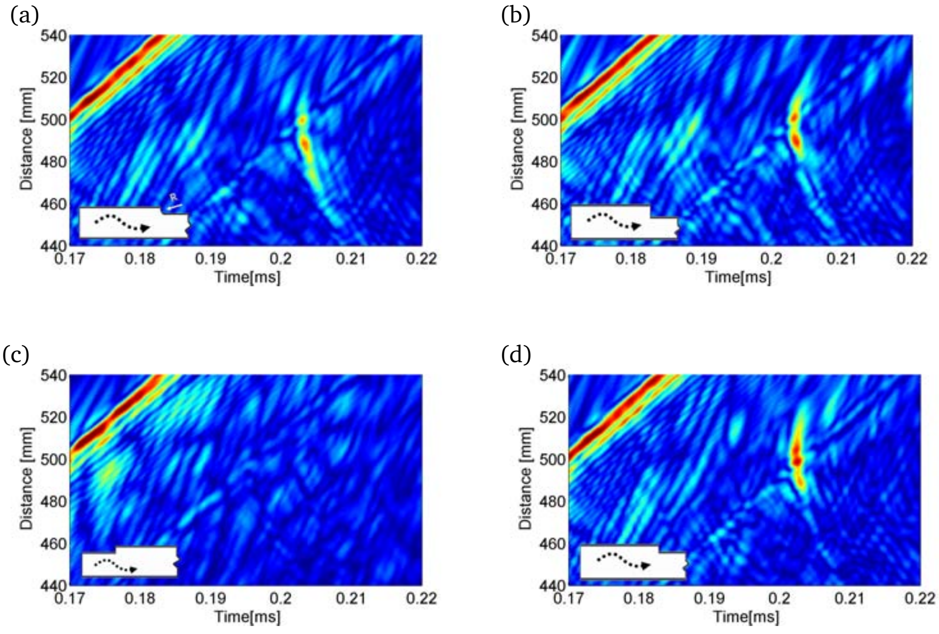

Figure 5.12: Energy distribution (envelope of the axial displacement signals) at the inner surface of the hollow cylinder for cylinder with geometrical transition at 500 mm: (a) downward step-change of thickness from 50 mm to 40 mm , (b) downward step change of thickness with radius 15 mm, from 50 mm to 40 mm, (c) upward step change of thickness from 40 mm to 50 mm. Colour levels referring to the magnitude of the wave amplitudes are the same as in figure 5.11 – the same for all cases.

To sum up, the conducted analysis confirms that a thickness change in a waveguide results in an energy redistribution between incident, reflected and transmitted modes. This phenomenon occurs to facilitate a guided wave propagation in the subsequent section of the structure i.e. section with different thickness×frequency value. Furthermore, for a thick-walled structure as a result of the 'quasi-surface' wave scattering, the near-field enhancement effect can be observed at the transition region. From the partial wave view point, the major energy component is associated with through thickness propagation of the converted partial shear waves. After the general discussion, the attention will be turned now to the case of a narrowband excitation.

5.3.3 Cylindrical waveguide with thickness transition - narrowband excitation

The broadband excitation analysis allowed to identify the strong enhancement effect due to reflection and conversion of the 'quasi-surface' wave. In practice however, a narrowband excitation is commonly used since it facilitates the separation of the guided modes and allows for easier interpretation of the results. Therefore, numerical simulations using eight cycles of Hanning windowed sine signal of frequency 265 kHz were carried out.

A hollow cylinder with an outer diameter reduction by 10 mm as shown in figure 5.13 was modelled with 2D LISA. The excitation frequency was selected according to the dispersion characteristics in figure 5.1; the two vertical lines marked as I and II correspond to the product of excitation frequency and the wall thickness of the waveguide sections, respectively 40 mm and 50 mm. It is noteworthy that, for the cylinder with the wall thickness of 50 mm, there exists fourteen modes with cut-off frequencies below 265 kHz; whereas, the cylinder with 40 mm thick wall supports only eleven modes at the same frequency. Consequently, the energy redistribution in form of mode conversion and reflection has to occur at the thickness reduction region, to facilitate further wave propagation in the waveguide section after the transition. Figure 5.14 compares the energy of the propagating wave at the inner surface of the cylinder around the geometrical transition region.

The high energy mode (red line) corresponding to the 'interior quasi-surface' wave is still

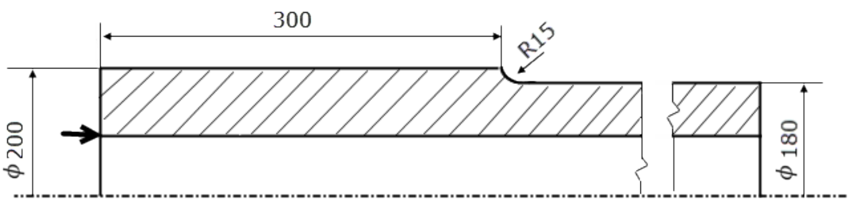

Figure 5.13: Sketch of the axisymetrical model of a hollow cylinder with inner diameter 100 mm and total length of 1000 mm. Excitation point located on the inner surface is marked with an arrow.

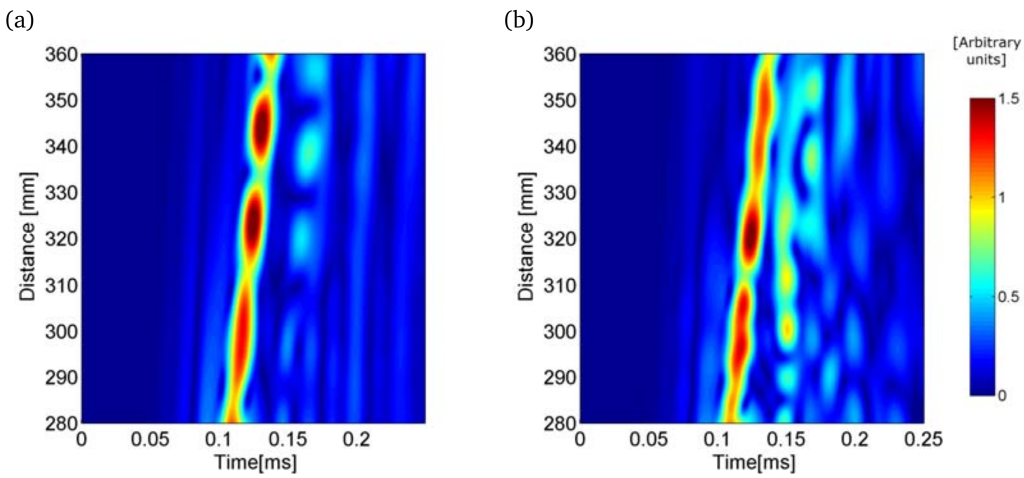

Figure 5.14: Energy distribution at the inner surface of the hollow cylinder (envelope of the axial displacement signals) for: (a) cylinder without outer diameter change, (b)cylinder with geometrical transition at 300 mm shown in figure 5.13

observed. The mode enhancement effect can be distinguished at around 0.15 ms from 295 mm to 330 mm. Following the discussion presented in the previous sections, it should be reminded that the enhancement effect depends on the geometry of the transition and the characteristic of the propagating modes. Particularly, for the relatively small thickness change as compared to the wavelength of the ‘quasi-surface’ modes, the magnitude of the effect is negligible (minor disturbance) and a propagation of the ‘quasi-surface’ wave to the downstream section of the waveguide is expected.

5.3.4 Summary

The near-field wave enhancement effect due to geometrical transition in a cylindrical waveguide has been investigated via numerous simulations with two-dimensional LISA. Due to the fact that the wave scattering for the high thickness-to-wavelength ratio involves rather complex behaviour i.e. multiple reflections and mode conversions, the explanation of the observed phenomena has to adopt both the guided waves and bulk waves approaches.

The presented numerical results indicate that the ‘quasi-surface’ wave scattering and the through-thickness propagation of the associated energy are the major contributors in the local enhancement.

Moreover, since the ‘quasi-surface’ wave has been found highly sensitive to on-surface discontinuities, a new method of damage detection based on the understanding of the examined phenomena is proposed in the following section.

5.4 Inspection method of a waveguide section

As has been discussed in this chapter, the propagation of ‘quasi-surface’ wave is strongly influenced by surface discontinuities such as surface-breaking cracks and geometrical transitions. On that premise, a presence of an on-surface-crack is expected to reduce the wave enhancement effect caused by a geometrical transition, if located before the transition. Accordingly, a change in the magnitude of the geometry induced near-field enhancement effect can be used as an indirect indication of the crack. Based on the aforementioned principle a novel inspection approach, which used the geometrical transitions in a waveguide as sensing and excitation locations is proposed.

The basis of the proposed damage detection method will be demonstrated here on a cylindrical model with single thickness transition used in section 5.3.3. For conciseness further studies on the proposed approach on more complex geometry examples will be given in chapter 6.

5.4.1 Method description

Wave propagation in a structure with geometry shown in figure 5.13 was simulated with 2-D cylindrical LISA. The modelled cylinder was 1 m long with an inner diameter of 100 mm. At the distance of 300 mm from the cylinder edge a transition from outer diameter 200 mm to 180 mm with a radius of 15 mm was modelled. To facilitate the formation of the ‘quasi-surface’ waves, the structure was excited at the edge of the inner surface. The outer diameter change region was selected for sensing. This excitation-sensing configuration allows for inspection of the cylinder section from the excitation edge to the transition region. At the later stage of the investigation, a crack was introduced to the model, at the outer surface, as a slot of 1 mm wide and of 5 mm deep at 150 mm (i.e. full circumferential crack). Figure 5.15 illustrates the three-dimensional setup equivalent to the discussed model.

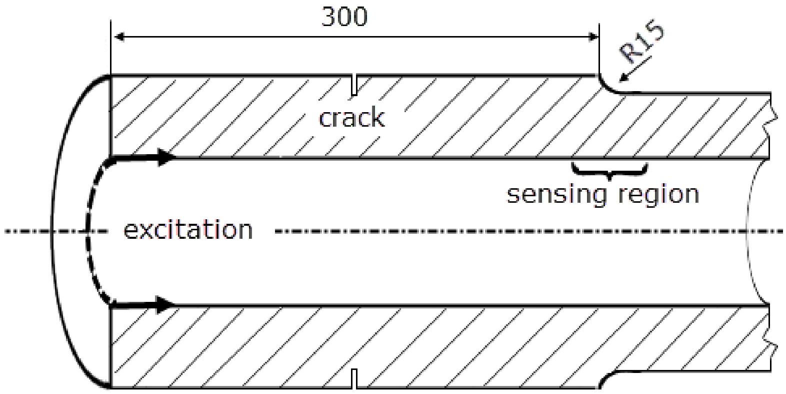

Figure 5.15: Sketch of the three-dimensional inspection setup of equivalent to the axisymetric 2D model of a hollow cylinder with an inner diameter of 100 mm and total a length of 1000 mm. Ring-type excitation on the inner surface is illustrated with two arrows and a dashed line. The exact dimensions of the cylinder are given in figure 5.13

For the undamaged structure, the wave scattering and wave enhancement occur only at the thickness transition region. Due to the wave interaction with the step, the energy is converted from the ’exterior quasi-surface’ wave to the higher order longitudinal modes. As a result of the interference of the waves, the near-field wave enhancement effect occurs at the transition region which can be detected at the inner surface of the cylinder as depicted in figure 5.16a.

On the other hand when an on-surface defect is present before the geometrical transition, the ‘exterior quasi-surface’ wave is first scattered from the defect, causing a decrease of the transmitted ’quasi-surface’ wave energy. Consequently, as shown in figure 5.16b, the magnitude of the wave enhancement effect at the transition is significantly reduced.

Figure 5.17 presents the same phenomenon by a comparison between the waveforms from the damaged and benchmark model at 315 mm from the excited edge. Here, the displacement signals obtained at the inner surface, at 315 mm from the edge are shown.

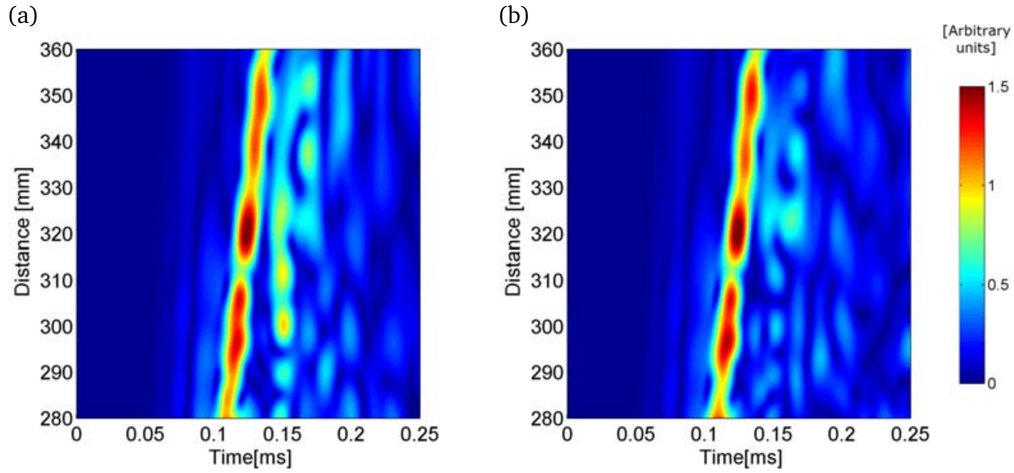

Figure 5.16: Near-field energy distribution (envelope of the axial displacement signals) at inner surface of a hollow cylinder at the geometrical transition at 300 mm. (a) Mode enhancement effect visible as brighter area around 300-330 mm; and (b) a lack of the enhancements due to a 5 mm deep crack at 150 mm (before the geometrical transition).

A significant drop in the wave amplitude corresponding to the enhancement effect can be seen at around 0.14 ms due to the crack presence.

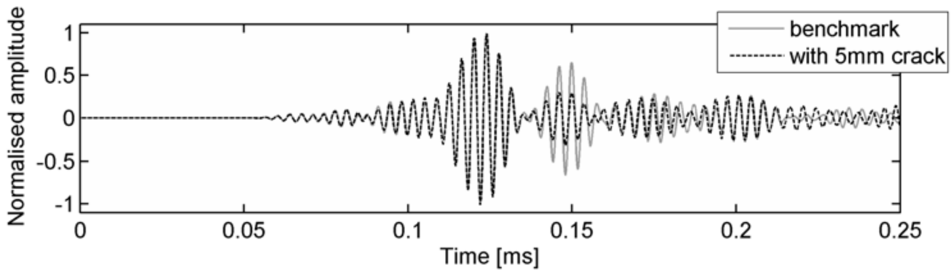

Figure 5.17: Reduction of the mode enhancement effect due to the 5 mm deep crack (a slot of 1 mm wide) located on outer surface at 150 mm from the edge of the cylinder. Axial displacements at the inner surface at 315 mm.

Finally, the influence of the crack severity on the enhancement effect is investigated in figure 5.18. Three locations at the inner surface were chosen for the analysis according to the energy distribution results (figure 5.16a), namely at 300 mm, 311 mm and 322 mm. The enhancement factor was calculated as a ratio of the enhanced wave package amplitude for the benchmark and 'damaged' case.

High sensitivity of the method for a crack with a depth of 3 mm and above is observed. In particular for the detection positions at 300 mm and 311 mm, 50% drop in the enhancement factor was produced.

The presented examples have demonstrated the proposed inspection method based on the

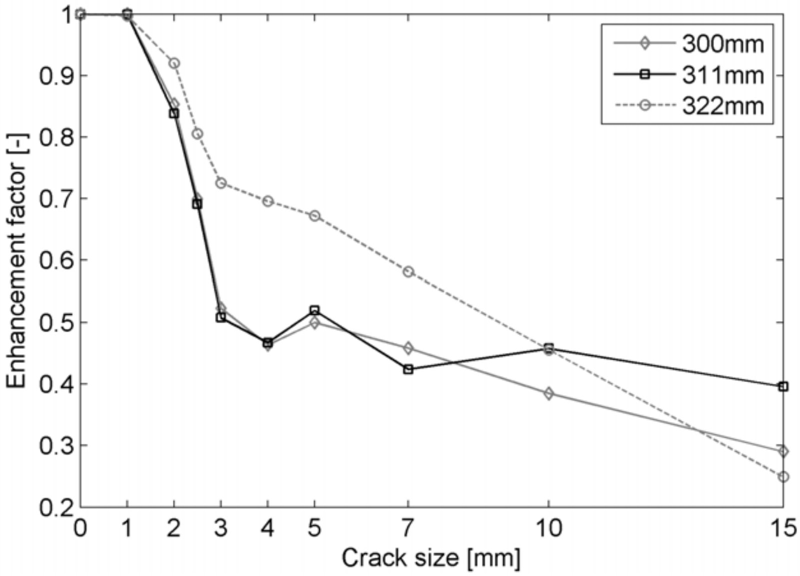

Figure 5.18: Decrease of the wave enhancement effect with the crack depth. Crack was modelled as a slot of 1 mm wide at the outer surface, 150 mm from the edge of the cylinder. The enhancement factor was calculated from the axial displacements at the inner surface at: 300 mm, 311 mm and 322 mm.

enhancement effect at the transition region of the structure. However, the limitation of the method is that to evaluate the exact location of the defect, additional analyses such as pulse-echo approach, need to be implemented. An example will be given later in this chapter.

5.4.2 Comments

The damage detection method proposed here utilizes the enhancement effect due to a geometrical transition as a 'marker' of the defect presence within a given section of a waveguide. The numerical results confirm the high sensitivity of the method to surface-breaking cracks. As shown, even a relatively small defect results in a significant change of the enhancement effect developed at the geometrical transition and this effect can be effectively used as a damage indication. Another advantage of the developed method is that both the excitation and sensing can be carried out from the inner surface of a hollow cylinder. This is highly important since it may allow for a development of a permanent monitoring system. The main drawback of the approach stems from the need of additional method for precise localization of the defect in the axial direction.

5.5 Experimental validation

The wave enhancement phenomenon discussed in this chapter was also investigated experimentally. For convenience in conducting the measurements instead of a full-scale hollow cylinder, aluminium beams with thickness variations were first investigated. The reason for this simplification was twofold. Firstly, the exciting transducer could be easily placed on the flat surface of the beam, and secondly the sensing region was more accessible. It was also assumed that uniform excitation across the beam width, may approximately correspond to the excitation of a hollow cylinder with a ring of transducers. The aforementioned simplifications have some significant shortcomings. Firstly, the additional boundaries of the beam's width, introduce wave reflections and formation of modes across the beam width. Also, it should be reminded that the formation of the 'quasi-surface' waves in a plate and a hollow cylinder is different i.e. for the former they result from the combination of the first two modes, while for the latter a single mode can form a 'quasi-surface' wave. However, since the aim of this experiment was to validate the enhancement phenomenon due to the transition region and its feasibility for damage detection, it is believed that the simplifications are acceptable.

In this section three experiments are discussed. The first experiment involves a beam with a single thickness change, the second is conducted on a beam with two geometrical transitions and finally the third experiment is carried out on a hollow cylinder with a single transition region.

5.5.1 Single step beam

An aluminium beam of a total length of 600 mm, a width of 19 mm and a thickness change from 50 mm to 40 mm at 300 mm with a radius of 15 mm, as shown schematically in figure 5.19 was used for the first experiment.

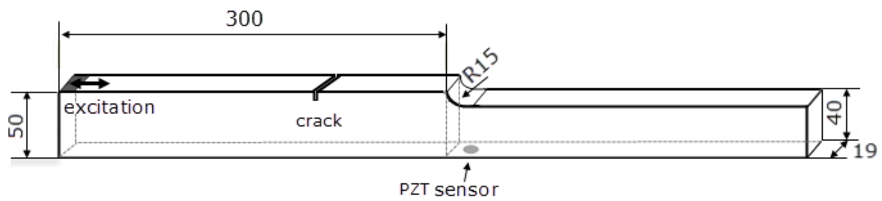

Figure 5.19: Sketch of the 'single step' beam used for the experiment.

Configuration design based on numerical simulations

Prior to the experimental investigation, a set of numerical stimulations was performed to select an appropriate actuation-sensing configuration considering the size of the transducers, their placement and the frequency of the excitation. A three-dimensional finite element model of the beam was analysed using FEM Abaqus software. The material properties for the model were assumed as $\rho = 2.7\ g/cm^3$, E=68.9 GPa, ν=0.33. The wave propagation was simulated with dynamic explicit algorithm, using mesh size of 1 mm and time step 0.05 μs.

In the previous sections the discussion considered only actuation and sensing at a single point; however, for the experiment piezoelectric transducers were mounted to the structure. The size of a transducer is an additional parameter in the system, which may introduce challenges to the signals' interpretation. Based on the simulations, the excitation region at the edge of the beam with 5 mm of length and uniform across the beam width was chosen to ensure efficient excitation of 'quasi-surface' wave. An eight cycles of Hanning windowed sine signal with central frequency of 265 kHz was used for the excitation. The numerical simulation results also pointed out that only the excitation at transition side of the beam is effective for this particular geometry of the structure, while the excitation at the opposite side of the beam cannot be used for the enhancement effect investigation. This may be due to the concentration of the 'surface' wave energy at the edges of the structure (the additional width dimension). Figure 5.20 shows the envelopes of the displacement signals along a line at the surface opposite to the step, in the middle of the beam width.

Both wave reflections, from the downward transition and from the crack, can be clearly seen in the results. The wave enhancement due to the thickness reduction is observed around 314 mm. Based on the obtained results, a sensor with diameter of 8 mm was mounted at 310 mm (-. lines mark the position of the sensor's edge).

5.5.1.1 Experimental setup

Consequently, the setup shown in figure 5.21 was developed. The 6061 aluminium beam (with dimensions as shown in figure 5.19) was excited by a 14x28 mm Macro Fiber Composite (MFC) transducer of Smart Material Corp., surface-bonded at the edge of the

(a)

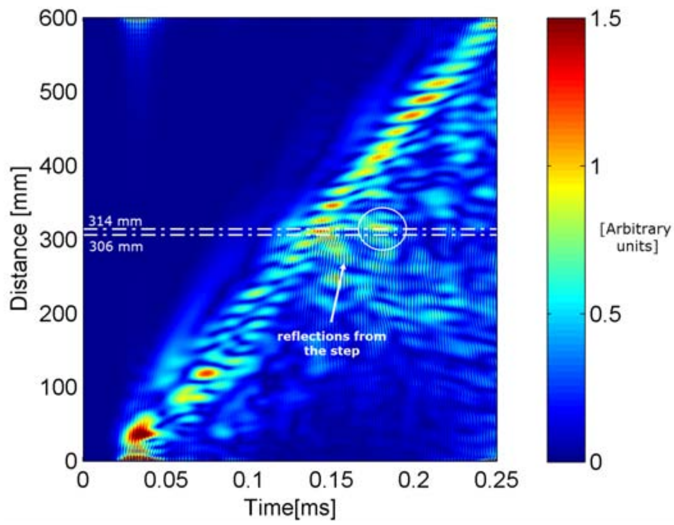

(b)

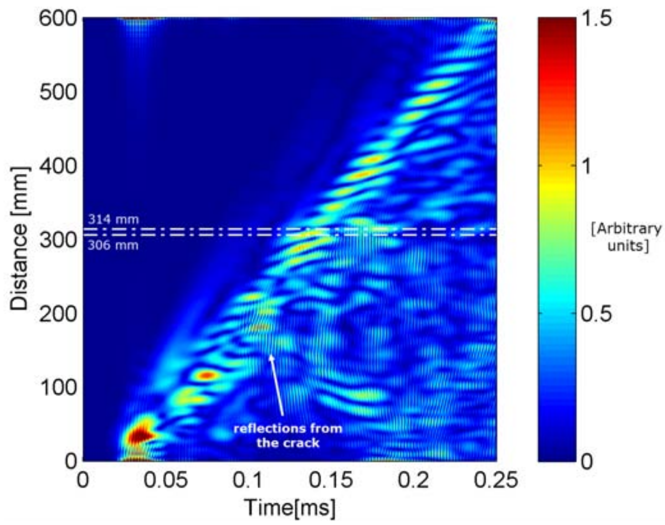

Figure 5.20: Energy distribution at the bottom surface of the beam (envelopes of in-plane displacement signals). -. lines shows the chosen sensor location. (a) Benchmark model, (b) model with a 5 mm deep damage (slot of width of 1 mm at 200 mm). Enhancement effect is marked with a circle.

beam. However, to ensure the propagation of the 'quasi-surface' wave, only 14x5 mm was used as an active region of the transducer. The use of the MFC transducer was motivated with the need for a powerful, robust and flexible excitation method for future application to a hollow cylinder inspection, thus a MFC was selected in this experiment. A PZT-disk transducer of a nominal diameter of 8 mm and thickness of 0.5 mm was glued to the surface at the opposite side of the step, at the distance of 310 mm from the excited edge.

The excitation signal was generated by NI PXI-5412 waveform generator, and then amplified by a US-TXP-3 linear power amplifier to 480 Vp-p before feeding the MFC actuator. The response signals were acquired by the PZT sensor through NI PXI-5105 signal digitizer at a sampling rate of 10 MHz.

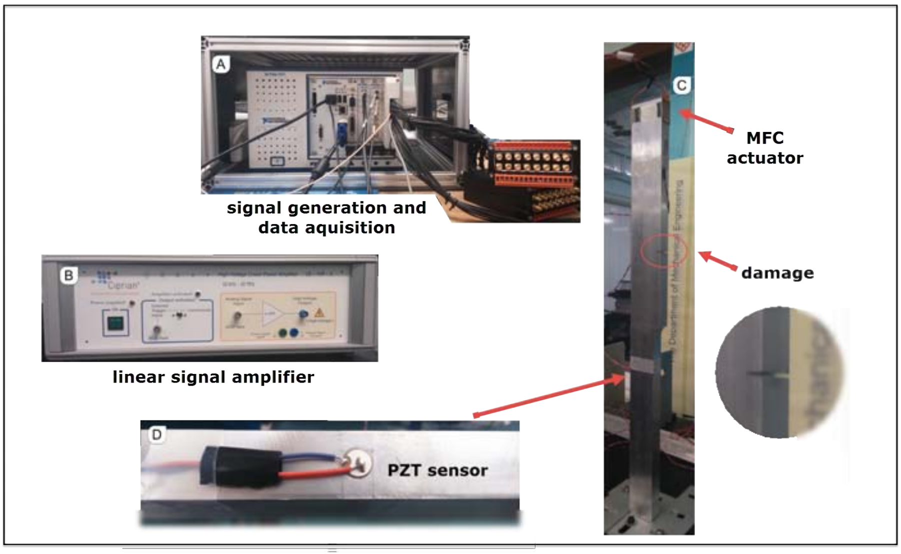

Figure 5.21: Experimental setup. (A) Signal generator and data acquisition unit, (B) linear signal amplifier, (C) Macro Fiber Composite (MFC) actuator, (D) PZT-sensor

To investigate the damaged scenario a saw-cut defect uniform across the entire beam width, with a depth of 5 mm and a width of 1.5 mm, was introduced in the later stage of the experiment. The damage was located at 200 mm from the excitation edge.

5.5.1.2 Results and conclusions

Figure 5.22 presents the comparison of the signals acquired from the intact and the damaged structure. Since the waveforms result from the propagation of multiple wave modes, it is difficult to identify a particular mode package. Nonetheless, significant changes in the signal amplitude can be noticed at 0.14 ms, 0.16 ms and for the wave package at 0.17-0.19 ms.

The experimentally observed behaviour is in good agreement with the simulation results presented earlier in figure 5.20. Although, the ‘quasi-surface’ wave scattering cannot be easily identified, the significant decrease in amplitude around 0.17-0.19 ms can be associated with the wave enhancement effect. The time-frequency representation of the measured waveforms obtained via Short Time Fourier transform is shown in figure 5.23.

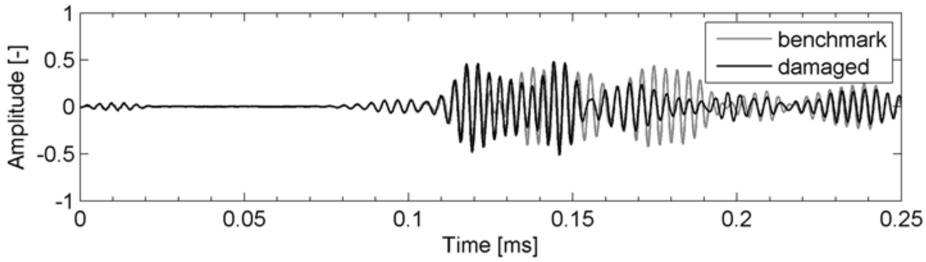

Figure 5.22: Comparison of the signals from the undamaged structure and the beam with saw-cut 5 mm deep damage.

Additionally, the results from the beam with crack depth enlarged to 7 mm are compared in the same figure.

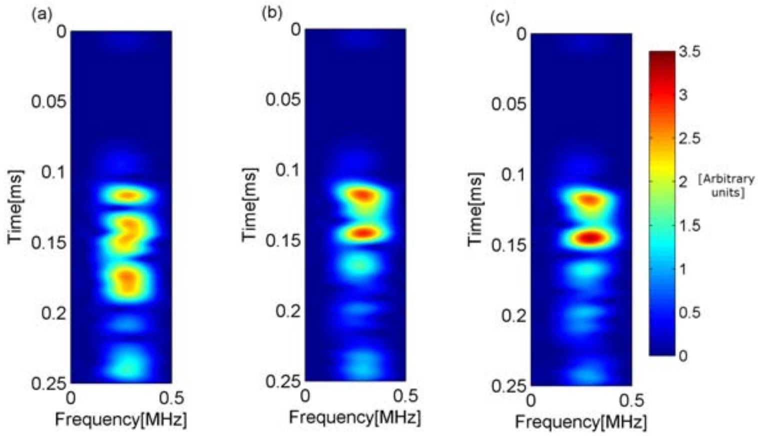

Figure 5.23: Spectrograms of the acquired signal for (a) an undamaged beam, and beam with introduced saw-cut crack of (b) 5 mm deep and (c) 7 mm deep.

The spectrograms of the signals indicate that the wave enhancement effect was significantly reduced by the crack presence, as expected.

Lastly, as an additional investigation the excitation was applied at the opposite side of the beam; once more an MFC actuator of active region 14x5 mm was used. The signals acquired from the PZT-sensor for the undamaged and damaged (5 mm deep crack) structures are compared in figure 5.24. It is noticed that the enhancement effect is not present in the signals, as the 'quasi-surface' wave was not developed at the surface with the crack . In this case, the damage signature is a drop of the amplitude visible around 0.13 ms.

5.5.2 Two-step beam

The second stage of the experimental investigation aimed at observation of the wave enhancement for a structure with two transition regions: at 100 mm and 300 mm. The

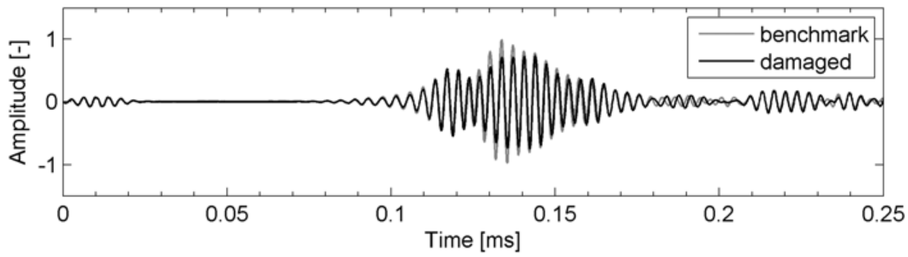

Figure 5.24: Comparison of the signals from the undamaged beam and with 5 mm deep crack for excitation placed on the side opposite to the damage location.

geometry of the beam used for the experiment is shown in figure 5.25. The experiment was designed with the excitation placed at the vicinity of the first transition and the detection of the enhancement effect at the region of the second transition.

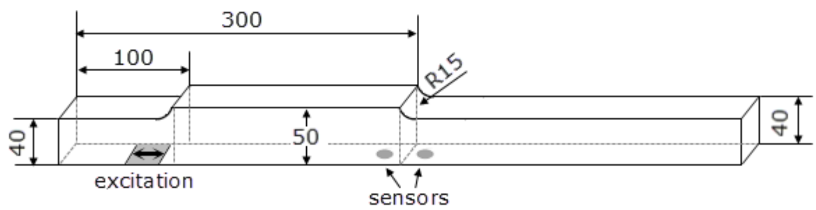

Figure 5.25: Sketch of the 'two-steps' beam used for the experiment.

5.5.2.1 Configuration design based on numerical simulations

As a reference, the numerical simulation results from ABAQUS/Explicit were used to design the effective actuation and sensing locations. The material and simulation parameters were the same as for the 'one-step' beam presented in section 5.5.1. The excitation was modelled as nodal in-plane displacements in the direction of the beam length, applied to all nodes at the distance between 75 and 85 mm (i.e. 10 mm long transducer) with amplitudes varying linearly from -1 to 1 along the length of the transducer and constant across the whole width of the beam/transducer.

Figure 5.26 compares the in-plane displacement signals obtained from: undamaged model, model with a 5 mm deep crack and model with only single transition at 100 mm. Two additional lines A and B are drawn for the convenience of visual comparison between the results. The A-line marks the high amplitude wave (with velocity of approximately 2.57 m/ms), while B-line corresponds to A-line shifted by the time the shear wave needs to reflect from the opposite surface and return to the excitation i.e. $2 \times$ thickness$/v_s$ ($v_s = 3.1m/m$).

In all three modelled scenarios strong reflections from the boundaries can be seen. This hampers the interpretation of the results and weakens the enhancement phenomenon. Nonetheless, the scattering from the geometrical transition at 300 mm and the crack at 200 mm can be still observed. Accordingly, the following two sensing locations were chosen: before the step at 289 mm and at the transition region at 310 mm (note that 310 mm is the same as in the previous experiment). The circular piezo-disc transducers of the same size as previously i.e. with 8 mm diameter, were used. In this measurement set, the structure was excited with 10 mm x 61 mm rectangular plate PZT transducer with applied voltage Vpp of 140 V. The other elements of the measurement system were the same as in the 'one-step' beam experiment.

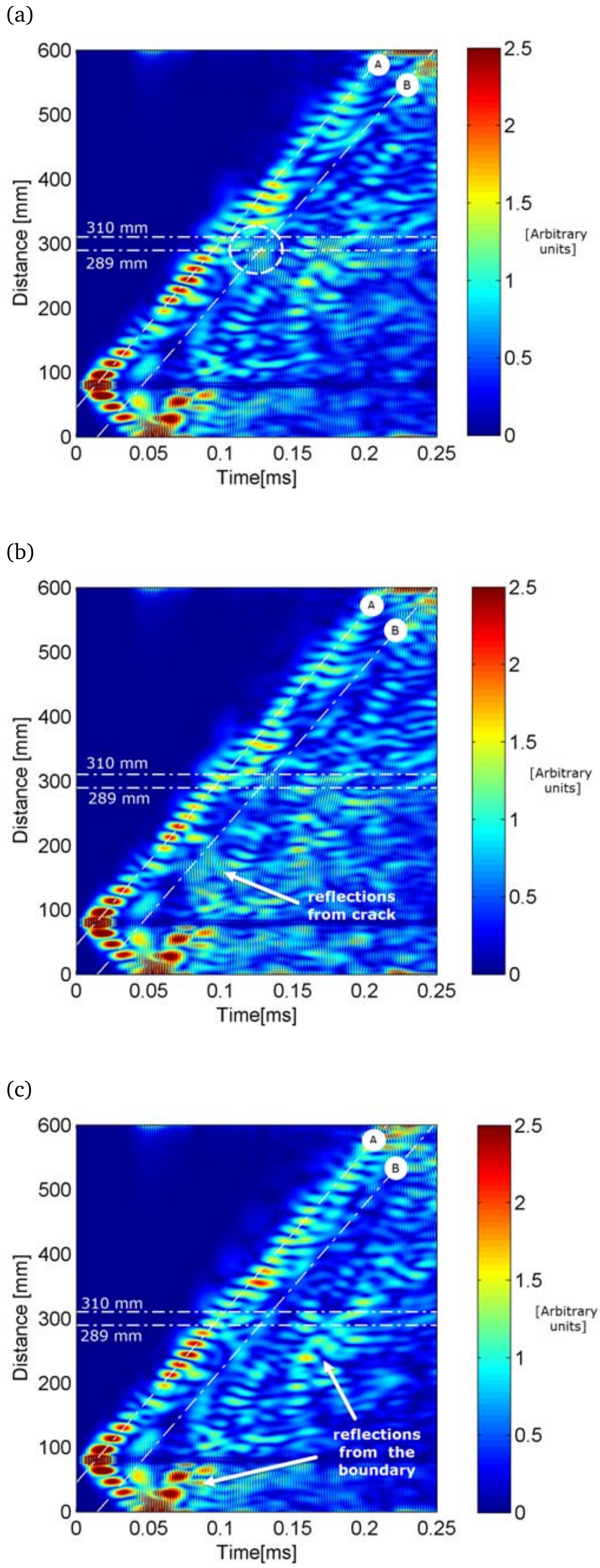

Figure 5.26: Energy distribution at the bottom surface of the beam (envelopes of in-plane displacement signals). (a) Benchmark , (b) with 5 mm damage at 200 mm, (c) with single transition at 100 mm. Enhancement region is marked with a circle. -. sensors' locations. Line A: a linear approximation following high amplitudes; line B: parallel to A shifted by $2\times$thickness/v_s.

5.5.2.2 Results

The waveforms acquired from the two PZT-sensors are shown in figures 5.27 (sensor at 289 mm) and 5.28 (sensor at 310 mm). Although, the signals have quite complex characteristics and it is impossible to distinguish between modes, in both plots the enhancement effect can be pinpointed –marked with circles. The influence of the crack presence on the signal is more visible for sensor located before the transition region; however, only slight variations with crack depths were observed.

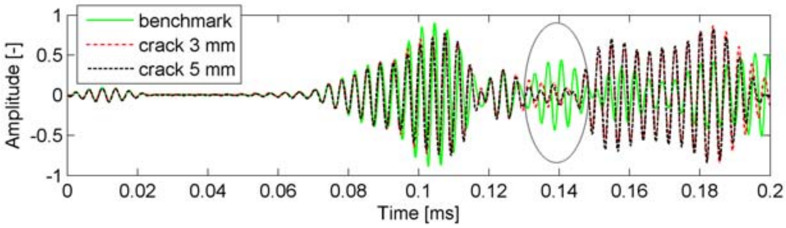

Figure 5.27: Time signal acquired from the PZT-sensor at 289 mm. The enhancement effect is marked with a circle.

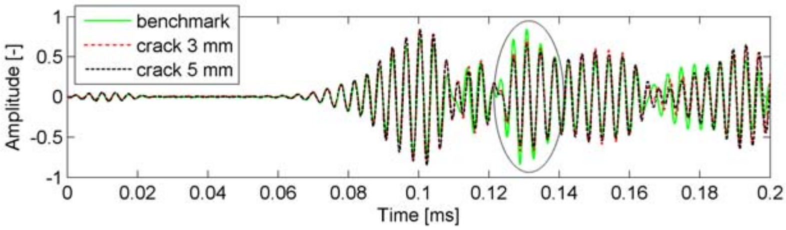

Figure 5.28: Time signals acquired from the PZT-sensor at 310 mm. The enhancement effect is marked with a circle.

According to the results from FEM simulations, the reflections from boundaries should be present in the signals after 0.15 ms. Thus, comparing the waveforms from both sensors, one can see that except the enhancement effect it is difficult to correlate the change of the signal before 0.15 ms with the damage occurrence. Surprisingly, for the sensor located at 289 mm some strong reflections from the crack can be seen after this time. The corresponding time-frequency representations of the signals from the beam with 3 mm,5 mm and 8 mm deep crack compared with the benchmark results are presented in figures 5.29 (sensor at 289 mm) and 5.30 (sensor at 310 mm). Although, the differences in the enhancement effect are observed, it is impossible to correlate the severity of the defect with the enhancements' magnitude.

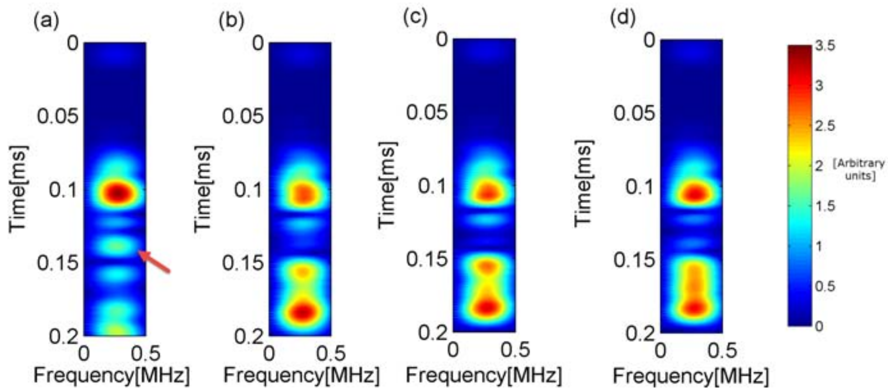

Figure 5.29: Comparison of spectrograms of signals from the PZT-sensor at 289 mm. Results from (a)undamaged beam and beam with crack of (b)with 3 mm, (c)5 mm, (d)8 mm depth. An arrow indicates the enhancement effect for undamaged structure.

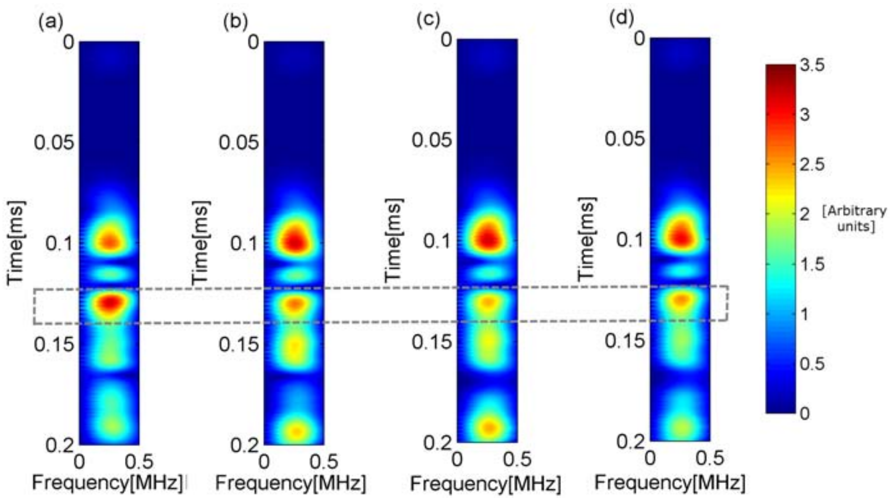

Figure 5.30: Comparison of spectrograms of signal form the PZT-sensor at 310 mm. Results from (a)undamaged beam and beam with crack of (b)with 3 mm, (c)5 mm, (d)8 mm depth. The enhancement effect is marked with a frame.

5.5.3 Hollow cylinder with a single transition

Lastly, the enhancement effect was investigated using a cylindrical hollow structure. An aluminium hollow cylinder of a total length of 500 mm, an inner diameter of 100 mm and a single transition with a radius of 15 mm from an outer diameter of 200 mm to 180 mm at 300 mm (see figure 5.31a) was used. For excitation, six Macro Fiber Composite transducers were bonded at the inner surface of the cylinder at its edge. Due to the limitations of commercially available MFC dimensions, the MFC transducers were cut into active dimensions of 5 mm$\times$14 mm. The response signals to a single MFC excitation were acquired from a circular piezo-disc transducer (with a diameter of 8 mm) mounted at the bore of the cylinder at the distance of 316 mm from the corresponding actuator. In total

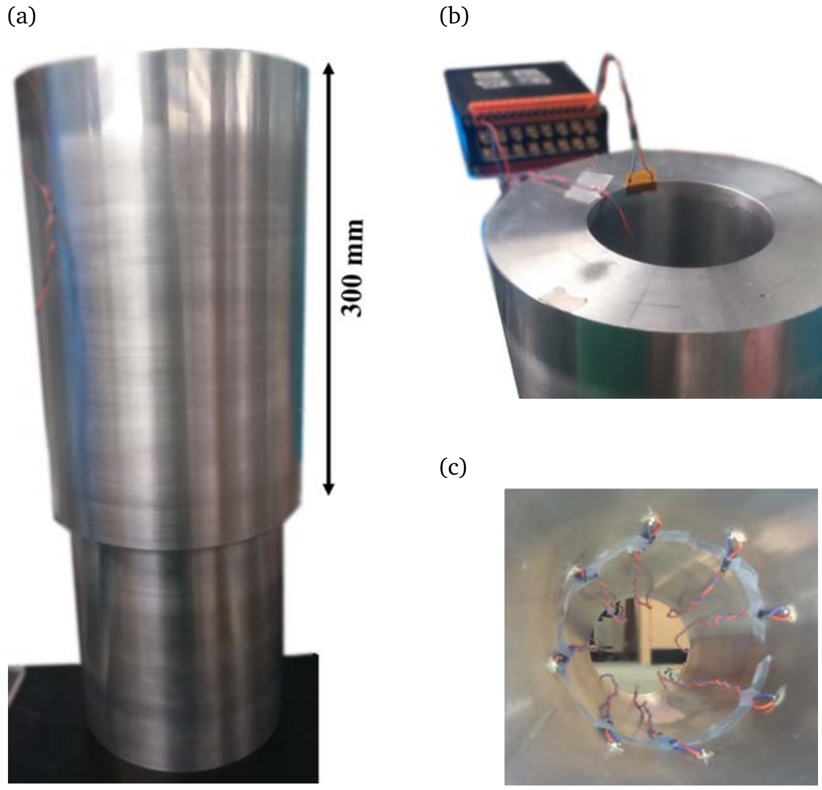

Figure 5.31: Experimental setup: (a) aluminium hollow cylinder with an inner diameter of 100 mm, a length of 500 mm and an outer diameter change from 200 mm to 180 mm (b) single MFC-actuator placement at the edge of inner surface (c) final configuration of eight PZT-sensors inside the cylinder.

six actuator-sensor pairs were tested (for details in configuration refer to section 6.4.4 in chapter 6). The path with the strongest enhancement effect was chosen for later analysis and damage location. An eight cycle Hanning windowed sine signal excitation with a central frequency of 365 kHz was used. This frequency was selected to maximise the signal-to-noise ratio. In the latter stage of the experiment a saw-cut circular damage (figure 5.32) was introduced using a DREMEL rotary tool with a cut-off wheel of 15/16”. The signals from the two damaged cases were collected, namely from a 16 mm long cut with a depth of 3.5 mm and from a 17 mm long defect with a depth of 4.5 mm. In both cases the width of the damage was approximately 1 mm.

Due to the difficulties in precisely locating and perfectly bonding the transducers inside the cylinder, the acquired signals differ between the excitation-sensing pairs as discussed in Appendix D. Figure 5.33 presents the results from the selected actuator-sensor pair with the strongest enhancement effect observed. A strong wave package after the ‘internal quasi-surface’ wave can be seen at around 0.15 ms. Based on the benchmark results, the

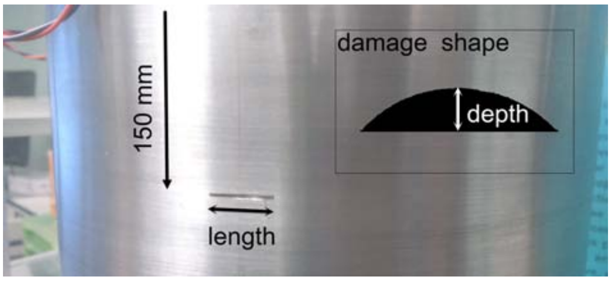

Figure 5.32: Damage location and geometry.

damage was introduced at the outer surface of the structure at 150 mm from the top face of the cylinder, on this selected actuator-sensor pair path. The envelope of the 'healthy' and 'damaged' signals and their spectrograms are also compared in figure 5.33.

It is observed that the presence of the damage caused a drop in the enhancement effect amplitude; however, this change is less significant than the one observed for the 2D structure. This could be attributed to the shape of the damage and the type of excitation used (i.e. with a single MFC transducer instead of a uniform ring-type excitation). On the other hand, hardly any changes in the signal are present before the enhancement effect. Another interesting feature is revealed when the differences between envelopes of the benchmark and damaged signals are investigated, namely symmetry about the 0.16 ms point of the two strong peaks. Further studies are needed to fully understand why this shape is observed, however it seems to be related with the reflection of the 'quasi-surface' wave as a part of the enhancement phenomenon.

5.5.4 Summary and comments

The first stage of experimental investigations on the wave enhancement effect was carried out on two thick beam structures. The major challenges during those experiments were associated with the selection of the effective actuation and sensing locations; in this regard finite element simulations were first used to validate the setup configuration. The second stage of the experimental validation of the proposed damage detection method was conducted on a hollow cylinder with a single outer diameter-transition. A number of technical limitations have been encountered at this stage including: (i) computational restrictions in simulation of a large three-dimensional cylindrical structure, (ii) a lack of the flexible ring-type transducers on the market with the desired size (the excitation using

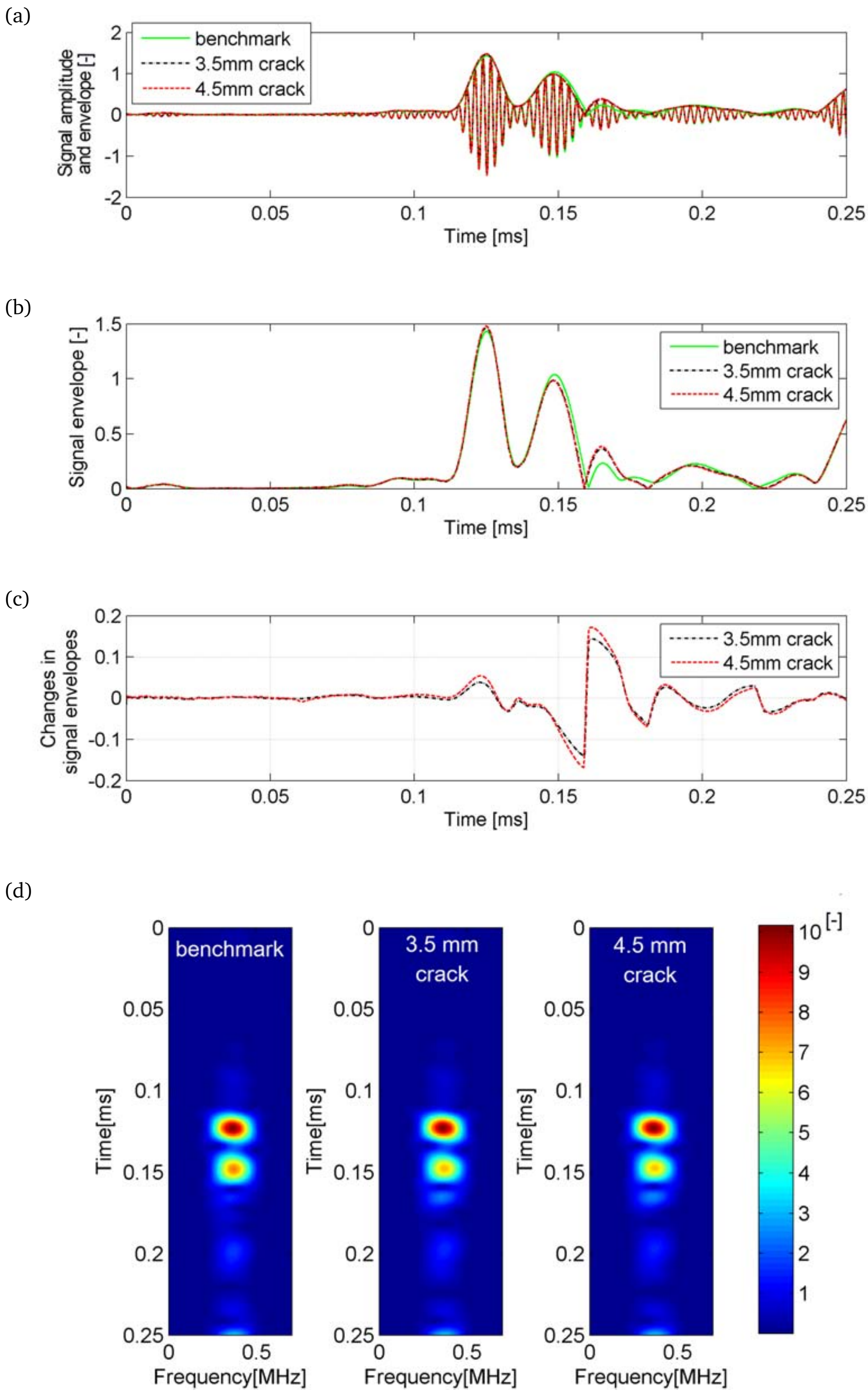

Figure 5.33: Experimental results of the enhancement phenomenon in an aluminium hollow cylinder with a single outer diameter change. Comparison of the signals from the pristine and damaged stages: (a) waveforms with envelopes marked, (b) signal envelopes, (c) changes in signal envelopes due to the damage, (d) spectrograms.

rectangular MFC actuators was performed instead), (ii) difficulties in bonding of the circular PZT transducers at the precise locations inside the cylinder.

The primary findings from this part of the work can be summarised as follows. The experimental results confirm the presence of the wave enhancement phenomenon due to a thickness reduction in thick-walled waveguides. It has been demonstrated that an on-surface damage within an examined section of the structure decreases the magnitude of the enhancement effect at the transition region. However, the qualitative studies yield little information about the correlation of the defect severity with the amplitude of the wave enhancement. This could be related to the aforementioned technical difficulties and to simplified beam geometries. In case of the hollow cylinder investigation another effect to be considered is the influence of shape of the damage on wave scattering, in particular the circumferential length of a defect. Moreover, the accuracy of the manufacturing of the specimens (especially of the transition region) may also influence the results, since the selected locations of the sensors were based purely on the preliminary numerical simulations. Therefore, further investigations preferably using contactless scanning of the surface are desirable.

5.6 Conclusions

In this chapter the near-field wave enhancement phenomenon has been studied through numerical and experimental investigations. There are several unique aspects of the presented discussion which have not been considered in the existing literature. Firstly, cylindrical guided waves were considered here, in particular the axisymmetric longitudinal modes. Secondly, thick-walled waveguides or more specifically with high thickness-to-wavelength ratios were analysed. Furthermore, an existence of the enhancement phenomenon at the geometrical transitions was postulated. Finally, a novel damage detection approach based on the enhancement effect was proposed. The major observations from this chapter are summarised in the following paragraphs.

The numerical results reveal the existence of the ‘quasi-surface’ wave and its interaction with on surface crack, subsequently resulting in local wave enhancement. This phenomenon is associated with through thickness propagation of strong partial shear waves. The correlation between the enhancement effect magnitude and a crack depth has been also observed for a two-dimensional model. The presented numerical analyses confirm the existence of the enhancement phenomenon due to a thickness change in the waveguide. It was noticed that the influence of multiple modes in a waveguide with a significant thickness-to-wavelength ratio can mask the enhancement effect, thus high amplitude modes were studied. The results show that the 'exterior quasi-surface' mode interaction with a downward step contribute to a strong enhancement phenomenon at the internal surface of the hollow cylinder. The enhancement effect has been found to depend on the shape of the transition (slope, curvature, depth) and the characteristics of the propagating modes.

Based on aforementioned findings a new damage detection method was proposed and examined. The method utilizes the wave enhancement effect due to a geometrical transition in a structure and sensitivity of the 'quasi-surface' modes to surface-breaking cracks.

The experimental results confirm the presence of the wave enhancement phenomenon at the thickness reduction region. Also, it has been demonstrated that an on-surface defect causes a decrease of the enhancement effect at the transition region, however, the correlation of the crack depth with the enhancement effect was not seen in the experimental investigation. This is probably due to the multiple reflections from the boundaries in case of the beam structures and complex wave scattering pattern for the hollow cylinder case (single MFC transducer and localised damage).

The major advantage of the proposed damage detection solution is that both the excitation and the sensing can be carried out from the inner surface of a hollow cylinder allowing for the detection of outer surface cracks. This is of a great importance considering in-service axle monitoring system applications, as it provides an effective inspection of inaccessible regions. Based on this approach a faulty section of an axle can be easily identified. The main limitation of the developed method, however, is the need of an additional analysis for precise localization of the defect within the section of the structure such as pulse-echo time of flight approach. In the following chapter a complete scheme of hollow axle inspection is discussed including multiple excitation-sensing locations and complementary damage detection and localization techniques.

Chapter 6

Railway axle inspection

6.1 Introduction

This chapter aims at discussing a complete methodology for railway axle inspection based on the guided wave approach. First, few general comments on Structural Health Monitoring of train axles are given. Then, an overview of a possible inspection methodology is presented, followed by detailed analysis of the selected guided wave-based methods. Finally, the inspection scheme is verified experimentally and conclusions from this part of the research are drawn.

6.2 Miscellaneous aspects of SHM of railway axles

In the Introduction chapter basic concepts of Structural Health Monitoring have been introduced. At this stage of the research we may proceed to the discussion on possible application of cylindrical guided waves to SHM of hollow railway axles, by utilizing the acquired understanding of the observed and investigated phenomena. To begin with, four main levels of the Structural Health Monitoring system for an axle can be distinguished following [112]: (I) damage detection, (II) damage localization (in angular and axial direction), (III) damage assessment, (IV) life prediction. Among them, the 'life prediction' level belongs mainly to the field of fatigue analysis and fracture mechanics, thus falls beyond the scope of this thesis. Nonetheless, from the monitoring view point it is worth mentioning that, a typical surface crack develops in an axle having a circumferential semi-elliptical shape till it reaches the critical size –associated with the fracture of a hollow axle– of wall breakthrough [125].

Transducer selection

One of the distinct features of SHM systems is the on-line structural inspection carried out – in passive or active manner – through network of permanently mounted transducers. Among other types, the piezoelectric elements are the most commonly used as both actuators and sensors for guided wave-based approaches. Various types of piezoelectric transducers are available, with a wide range of different shapes and sizes (see figure 6.1). Due to the low costs and compactness, the piezoelectric wafers made of lead zirconate titanate ceramics (PZT) are the most common surface-bonded transducers. In contrast to PZTs, which are very brittle in nature, the polymer film transducers manufactured from the polyvinylidene fluoride (PVDF) material exhibit better flexibility. PVDF can be easily attached to curved surfaces e.g. pipes [46]. However, when compared to PZTs the PVDF actuators exhibit much weaker performance in terms of energy generation, and therefore their application for excitation of thick-walled structures is ineffective. Another solution

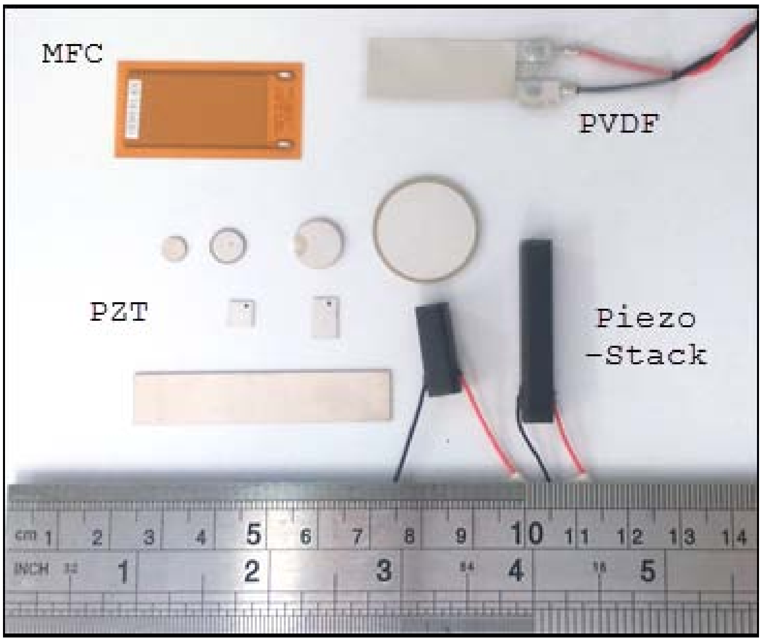

Figure 6.1: Piezoelectric transducers of various shapes and sizes

which allows for an effective bonding to a curved surface is Macro Fiber Composite (MFC) transducer designed by Wilkie *et al.* [122]. A MFC consists of rectangular piezoceramic rods embedded between two layers of epoxy and interdigitated electrodes on polyamid films. This design allows for flexibility and durability as well as provide higher actuation power than monolithic PZT wafers. These features make MFCs highly attractive for the present application. (Both PZTs and MFC transducers were used in the experiments presented in this thesis.)

Structural integrity evaluation

Another point of consideration is an optimal number of transducers and their location within the inspected structure. For guided wave-based applications, *pulse-echo* and *pitch-catch* configurations of actuator-sensor pairs are usually used. In the former, the wave reflection from a defect is detected by a sensor collocated with the actuator. Then, given the wave speed of the guided mode used for the inspection, the distance to the crack is evaluated directly from the *time-of-flight* (TOF) of the reflected wave package. In the pitch-catch approach a signal sent directly to the sensor located across the inspected region is examined. In this configuration various damage related features (e.g. changes in amplitudes of particular modes or phase shift between signals) are extracted from the acquired signal to asses the current condition of the structure. In contrast to the pulse-echo approach, precise localization of a crack is impossible using only pitch-catch method.

In both of the aforementioned techniques the qualitative information about the defect is extracted using numerous signal processing methods. However, due to the complexity of the waves in a thick-walled components with multiple geometric discontinuities, the applicability of approaches commonly used for plate-like structures and thin-walled pipes is difficult for the case of a hollow axle inspection. Therefore alternative damage detection methods need to be established.

6.3 General concept of inspection methodology

Up to this point in the thesis, the guided wave theory has been investigated for a simple hollow cylindrical structure. The railway axle geometry however, comprises multiple outer diameter transition regions as illustrated in figure 6.2. This complexity of the structure becomes a challenge for the ultrasonic NDT inspection techniques due to the wave scattering from the structural edges. On the other hand, since guided wave-based SHM is based on permanently mounted network of transducers, the influence of the transition regions on wave propagation may be reduced or integrated into the inspection strategy. Here, a multiple section-based approach for a hollow railway axle monitoring, with excitation and sensing carried out from the bore of the axle, is proposed and examined. The inspection assumes a separate examination of consecutive axle sections I-V, to utilize the damage detection technique based on the wave enhancement effect and to allow for more effective excitation of the inspected regions.

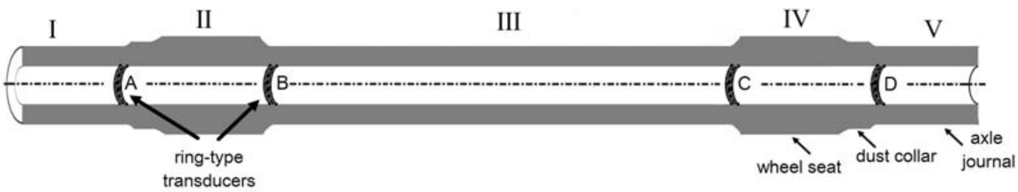

Figure 6.2: Simplified model of a railway axle (tapered ends with threaded holes are not considered). Proposed excitation/sensing locations are marked as A, B, C, D.

It is important, particularly for thick-walled structures, to limit the number of propagating modes through selection of an appropriate excitation type, e.g. ring-shape transducers allow for excitation of only axisymmetric longitudinal modes. In the proposed approach, an array of flexible transducers in ring configuration should be bonded to the inner surface of the axle for effective excitation of a limited number of flexural modes, and furthermore to allow for localisation of a damage in angular direction (to be discussed later in the chapter). Each section of the axle is examined separately using a single ring-type excitation. Considering the given axle geometry, four excitation/sensing locations, marked in the figure 6.2 with capital letters from A to D, were selected to inspect the five consecutive sections of the structure. To further improve damage localisation and assessment, additional sensor sets can be placed at both ends of the axle and at the two wheel seat-dust collar transition regions. The inspection methodology can be summarised as follows.

Level I: DAMAGE DETECTION

During railway axle maintenance, particular attention is required for inspection of the surface underneath the wheel seats, and the transition regions (i.e. sections II and IV in figure 6.2). However, scattering of the propagating wave from the edges may cause masking of the damage related feature in a guided wave signal. Hence, for these regions the damage detection needs to be based on the near field wave enhancement phenomenon discussed in section 5.4 of the previous chapter. This approach allows for a scrutinized inspection of the outer surface of the axle by utilizing the 'quasi-surface' wave propagation and wave scattering at surface discontinuities. The premise of the damage detection is that, using the pulse-echo configuration of the actuator-sensor pairs A-B and D-C, a change in the enhancement effect at the outer diameter transition regions is used as an indirect indication of a damage presence. Note that the proposed solution relies upon a baseline; thus, it requires a comparison of the acquired signal with the reference response of the 'healthy' structure.

The inspection procedure is as follows. First, the cross-correlation with the corresponding benchmark signal is evaluated for each transducer's response separately. Then, the signals with the lowest correlation coefficients are further analysed. In this regard, the changes in the wave enhancement effect are investigated directly by comparing the magnitude of the wave enhancement, and through subsequent signal assessment methods including envelope analysis (Hilbert Transform) and time-frequency spectrogram representation. Finally, the damage can be identified (also in an automatic mode) by setting thresholds for the conducted analyses .

The first level of the proposed inspection scheme provides information about a damage occurrence at a particular section of the axle. Moreover, it reveals the approximated angular localisation of the damage, assuming that the signal with the greatest changes corresponds to the defect circumferential position. The following levels of the inspection procedure aim at precise axial localization of the defect within the given section, and qualitative assessment of the damage.

Level II & III: DAMAGE LOCALISATION AND ASSESSMENT

With the known section of the axle at which the crack occurred, the axial position of the crack can be evaluated from the time-of-flight analysis using the pulse-echo technique. Accordingly, a single ring transducer array needs to be used for both actuation and sensing, and the wave reflection from the crack is utilized for distance evaluation. Finally, with both angular and axial position of the crack determined, the signal change magnitude is analysed using methods such as signal envelope and cross-correlation, to determine the severity of the damage. However, a reference dataset with various detect sizes and locations or an imaging technique is needed in practice to estimate the precise defect size (this will not be addressed here).

On the other hand, due to a relatively simple geometry of the sections I and V of the axle, it is expected that the pulse-echo approach using the transducers at location A or D respectively, can be used for damage identification within these regions. Similarly, the inspection of the section III of the axle can be performed with the pulse-echo and/or the pitch-catch approach using the transducer sets B and C.

In the following, the aforementioned methods of damage detection, localisation and assessment will be presented and investigated in detail using numerical and experimental analyses. However, since the crucial part of the inspection procedure is the investigation of the locations which are prone to fatigue crack initiation, such as the wheel seat regions and the geometrical transitions [128], a special consideration is given in this chapter to the inspection of these regions.

6.4 Damage identification and assessment methods

This section provides thorough analysis of the methods listed in the previous section as a basis of the proposed SHM for hollow axles. First, the enhancement effect-based damage detection approach for scrutinizing the outer surface of an axle section is presented, followed by an example of using the pulse-echo technique for axial localisation of the damage. Then, the cross-correlation analysis is introduced and examined both numerically and experimentally. Finally, an experimental investigation of the proposed inspection scheme is demonstrated on a hollow cylinder sample with a single outer diameter transition region.

6.4.1 Damage detection utilizing wave enhancement phenomenon

As mentioned, there are locations in train axles where fatigue crack initiation is likely to occur, such as press-fit underneath the wheel/gear/disc brake seats and the geometrical transition (T transition) next to the wheel seat [128]. These regions are of interest in this analysis, using the damage detection method based on the wave enhancement phenomenon discussed in chapter 5.

To analyse the feasibility of the near-field enhancement effect for inspection of a section of a hollow axle, numerical simulations on a simplified two-dimensional axle model were carried out. An axisymmetric cylindrical LISA model with a geometry presented in figure 6.3 was investigated. The modelled structure was 2 m long with the inner radius of 50 mm and the wall thickness of 50 mm and 40 mm. The model was meshed using 0.5 mm square elements and to ensure the stability of the simulation the time step was set to 0.05 μs .

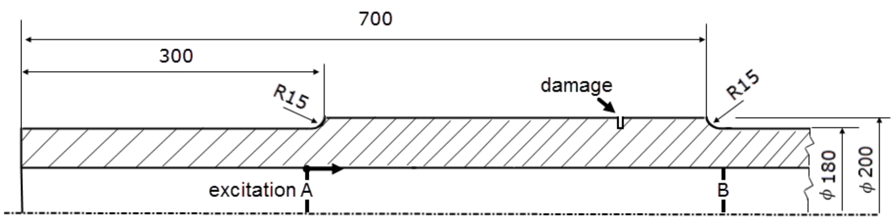

Figure 6.3: Geometry of the axle model used for the analysis (length of 2 m, inner diameter of 100 mm, the second symmetric part is not shown). Excitation/sensing locations at the inner surface are marked as A, B (details are given in the text).

The inspection technique utilises the 'exterior quasi-surface' wave propagation and the wave enhancement effect at the geometrical transition. The basis of the method is as follows. The excitation location is chosen to facilitate the propagation of the 'exterior quasi-surface' wave within the inspected region with sufficient energy e.g. upward thickness change of the waveguide. The sensing position is selected at the downward transition region across the examined region. In the case of the undamaged structure, the wave enhancement effect is observed at the transition region due to the scattering of the 'exterior quasi-surface' wave. For damaged case the energy of the 'quasi-surface' wave and consequently of the enhancement effect is reduced due to the prior crack-wave interaction.

To apply this damage detection method for the axle section, first the location of the excitation point needs to be decided on. Following the discussion in section 5.2.1, for an effective excitation of the ‘exterior quasi-surface’ wave from the inner surface of the axle, the excitation should be placed at the close distance to the structure edge or the outer diameter transition. The additional conducted numerical simulations (not shown here) confirmed, that an excitation at the edge of the model is ineffective for the inspection of the wheel press-fit regions, since the ‘exterior quasi-surface’ wave is scattered at the transition region A or D. Therefore, the outer diameter change regions, marked in figure 6.3 as A and B, were identified as potential excitation points. For numerical simulations the excitation points were chosen as A: 285 mm, B: 715 mm, C: 1285 mm and D: 1715 mm, (i.e. 15 mm before the geometrical transition) to allow for inspection of the transition regions. For each of the potential excitation locations, the corresponding sensor position at the opposite side of the wheel seat was assigned. In this manner the excitation-sensing pairs A-B and D-C were formed. An eight cycles of sine signal with the central frequency of 265 kHz modulated with Hanning window was used as the excitation. Two damage scenarios are studied here: a crack underneath the wheel seat and at the transition region.

Case study 1 - crack underneath the wheel seat

As a first damage scenario a crack at the outer surface of the axle at the wheel press-fit region is investigated. A rectangular based slot with a depth of 5 mm and a width of 1 mm, was modelled at 600 mm from the end of the axle.

The energy distributions (more precisely signal envelopes) of the benchmark and the damaged models, obtained at the inner surface of the cylinder at the transition region B, are compared in figure 6.4. The high energy mode (brighter lines across the figures) corresponds to the ‘interior quasi-surface’ wave. The wave enhancement can be observed at around 0.18 ms, at the distance from 695 mm to 735 mm. Note that as discussed in chapter 5 the exact region of the enhancement depends on the geometry of the waveguide and selected excitation frequency.

The axial displacement signals from a single location at the inner surface, for the

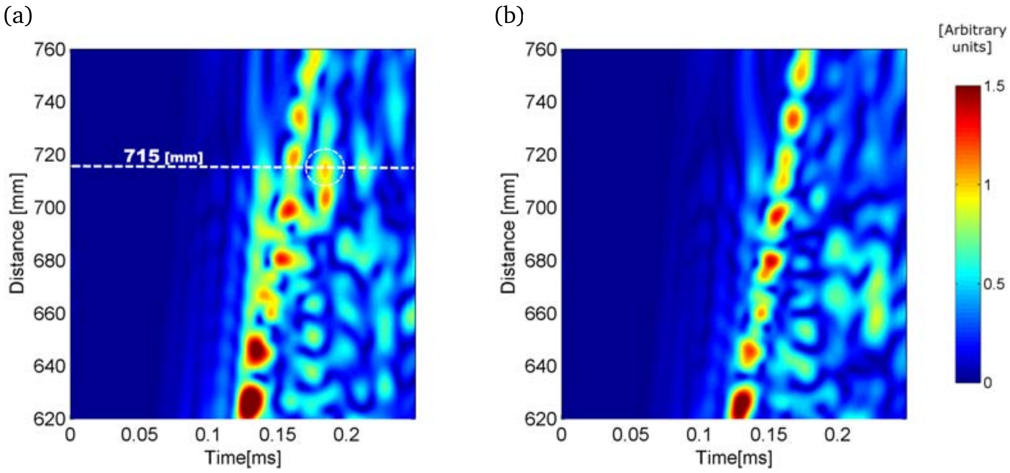

Figure 6.4: Wave enhancement effect at the inner surface. Energy distribution (signal envelopes). Excitation at the inner surface at location A (285 mm). (a) Benchmark model, and (b) model with 5 mm deep crack at the press-fit region – at 600 mm.

undamaged model and model with 5 mm deep crack, are compared in figure 6.5. In addition, the sensitivity of the method is studied in figure 6.6. To facilitate the visual comparison, the results are presented using time-frequency representation (spectrograms) of the signals.

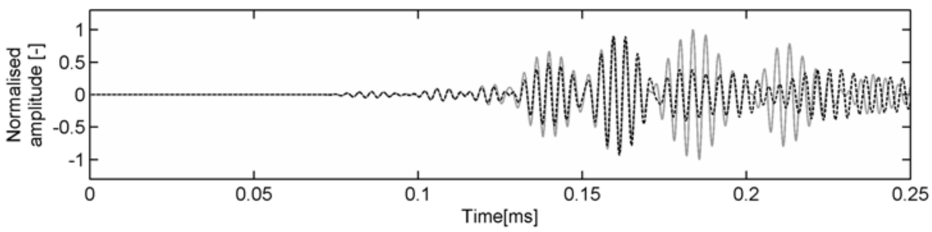

Figure 6.5: Comparison of axial displacements at 715 mm at inner surface of benchmark signal (–) and model with crack at 600 mm of 5 mm depth (- -). Wave enhancement is visible at around 0.18 ms.

The wave enhancement effect due to the ‘exterior quasi-surface’ wave scattering can be clearly seen at around 0.18 ms for the undamaged signal. It is noted that the magnitude of this phenomenon is significantly reduced, if a crack occurs at the outer surface within the press-fit region. This change in the wave enhancement effect can be therefore used as a signature of a crack presence. Second distinctive feature in the ‘damaged’ signals is the decrease of the amplitude of the wave package propagating before the L(0,2) mode i.e. at around 0.14 ms. This is not observed for a crack at the transition region, as will be discussed in following.

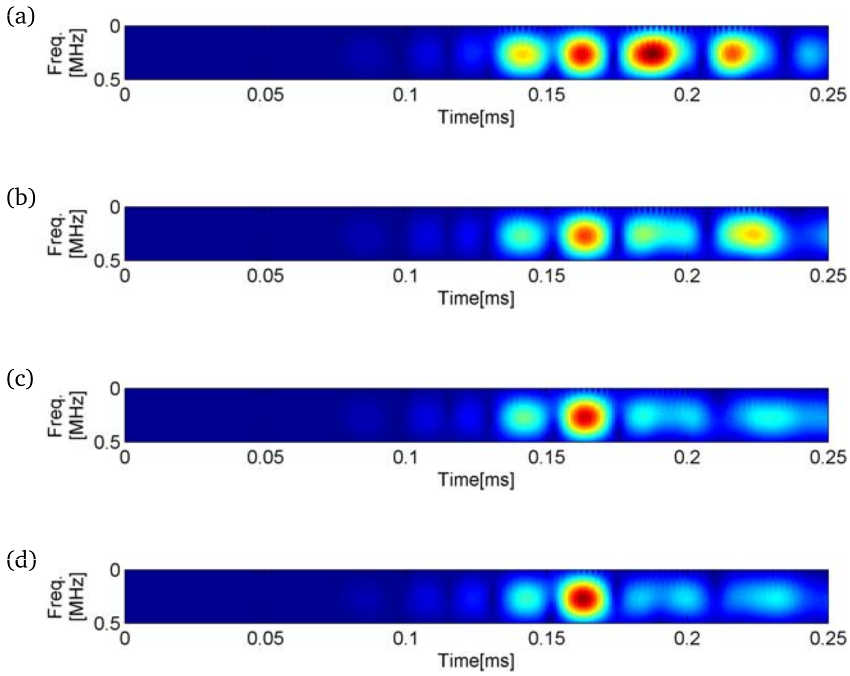

Figure 6.6: Spectrograms of axial displacements at inner surface 715 mm from the excitation point A (285 mm); (a) benchmark signal and with crack at 600 mm with: (b) 3 mm depth (c) 5 mm depth (d) 10 mm depth. Enhancement effect can be observed at around 0.18 ms.

Case study 2 - crack at transition region

The second damage scenario analysed here is a defect at the geometrical transition B of the axle (next to the wheel seat). This region is a common fatigue cracks initiation location due to the stress concentration at the transition. Furthermore, according to [128] the growth rate of a defect at the transition region in an axle is even higher than of the crack underneath the wheel seat; thus, scrutinized inspection of this region is highly important.

The sketch of the simulated setup is shown in figure 6.7. An excitation at the position A (285 mm) and sensing at B (715 mm) were assumed .

The influence of a 5 mm deep crack located at the geometrical transition B (707 mm from the end of the model) on the enhancement effect is illustrated in figure 6.8. One can notice a significant drop in the magnitude of the effect for the damaged case. In particular, at the sensing position B (715 mm) the wave magnitude at around 0.18 ms is reduced by half (compare the circled area in the figure). This change is also clear in the time signals as shown in figure 6.9. Interestingly, in contrast to the crack at the wheel press-fit region, the

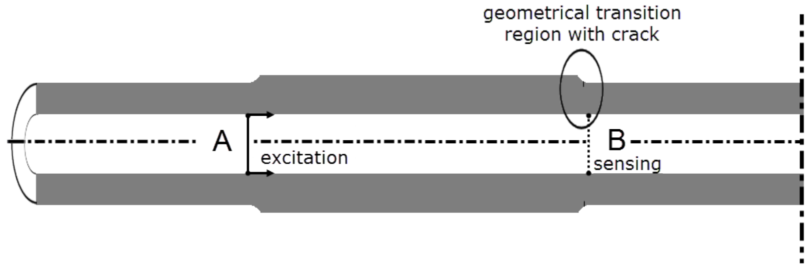

Figure 6.7: Investigated model. Horizontal lines correspond to excitation(A: 285 mm) and sensing (B: 715 mm) locations. The crack was modelled at the geometrical transition at 707 mm.

amplitude of the wave package before L(0,2) mode i.e. at 0.14 ms for 715 mm signal, was not influenced by the crack presence (compare figures 6.4b and 6.8b).

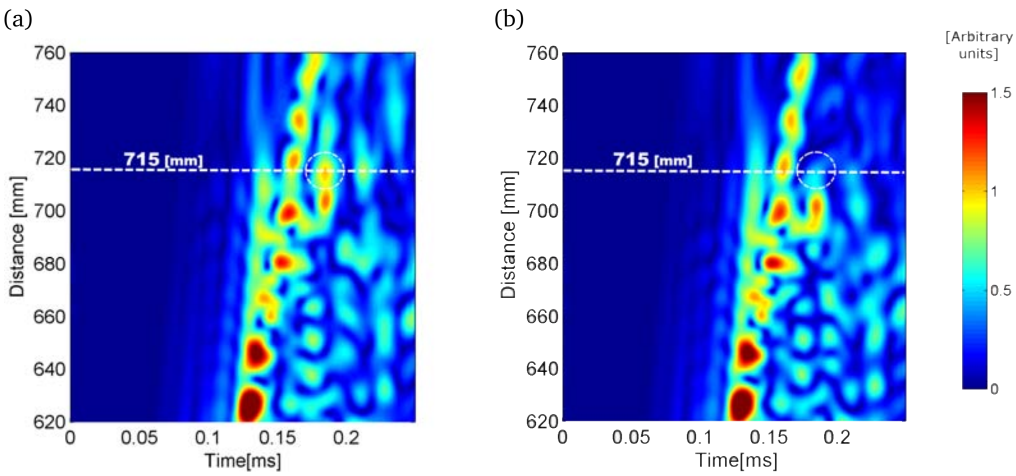

Figure 6.8: Wave enhancement effect observed at the inner surface –energy distribution. Excitation at the inner surface at location A (285 mm). Colour scale as in figure 6.4

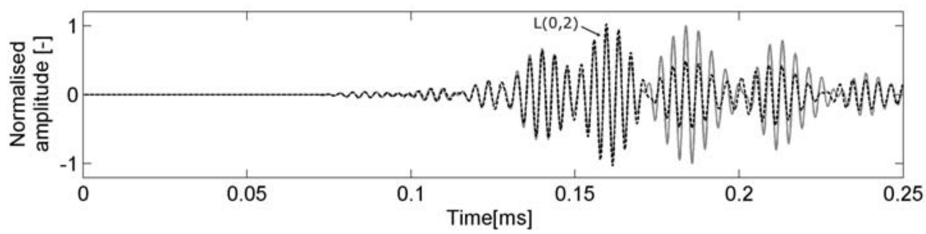

Figure 6.9: Changes in axial displacement signals at 715 mm, at the inner surface of the cylinder. Benchmark signal (–) and model with a 5 mm deep crack (- -). Wave enhancement is visible around 0.18 ms. Crack was introduced at 707 mm

Various defect severity scenarios were also investigated. As illustrated in figure 6.10, when the defect is localised at the transition, the size of the damage is barely revealed in the enhancement effect. Nonetheless, even for the relatively small crack depth of 1.5 mm, almost 40% decrease in the enhancement effect magnitude is observed. On the other hand, the size of the crack can be correlated with the increase in the amplitude of L(0,2) mode. This phenomenon can be explained by an analysis of the displacement field around the crack shown in figure 6.11. Here, the excitation in the position B was selected. (Note, that although the displacement field is different for the excitation at A and B due to the crack presence, according to the reciprocity principle [7], the time signals at the sensing positions B and A respectively, are the same for linear system.)

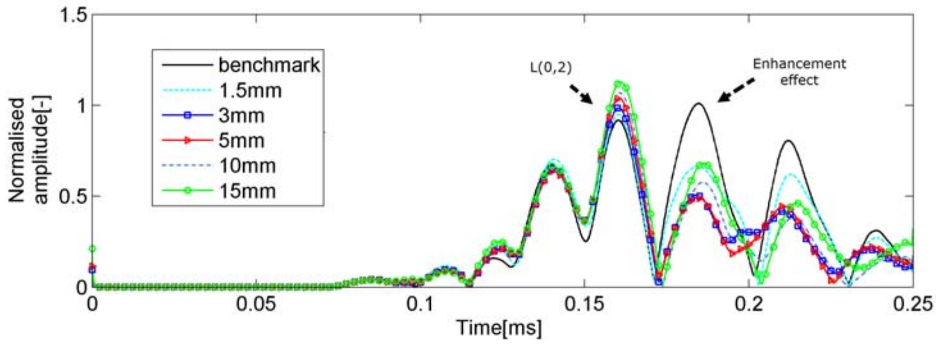

Figure 6.10: Damage severity influence on wave enhancement effect for the crack was at geometrical transition – 707 mm. Envelopes of axial displacement signals obtained at position B (715 mm at inner surface). Enhancement effect is visible around 0.18 ms.

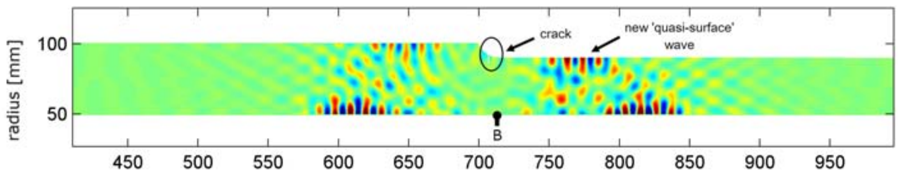

Figure 6.11: Radial displacement field. Crack located at 707 mm, excitation at 715 mm (B).

The investigation of the wave field has shown, that the crack position at the transition region – in the near-field of the excitation or sensing point– influences the magnitude of the formed 'exterior quasi-surface' wave. The energy associated with the 'quasi-surface' waves propagating to the left and to the right side of the waveguide changes with different crack locations. The depth of the crack is insignificant in this aspect. Furthermore, the crack presence at the transition region of the excitation is associated with the formation of a crack-induced 'exterior quasi-surface' wave propagating at the lower diameter region, which is due to the wave conversion at the surface discontinuity.

Comments

The numerical studies presented here illustrated the possibility of employment of the enhancement phenomenon-based method into the inspection procedure of an axle section. It is important to notice however, that the modelling used here was limited to a two-dimensional case thus, the modelled damage corresponds in fact to a groove at the outer surface of the axle. Nonetheless, it is expected that a crack of semi-elliptical shape would also cause a scattering of the 'quasi-surface' wave and a similar (although weaker effect) should be observed.

At this point the effect of the wheel presence on the wave propagation characteristic should be mentioned. Although this has not been studied in this work, based on the analysis of the influence of axle–wheel interface on ultrasonic testing presented in [72] and qualitative simulation results given in [76], it is believed that some comments on this aspect can be made here. The contact interface between the axle and the wheel transmits some portion of the ultrasound energy to the press fitted wheel; therefore, in common ultrasonic NDT approach the echo signal from the crack underneath the wheel is significantly weaker than in the case of the axle inspection with dismounted wheelsets. It is expected that also the amplitude of the formed 'exterior-quasi surface' wave will be effected by the wheels presence however, it requires further analysis to establish how this will effect the sensitivity of the proposed inspection method. Nonetheless, since the method is a baseline approach, it assumes consistent boundary and environmental conditions and a change in the response signal is attributed to the presence of a structural defect.

6.4.2 Axial localisation within a given section

At a final stage of the inspection procedure, the pulse-echo approach (with excitation and sensing at the same location) is used to evaluate the approximate location of the defect. Due to the multi-modal and dispersive character of the signals, it is difficult to evaluate the time-of-flight (TOF) of the first reflected mode package and to associate a specific group velocity with it. Therefore, the TOF of the 'exterior quasi-surface' wave reflection was used instead. A cross-correlation of the reflected waveform with the excitation signal was calculated to automatically distinguish the dominant package and obtain the delay corresponding to its TOF. Figure 6.12 shows the pulse-echo signals for various crack positions along with the reference excitation toneburst signal aligned through cross-correlation [82](i.e., the highest value of cross-correlation of the response and excitation signals indicates the arrival of the non-dispersive 'exterior quasi-surface' wave).

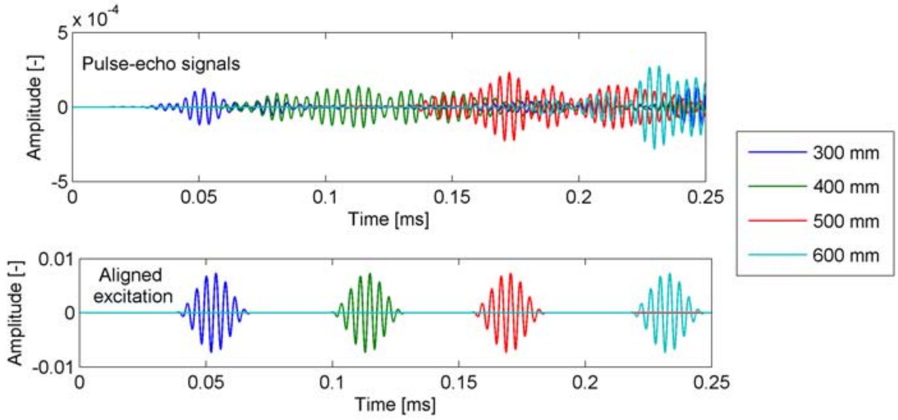

Figure 6.12: Reflection signals from cracks at various locations (top plots) with aligned excitation package (bottom plots).

Then a simple ray-tracing formula assuming shear-to-Rayleigh wave conversion at the boundaries (see figure 6.13) can be also used

$$TOF_{geom} = \frac{\sqrt{(50_{mm})^2 + (15_{mm})^2}}{v_s} + \frac{x}{v_r} + \frac{\sqrt{(50_{mm})^2 + (x + 15mm)^2}}{v_s}, \tag{6.1}$$

where v_s, v_r correspond to shear bulk wave velocity and Rayleigh wave velocity.

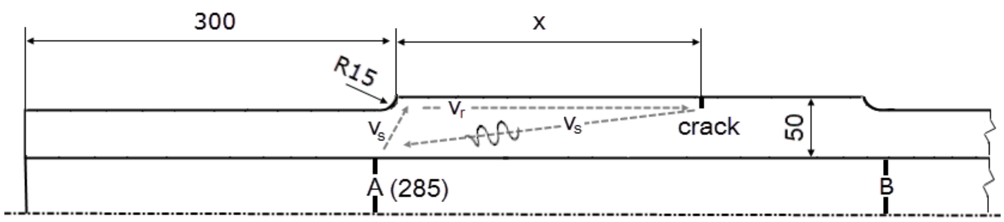

Figure 6.13: Ray-tracing sketch used to establish the pulse-echo formula.

The comparison of evaluated time-of-flights from pulse-echo method with ones calculated based with ray-tracing approach (Eq. 6.1) is given in table 6.1.

A good agreement was found between the estimated TOF and the proposed geometry-based formula, suggesting that Eq. (6.1) can be used for an inverse problem of a crack location (i.e. obtaining the TOF from the pulse-echo approach the location of the crack

Table 6.1: *Estimated time of flight of reflected 'quasi-surface' wave*

distance $[mm]$	pulse-echo method $[ms]$	ray-tracing formula (6.1) $[ms]$
300	0.0378	0.0335
400	0.0987	0.0913
500	0.1544	0.1563
600	0.2173	0.2222

can be estimated). It is however apparent, that this simple pulse-echo approach in real-life applications may be inaccurate due to the measurement noise, particularly because of the low level of the reflected energy for small cracks. Thus, this method serves as a complementary analysis to the wave enhancement-based damage detection approach, that allows for damage localisation.

6.4.3 Angular localisation method based on cross-correlation estimate

One of the primary signal processing methods for comparing two waveforms is their correlation. For two discrete signals X and Y of equal length N, the cross-correlation coefficient is defined as

$$R_{XY} = \frac{C_{XY}}{\sigma_X \, \sigma_Y} = \frac{\sum_{i=1}^{N}(X_i - \mu_X)(Y_i - \mu_Y)}{\sqrt{\sum_{i=1}^{N}(X_i - \mu_X)^2 \, \sum_{i=1}^{N}(Y_i - \mu_Y)^2}}, \tag{6.2}$$

where C_{XY} is the covariance of X and Y; σ and μ are the standard deviation and the mean of the signal in the subscript, respectively. The cross-correlation coefficient gives a single value of similarity between the signals. Two examples of application of this technique to damage localisation are studied in the following.

Case 1: Numerical simulation

A sketch of the investigated structure is shown in figure 6.14. An aluminium cylinder with a length of 250 mm, an inner diameter of 100 mm and a wall thickness of 50 mm was simulated with 3D LISA implemented using parallel computing [84] (simulation parameters used: $dx = 0.5\ mm$, $dt = 0.05\mu s$). As a damaged scenario, a crack modelled as a rectangular base slot at a distance of 100 mm from the excited end of the model, with various depths (h = 2.5/5/7/10/14 mm) and a width of 1 mm was investigated. The presented results are obtained assuming the pitch-catch configuration (similar results were obtained from pulse-echo signals). The inner ring-type excitation of the edge of the cylinder was modelled as nodal displacements in the axial direction. Axial displacement signals were collected at the inner surface of the cylinder, at 245 mm from the excited edge.

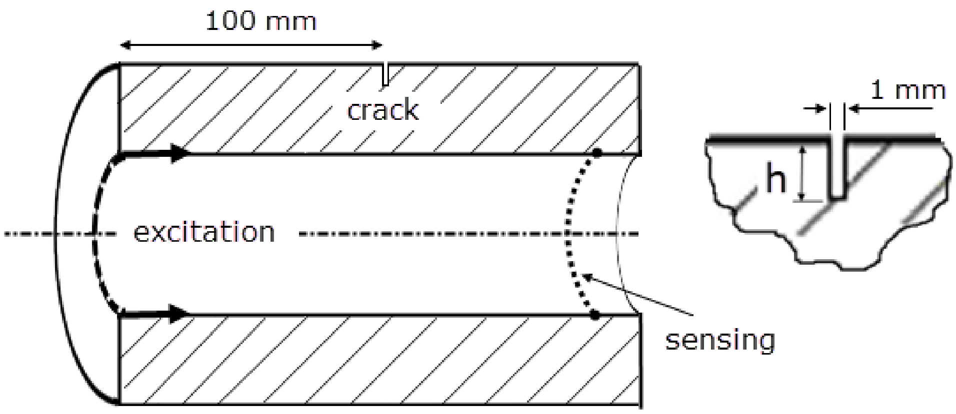

Figure 6.14: Sketch of the modelled structure : an aluminium hollow cylinder, 250 mm long, with an inner diameter of 100 mm and an outer diameter if 200 mm.

Figure 6.15 investigates the correlation between signal from the pristine and damaged models. The cross-correlation coefficients were evaluated from 0.25 ms long waveforms. Another representation of the obtained results is given in figure 6.16. In this case 36 points around the inner circumference (every 10°) were selected.

The results confirm that using the cross-correlation analysis the angular localisation of a defect as well as damage assessment can be achieved. One should note however, that a cross-correlation coefficient is sensitive to axial position of the crack (i.e. for the pitch-catch configuration the smaller the distance between a crack and the sensor, the greater is the distortion of the signal), therefore first the assessment of the axial location has to be performed.

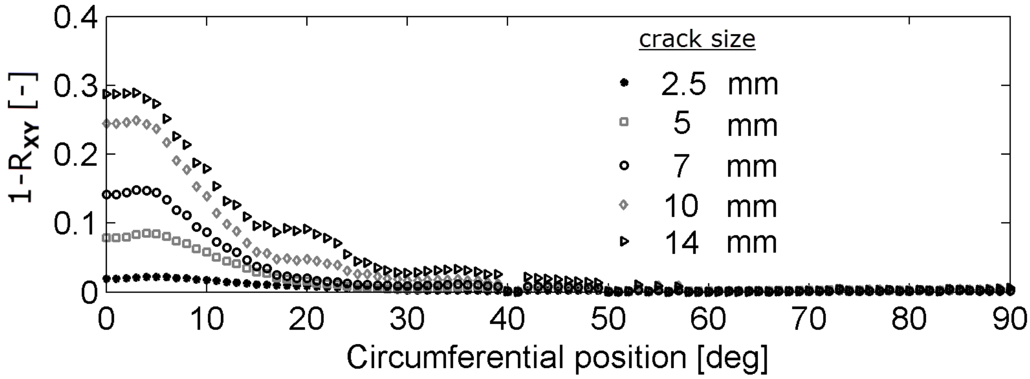

Figure 6.15: Correlation between the benchmark and the ‘damaged’ signals.

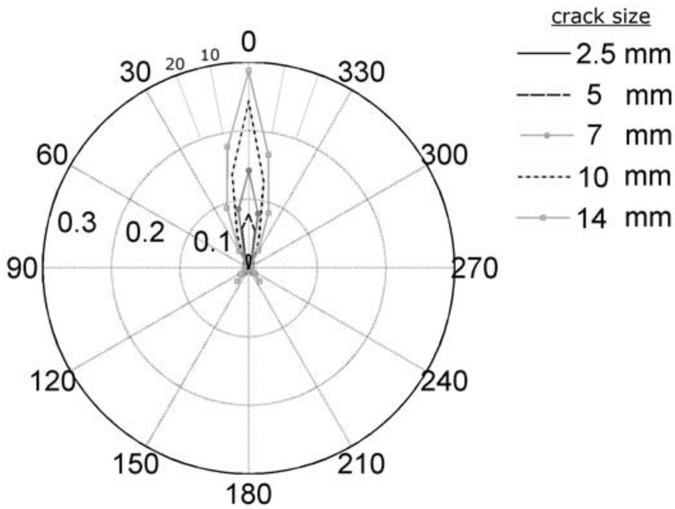

Figure 6.16: $1 - R_{xy}$ (1– cross-correlation coefficient) evaluated for 36 points around circumference at 245 mm (the reference signals at the same location).

Case 2: Experimental validation with hollow cylinder

The feasibility of the cross-correlation technique was also validated experimentally. A 500 mm long aluminium cylinder with an inner diameter of 100 mm and a wall thickness of 50 mm was investigated. Two Macro Fiber Composite transducers of dimensions 28 mm$\times$14 mm were alternately used to excite the structure from its inner surface. For sensing, six circular piezoelectric transducers with a diameter of 8 mm were bonded to the outer surface of the cylinder as shown in figure 6.17a. The details of the setup configuration are given in table 6.2. An eight cycles of Hanning windowed sine signal with a central frequency of 265 kHz was used in this study as an excitation. The signal was generated by NI PXI-5412 waveform generator and amplified to 480 Vp-p (by US-TXP-3 linear power amplifier) before feeding a MFC actuator. The response signals were

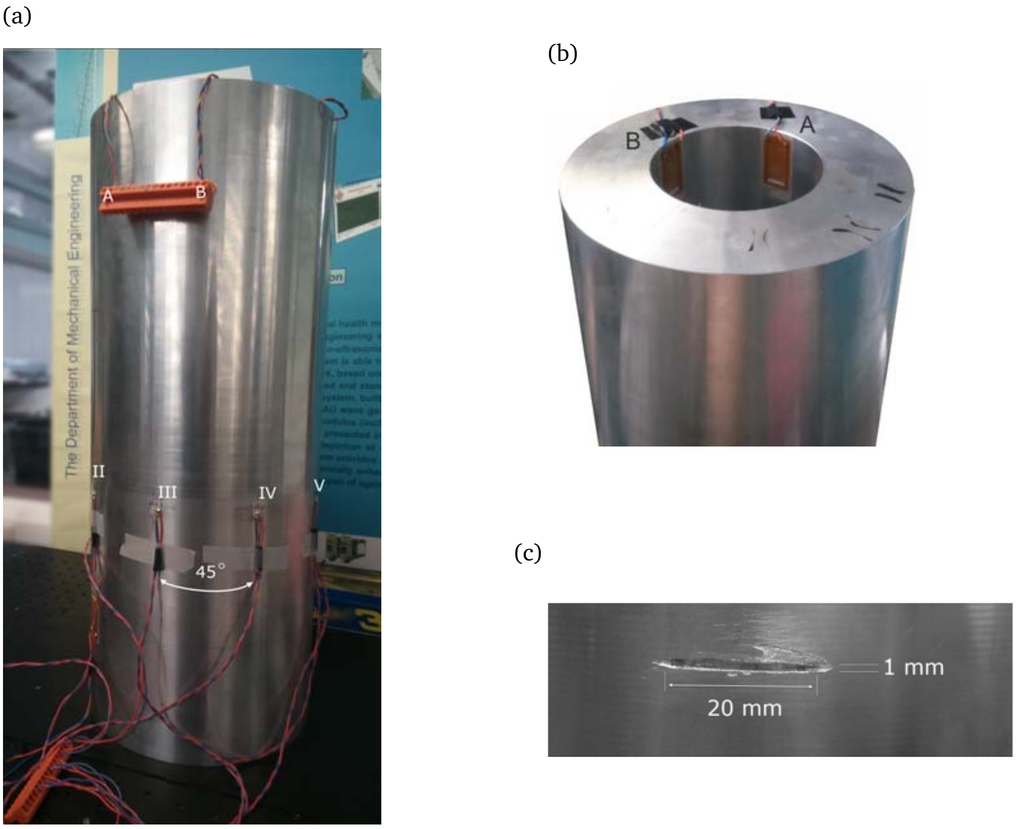

Figure 6.17: Experimental setup (a) aluminium hollow cylinder with an inner diameter of 100 mm, a length of 500 mm and outer diameter of 200 mm, (b) placement of actuators (c) damage dimensions.

acquired at a sampling rate of 10 MHz. To additionally enhance the signal-to-noise ratio, 100 times averaging of the time signal was set during the measurements. In the second stage of the experiment a semi-elliptical saw-cut damage was artificially introduced using cut-off wheel of 15/16” (DREMEL rotary tool). The signals were collected from 20 mm long damages of a width of 1 mm and with a maximal depth of: (a) 2.5 mm and (b) 3.5 mm.

During the experimental investigation, two sets of measurements were carried out; one for each actuator A and B. For the evaluation of the cross-correlation coefficient, 0.25 ms long signals (pre-filtered with Butterworth bandpass filter with passband of 150-350 kHz, and with the electromagnetic crosstalk removed from signals) were used. The same length of the signal was chosen for all six sensors, based on the analysis of the acquired waveforms (avoid reflections, but ensure the generated wave had reached the sensor). Exemplary waveforms from damaged and ‘healthy’ structure are shown in figure 6.18.

Table 6.2: Configuration of the experimental setup.

name		axial position	circumferential position
A	MFC actuator	0-28 mm	45°
B	MFC actuator	0-28 mm	135°
I	PZT-sesnor	300 mm	0°
II	PZT-sesnor	300 mm	45°
I	PZT-sesnor	300 mm	90°
IV	PZT-sesnor	300 mm	135°
V	PZT-sesnor	300 mm	180°
VI	PZT-sesnor	300 mm	225°
	damage	150 mm	45°

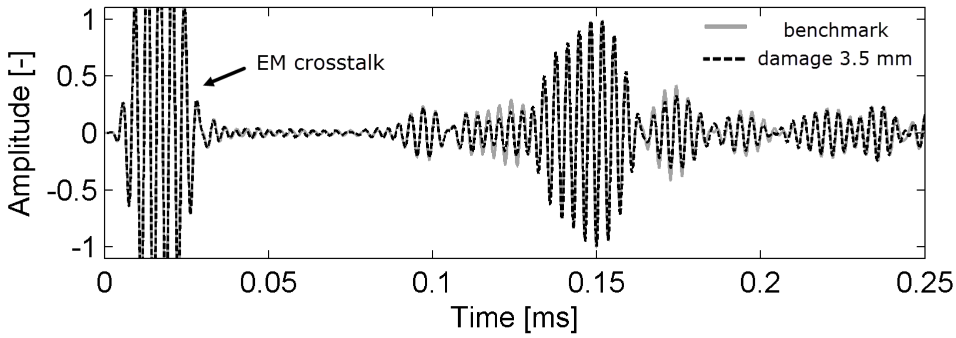

Figure 6.18: Comparison of the signals acquired from the undamaged structure and with a 3.5 mm deep defect. Signals from the pair: actuator A and sensor II, are shown. Waveforms were normalised by the magnitude of the benchmark signal after crosstalk was removed.

The results of the cross-correlation coefficient for the six equally distributed measurement locations at the outer circumference of the structure are shown in figure 6.19.

It is noticed that for both excitation cases (A and B) it is possible to estimate the position of the damage. Surprisingly, for the excitation A –in line with the defect– and the damage depth of 3.5 mm, the evaluated cross-correlation coefficients for sensors I and II are comparable. The results for excitation at position B more distinctively point to the 3.5 mm deep damage position. This indicates that larger damage causes greater changes to the wave field and multiple sensor responses have to be compared to successfully identify the crack location.

(a)

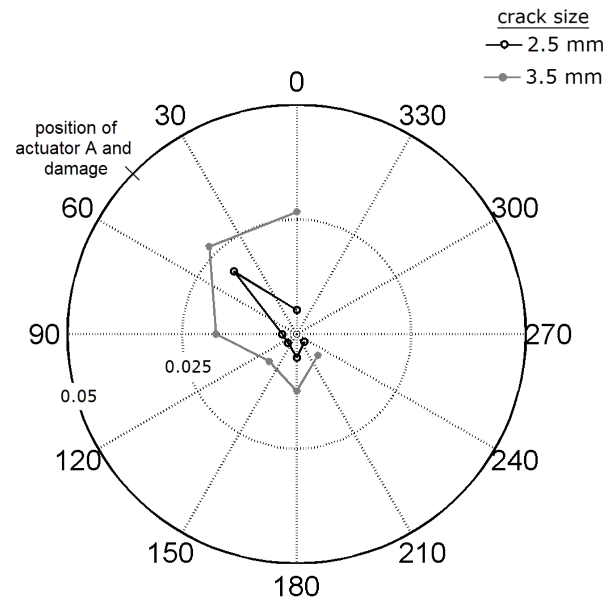

(b)

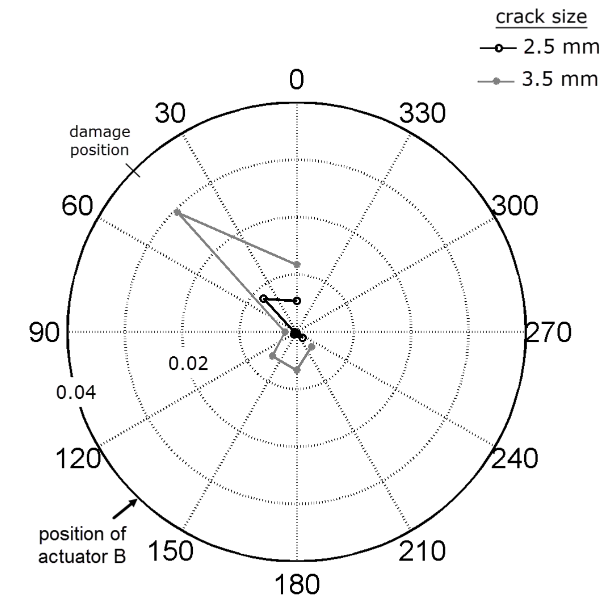

Figure 6.19: $1 - R_{xy}$(1– cross-correlation coefficient) between the benchmark and 'damaged' signals for excitation with: (a) the actuator A at angular position of $45°$, (b) the actuator B at angular position of $135°$.

Comments

In both investigated cases the cross-correlation estimates reveal good sensitivity to a crack presence. Note however, that the presented numerical and experimental results cannot be directly compared due to the differences in the setup. In the case of the numerical simulation model, only the longitudinal modes were excited as the inner ring-type excitation was assumed. Also, since the modelled cylinder was restricted by computational capabilities to the length of 250 mm, reflections from the boundaries were present in the signals. For the experimental measurements, a single MFC actuator was used to excite the structure resulting in propagation of flexural modes in the structure. Nonetheless, the possibility of using cross-correlation for angular damage localization was validated.

6.4.4 Experimental validation of the inspection procedure

The complete inspection approach was investigated using a hollow cylinder sample with a single transition region. The major part of the experiment discussed here has been already presented and analysed in section 5.5.3 of chapter 5 while investigating the wave enhancement effect itself. In that section it has been shown that using the transition region as a sensing location and the wave enhancement effect as a 'marker', a clear damage signature can be obtained. Therefore, here only the second level of inspection i.e. damage assessment and localization, is addressed. In this regard, the results from the cross-correlation analysis and time-of-flight estimate of pulse-echo signal are discussed.

First, a brief recall of the experimental setup should be made. As shown in figure 6.20 six Macro Fiber Composite transducers were used during the experiment. The transducers were cut into an active dimensions of 5 mm$\times$14 mm and bonded to the inner surface of the cylinder with cyanoacrylate adhesive. For signal acquisition, eight equally spaced circular PZT-disc transducers with a diameter of 8 mm and thickness of 0.48 mm were mounted at the bore of the cylinder at the axial distance of 316 mm from the collocated actuator. The structure was excited with eight cycles of Hanning windowed sine signal with a central frequency of 365 kHz.

As discussed, the inspection procedure should follow few consecutive steps. At the first stage, the cross-correlation analysis for six actuator-sensor paths is performed to estimate an angular location of the potential damage. For the lowest correlation between the benchmark and measured signal, a detailed analysis regarding changes in the wave

(a)

(b)

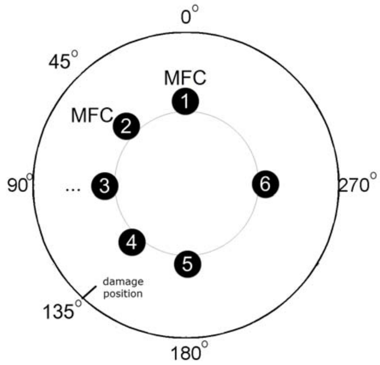

Figure 6.20: (a) Configuration of the experimental setup, (b) illustration of the actuator locations.

enhancement magnitude is then carried out. After verification and assessment of the damage using the enhancement-based method, the localisation of the defect with time-of-flight analysis in pulse-echo configuration can be performed.

Figure 6.21 presents the results of the cross-correlation analysis for two damage scenarios: with maximal depth of 3.5 mm and 4.5 mm, respectively. The cross-correlation coefficients were calculated for each of the actuator-sensor pairs (with the same angular position) separately.

It can be seen that a good directivity was achieved as the results clearly point out to a damage at position of 135°. Also, a decrease in signals correlation is observed with an increase of a damage size. Lastly, the MFC transducers were used in the pulse-echo configuration to evaluate the axial position of the damage. The results from the excitation with transducer number 4 (at 135°) and signal measured with transducer 3 (at 90°) are shown in figure 6.22. The time-of-flight of the strongest wave package in the signal

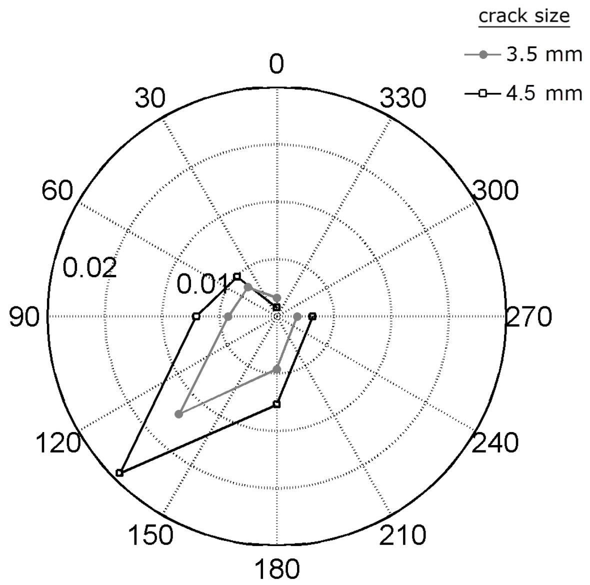

Figure 6.21: $1 - R_{xy}$ (1– cross-correlation coefficient) for six collocated actuator-sensor pairs.

evaluated using cross-correlation estimate, after subtraction of the benchmark waveform, is 0.1378 ms.

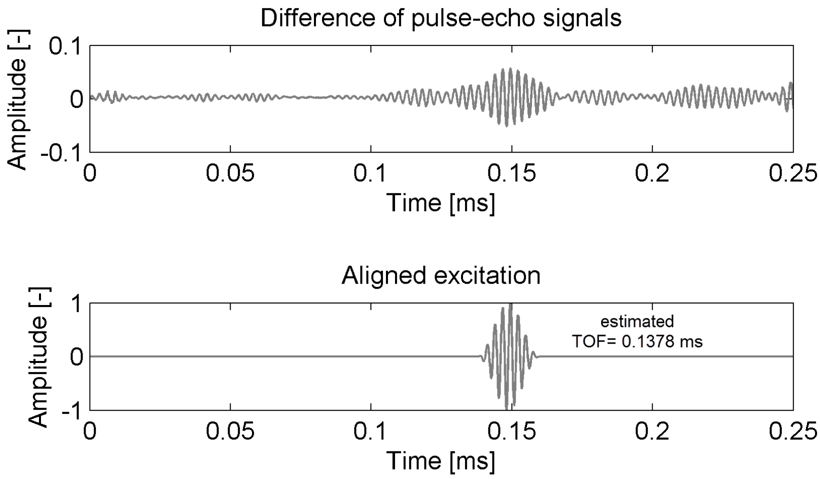

Figure 6.22: Results of pulse-echo measurements for excitation with MFC no.4 and sensing with MFC no.3 (see figure 6.20).

It was noted that this wave package corresponds to the 'exterior quasi-surface' wave reflected from the damage; therefore, based on the geometry of the investigated structure the damage location (x_{dam}) can be estimated from the relation $TOF = 2 \cdot \frac{wall\,thickness}{v_s} + 2 \cdot \frac{x_{dam}}{v_r}$, where v_r and v_s are the Rayleigh and shear wave velocities, respectively. The obtained TOF = 0.1378 ms, indicates that the damage position is at 151 mm from the excited end of the cylinder.

Comments

The experimental results from a hollow cylinder with a single transition region show good detectability of the inspection procedure and good angular localization ability. On the other hand, the study has revealed some limitations of the proposed approach in particular for axial localization of a damage. It was noted that due to the multiplicity of modes and propagation paths, the formula used for evaluation of the damage position should be used with care.

6.5 Summary and conclusions

Railway axle inspection using guided wave approaches implemented in Structural Health Monitoring system has a great advantage over scheduled inspection-based maintenance. This is particularly because a fatigue crack propagation has non-deterministic, often abrupt character. However, due to the complex geometry of train axles, an understanding of elastic wave characteristics is required to reveal and strengthen the influence of the crack on the acquired signals. In this regard, the utilization of phenomena such as the 'external quasi-surface' wave formation and the near-field wave enhancement at geometrical transition is believed to be an important development.

This chapter aimed at proposing a complete inspection scheme for a thick-walled hollow axle structure based on an investigation of consecutive axle sections. Three levels of damage identification were addressed, namely detection, localization and assessment of the crack. To optimise the effectiveness of the inspection, it was proposed that the excitation and sensing locations need to be chosen at outer diameter transitions; this allows for utilizing the enhancement-based approach for monitoring of particular sections of the axle. Figure 6.23 summarises the developed inspection methodology through steps 1 (angular cross-correlation) to 4 (damage assessment). Additionally, a possibility of introducing a damage index (DI) i.e. a single value signal change estimate evaluated from different signal analyses, for automation of the SHM analysis is pointed out. Another important fact is that, although in the current solution all three levels of inspection are considered, depending on the specific monitoring system requirements, the level I of the inspection may be considered as sufficient for the axle structural evaluation.

Various numerical and experimental investigations were carried out to validate both the damage detection and the damage localisation techniques. The results of the conducted analyses confirm the feasibility of the wave enhancement effect for inspection of the surface underneath the wheel seats. The baseline approach based on evaluation of the cross-correlation coefficients, has been demonstrated as highly effective tool for angular localisation of a crack. It should be noted that the cross-correlation analysis depends on the sensor location; therefore, changes in the enhancement effect are intrinsically incorporated into the cross-correlation value. For determination of a crack location in the axial direction of the structure, the time-of-flight analysis using pulse-echo transducer configuration is an attractive approach, which however requires careful interpretation of the reflected signal, based on the geometry of the structure and the dominant wave components.

The investigations discussed in this chapter were mostly limited to a relatively simple, short components and rather idealised models; therefore, further studies with full-scale axle specimen are required.

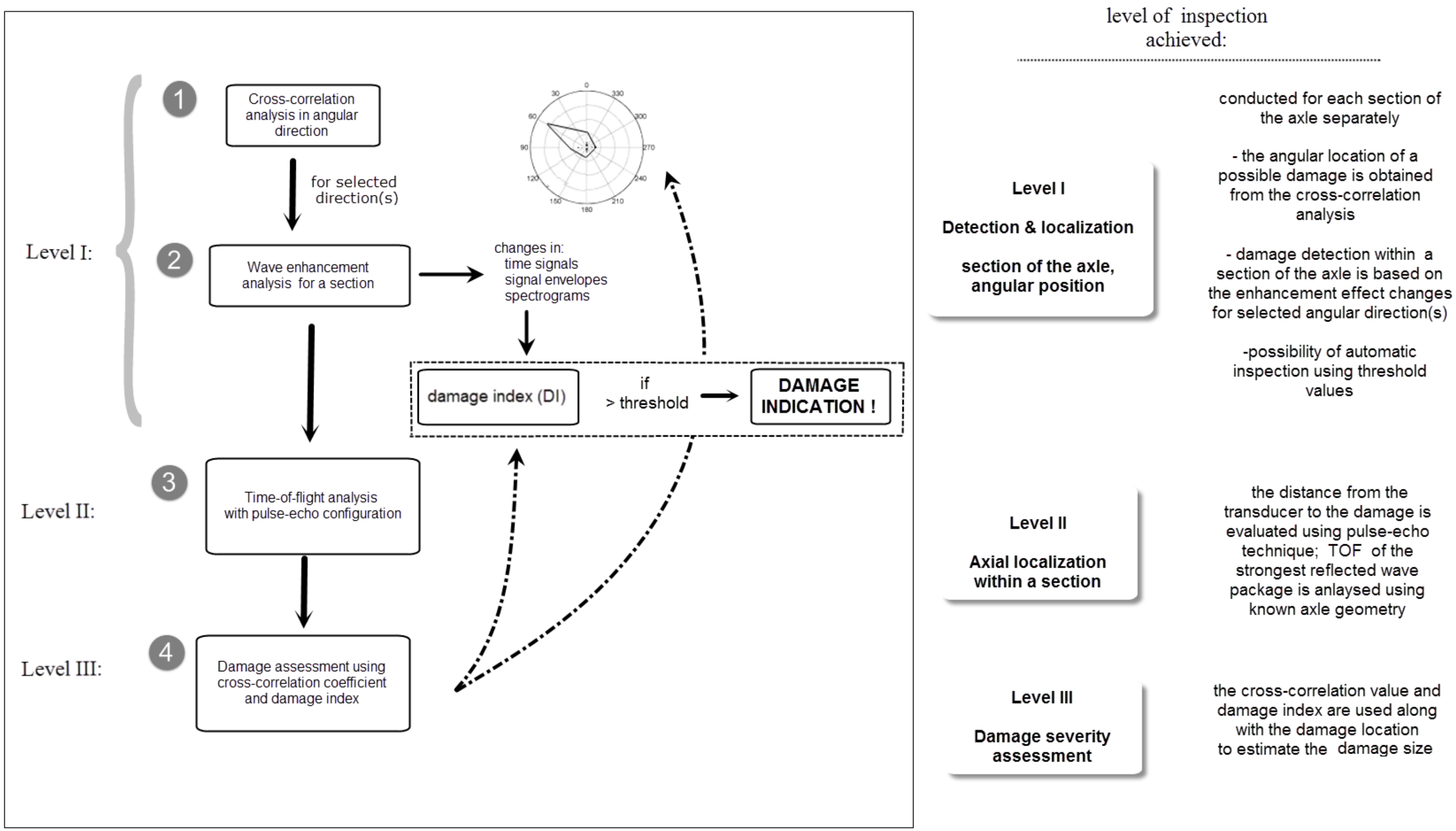

Figure 6.23: Railway axle inspection methodology.

Chapter 7

Summary, conclusions and future directions

7.1 Review of the thesis

The main focus of this thesis was to develop a broader understanding on the guided wave phenomenon in thick-walled cylindrical structures. In addition an attempt for utilizing guided wave-based approaches for hollow railway axle inspection was made.

In the first chapter, the motivation of the work was discussed along with the overview of the existing inspection solutions for train axles. It was shown that the current axle inspection techniques, based on nondestructive testing, are limited by requirement of accessibility to the inspection region and reliance on expertise of human operators. A structural health monitoring approach is an alternative that allows to replace the costly periodic check-ups by in-service structural evaluation. However, the fully effective and efficient SHM can only be established with prior in-depth knowledge of the phenomena existing in the examined structure. The review of the literature pointed out the fact that there exists a scientific gap in the understanding of cylindrical waveguides with significant thickness-to-wavelength ratio. This thesis was an attempt to fill this gap.

Chapter 2 reviewed the theory of guided wave propagation in various geometries including Rayleigh surface waves, Lamb waves in plates and cylindrical guided waves in solid and hollow cylinders. The discussion was carried out within a common analytical framework in order to analyse the relationships between the solutions for different waveguides and to reveal common phenomena. In addition, a literature overview on hollow cylindrical guided waves was presented at the end of that chapter.

Chapter 3 was focused on theoretical and experimental investigations of guided waves in hollow cylinders; in particular the thick-walled structures and higher order modes were studied. The semi-analytical analysis of dispersion characteristics and mode displacement patterns was carried out to establish the relationship between the solutions to wave propagation problem in plates and in hollow cylinders. The analysis of displacements of the axisymmetric longitudinal modes using asymptotic approximations of Bessel functions was performed. The dispersion characteristics of the longitudinal and flexural modes for various geometrical parameters of a hollow cylinder were analysed. Experimental studies were conducted to confirm the possibility of inner and outer surface excitation and to provide a better insight into wave propagation characteristic.

In chapter 4 the framework of the simulation methods used in this work namely, local interaction simulation approach and finite element method were presented. In addition the two-dimensional axisymmetric cylindrical formulation of LISA for investigation of longitudinal modes was developed. The preliminary results on the dispersion characteristics and narrowband wave propagation were also given as a background for the experimental investigations in chapter 2.

Chapter 5 reveals a near-field wave enhancement phenomenon due to the crack-wave interaction and geometry variation in a waveguide. The influence of the defect size on local enhancements was analysed, followed by an analysis of the effect of the outer diameter change of the cylinder on guided waves behaviour. Based on the developed understanding of the enhancement effect, a novel inspection method was proposed and investigated numerically and experimentally. The experimental validation of the technique was carried out on beam-type components with single and double thickness transitions and a hollow cylinder structure.

Chapter 6 proposes a complete methodology for axle inspection including detection and localization of a damage. In addition to the wave enhancement-based damage detection approach, conventional methods using the cross-correlation analysis of damaged and benchmark signals and the time-of-flight estimation in pulse-echo system configuration, were tested both numerically and experimentally.

7.2 Major findings

- The review of guided wave solutions revealed similarities in the behaviour of higher order modes of plate-like and cylindrical waveguides including: interlacing of dispersion curves, flattening of phase velocity curves at compressional bulk wave velocity limit (maximal group velocity), and the development of 'quasi-surface' waves i.e. modes with displacement patterns confined to the boundaries. Although the discussion in this thesis was mainly focused on wave propagation in hollow isotropic cylinders, it was shown that a hollow cylindrical structure can be treated as a generic case which for limiting values of thickness, curvature and inner radius leads to corresponding surface, plate or solid cylinder solutions. This generalized treatment of guided waves related phenomena gives a more complete theoretical framework and insight into the behaviour of elastic waves for different types of geometries.

- Despite the common features, it is highly important to understand the differences in the phenomena existing in various types of waveguides. The analytical analysis of the displacement patterns of the axisymmetric longitudinal modes in a hollow cylinder, revealed the pseudo-symmetry of the modeshapes and allowed to distinguish groups of pseudo-symmetric and pseudo-antisymmetric longitudinal modes. In contrast to Lamb waves, these two groups of longitudinal modes exhibit coupled behaviour due to the curvature of the structure. The investigation of their dispersion characteristics shows a common pattern of seemingly interlacing curves analogous to terrace-like structures in plates. Due to the the radial stress component, coupling between pairs of consecutive pseudo-symmetric and pseudo-antisymmetric longitudinal modes occurs, resulting in a hyperbolic behaviour of the dispersion curves at the cross-section points of the corresponding Lamb wave modes. The developed understanding of the mode coupling phenomenon is believed to be fundamental for future work in this field, for instance when considering mode conversions.

- Some observations on frequency/wavelengths regions of dispersion characteristics were also made. The conducted analyses indicated that for large wavelengths region the mean radius-to-thickness ratio is a geometric parameter that influences the shape of the dispersion curves, while in the high-frequency region the cylinder's curvature manifests its effects mainly by the coupling between the modes. It is therefore possible to approximate the dispersion curves of longitudinal modes in the short wavelengths limit with Lamb wave modes curves to significantly reduce the calculation effort.

- The experimental tests with laser vibrometry confirmed the multiplicity of the modes propagating in a thick-walled cylinder and the difficulty in differentiating particular mode packages in the time domain signals. Also, different wave propagation patterns were observed at the outer surface of the cylinder for internal and external surface excitations. For the external excitation the 'exterior quasi-surface' wave becomes a dominant wave component, while for excitation at the internal surface the higher order modes are also clearly excited. Moreover, for both excitation scenarios the presence of strong modes of Rayleigh wave velocity can be observed. These findings were utilized in chapter 5 for development of the outer surface inspection approach.
- Two-dimensional formulation of local interaction simulation method in cylindrical coordinates was developed for stimulation of solely longitudinal modes. This numerical approach allows to efficiently model large –in terms of element numbers– structures with limited computing capacity and to avoid the 'staircase' discretization problem of the Cartesian LISA formalism.
- The local wave enhancement phenomenon due to the crack presence or thickness variation in a waveguide was revealed and analysed. In general, the enhancement effect can be understood as a result of the incident, reflected and converted wave mode interference in the vicinity of the thickness change which causes the wave scattering. The phenomenon depends on the characteristics of the propagating modes at given excitation frequency, and the interface of the geometrical discontinuity i.e. its depth, curvature and slope. The numerical results revealed that the 'quasi-surface' wave interaction with a surface breaking crack results in strong wave enhancement across the waveguide thickness. This phenomenon is associated with through thickness propagation of strong scattered partial shear waves. The positive correlation of the magnitude of the enhancement effect with the crack depth was also shown.

- The near-field wave enhancement phenomenon due to the outer diameter transition in a thick-walled hollow cylindrical structure was observed for both broadband and narrowband excitations. Different effects for upward and downward geometrical transitions occur as a consequence of the different number of modes supported at given frequency$\times$thickness. It was noticed that for the ‘step-up’ transition the wave reflection is mainly related to large wavelength modes, while for ‘step-down’ the step depth is an important parameter for mode reflection. Due to the significant thickness-to-wavelength ratio, the influence of multiple modes may mask the phenomenon, thus high energy mode needs to be studied. In the analysed examples the ’exterior quasi-surface’ wave was found to be the main contributor to the enhancement effect observed at the inner surface of a hollow cylinder due to its sensitivity to the surface discontinuities. The enhancement effect observed at the inner surface depends on the shape of the transition (i.e. slope, curvature, depth) and the incident wave characteristic. The understanding of this phenomenon was utilized for the development of a new damage detection method.
- A novel inspection approach based on the wave enhancement effect was proposed and examined. The method is highly effective for on surface crack detection within waveguide sections i.e. between two downward geometrical transition regions such as wheel press-fit region in an axle. The advantage of the developed solution is that while inspecting for outer surface cracks, both the excitation and sensing can be carried out from the inner surface of the hollow cylinder. This has great potential for in-service axle monitoring systems, as it provides a technique for inspection of inaccessible surfaces with transducers mounted at the bore of the axle. As supplementary means, cross-correlation, time-of-flight and signal envelope analyses can be implemented for precise damage localisation and assessment at later stages of inspection.

7.3 Future recommendations

Some aspects of this research require further investigations for complete understanding of the new phenomena and validation of the proposed solutions. Future paths in this field may include the following.

Modes coupling phenomenon: Further theoretical developments on the modes coupling (i.e. hyperbolic behaviour of the seemingly interlacing dispersion curves) should include investigation of circumferential Lamb waves for which the coupling effect is expected, and comparison with curved plate solution. Moreover, the magnitude of the coupling between modes and its dependence on both the geometrical parameters and wave excitation related features needs to be established analytically.

Simulation methods: The extension of the two-dimensional LISA for a three-dimensional model developed in cylindrical coordinates is expected since it allows to omit the discretization problem in circumferential direction and thus efficiently model the cylindrical structures. Also solid cylinder case i.e. zero value of the inner radius, should be incorporated into the approach.

'Quasi-surface' waves: In this work the scattering of strong surface confined modes was used as a damage signature; firstly due to the predictable behaviour of these modes similar to Rayleigh surface waves, and secondly because of their sensitivity to on-surface and sub-surface cracks. In future, the conditions of formation of the 'quasi-surface' waves such as critical angle and transition depth needs to be scrutinized.

Wave scattering effect due to the geometrical transition in the waveguide: The analyses of wave scattering presented in this work have only explanatory character without mathematical background, as it was used directly as a damage related feature. Future investigation of guided wave behaviour at geometrical transitions should include the analysis of the reflection, conversion and transmission coefficients for particular modes. In this regard other numerical methods should be considered such as semi analytical finite element method [20, 21].

Near-field enhancement effect: Although the wave enhancement phenomenon was observed in this research both in the numerical simulation results and in the experiments, the investigation was limited to the ‘exterior quasi-surface’ wave behaviour. The following studies should focus on understanding the enhancement effect for other guided modes and experimental validation preferably with contactless sensing such as laser vibrometry.

Inspection approach: The proposed monitoring techniques need to be validated on a full-scale railway axle since the effect of attenuation and measurement noise were not included into the simulations. From practical view point, this requires manufacturing of flexible ring-type transducers for excitation of limited number of axially propagating modes . Alternatively a phased array technique [59] or directional transducers [15] can also be used to angularly scan an axle. For sensing, the interpolation between finite number of sensing points using the probability distribution function as shown in [130] can be utilized. Also the effect of the wheel presence on the axle during the inspection needs further careful consideration.

Structural health monitoring system for hollow train axles: Based on the developed damage detection procedures incorporating the near-field enhancement effect, some automation of the axle monitoring process can be performed. This is typically done by establishing damage related thresholds for the results and configuring alarm notifications for violating cases. Alternatively, neural network approach may be used to combine various signal processing analyses. The benefit from neural network methods is the possibility of incorporating changing environmental conditions into the teaching set of results.

Appendix A

Mathematical notation

Cartesian coordinates notation

Del operator

$$\nabla = \frac{\partial}{\partial x}\widehat{x} + \frac{\partial}{\partial y}\widehat{y} + \frac{\partial}{\partial z}\widehat{z} \tag{A.1}$$

Gradient of scalar function

$$\nabla\phi = \widehat{\mathbf{x}}\frac{\partial\phi}{\partial x} + \widehat{\mathbf{y}}\frac{\partial\phi}{\partial y} + \widehat{\mathbf{z}}\frac{\partial\phi}{\partial z} \tag{A.2}$$

Divergence of vector function **D**

$$\nabla \cdot \mathbf{D} = \frac{\partial}{\partial x}D_x + \frac{\partial}{\partial y}D_y + \frac{\partial}{\partial z}D_z. \tag{A.3}$$

Curl of vector function **A**

$$\nabla \times \mathbf{A} = \widehat{\mathbf{x}}\left[\frac{\partial A_z}{\partial y} - \frac{\partial A_y}{\partial z}\right] + \widehat{\mathbf{y}}\left[\frac{\partial A_x}{\partial z} - \frac{\partial A_z}{\partial x}\right] + \widehat{\mathbf{z}}\left[\frac{\partial A_y}{\partial x} - \frac{\partial A_x}{\partial z}\right] \tag{A.4}$$

Laplace operator

$$\nabla^2 = \nabla \cdot \nabla = \frac{\partial^2}{\partial x^2} + \frac{\partial^2}{\partial y^2} + \frac{\partial^2}{\partial z^2} \tag{A.5}$$

Accordingly, the symmetric gradient operator in the matrix representation(strain)

$$
\nabla_s = \begin{bmatrix} \frac{\partial}{\partial x} & 0 & 0 \\ 0 & \frac{\partial}{\partial y} & 0 \\ 0 & 0 & \frac{\partial}{\partial z} \\ 0 & \frac{\partial}{\partial z} & \frac{\partial}{\partial y} \\ \frac{\partial}{\partial z} & 0 & \frac{\partial}{\partial x} \\ \frac{\partial}{\partial y} & \frac{\partial}{\partial x} & 0 \end{bmatrix} \tag{A.6}
$$

and the divergence of stress

$$
\nabla \cdot \boldsymbol{\sigma} = \begin{bmatrix} \frac{\partial}{\partial x}\sigma_{xx} + \frac{\partial}{\partial y}\sigma_{xy} + \frac{\partial}{\partial z}\sigma_{xz} \\ \frac{\partial}{\partial x}\sigma_{xy} + \frac{\partial}{\partial y}\sigma_{yy} + \frac{\partial}{\partial z}\sigma_{yz} \\ \frac{\partial}{\partial x}\sigma_{xz} + \frac{\partial}{\partial y}\sigma_{yz} + \frac{\partial}{\partial z}\sigma_{zz} \end{bmatrix}. \tag{A.7}
$$

Cylindrical coordinates notation

Gradient of scalar function

$$
\nabla \phi = \frac{\partial \phi}{\partial r}\widehat{\mathbf{r}} + \frac{1}{r}\frac{\partial \phi}{\partial \theta}\widehat{\boldsymbol{\theta}} + \frac{\partial \phi}{\partial z}\widehat{\mathbf{z}} \tag{A.8}
$$

Divergence of vector function **D**

$$
\nabla \cdot \mathbf{D} = \frac{1}{r}\frac{\partial}{\partial r}(rD_r) + \frac{1}{r}\frac{\partial D_\theta}{\partial \theta} + \frac{\partial D_z}{\partial z}. \tag{A.9}
$$

Curl of vector function **A**

$$
\nabla \times \mathbf{A} = \widehat{\mathbf{r}}\left[\frac{1}{r}\frac{\partial A_z}{\partial \theta} - \frac{\partial A_\theta}{\partial z}\right] + \widehat{\boldsymbol{\theta}}\left[\frac{\partial A_r}{\partial z} - \frac{\partial A_z}{\partial r}\right] + \widehat{\mathbf{z}}\left[\frac{1}{r}\frac{\partial (rA_\theta}{\partial r} - \frac{1}{r}\frac{\partial A_r}{\partial \theta}\right] \tag{A.10}
$$

Laplace operator

$$
\nabla^2 = \nabla \cdot \nabla = \frac{\partial^2}{r^2} + \frac{1}{r}\frac{\partial}{\partial r} + \frac{1}{r^2}\frac{\partial^2}{\partial \theta^2} + \frac{\partial^2}{\partial z^2} \tag{A.11}
$$

Vector Laplacian $\nabla^2\mathbf{A}$

$$\nabla^2\mathbf{A} = \begin{bmatrix} \dfrac{\partial^2 A_r}{\partial r^2} + \dfrac{1}{r^2}\dfrac{\partial^2 A_r}{\partial \theta^2} + \dfrac{\partial^2 A_r}{\partial z^2} + \dfrac{1}{r}\dfrac{\partial A_r}{\partial r} - \dfrac{2}{r^2}\dfrac{\partial A_\theta}{\partial \theta} - \dfrac{A_r}{r^2} \\ \dfrac{\partial^2 A_\theta}{\partial r^2} + \dfrac{1}{r^2}\dfrac{\partial^2 A_\theta}{\partial \theta^2} + \dfrac{\partial^2 A_\theta}{\partial z^2} + \dfrac{1}{r}\dfrac{\partial A_\theta}{\partial r} + \dfrac{2}{r^2}\dfrac{\partial A_r}{\partial \theta} - \dfrac{A_\theta}{r^2} \\ \dfrac{\partial^2 A_z}{\partial r^2} + \dfrac{1}{r^2}\dfrac{\partial^2 A_z}{\partial \theta^2} + \dfrac{\partial^2 A_z}{\partial z^2} + \dfrac{1}{r}\dfrac{\partial A_z}{\partial r} \end{bmatrix} \tag{A.12}$$

Accordingly, the symmetric gradient operator in the matrix representation(strain)

$$\nabla_s = \begin{bmatrix} \dfrac{\partial}{\partial r} & 0 & 0 \\ \dfrac{1}{r} & \dfrac{1}{r}\dfrac{\partial}{\partial \theta} & 0 \\ 0 & 0 & \dfrac{\partial}{\partial z} \\ 0 & \dfrac{\partial}{\partial z} & \dfrac{1}{r}\dfrac{\partial}{\partial \theta} \\ \dfrac{\partial}{\partial z} & 0 & \dfrac{\partial}{\partial r} \\ \dfrac{1}{r}\dfrac{\partial}{\partial \theta} & \dfrac{\partial}{\partial r} - \dfrac{1}{r} & 0 \end{bmatrix}, \tag{A.13}$$

and the divergence of stress

$$\nabla \cdot \boldsymbol{\sigma} = \begin{bmatrix} \frac{\partial}{\partial r} + \dfrac{1}{r} & -\dfrac{1}{r} & 0 & 0 & \dfrac{\partial}{\partial z} & \dfrac{1}{r}\dfrac{\partial}{\partial \theta} \\ 0 & \dfrac{1}{r}\dfrac{\partial}{\partial \theta} & 0 & \dfrac{\partial}{\partial z} & 0 & \dfrac{\partial}{\partial r} + \dfrac{2}{r} \\ 0 & 0 & \dfrac{\partial}{\partial z} & \dfrac{1}{r}\dfrac{\partial}{\partial \theta} & \dfrac{\partial}{\partial r} + \dfrac{1}{r} & 0 \end{bmatrix} \begin{bmatrix} \sigma_{rr} \\ \sigma_{\theta\theta} \\ \sigma_{zz} \\ \sigma_{\theta z} \\ \sigma_{rz} \\ \sigma_{r\theta} \end{bmatrix}. \tag{A.14}$$

Bessel functions recurrence relations

$$Z_{n+1}(x) = \frac{2n}{x} Z_n(x) - Z_{n-1}(x), \tag{A.15}$$

$$Z_n'(x) = \frac{n}{x} Z_n(x) - Z_{n+1}(x), \tag{A.16}$$

where $Z_n(x)$ is a J_n or Y_n Bessel function

Appendix B

Elasticity relations in cylindrical coordinates

Strain-displacement relations

$$\nabla_s u = \begin{bmatrix} \dfrac{\partial}{\partial r} & 0 & 0 \\ \dfrac{1}{r} & \dfrac{1}{r}\dfrac{\partial}{\partial \theta} & 0 \\ 0 & 0 & \dfrac{\partial}{\partial z} \\ 0 & \dfrac{\partial}{\partial z} & \dfrac{1}{r}\dfrac{\partial}{\partial \theta} \\ \dfrac{\partial}{\partial z} & 0 & \dfrac{\partial}{\partial r} \\ \dfrac{1}{r}\dfrac{\partial}{\partial \theta} & \dfrac{\partial}{\partial r} - \dfrac{1}{r} & 0 \end{bmatrix} \begin{bmatrix} u_r \\ u_\theta \\ u_z \end{bmatrix} = \begin{bmatrix} e_{rr} \\ e_{\theta\theta} \\ e_{zz} \\ 2e_{\theta z} \\ 2e_{rz} \\ 2e_{r\theta} \end{bmatrix}. \tag{B.1}$$

$$e_{rr} = \frac{\partial u_r}{\partial r} \tag{B.2a}$$

$$e_{\theta\theta} = \frac{u_r}{r} + \frac{1}{r}\frac{\partial u_\theta}{\partial \theta} \tag{B.2b}$$

$$e_{zz} = \frac{\partial u_z}{\partial z} \tag{B.2c}$$

$$e_{\theta z} = \frac{1}{2}(\frac{\partial u_\theta}{\partial z} + \frac{1}{r}\frac{\partial u_z}{\partial \theta}) \tag{B.2d}$$

$$e_{rz} = \frac{1}{2}(\frac{\partial u_r}{\partial z} + \frac{\partial u_z}{\partial r}) \tag{B.2e}$$

$$e_{r\theta} = \frac{1}{2}(\frac{1}{r}\frac{\partial u_r}{\partial \theta} + \frac{\partial u_\theta}{\partial r} - \frac{u_\theta}{r}) \tag{B.2f}$$

Hooke's law

$$\sigma_{rr} = \lambda\Delta + 2\nu e_{rr} \tag{B.3a}$$

$$\sigma_{\theta\theta} = \lambda\Delta + 2\nu e_{\theta\theta} \tag{B.3b}$$

$$\sigma_{zz} = \lambda\Delta + 2\mu e_{zz} \tag{B.3c}$$

$$\sigma_{\theta z} = 2\mu e_{\theta z} \tag{B.3d}$$

$$\sigma_{rz} = 2\nu e_{rz} \tag{B.3e}$$

$$\sigma_{r\theta} = 2\mu e_{r\theta} \tag{B.3f}$$

where $\Delta = e_{rr} + e_{\theta\theta} + e_{zz}$

Displacements of longitudinal modes

$$\begin{aligned} u_r =& A[n/rZ_n(\alpha r) - \alpha\lambda_1 Z_{n+1}(\alpha r)] + B[n/rW_n(\alpha r) - \alpha W_{n+1}(\alpha r)] \\ &+ i\xi A_1 Z_{n+1}(\beta r) + i\xi B_1 W_{n+1}(\beta r), \\ u_z =& Ai\xi Z_n(\alpha r) + Bi\xi W_n(\alpha r) - A_1\beta Z_n(\beta r) - B_1\beta\lambda_2 W_n(\beta r) \end{aligned} \tag{B.4}$$

Wavenumbers relation

$$\frac{\lambda}{\mu}\xi^2 + 2\alpha^2 + \frac{\lambda}{\mu}\alpha^2 = (\beta^2 - \xi^2), \tag{B.5}$$

where λ, μ are the Lame constants, and α, β are defined as $\alpha^2 = \omega^2/v_c^2 - \xi^2$, $\beta^2 = \omega^2/v_s^2 - \xi^2$. (Eq. 2.15).

Appendix C

Finite difference approximations

The Taylor expansion of the unknown value of the function at the point x_{i+1}

$$f(x_{i+1}) = f(x_i) + \Delta x f'(x) + \frac{\Delta x^2}{2!} f"(x_i) + ... + \frac{\Delta x^n}{n!} f^{(n)}(x_i), \tag{C.1}$$

where the $\Delta x = x_{i+1} - x_i$ is the distance between the points and f' denotes the differentiation.

Forward difference estimate

$$f'(x_i) = \frac{f(x_{i+1}) - f(x_i)}{\Delta x}. \tag{C.2}$$

Similarly the formulas for second order derivatives can be obtained as

$$f''(x_i) = \frac{f(x_{i+1}) - 2f(x_i) + f(x_{i-1})}{(\Delta x)^2} \quad \text{or} \quad f''(x_i) = 2! \frac{f(x_{i+1}) - f(x_i) - \Delta x f'(x_i)}{(\Delta x)^2}. \tag{C.3}$$

For a two-dimensional square grid of points (i, j)

$$\begin{aligned} f,ij &= \frac{f(i+1,j+1) - f(i-1,j+1) - f(i+1,j-1) + f(i-1,j-1)}{4(\Delta x)^2}, \\ &\text{also} \\ f,ij &= \frac{f(i+1,j+1) - f(i+1,j) - f(i,j+1) + f(i,j)}{(\Delta x)^2}, \end{aligned} \tag{C.4}$$

f, ij denotes second order mixed derivative with respect to i, j.

Appendix D

Repeatability study of the enhancement effect experiment

The results presented here, are a part of enhancement effect experiment discussed in section 5.5.3 of chapter 5. An aluminium hollow cylinder of a length of 500 mm, an inner diameter of 100 mm and an outer diameter transition from 200 mm to 180 mm at 300 mm was examined. In total six Macro Fiber Composite transducers were bonded to the inner surface of the cylinder in the locations as shown in figure 6.20. The transducers were cut into active dimensions of 5 mm$\times$14 mm and bonded to the inner surface of the cylinder with cyanoacrylate adhesive.

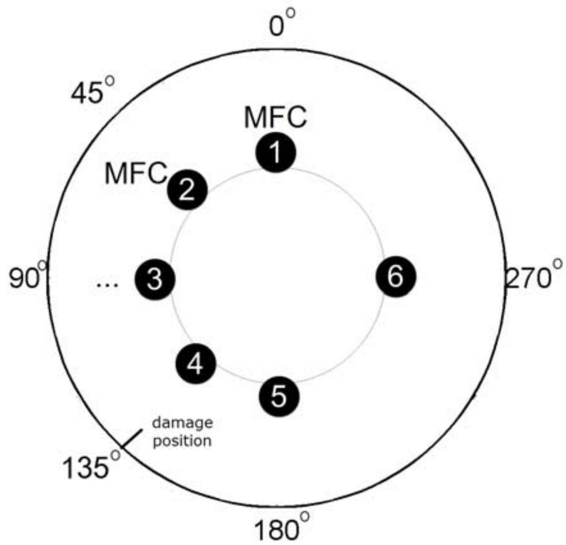

Figure D.1: Graphical representation of the angular locations of Macro Fiber Composite(MFC) actuators.

For the measurements, eight –equally spaced around the inner circumference– circular PZT-disc transducers with a diameter of 8 mm and a thickness of 0.48 mm were mounted at the bore of the cylinder, at the axial distance of 316 mm from the cylinder end. Six of these sensors were aligned with the MFC actuators and two additional sensors were bonded at angular positions of 225° and 315°. The structure was excited with an eight cycle Hanning windowed sine signal with a central frequency of 365 kHz.

Figure D.2 compares the results acquired from various actuator-sensor pairs. Significant differences in the obtained waveforms can be seen, which indicates that the location and the quality of bonding of the transducers have considerable influence on the signals. Nonetheless, based on the arrival time of the wave packages the entrancement effect expected around 0.15 ms can be identified in particular for paths 2, 3 and 4.

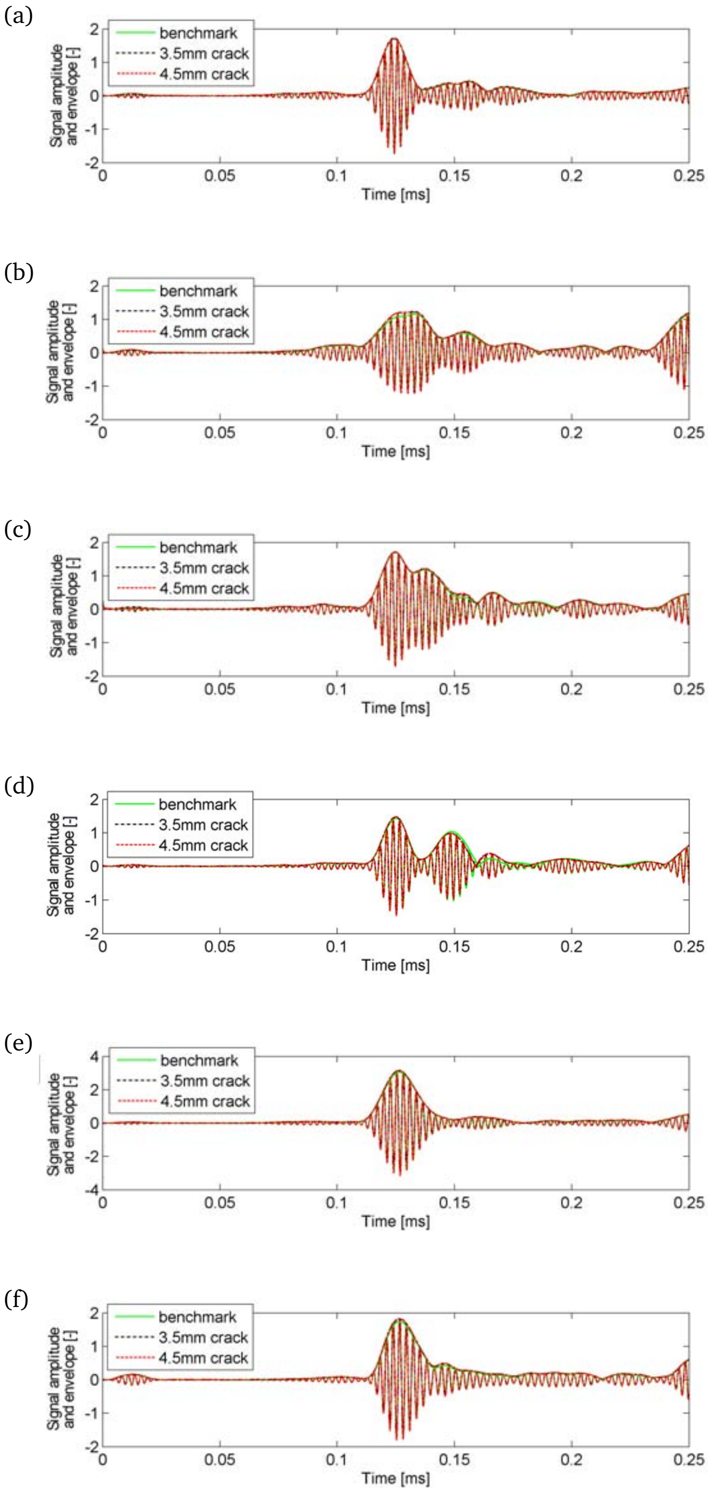

Figure D.2: Experimental results for six actuator-sensor pairs. The envelopes of the measured signals for pristine and damaged cases, plots (a) to (f) corresponds respectively to actuator locations 1 to 6 in figure D.1

Bibliography

[1] J. D. Achenbach, A. K. Gautesen, and D. A. Mendelsohn. Ray analysis of surface-wave interaction with an edge crack. *Transitions on sonics and ultrasonics*, SU-27(3):124–129, 1980.

[2] D. N. Alleyne and P. Cawley. A 2-dimensional fourier transform method for the quantitative measurement of lamb modes. In *in Proceedings of the IEEE Ultrasonics Symposium, Honolulu*, volume 2, page 1143–1146, 1990.

[3] D. N. Alleyne and P. Cawley. The excitation of lamb waves in pipes using dry-coupled piezoelectric transducers. *J. Nondestruct. Eval.*, 15(1), 1998.

[4] D. N. Alleyne, M. Lowe, and P. Cawley. The inspection of chemical plant pipework using lamb waves: Defect sensitivity and field experience. In D. Thompson and D. Chimenti, editors, *Review of Progress in Quantitative Nondestructive Evaluation*, pages 1859–1866. Springer US, 1996.

[5] A. E. Armenakas, D. C. Gazis, and G. Hermann. *Free Vibrations of Circular Cylindrical Shells*. Pergamon Press, 1969.

[6] J. Arnold and L. Felsen. Coupled mode theory of intrinsic modes in a wedge. *The Journal of the Acoustical Society of America*, 79(1):31–40, 1986.

[7] B. Auld. *Acoustic fields and waves in solids*, volume II. Krieger Publishing Company, Malabar, Florida, 1973.

[8] P. K. Banerjee and R. Butterfield. *Boundary element methods in engineering science*, volume 17. McGraw-Hill London, 1981.

[9] J. A. Benyon and A. S. Watson. The use of Monte Carlo analysis to increase axle inspection intervals. In *International Wheelset Conference, Rome 2001*.

[10] S. Beretta, A. L. Conte, J. Rudlin, and D. Panggabean. From atmospheric corrosive attack to crack propagation for a1n railway axles steel under fatigue: damage process and detection. *Engineering Failure Analysis*, 47:252–264, 2015.

[11] R. J. Blake and L. J.Bond. Rayleigh wave scattering from surface features: wedges and down-steps. *Ultrasonics*, 28:214–228, 1990.

[12] R. J. Blake and L. J.Bond. Rayleigh wave scattering from surface features: up-steps and troughs. *Ultrasonics*, 30(4):255–265, 1992.

[13] S. Burke and R. Ditchburn. Review of literature on probability of detection for magnetic particle nondestructive testing. Technical report, Maritime Platforms Division Defence Science and Technology Organisation, 2013.

[14] R. Carandente and P. Cawley. The effect of complex defect profiles on the reflection of the fundamental torsional mode in pipes. *NDT & International*, 46:41–47, 2012.

[15] M. Carrara and M. Ruzzene. Frequency-wavenumber design of spiral macro fiber composite directional actuators. In *SPIE Smart Structures and Materials+ Nondestructive Evaluation and Health Monitoring*, pages 94350M–94350M. International Society for Optics and Photonics, 2015.

[16] A. Cavuto, M. Martarelli, G. Pandarese, G. Revel, and E. Tomasini. Experimental investigation by laser ultrasonics for high speed train axle diagnostics. *Ultrasonics*, 55(0):48 – 57, 2015.

[17] L. Cheng and J. Nicolas. Free vibration analysis of a cylindrical shell—circular plate system with general coupling and various boundary conditions. *Journal of Sound and Vibration*, 155(2):231–247, 1992.

[18] V. K. Chillara and C. J. Lissenden. Analysis of second harmonic guided waves in pipes using a large-radius asymptotic approximation for axis-symmetric longitudinal modes. *Ultrasonics*, 53(4):862–869, 2013.

[19] Y. Cho. Estimation of ultrasonic guided wave mode conversion in a plate with thickness variation. *IEEE transactions on ultrasonics, ferroelectrics, and frequency control*, 47(3):591–603, 2000.

[20] Y. Cho and J. L. Rose. A boundary element solution for a mode conversion study on the edge reflection of lamb waves. *The Journal of the Acoustical Society of America*, 99(4):2097–2109, 1996.

[21] Y. Cho and J. L. Rose. An elastodynamic hybrid boundary element study for elastic guided wave interactions with a surface breaking defect. *International Journal of Solids and Structures*, 37(30):4103–4124, 2000.

[22] C. Chree. The equation of an isotropic elastic solid in polar and cylindrical coordinates, their solution and applications. *Transactions of the Cambridge Philosophical Society*, 14, 1889.

[23] A. Clough and R. Edwards. Lamb wave near field enhancements for surface breaking defects in plates. *Journal of Applied Physics*, 11(10):104906, 2012.

[24] A. Clough and R. Edwards. Characterisation of hidden defects using the near-field ultrasonic enhancement of lamb waves. *Ultrasonics*, 59(0):64–71, 2015.

[25] J. A. Collins, H. R. Busby, and G. H. Staab. *Mechanical Design of Machine Elements and Machines*, chapter 9. Wiley, 2010.

[26] R. Courant, K. Friedrichs, and H. Lewy. Über die partiellen differenzengleichungen der mathematischen physik. *Mathematische Annalen*, 100(1):32–74, 1928.

[27] P. P. Delsanto, R. S. Schechter, H. H. Chaskelis, R. B. Mignogna, and R. Kline. Connection machine simulation of ultrasonic wave propagation in materials. II: The two-dimensional case. *Wave Motion*, 20(4):295–314, 1994.

[28] P. P. Delsanto, R. S. Schechter, and R. B. Mignogna. Connection machine simulation of ultrasonic wave propagation in materials III: The three-dimensional case. *Wave Motion*, 26(4):329–339, 1997.

[29] P. P. Delsanto, T. Whitcombe, H. H. Chaskelis, and R. B. Mignogna. Connection machine simulation of ultrasonic wave propagation in materials. I: The one-dimensional case. *Wave motion*, 16(1):65–80, 1992.

[30] A. Demma, P. Cawley, M. Lowe, and A. Roosenbrand. The reflection of the fundamental torsional mode from cracks and notches in pipes. In A. Morassi and F. Vestroni, editors, *Dynamic Methods for Damage Detection in Structures*, volume 499 of *CISM International Centre for Mechanical Sciences*, pages 195–209. Springer Vienna, 2008.

[31] A. Demma, P. Cawley, M. Lowe, A. Roosenbrand, and B. Pavlakovic. The reflection of guided waves from notches in pipes: a guide for interpreting corrosion measurements. *NDT & International*, 37:167–180, 2004.

[32] J. J. Ditri and J. Rose. Excitation of guided waves in hollow cylinders by applied surface tractions. *Journal of Applied Physics*, 7(1):2589–2597, October 1992.

[33] S. Dixon, B. Cann, D. L. Carroll, Y. Fan, and R. S. Edwards. Non-linear enhancement of laser generated ultrasonic Rayleigh waves by cracks. *Nondestructive Testing and Evaluation*, 23(1):25–34, 2008.

[34] B. Dutton, A. Clough, and R. Edwards. Near field enhancements from angled surface defects; a comparison of scanning laser source and scanning laser detection techniques. *Journal of Nondestructive Evaluation*, 30(2):64–70, 2011. Available at *http://dx.doi.org/10.1007/s10921-011-0091-y*.

[35] R. S. Edwards, S. Dixon, and X. Jian. Enhancement of the Rayleigh wave signal at surface defects. *Journal of Physics D: Applied Physics*, 37(16):2291–2297, 2004.

[36] R. S. Edwards, X. Jian, Y. Fan, and S. Dixon. Signal enhancement of the in-plane and out-of-plane rayleigh wave components. *Applied Physics Letters*, 87(19):194104, 2005.

[37] M. E.-C. El-Kettani, F. Luppé, and A. Guillet. Guided waves in a plate with linearly varying thickness: experimental and numerical results. *Ultrasonics*, 42(1–9):807–812, 2004. Proceedings of Ultrasonics International 2003.

[38] A. Erhard, N. Bertus, H. Montag, G. Schenk, and H. Hintze. Ultrasonic phased array system for railroad axle examination. *Journal of Nondestructive Testing*, 8(3):1–6, 2003.

[39] C. A. Felippa. Introduction to finite element methods. *Course Notes, Department of Aerospace Engineeing Sciences, University of Colorado at Boulder*, 2004.

[40] D. C. Gazis. Three-dimentional investigation of the propagation of waves in hollow circular cilinders. I. Analytical Foundation ,II. Numerical Results. *Journal of Acoustic Society of America*, 31(5):568–578, 1959.

[41] S. Gopalakrishnan, M. Ruzzene, and S. Hanagud. Spectral finite element method. In *Computational Techniques for Structural Health Monitoring*, pages 177–217. Springer, 2011.

[42] K. F. Graff. *Wave motion in elastic solids*. Dover Publications, INC., New York, 1991.

[43] D. Gridin, R. Craster, J. Fong, M. Lowe, and M. Beard. The high-frequency asymptotic analysis of guided waves in a circular elastic annulus. *Wave Motion*, 38(1):67–90, 2003.

[44] V. T. Grinchenko and G. L. Komissarova. Properties of surface waves in an elastic hollow cylinder. *Acoustic bulletin*, 7(3):39–48, 2004.

[45] Z. Hamitouche, M. El-Kettani, J.-L. Izbicki, and H. Djelouah. Reflection at the cut-off and transmission by tunnel effect in a waveguide with linear section variation. *Acta Acustica united with Acustica*, 95(5):789–794, 2009.

[46] T. R. Hay and J. L. Rose. Flexible PVDF comb transducers for excitation of axisymmetric guided waves in pipe. *Sensors and Actuators A: Physical*, 100(1):18–23, 2002.

[47] T. Hayashi, K. Kawashima, Z. Sun, and J. Rose. Analysis of flexural mode focusing by semianalytical finite element method. *Journal of Acoustical Society of America*, 113(3):1241–1248, 2003.

[48] T. Hayashi, K. Kawashima, Z. Sun, and J. L. Rose. Analysis of flexural mode focusing by a semianalytical finite element method. *The Journal of the Acoustical Society of America*, 113(3):1241–1248, 2003.

[49] T. Hayashi, W.-J. Song, and J. L. Rose. Guided wave dispersion curves for a bar with an arbitrary cross-section, a rod and rail example. *Ultrasonics*, 41(3):175–183, 2003.

[50] G. Hermann and I. Mirsky. Three-dimensional and shell theory analysis of axially-symmetric motion of cylinders. *Journal of the Acoustical Society of America*, 23:563–658, 1956.

[51] A.-C. Hladky-Hennion. Finite element analysis of acoustic waves in waveguides. *Journal of Sound and Vibration*, 194(2):119–136, 1996.

[52] D. Hoddinott. Railway axle failure investigations and fatigue crack growth monitoring of an axle. *Proceedings of the Institution of Mechanical Engineers, Part F: Journal of Rail and Rapid Transit*, 218(4):283–292, 2004.

[53] C. Klinger and D. Bettge. Axle fracture of an ICE3 high speed train. *Engineering Failure Analysis*, 35:66–81, 2013.

[54] T. Kundu. *Ultrasonic Nondestructive Evaluation: Engineering and Biological Material Characterization*. Boca Raton, FL : CRC Press, 2004.

[55] H. Lamb. On the propagation of tremors over the surface of an elastic solid. *Philosophical Transactions of the Royal Society of London A: Mathematical, Physical and Engineering Sciences*, 203(359-371):1–42, 1904.

[56] H. Lamb. On waves in an elastic plate. *Philosophical Transactions of the Royal Society of London. Series A*, page 114–128, 1917.

[57] F. Li, X. Sun, J. Qiu, L. Zhou, H. Li, and G. Meng. Guided wave propagation in high-speed train axle and damage detection based on wave mode conversion. *Structural Control and Health Monitoring*, 2015.

[58] J. Li and J. Rose. Excitation and propagation of non-axisymmetric guided waves in a hollow cylinder. *Journal of Acoustical Society of America*, 109(2):457–464, 2001.

[59] J. Li and J. L. Rose. Angular-profile tuning of guided waves in hollow cylinders using a circumferential phased array. *IEEE Transactions on Ultrasonics, Ferroelectrics, and Frequency Control*, 49(12):1720–1729, 2002.

[60] J. Li and J. L. Rose. Natural beam focusing of non-axisymmetric guided waves in large-diameter pipes. *Ultrasonics*, 44:35–45, 2006.

[61] G. Liu and J. Qu. Guided circumferential waves in a circular annulus. *Journal of Applied Mechanics*, 65(2), 1998.

[62] G.-R. Liu and S. S. Quek. *The finite element method: a practical course*. Butterworth-Heinemann, 2013.

[63] Y. Liu, E. Khajeh, C. J. Lissenden, and J. L. Rose. Interaction of torsional and longitudinal guided waves in weakly nonlinear circular cylinders. *The Journal of the Acoustical Society of America*, 133(5), 2013.

[64] Y. Liu, E. Khajeh, C. J. Lissenden, and J. L. Rose. Higher order interaction of elastic waves in weakly nonlinear hollow circular cylinders. II. Physical interpretation and numerical results. *Journal of Applied Physics*, 115(21):214902, 2014.

[65] Y. Liu, Z. Li, and K. Gong. Detection of a radial crack in annular structures using guided circumferential waves and continuous wavelet transform. *Mechanical Systems and Signal Processing*, 30(0):157 – 167, 2012.

[66] Y. Liu, C. J. Lissenden, and J. L. Rose. Higher order interaction of elastic waves in weakly nonlinear hollow circular cylinders. I. Analytical foundation. *Journal of Applied Physics*, 115(21):214901, 2014.

[67] Z. Liu, Q. Xu, Y. Gong, C. He, and B. Wu. A new multichannel time reversal focusing method for circumferential Lamb waves and its applications for defect detection in thick-walled pipe with large-diameter. *Ultrasonics*, 54(7):1967 – 1976, 2014.

[68] G. Lutenco, V. Uchanin, V. Mishchenko, and A. Opanasenko. Eddy currents versus magnetic particles. In *18th World Conference on Nondestructive Testing, 16-20 April 2012, Durban, South Africa*.

[69] A. Løvstad and P. Cawley. The reflection of the fundamental torsional guided wave from multiple circular holes in pipes. *NDT & E International*, 44(7):553 – 562, 2011.

[70] A. Løvstad and P. Cawley. The reflection of the fundamental torsional mode from pit clusters in pipes. *NDT & E International*, 46(0):83 – 93, 2012.

[71] M. Maass, W. A. Deutsch, and F. Bartholomai. Magnetic particle inspection on train components. In *11th European Conference on Non-Destructive Testing (ECNDT), October 6-10, 2014, Prague, Czech Republic*.

[72] K. Makino and S. Biwa. Influence of axle–wheel interface on ultrasonic testing of fatigue cracks in wheelset. *Ultrasonics*, 53(1):239–248, 2013.

[73] P. N. Marty and G. Engl. Latest development in the UT inspection of train wheels and axles. In *18th World Conference on Nondestructive Testing, 16-20 April 2012, Durban, South Africa*.

[74] J. McFadden. Radial vibrations of thick-walled hollow cylinders. *The Journal of the Acoustical Society of America*, 26(5):714–715, 1954.

[75] R. D. Mindlin. Waves and Vibrations in Isotropic, Elastic Plates. In *The Collected Papers of Raymond D. Mindlin*, volume 1, pages 425–458. 1960.

[76] C. Mineo, D. Cerniglia, and A. Pantano. Numerical study for a new methodology of flaw detection in train axles. *Ultrasonics*, 54(3):841–9, March 2014.

[77] G. Mohr and P. Holler. On inspection of thin-walled tubes for transverse and longitudinal flaws by guided ultrasonic waves. *IEEE Transitions on Sonics and Ultrasonics*, SU-23(5), 1976.

[78] R. Morgan, K. Gonzales, E. Smith, and B. Smith. Remotely detecting cracks in moving freight railcar axles. final report safety idea project 08. Technical report, Transportation Technology Center, Inc. a Subsidiary of the Association of American Railroads, 2006.

[79] M. Munasinghe and G. W. Farnell. Finite difference analysis of rayleigh wave scattering at vertical discontinuities. *Journal of geophysical research*, 78(14):2454–2466, 1973.

[80] G. Narayanan and D. Beskos. Use of dynamic influence coefficients in forced vibration problems with the aid of fast fourier transform. *Computers & Structures*, 9(2):145–150, 1978.

[81] N. Nicholson and W. McDicken. Mode propagation of ultrasound in hollow waveguides. *Ultrasonics*, 29(5):411–416, 1991.

[82] A. Oppenheim, A. Willsky, and I. Young. *Signals and Systems*, volume 1. 1997.

[83] P. Packo, T. Bielak, A. Spencer, T. Uhl, W. Staszewski, K. Worden, T. Barszcz, P. Russek, and K. Wiatr. Numerical simulations of elastic wave propagation using graphical processing units—comparative study of high-performance computing capabilities. *Computer Methods in Applied Mechanics and Engineering*, 290:98–126, 2015.

[84] P. Packo, T. Bielak, A. B. Spencer, W. J. Staszewski, T. Uhl, and K. Worden. Lamb wave propagation modelling and simulation using parallel processing architecture and graphical cards. *Smart Materials and Structures*, 21(7), 2012.

[85] Y.-H. Pao and R. Mindlin. Dispersion of flexural waves in an elastic, circular cylinder. *Journal of Applied Mechanics*, 27(3):513–520, 1960.

[86] B. Pavlakovic. *Leaky guided ultrasonic waves in NDT*. PhD thesis, Mechanical Engineering Department, Imperial College London, 1998.

[87] L. Pochhammer. Uber die fortpflanzungsgeschwindigkeiten kleiner schwingungen in unbegrenzten isotropen kreiszylinder (On the propagation velocities of small vibrations in an infinite isotropic cylinder). *Journal für die Reine und Angewandte Mathematik*, 81, 1876.

[88] K. Portz, G. I. Stegeman, and A. A. Maradudin. Rayleigh wave reflection at plate edges. *Applied Physics Letters*, 38(11), 1981.

[89] W. H. Press, S. A. Teukolsky, W. T. Vetterling, and B. P. Flannery. *Numerical Recipes in C: The Art of Scientific Computing*, volume II. Cambridge University Press, 1973.

[90] A. Puckett. *An experimental and theoretical investigation of axially symmetric wave propagation in thick cylindrical waveguides*. PhD thesis, University of Maine, Orono, ME, 2004.

[91] A. D. Puckett and M. Peterson. A semi-analytical model for predicting multiple propagating axially symmetric modes in cylindrical waveguides. *Ultrasonics*, 43(3):197–207, 2005.

[92] P. Puthillath, J. M. Galan, B. Ren, C. J. Lissenden, and J. L. Rose. Ultrasonic guided wave propagation across waveguide transitions: Energy transfer and mode conversion. *The Journal of the Acoustical Society of America*, 133(5):2624–2633, 2013.

[93] A. Quinn, M. Hayward, C. Baker, F. Schmid, J. Priest, and W. Powrie. A full-scale experimental and modelling study of ballast flight under high-speed trains. *Proceedings of the Institution of Mechanical Engineers, Part F: Journal of Rail and Rapid Transit*, 224(2):61–74, 2010.

[94] L. Rayleigh. On waves propagated along the plane surface of an elastic solid. *Proceedings of the London Mathematical Society*, 17:4–11, 1885.

[95] L. Rayleigh. On the free vibrations of an infinite plate of homogeneous isotropic elastic matter. 20(357):225–237, 1889.

[96] M. Redwood. Velocity and attenuation of a narrow-band, high-frequency compressional pulse in a solid wave guide. *The Journal of the Acoustical Society of America*, 31(4):442–448, 1959.

[97] M. Redwood and J. Lamb. On the propagation of high frequency compressional waves in isotropic cylinders. *Proceedings of the Physical Society*, 70(1):136–143, 1957.

[98] F. Richart, R. Woods, and J. Hall. *Vibrations of Soils and Foundations*. Prentice Hall, Engelwood Cliffs, USA., 1970.

[99] J. Rose. *Ultrasonic Guided Waves in Solid Media*. Cambridge University Press, 2014.

[100] R. Rosenberg and R. Thurston. Relationship between plate and surface modes of a tube. *The Journal of the Acoustical Society of America*, 61(6):1499–1502, 1977.

[101] J. Rudlin. Report on NDT performance (various techniques) for conventional wheelsets. D6.2.1: Inspection performance of axle inspection methods on existing designs. D6.2.2: use of inspection performance information for new axle design. european project "Wheelset integrated design and effective maintenance (WIDEM)", 2008. Available at: *http://www.widem.org/file.php?id=53{&}save_dialogue=1*.

[102] J. Rudlin. Final report summary - whole life rail axle assessment and improvement (WOLAXIM) project. Technical report, European Union, 2015. Available at *http://cordis.europa.eu/result/rcn/62072_en.html*.

[103] J. Rudlin, A. Raude, and U. V. nad Antonietta Lo Cinte. New Methods of Rail Axle Inspection and Assessment. In *18th World Conference on Nondestructive Testing, 16-20 April 2012, Durban, South Africa*.

[104] W. Sachse and Y. Pao. On the determination of phase and group velocities of dispersive waves in solids. *Journal of Applied Physics*, 49(8), 1978.

[105] N. Saffari and L. Bond. Body to Rayleigh wave mode-conversion at steps and slots. *Journal of Nondestructive Evaluation*, 6(1):1–22, 1987.

[106] M. G. Silk and K. F. Bainton. The propagation in metal tubing of ultasonic wave modes equivalent to Lamb waves. *Ultrasonics*, 17(1):11–19, January 1979.

[107] R. Smith. Fatigue of railway axles: a classic problem revisited. *European Structural Integrity Society*, 26:173–181, 2000.

[108] P. Sriram, S. Hanagud, and J. I. Craig. Scanning laser Doppler techniques for vibration testing. *Experimental Techniques*, 16(6):21–26, 1992.

[109] A. B. Stanbridge and D. J. Ewins. Modal testing using a scanning laser doppler vibrometer. *Mech. Syst. Signal Process.*, 13:255–70, 1999.

[110] W. Staszewski. Structural health monitoring using guided ultrasonic waves. In J. Holnicki-Szulc and C. Soares, editors, *Advances in Smart Technologies in Structural Engineering*, volume 1 of *Computational Methods in Applied Sciences*, pages 117–162. Springer Berlin Heidelberg, 2004.

[111] W. J. Staszewski, B. C. Lee, and R. Traynor. Fatigue crack detection in metallic structures with lamb waves and 3d laser vibrometry. *Measurement Science and Technology*, 18(3):727, 2007.

[112] T. Stepinski, T. Uhl, and W. Staszewski. *Advanced Structural Damage Detection: From Theory to Engineering Applications*. Wiley, 2013.

[113] Z. Sun, L. Zhang, and J. Rose. Flexural torsional guided wave mechanics and focusing in pipe. *SME. J. Pressure Vessel Technol.*, 127(4):471–478, 2005.

[114] The European Railway Agency. European visual inspection catalogue (EVIC) implementation guide, 2010. Available at *http://jsgrail.eu/download.asp?item_id=142*.

[115] The European Railway Agency. Railway safety performance in the european union, 2011. Available at *http://www.era.europa.eu/Document-Register/Documents/Safety-Performance-Report-2011.pdf*.

[116] The European Railway Agency. Railway safety performance in the european union, 2014. Available at: *http://www.era.europa.eu/Document-Register/Documents/SPR2014.pdf*.

[117] R. Thompson, G. Alers, and M. Tennison. Application of direct electromagnetic lamb wave generation to gas pipeline inspection. *New York: Ultrasonic Symposium Proceedings, IEEE,*, page 91–93, 1972.

[118] I. Tolstoy and E. Usdin. Wave propagation in elastic plates: Low and high mode dispersion. *Journal of Acoustic Society of America*, 29(1):37–42, 1957.

[119] C. Valle, M. Niethammer, J. Qu, and L. Jacobs. Crack characterization using guided circumferential waves. *The Journal of the Acoustical Society of America*, 110(3), 2001.

[120] I. A. Veres, T. Berer, C. Grünsteidl, and P. Burgholzer. On the crossing points of the lamb modes and the maxima and minima of displacements observed at the surface. *Ultrasonics*, 54(3):759–762, 2014.

[121] I. A. Viktorov. *Rayleigh and Lamb waves: physical theory and applications*. Plenum Press, 1970.

[122] W. K. Wilkie, R. G. Bryant, J. W. High, R. L. Fox, R. F. Hellbaum, A. Jalink, Jr., B. D. Little, and P. H. Mirick. Low-cost piezocomposite actuator for structural control applications. volume 3991, pages 323–334, 2000.

[123] C. Willberg, S. Duczek, J. Vivar-Perez, and Z. Ahmad. Simulation methods for guided wave-based structural health monitoring: A review. *Applied Mechanics Reviews*, 67(1):010803, 2015.

[124] U. Zerbst and S. Beretta. Failure and damage tolerance aspects of railway components. *Engineering Failure Analysis*, 18(2):534–542, 2011.

[125] U. Zerbst, S. Beretta, G. Köhler, A. Lawton, M. Vormwald, H. T. Beier, C. Klinger, I. Černỳ, J. Rudlin, T. Heckel, et al. Safe life and damage tolerance aspects of railway axles – a review. *Engineering Fracture Mechanics*, 98:214 – 271, 2013.

[126] U. Zerbst, C. Klinger, and D. Klingbeil. Structural assessment of railway axles–a critical review. *Engineering Failure Analysis*, 35:54–65, 2013.

[127] U. Zerbst, K. Mädler, and H. Hintze. Fracture mechanics in railway applications—-an overview. *Engineering Fracture Mechanics*, 72(2):163–194, 2005.

[128] U. Zerbst, M. Schödel, and H. T. Beier. Parameters affecting the damage tolerance behaviour of railway axles. *Engineering Fracture Mechanics*, 78(5):793–809, 2011.

[129] X. Zhao and J. L. Rose. Guided circumferential shear horizontal waves in an isotropic hollow cylinder. *The Journal of the Acoustical Society of America*, 115(5), 2004.

[130] C. Zhou, Z. Su, and L. Cheng. Probability-based diagnostic imaging using hybrid features extracted from ultrasonic lamb wave signals. *Smart Materials and Structures*, 20(12):125005, 2011.

[131] O. C. Zienkiewicz and R. L. Taylor. *The finite element method*, volume 3. McGraw-hill London, 1977.